Absolute Quantification of Human In Vivo Hepatic ^{31}P Magnetic Resonance Spectroscopy at 7 Tesla

by

Lucian A. B. Purvis

A thesis submitted in partial fulfilment of the requirements for the degree of
Doctor of Philosophy

Hilary Term 2018

University of Oxford

Oxford Centre for Clinical Magnetic Resonance Research

and

St Cross College

Abstract

Absolute Quantification of Human In Vivo Hepatic ^{31}P Magnetic Resonance Spectroscopy at 7 Tesla

Lucian A. B. Purvis
Oxford Centre for Clinical Magnetic Resonance Research and St Cross College.
Abstract of a thesis submitted for the degree of Doctor of Philosophy.
Hilary Term 2018

Phosphorus (^{31}P) metabolites are emerging liver disease biomarkers. This work aims to develop a quantification protocol for human hepatic ^{31}P magnetic resonance spectroscopy (MRS) at 7 tesla (T). It should have high SNR, deliver robust measurements of metabolite concentrations with high reproducibility, and be feasible to use in clinical studies. This will allow detailed characterization of liver metabolism in diseases such as cirrhosis, increasing the utility of ^{31}P-MRS as a clinical tool.

A 3D chemical shift imaging method using a 16 channel ^{31}P array at 7 T is chosen to give high SNR ^{31}P spectra from the human liver in vivo, while also providing good spatial localization and spectral resolution.

The Oxford Spectroscopy Analysis (OXSA) toolbox, our MATLAB-based processing software package, is introduced and adaptations for analysis of liver spectra are described.

Five volunteers were scanned to determine T_1s for the ten visible ^{31}P metabolites. Simulations were used to determine design criteria for calibration phantoms at 1.5, 3 and 7 T. I compare three candidate approaches to give “absolute” concentrations in mmol/L wet tissue using a 10 cm loop coil, and then extend these approaches to data acquired using the 16 element receive array.

The final protocol was applied to data acquired in ten healthy volunteers and eleven patients with cirrhosis to determine reproducibility and the differences between healthy and diseased livers. This protocol allows distinction between healthy and cirrhotic livers with 90% specificity and sensitivity, using cut-offs in either γ-adenosine triphosphate or inorganic phosphate concentrations.

This ^{31}P-MRS absolute quantification protocol is an important first step in fully utilising the increased SNR afforded by the 7 T scanner, offering valuable insight into liver metabolism, and paving the way for other novel ^{31}P-MRS methods to be developed in the liver at 7 T.

Acknowledgements

I would not have been able to achieve this without the help of many people. I would like to thank them all for their support, but there are a few that I must mention in particular.

Without the enthusiastic encouragement of my supervisor, Chris Rodgers, I would never have embarked on a Part II in MR, let alone a DPhil. Nothing that I have achieved in the last four and a half years would have been possible without him, and I am hugely grateful.

The day Laci Valkovic arrived in Oxford, he stepped into a role as my co-supervisor (seemingly) without effort. The depth of his knowledge of all things ^{31}P (especially in the liver) has been invaluable. Even as his workload has increased, he has always been willing to offer his advice.

Will Clarke was there to answer my questions on the day I looked round the group, and, despite being a splitter, still finds the time to answer my questions now. Whether in the scanner room, or on the river, he has been a fantastic friend.

Christina Levick, Michael Pavlides, Jeremy Cobbold, and Ellie Barnes were amazingly kind to Chris and me when we started to consider a project in the liver. In the beginning, our knowledge of the liver was limited, and without them we would have had no idea where to start. I would also like to thank them for recruiting patients with liver cirrhosis for us to scan at 7 T as part of the NICOLA study. The best protocol in the world is useless without subjects to scan!

Matt Robson and the OCMR Physics Group have provided support, enthusiasm, and entertainment throughout my project. They have made every day enjoyable, through lunchtime chats, braais, and boardgames, and they have been ‘willing’ volunteers for hours of scanning.

All the staff and students in OCMR have made me feel welcome from the moment I arrived. It has been a pleasure to be a part of this community.

The denizens of 26 Western Road have kept me well fed and watered every night after returning home from work. They celebrated every success with me, and kept me from dwelling on the failures. A South African wedding was a good way to mark the end of an era, and I look forward to a Scottish one too!

I appreciate my sisters’ effort in pretending to be interested in my work, and Mike’s effort in attempting to explain it to them. I am more grateful than I can say for my parents’ support and understanding in all of my decisions.

And lastly, Kirstin’s support means so much to me, whether she is nearby or on the other side of the world.

Contents

List of common abbreviations

^{1}H	proton
^{31}P	Phosphorus-31
ADC	analogue-to-digital conversion
ADP	adenosine diphosphate
AMARES	advanced method for accurate, robust and efficient spectral fitting
AMP	adenosine monophosphate
ATP	adenosine triphosphate
$\boldsymbol{B}$	magnetic field
$\boldsymbol{B}_0$	static magnetic field
$\boldsymbol{B}_1$	oscillating magnetic field
$\boldsymbol{B}_1^+ / \boldsymbol{B}_1^-$	$\boldsymbol{B}_1$ in the positive / negative rotating reference frame
BISTRO	B1-insensitive train to obliterate signal
BMI	body mass index
CoR	coefficient of repeatability
CRLB	Cramér-Rao lower bound
CSA	chemical shift anisotropy
CSI	chemical shift imaging
δ	chemical shift in ppm
DFT	discrete Fourier transform
DICOM	Digital Imaging and Communications in Medicine data format
DRESS	depth-resolved surface coil spectroscopy
EM	electromagnetic
emf	electromotive force
ER	endoplasmic reticulum
FID	free induction decay

FLASH	fast low angle shot
FOV	field of view
FT	Fourier transform
FWHM	full width at half maximum
γ	gyromagnetic ratio
GPC	glycerophosphocholine
GPE	glycerophosphoethanolamine
GRE	gradient echo
HS8	full passage hyperbolic-secant pulse
ICE	image calculation environment
ISIS	image-selected in vivo spectroscopy
jMRUI	java magnetic resonance user interface
k-space	spatial wavelength i.e. Fourier transform of position
LL-CSI	Look-Locker chemical shift imaging
MR	magnetic resonance
MRI	magnetic resonance imaging
MRS	magnetic resonance spectroscopy
$NAD(P)^+$	oxidised form of nicotinamide adenine dinucleotide (phosphate)
NAD(P)H	reduced form of nicotinamide adenine dinucleotide (phosphate)
NAFLD	non-alcoholic fatty liver disease
NOE	nuclear Overhauser effect
OVS	outer volume suppression
OXSA	Oxford Spectroscopy Analysis toolbox
PC	phosphocholine
PCr	phosphocreatine
PDE	phosphodiesters (GPC and GPE)
PE	phosphoethanolamine

PEP	phosphoenol pyruvate
P_i	inorganic phosphate
PME	phosphomonoesters (PC and PE)
PSF	point spread function
PtdC	phosphatidylcholine
PtdE	phosphatidylethanolamine
QA	quality assurance
RF	radiofrequency
RMSE	root mean square error
ROI	region of interest
SAR	specific absorption rate
SD	standard deviation
SNR	signal-to-noise ratio
T	tesla
T_1	spin-lattice relaxation time
T_2	spin-spin relaxation time
T_2^*	apparent T_2
T2DM	type-2 diabetes mellitus
T_A	total acquisition time
τ_c	rotational correlation time
θ	flip angle
TI	inversion time
T_R	repetition time
UDPG	uridine diphosphoglucose
UTE	ultra-short echo time
WSVD	whitened singular value decomposition

1. Introduction

The liver is the largest organ within the body and plays a central role in human metabolism. Besides its main role in homeostasis, it has around 500 functions (1). Metabolism within the liver is therefore complex.

Liver disease is becoming increasingly prevalent (2), and is now estimated to affect more than 10% of adults in Europe and North America (3). In England, mortality primarily due to liver disease was 2% in 2012, with the major causes of death being: alcoholic liver disease, cancer, and other chronic liver diseases (largely fibrosis and cirrhosis) (4). 90% of people who die from liver disease are under 70 years of age, and 70% of people who die from liver disease die in a hospital environment (4). Liver disease occurs in several stages, each of which have different treatment and outcomes (5). As the liver is capable of regeneration, many liver diseases can be treated with simple lifestyle changes if they are caught early enough (6). This makes liver disease an important target for methodologies for early diagnosis and staging of disease.

Liver biopsy is the only accepted standard test for diagnosis of liver disease. However, liver biopsy is invasive, can cause pain and bleeding, and has a non-negligible associated mortality (7). In addition, since liver biopsies sample less than 0.0002% of the liver by mass (8), they suffer undesirable sampling variability (9-11). This variability can be seen in studies of paired biopsies for chronic Hepatitis-C (12, 13), and has been blamed for causing "substantial misdiagnosis and staging inaccuracy" in non-alcoholic fatty liver disease (NAFLD) (14).

Various non-invasive tests have been proposed to replace biopsy. Most of these are based on measuring serum biomarkers or the liver's physical stiffness (15). Fibroscan, a popular tool for diagnosis, uses transient elastography (16). Magnetic resonance elastography, the most effective non-invasive test, has up to 100% sensitivity and 96% sensitivity in detecting cirrhosis (17). However, these approaches have shown only limited power to differentiate between early stages of disease (18, 19). By contrast, proton (^{1}H) magnetic resonance (MR) methods have shown greater potential for differentiating between disease stages (20).

The ^{1}H MR methods that have shown promising results thus far use the environment of water or fat molecules within the liver to diagnose disease severity. But other types of magnetic resonance method can investigate the *metabolism* of the liver directly. In particular, phosphorus-31 MR spectroscopy (^{31}P-MRS) is a promising tool for the study of liver metabolism, for research and clinical purposes.

^{31}P metabolites measured using in vivo MRS are emerging biomarkers for several liver diseases including NAFLD (21-23) and cirrhosis (24), suggesting that ^{31}P-MRS has potential as a diagnostic tool in the liver.

In order to use ^{31}P-MRS to gain insight into the metabolism of the liver, its results must be expressed in consistent, quantitative units. These can either be in “absolute” concentration units, such as mol / L or mol / kg, or ratios relative to other metabolite concentrations. The simplest equation describing absolute quantification using magnetic resonance methods is:

$$S = kN \tag{1.1}$$

where S is the signal intensity, N is the number of spins, and k is the constant of proportionality.

There are five steps in a full absolute quantification process: acquisition, pre-processing, analysis, normalization, and calibration. These can be understood by rewriting Eq. [1.1] as:

$$[\mathrm{m}] = n_{\mathrm{m}} c S_{\mathrm{m}} \qquad [1.2]$$

where [m] is the concentration of metabolite M, n_{m} is the normalization factor for metabolite M, c is the calibration constant, and S_m is the signal due to metabolite M.

Acquisition is the process of excitation and reception of raw MR signals. **Pre-processing** is then required to convert these raw signals into usable data by using a mixture of combination, transformation and filtering methods. **Analysis** of the data is then used to estimate the true signal, i.e. S_{m} in Eq. [1.2].

Normalization is the correction of signal variation due to known inhomogeneity in the methods used to acquire S_{m}. This gives a result that can be compared to other experiments within a site, or even between sites. The normalization factor n_{m} can change considerably between or within scans using the same method.

But even after normalization there is some unknown constant between the result and the concentration in standard units. This is signified by c, the **calibration** constant. The simplest and most accurate method to determine c is to compare the normalized signal of the metabolite to some known calibration standard. c does not change between scans. The metabolite concentration is therefore given by:

$$[\mathrm{m}] = \frac{n_{\mathrm{m}} S_{\mathrm{m}}}{n_{\mathrm{R}} S_{\mathrm{R}}} [\mathrm{R}] \qquad [1.3]$$

where R stands for the reference chosen for calibration.

The more precisely and accurately we can determine metabolite concentrations, the better we will be able to distinguish between disease stages and types where concentrations change, including viral and alcoholic liver disease, cirrhosis, NAFLD, and type-2 diabetes (25). To do this, the errors must be reduced for either the determination of the signal S, or the normalisation n.

In any MR experiment, noise is acquired mixed with the desired signal. One route to reducing the error in S is therefore to improve the signal-to-noise ratio (SNR). For a given set of hardware, there is a trade-off between SNR, the knowledge of where in space the signal arises from (i.e. localization), and the time it takes to acquire the signal. However, the hardware can be improved in order to alleviate this situation, for example by increasing the field strength of the MR scanner. The standard clinical field strength is 1.5 T, with 3 T scanners now also widely available. This work was performed using a research-only whole-body Magnetom 7 T system (Siemens, Erlangen, Germany). Although the first whole-body 7 T scanner was installed in 1999 (26, 27), the technology has taken some time to develop (28). The first paper on ^{31}P-MRS acquired at 7 T was published for the brain in 2003 (29), and for the heart and liver in 2014 (30, 31).

The coil that is used to excite and receive MR signals also has a large effect on SNR. There are many different coil designs, with different strengths and weaknesses. In general, small coils have better SNR but are limited in the region that they can acquire. On the other hand, larger coils can excite the region of interest more uniformly. Fortunately, different coils can be combined to achieve a certain desired performance. The main body of this work was performed using a 16 channel ^{31}P receive array coil (Rapid Biomedical, Germany). Unlike more commonly used single loop coils, this array has a large transmit loop for uniform excitation over a large volume, with 16 small receive loops that have high SNR and can be combined to give good coverage. This means that the array can receive signal from a large region without compromising SNR (32).

Other than improving the acquisition, the errors on S can also be reduced by improving the ability to distinguish the true signal from the noise. In other words, by improving the analysis. The simplest method of analysis involves using a pencil and ruler to measure peak heights on a spectrum, as was done for the first MR scans. The next step up is peak area integration. However, underlying broad resonances, overlapping and low signal-to-noise ratio peaks, and operator error can cause biased or inaccurate results (33). The answer is to use model-based fitting. The level of prior knowledge that can be included in the model depends on the fitting algorithm. Clearly, the more prior knowledge is introduced, the less variation there will be between fits. However, the additional prior knowledge is also likely to introduce bias, so the trade-off between bias and variance must be considered. The fitting algorithm used in this work is based on the *advanced method for accurate, robust and efficient spectral fitting* (AMARES), which has been implemented in the MATLAB programming environment as part of our group's analysis tool, the Oxford Spectroscopy Analysis (OXSA) toolbox (34, 35).

Changing the acquisition methods also requires a change in the normalization methods. As field strength increases, metabolite relaxation times are expected to change (36), and the fields produced by coils become more inhomogeneous (37). The combination of signal received by the array coil must also be considered (38, 39). If these factors can be effectively accounted for, the improvements in the acquisition strategy will become apparent.

1.1. Aims

The aim of this work is to develop a quantification protocol for human hepatic ^{31}P-MRS at 7 T, from acquisition to post-processing. This protocol should have high SNR, and deliver robust measurements of metabolite concentrations with high reproducibility. The protocol should also be feasible to use in clinical studies. This will allow detailed characterization of liver metabolism in diseases such as cirrhosis, increasing the utility of ^{31}P-MRS as a clinical tool.

1.2. Thesis Outline

Chapter 1 has introduced the need for additional tools to aid diagnosis, prognosis and treatment of hepatic disease, and the potential for ^{31}P-MRS at 7 T to fulfil this.

Chapter 2 introduces the background theory required for the quantification of signals in MR spectroscopy, focusing on the acquisition step.

Chapter 3 describes the metabolism of the liver relating to processes that might be visible with ^{31}P-MRS. Normal values of relaxation times and concentrations are given. The chapter then goes on to detail ^{31}P experiments that have already been performed, both in healthy subjects and in patients with liver disease.

Chapter 4 shows the development of a protocol for quantifying ^{31}P-MRS of the liver at 7 T. Acquisition parameters are considered and a long and a short protocol are implemented. Ten healthy volunteers and eleven patients with liver cirrhosis were scanned. The data is processed in later chapters.

Chapter 5 describes the development of, and improvements to, the OXSA toolbox, e.g. the implementation of the Voigt lineshapes into the AMARES algorithm, and feasibility of their use for the analysis of phantom and in vivo data.

Chapter 6 details the determination of T_1 relaxation times of ^{31}P hepatic metabolite at 7 T.

Chapter 7 describes the process developed for normalization and calibration of signal at 7 T. First, the theoretical requirements for the materials used in the phantom are determined using electromagnetic simulations. Transmit and receive sensitivity corrections are then implemented for our simplest RF coil design, a 10 cm transmit/receive loop.

Chapter 8 expands the normalization and calibration processes defined in Chapter 7 to the 16 channel receive array.

In Chapter 9, the quality and repeatability of each of the potential protocols and processing pipelines are determined. A final protocol is chosen.

Chapter 10 applies the optimised protocol in 10 healthy volunteers and 11 patients with liver cirrhosis. The concentrations are compared to literature values. The differences between healthy volunteers and eleven patients with liver cirrhosis are considered.

Chapter 11 summarises the results and discusses them in relation to the aim of this project. Suggestions for future work are presented.

1.3. References

1. Boyer TD, Manns MP, Sanyal AJ, Zakim D. Zakim and Boyer's Hepatology: A Textbook of Liver Disease: Elsevier Health Sciences; 2012.
2. Younossi ZM, Stepanova M, Afendy M, Fang Y, Younossi Y, Mir H, Srishord M. Changes in the Prevalence of the Most Common Causes of Chronic Liver Diseases in the United States From 1988 to 2008. Clinical Gastroenterology and Hepatology. 2011; 9(6):524-30.e1.
3. Blachier M, Leleu H, Peck-Radosavljevic M, Valla D-C, Roudot-Thoraval F. The burden of liver disease in Europe: A review of available epidemiological data. J Hepatol. 2013; 58(3):593-608.
4. Effiong K, Osinowo A, Pring A, Verne J. Deaths from Liver Disease: Implications for end of life care in England. Published by: National End of Life Care Intelligence Network, Department of Health, 2012.
5. Goodman ZD. Grading and staging systems for inflammation and fibrosis in chronic liver diseases. J Hepatol. 2007; 47(4):598-607.
6. Nobili V, Carter-Kent C, Feldstein AE. The role of lifestyle changes in the management of chronic liver disease. Bmc Med. 2011; 9.
7. Rockey DC, Caldwell SH, Goodman ZD, Nelson RC, Smith AD. Liver biopsy. Hepatology. 2009; 49(3):1017-44.
8. Lee RG. General Principles. Diagnostic liver pathology. St. Louis: Mosby-Year Book; 1994. p. 1-21.
9. Maharaj B, Leary WP, Naran AD, Maharaj RJ, Cooppan RM, Pirie D, Pudifin DJ. Sampling variability and its influence on the diagnostic yield of percutaneous needle biopsy of the liver. The Lancet. 1986; 327(8480):523-5.
10. Baunsgaard P, Sanchez GC, Lundborg CJ. The variation of pathological changes in the liver evaluated by double biopsies. Acta Pathol Microbiol Scand A. 1979; 87(1):51-7.
11. Abdi W, Millan JC, Mezey E. Sampling variability on percutaneous liver biopsy. Arch Intern Med. 1979; 139(6):667-9.
12. Skripenova S, Trainer TD, Krawitt EL, Blaszyk H. Variability of grade and stage in simultaneous paired liver biopsies in patients with hepatitis C. J Clin Pathol. 2007; 60(3):321-4.
13. Bedossa P, Dargère D, Paradis V. Sampling variability of liver fibrosis in chronic hepatitis C. Hepatology. 2003; 38(6):1449-57.
14. Ratziu V, Charlotte F, Heurtier A, Gombert S, Giral P, Bruckert E, Grimaldi A, Capron F, Poynard T. Sampling Variability of Liver Biopsy in Nonalcoholic Fatty Liver Disease. Gastroenterology. 2005; 128(7):1898-906.
15. EASL-ALEH Clinical Practice Guidelines: Non-invasive tests for evaluation of liver disease severity and prognosis. J Hepatol. 63(1):237-64.
16. Afdhal NH. Fibroscan (Transient Elastography) for the Measurement of Liver Fibrosis. Gastroenterology & Hepatology. 2012; 8(9):605-7.
17. Sharma S, Khalili K, Nguyen GC. Non-invasive diagnosis of advanced fibrosis and cirrhosis. World J Gastroenterol. 2014; 20(45):16820-30.
18. Friedrich-Rust M, Rosenberg W, Parkes J, Herrmann E, Zeuzem S, Sarrazin C. Comparison of ELF, FibroTest and FibroScan for the non-invasive assessment of liver fibrosis. BMC Gastroenterology. 2010; 10.
19. Tsochatzis EA, Gurusamy KS, Ntaoula S, Cholongitas E, Davidson BR, Burroughs AK. Elastography for the diagnosis of severity of fibrosis in chronic liver disease: A meta-analysis of diagnostic accuracy. J Hepatol. 2011; 54(4):650-9.
20. Banerjee R, Pavlides M, Tunnicliffe EM, Piechnik SK, Sarania N, Philips R, Collier JD, Booth JC, Schneider JE, Wang LM, Delaney DW, Fleming KA, Robson MD, Barnes E, Neubauer S. Multiparametric magnetic resonance for the non-invasive diagnosis of liver disease. J Hepatol. 2014; 60(1):69-77.
21. Abrigo JM, Shen J, Wong VWS, Yeung DKW, Wong GLH, Chim AML, Chan AWH, Choi PCL, Chan FKL, Chan HLY, Chu WCW. Non-alcoholic fatty liver disease: Spectral patterns observed from an in vivo phosphorus magnetic resonance spectroscopy study. J Hepatol. 2014; 60(4):809-15.

22. Valkovič L, Gajdošík M, Traussnigg S, Wolf P, Chmelík M, Kienbacher C, Bogner W, Krebs M, Trauner M, Trattnig S, Krššák M. Application of localized 31P MRS saturation transfer at 7 T for measurement of ATP metabolism in the liver: reproducibility and initial clinical application in patients with non-alcoholic fatty liver disease. Eur Radiol. 2014; 24(7):1602-9.
23. Traussnigg S, Kienbacher C, Gajdošík M, Valkovič L, Halilbasic E, Stift J, Rechling C, Hofer H, Steindl-Munda P, Ferenci P, Wrba F, Trattnig S, Krššák M, Trauner M. Ultra-high-field magnetic resonance spectroscopy in non-alcoholic fatty liver disease: Novel mechanistic and diagnostic insights of energy metabolism in non-alcoholic steatohepatitis and advanced fibrosis. Liver Int. 2017; 37(10):1544-53.
24. Dezortova M, Taimr P, Skoch A, Spicak J, Hajek M. Etiology and functional status of liver cirrhosis by 31P MR spectroscopy. World J Gastroenterol. 2005; 11(44):6926-31.
25. Valkovic L, Chmelik M, Krssak M. In-vivo P-31-MRS of skeletal muscle and liver: A way for non-invasive assessment of their metabolism. Anal Biochem. 2017; 529:193-215.
26. Vaughan JT, Garwood M, Collins CM, Liu W, DelaBarre L, Adriany G, Andersen P, Merkle H, Goebel R, Smith MB, Ugurbil K. 7T vs. 4T: RF power, homogeneity, and signal-to-noise comparison in head images. Magn Reson Med. 2001; 46(1):24-30.
27. Moser E. Ultra-high-field magnetic resonance: Why and when? World J Radiol. 2010; 2(1):37-40.
28. Hennig J. Ultra high field MR: useful instruments or toys for the boys. Magn Reson Mater Phy. 2008; 21(1-2):1-3.
29. Lei H, Zhu XH, Zhang XL, Ugurbil K, Chen W. In vivo P-31 magnetic resonance spectroscopy of human brain at 7 T: An initial experience. Magn Reson Med. 2003; 49(2):199-205.
30. Rodgers CT, Clarke WT, Snyder C, Vaughan JT, Neubauer S, Robson MD. Human cardiac 31P magnetic resonance spectroscopy at 7 Tesla. Magn Reson Med. 2014; 72(2):304-15.
31. Chmelik M, Považan M, Krššák M, Gruber S, Tkačov M, Trattnig S, Bogner W. In vivo 31P magnetic resonance spectroscopy of the human liver at 7 T: an initial experience. NMR Biomed. 2014; 27(4):478-85.
32. Rodgers CT, Clarke WT, Berthel D, Neubauer S, Robson MD. A 16-element receive array for human cardiac ^{31}P MR spectroscopy at 7T. In the Proceedings of the 22rd Annual Meeting of ISMRM, Milan, Italy, 2014. p. 2896.
33. Cady EB. A Reappraisal of the Absolute Concentrations of Phosphorylated Metabolites in the Human Neonatal Cerebral-Cortex Obtained by Fitting Lorentzian Curves to the P-31 Nmr-Spectrum. J Magn Reson. 1991; 91(3):637-43.
34. Vanhamme L, van den Boogaart A, Van Huffel S. Improved method for accurate and efficient quantification of MRS data with use of prior knowledge. J Magn Reson. 1997; 129(1):35-43.
35. Purvis LAB, Clarke WT, Biasiolli L, Valkovic L, Robson MD, Rodgers CT. OXSA: An open-source magnetic resonance spectroscopy analysis toolbox in MATLAB. Plos One. 2017; 12(9):e0185356.
36. Bogner W, Chmelik M, Schmid AI, Moser E, Trattnig S, Gruber S. Assessment of (31)P Relaxation Times in the Human Calf Muscle: A Comparison between 3 T and 7 T In Vivo. Magn Reson Med. 2009; 62(3):574-82.
37. Vaidya MV, Collins CM, Sodickson DK, Brown R, Wiggins GC, Lattanzi R. Dependence of B1− and B1+ field patterns of surface coils on the electrical properties of the sample and the MR operating frequency. Concepts in Magnetic Resonance Part B: Magnetic Resonance Engineering. 2016; 46(1):25-40.
38. Rodgers CT, Robson MD. Coil combination for receive array spectroscopy: Are data-driven methods superior to methods using computed field maps? Magn Reson Med. 2016; 75(2):473-87.
39. Roemer PB, Edelstein WA, Hayes CE, Souza SP, Mueller OM. The NMR Phased Array. Magn Reson Med. 1990; 16(2):192-225.

2. Background MR theory

This chapter describes the background theory required for the quantification of signals in MR spectroscopy, focusing on the acquisition step before introducing some basic aspects of the pre-processing and analysis steps. This theory is explained in many textbooks, but there are a few that have been particularly referenced for this chapter. Levitt's Spin Dynamics and Slichter's Principles of Magnetic Resonance give good introductions to spin interactions in a magnetic field, approached using quantum mechanics (1, 2). Haacke et al.'s Magnetic Resonance Imaging addresses commonly used techniques in MRI (3), and de Graaf's In Vivo NMR Spectroscopy introduces the specific concerns of MRS methods (4).

2.1. Acquisition

2.1.1. Nuclear Spin

Matter in a human MRI scan subject or in a test object is composed of atoms. At the heart of each atom lies an atomic nucleus. Different chemical elements have different types of nucleus. Atomic nuclei have various intrinsic properties, such as their mass, electric charge, and importantly for MRI, nuclear spin. Nuclear spin is a form of angular momentum. Despite the name "spin", it is an intrinsic property of elementary particles, not involving the rotation of any physical object. Because of the way matter combines, spin cancels out in large objects (1). But for small particles, it has many consequences. In particular, any given particle with a nuclear spin quantum number I has $2I$+1 degenerate energy levels. This degeneracy is broken under an external magnetic field giving a splitting of these states, called the nuclear Zeeman splitting. Probing these different energy levels is the basis of MR techniques.

The nuclear angular momentum operator $\hat{\boldsymbol{J}}$, is given in terms of the nuclear spin operator $\hat{\boldsymbol{I}}$ by:

$$\hat{\boldsymbol{J}} = \hbar\hat{\boldsymbol{I}} \qquad [2.1]$$

where $\hbar$ is Planck's constant divided by 2π and the eigenvalues of $\boldsymbol{I}$ are $[I(I+1)]^{1/2}$. The component of the spin in the z-direction is given by:

$$\hat{I}_z = \hbar m \qquad [2.2]$$

where the magnetic quantum number m can have $2I+1$half-integer values.

The electron, neutron and proton are all spin ½. Proton and neutron spins combine in a nucleus to give a total spin according to the Clebsch-Gordon expansion for coupled angular momenta. There are contributions (given by the Clebsch-Gordon coefficients) with the following overall nuclear spins (1, 5):

$$I_3 = I_1 + I_2, I_1 + I_2 - 1, \ldots, I_1 - I_2 \qquad [2.3]$$

In general, these different spin combinations have different nuclear energy levels, and stable nuclei will naturally be found in the lowest of these. For example, ^{12}C, ^{16}O and ^{32}S have $I = 0$ (they are "spin-zero"), proton (^{1}H) and phosphorus-31 (^{31}P) have I = ½ (are "spin-half"), deuterium (^{2}H) and nitrogen-14 (^{14}N) have I = 1 (are "spin-one"), and so on. The difference in energy between the excited state energy level and the ground state is so large that the excited states can be ignored in conventional MR spectroscopy. In contrast, the Zeeman splitting is much smaller than thermal energy and can be probed by low energy electromagnetic fields.

2.1.2. Electromagnetic fields

An electromagnetic wave is formed from an electric field $\boldsymbol{E}$ and a magnetic field $\boldsymbol{B}$. A particle with charge q moving with velocity $\boldsymbol{v}$ within these two fields experiences a force $\boldsymbol{F}$, according to:

$$\boldsymbol{F} = q(\boldsymbol{E} + \boldsymbol{v} \times \boldsymbol{B}) \qquad [2.4]$$

These fields are governed by Maxwell's equations. The macroscopic formulations of Maxwell's equations include two auxiliary fields to simplify the equations, one of which is the magnetic field intensity $\boldsymbol{H}$. Confusingly, both $\boldsymbol{B}$ and $\boldsymbol{H}$ can be referred to as the magnetic field. Adhering to common practise in human in vivo MR, the term magnetic field will only be applied to $\boldsymbol{B}$ throughout the remainder of this thesis.

2.1.3. Magnetism

The manner in which particles interact with an external magnetic field is defined by the magnetic moment vector, which can be deduced to be proportional to spin from the Wigner-Eckart theorem (6).

$$\hat{\boldsymbol{\mu}} = \gamma \hat{\boldsymbol{J}} \qquad [2.5]$$

where $\boldsymbol{J}$ is given by Eq. [2.1]. The proportionality constant γ is called the gyromagnetic ratio, and it is specific to each nuclear isotope.

The magnetic moment can either be permanent or induced. If it is induced, as is the case for most substances, it is proportional to the applied magnetic field.

$$\boldsymbol{\mu}_{\text{induced}} = \frac{V \chi \boldsymbol{B}}{\mu_0} \qquad [2.6]$$

where V is the volume of the object, χ is called the magnetic susceptibility of the material, and μ_0 ($= 4\pi \times 10^{-7}$ Hm^{-1}) is the permeability of free space.

In most materials, the electronic ground state has no net electron spin; and, as a consequence of the Pauli principle, it has no net orbital angular momentum. This means that these materials are weakly diamagnetic ($\chi < 0$) due to electron orbital currents induced by the applied magnetic field. In this case, electronic magnetism can be largely ignored, as it is time independent.

2.1.4. Spins in magnetic fields

Classically, a field $\boldsymbol{B}$ will produce a torque $\boldsymbol{\tau}$ on magnetic moment $\boldsymbol{\mu}$:

$$\boldsymbol{\tau} = \boldsymbol{\mu} \times \boldsymbol{B} \qquad [2.7]$$

Torque is the derivative of angular momentum with respect to time, so combining Eqs [2.5] and [2.7] gives:

$$\frac{\mathrm{d}\boldsymbol{\mu}}{\mathrm{d}t} = \gamma \boldsymbol{\mu} \times \boldsymbol{B} \qquad [2.8]$$

A consequence of this equation is that the magnetic moment precesses around the external magnetic field with unchanging magnitude, i.e. the magnetic moment has fixed magnitude but its direction continually rotates around the $\boldsymbol{B}$ field direction. The angular frequency of this precession, ω, can be deduced, giving the famous Larmor equation:

$$\omega = -\gamma B \qquad [2.9]$$

where the axis of rotation is defined by a left-handed screw rotation around $\boldsymbol{B}$.

The magnetic moment has an associated magnetic potential energy:

$$E = -\boldsymbol{\mu}.\boldsymbol{B} (= \mu B \cos\theta) \qquad [2.10]$$

where θ is the angle between $\boldsymbol{\mu}$ and $\boldsymbol{B}$.

The classical magnetic moment can take any angle $0° \leq \theta \leq 180°$. However, this treatment does not explain the resonance condition that is seen in experiments. For that, we must use a quantum mechanical treatment.

The Hamiltonian gives the interaction of a magnetic moment and an external magnetic field, and is analogous to Eq. [2.10]:

$$\widehat{H} = -\widehat{\boldsymbol{\mu}}.\boldsymbol{B} \qquad [2.11]$$

Taking the field to be B_0 along the z-direction, the Hamiltonian becomes:

$$\widehat{H} = -\gamma\hbar B_0 \hat{I}_z \qquad [2.12]$$

The eigenvalues of this Hamiltonian, which give us the allowed energy levels, are simply multiples of the eigenvalues of $\hat{I}_z$.

$$E = -\gamma\hbar B_0 m_z, \quad m_z = I, I-1, \ldots, -I \qquad [2.13]$$

From Eqs. [2.10] and [2.13], it can be seen that:

$$\cos\theta = \frac{m}{\sqrt{\left\langle \hat{\boldsymbol{I}}^2 \right\rangle}} = \frac{m}{\sqrt{I(I+1)}} \qquad [2.14]$$

For a spin-half nucleus, the two possible angles are 54.7° from the +z and –z directions.

The difference in energy for these two discrete orientations is:

$$\Delta E = \hbar\gamma B_0 \qquad [2.15]$$

This is the resonance condition. The required energy can be transmitted using electromagnetic waves, which have a frequencies according to the Planck-Einstein relation:

$$E = \hbar\omega \qquad [2.16]$$

Combining Eqs [2.15] and [2.16] gives the Larmor equation once more (Eq. [2.9]):

$$\omega_0 = -\gamma B_0 \qquad [2.17]$$

2.1.5. Net magnetization

The previous section explains the interaction between a single spin and a magnetic field. But a typical MR experiment involves many millions of spins. These will be distributed between the different energy levels. The equilibrium population difference can be calculated according to the Boltzmann distribution. So, for a spin-half nucleus:

$$\frac{n_\alpha}{n_\beta} = e^{\frac{\Delta E}{kT}} \qquad [2.18]$$

where k is the Boltzmann constant, and T is the temperature.

The net magnetization $\boldsymbol{M}$ is the sum of all the individual magnetic moments $\boldsymbol{\mu}$. As the magnetic moments are randomly aligned around the z-axis for each energy level, the moments in the xy plane cancel out, leaving a net component parallel to the +z axis. The microscopic magnetic moment in the z-direction can be calculated by combining Eqs [2.1] and [2.5],

$$\mu_z = \gamma\hbar m_z \qquad [2.19]$$

Therefore, as $m_z = ½$ for ^{31}P, at thermal equilibrium the net magnetization is equal to:

$$M_0 = \sum_{i=1}^{n} \mu_i = n_\alpha \mu_z - n_\beta \mu_z = \frac{\gamma\hbar(n_\alpha - n_\beta)}{2} \qquad [2.20]$$

As the energy difference between the two levels is small, a truncated Taylor expression can be used to approximate Eq. [2.18]. By noting that this also means that $n_\alpha \approx n_\beta$, and that $n_\alpha + n_\beta = n$, this can be rewritten:

$$\frac{n_\alpha}{n_\beta} = 1 + \frac{\Delta E}{kT} + \ldots \approx 1 + \frac{\hbar \gamma B_0}{kT} \qquad [2.21]$$

$$n_\alpha - n_\beta \approx n_\beta \frac{\hbar \gamma B_0}{kT} \qquad [2.22]$$

$$n_\alpha - n_\beta \approx \frac{n \hbar \gamma B_0}{2kT} \qquad [2.23]$$

This can be substituted back into Eq. [2.20] to give:

$$M_0 = \gamma^2 \hbar^2 \frac{n B_0}{4kT} \qquad [2.24]$$

2.1.6. Excitation and reception

With the knowledge that the total magnetization is simply the sum of the individual magnetic moments, the motion of the total magnetization under the influence of an external magnetic field can be generalized from Eq. [2.8]:

$$\frac{\mathrm{d}\boldsymbol{M}}{\mathrm{d}t} = \gamma \boldsymbol{M} \times \boldsymbol{B} \qquad [2.25]$$

As was the case for a single spin, this leads to the magnetization precessing around the applied magnetic field.

A precessing nuclear magnetic moment generates a changing magnetic field. According to the Maxwell-Faraday equation, this is associated with an electric field:

$$\nabla \times \boldsymbol{E} = -\frac{\delta \boldsymbol{B}}{\delta t} \qquad [2.26]$$

The simplest way to detect the precessing magnetization is therefore a loop coil, which will have a voltage induced in it.

However, because the net magnetization is built up of many spins, it is not bound to any discrete angle of precession. This means that the ground state of the net magnetization is aligned with the static magnetic field $\boldsymbol{B}_0$. Thus, before a signal can be detected, the magnetization must be “tipped” away from the $\boldsymbol{B}_0$ direction.

This can be achieved by taking a coil and driving a radiofrequency oscillating current through it causing an oscillating $\boldsymbol{B}$ field. This follows from another of Maxwell’s equations:

$$\nabla \times \boldsymbol{B} = \mu_0 (\boldsymbol{J} + \varepsilon_0 \frac{\delta \boldsymbol{E}}{\delta t}) \qquad [2.27]$$

where $\boldsymbol{J}$ is the total current density.

This oscillating field $\boldsymbol{B}_1$ is polarized. A linearly polarized, oscillating magnetic field in the x-direction can be described as:

$$\boldsymbol{B}_{1\mathrm{x}}(t) = B_{1\mathrm{x,max}} \cos(\omega t + \phi)\hat{\boldsymbol{x}} \qquad [2.28]$$

where $B_{1,\mathrm{max}}$ is the maximum amplitude of the applied field, ω is the angular frequency of the $\boldsymbol{B}_1$ field and $\hat{\boldsymbol{x}}$ is the unit vector along the x axis. ϕ is the initial phase of $\boldsymbol{B}_1$. Let us consider the case where $\phi = 0$ so that $B_{1,\mathrm{max}} = B_1(0)$. The field can be decomposed into two circularly polarized fields rotating around the z-axis:

$$\boldsymbol{B}_{1\mathrm{x}}(t) = \frac{B_{1\mathrm{x,max}}(\hat{\boldsymbol{x}} \cos \omega t + \hat{\boldsymbol{y}} \sin \omega t)}{2} + \frac{B_{1\mathrm{x,max}}(\hat{\boldsymbol{x}} \cos \omega t - \hat{\boldsymbol{y}} \sin \omega t)}{2} \qquad [2.29]$$

Given the magnetization’s continuous precession around $\boldsymbol{B}_0$, it is useful to define a new coordinate system to allow us to consider the effect of $\boldsymbol{B}_1$ alone. This new frame of reference rotates around the $\boldsymbol{B}_0$ field with frequency ω’ (see Fig 2.1).

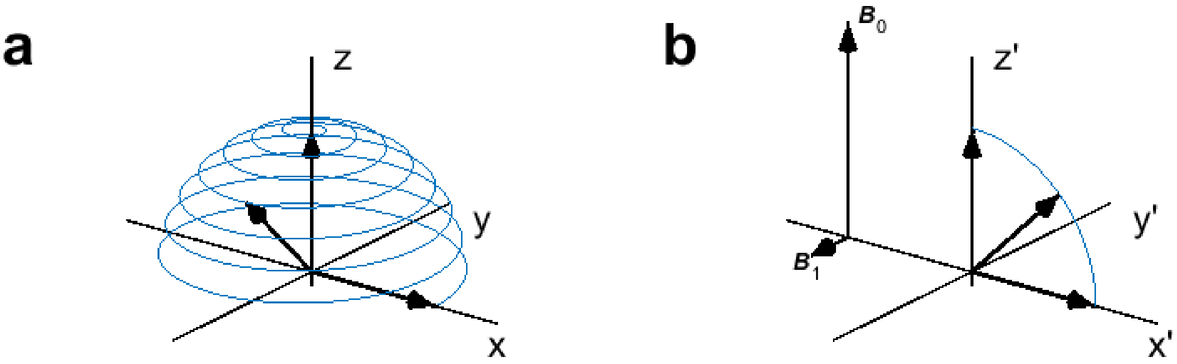

Fig 2.1. Frames of reference. (a) shows excitation in the laboratory frame of reference, and (b) shows the equivalent excitation in the rotating frame of reference.

The unit vectors are then given by:

$$\hat{\boldsymbol{x}} = \hat{\boldsymbol{x}}'\cos\omega' t - \hat{\boldsymbol{y}}'\sin\omega' t$$

$$\hat{\boldsymbol{y}} = \hat{\boldsymbol{y}}'\cos\omega' t + \hat{\boldsymbol{x}}'\sin\omega' t \qquad [2.30]$$

$$\hat{\boldsymbol{z}} = \hat{\boldsymbol{z}}'$$

We can then substitute these terms into Eq. [2.29]:

$$\boldsymbol{B}_{1x}'(t) = \frac{B_{1x,\max}(\hat{\boldsymbol{x}}'\cos(\omega-\omega')t + \hat{\boldsymbol{y}}\sin(\omega-\omega')t)}{2} + \frac{B_{1x,\max}(\hat{\boldsymbol{x}}\cos(\omega+\omega')t - \hat{\boldsymbol{y}}\sin(\omega+\omega')t)}{2} \qquad [2.31]$$

To see the effect of the $\boldsymbol{B}_1$ field on the magnetization, consider the spin's frame of reference precessing around $\boldsymbol{B}_0$, (i.e. $\omega' = \omega_0$). On the timescale of an MR experiment $\omega + \omega_0$ is very fast, and using the rotating wave approximation we can consider only the terms containing $\omega - \omega_0$. In other words, only the field rotating in the same direction as the magnetic moment ($\boldsymbol{B}_1^+$) interacts with it significantly. The effect of the counter-rotating field, sometimes called the Bloch-Siegert shift, is only on the order of $(B_1/2B_0)^2$. This is normally very small as B_1 is on the order of μT and B_0 is on the order of T (7).

Another way to use a rotating reference frame is to have it rotate at the same frequency as the $\boldsymbol{B}_1$ field. Setting $\omega' = \omega$ in Eq. [2.31], we see that:

$$\boldsymbol{B}_{1\mathrm{x}}'(t) = \frac{B_{1\mathrm{x,max}}\hat{\boldsymbol{x}}'}{2} + \frac{B_{1\mathrm{x,max}}(\hat{\boldsymbol{x}}\cos 2\omega t - \hat{\boldsymbol{y}}\sin 2\omega t)}{2} \qquad [2.32]$$

Once more ignoring the rapidly changing $2\omega t$ terms, the time-dependent $\boldsymbol{B}_1(t)$ has become time-independent. This treatment is especially effective in the quantum mechanical analysis of the spins (1, 2). Comparing Eq. [2.28] and Eq. [2.32], it can be seen that an oscillating field in the laboratory frame x-direction becomes a static field of half the magnitude in the rotating frame x-direction:

$$B_{1\mathrm{x}}' = \frac{B_{1\mathrm{x,max}}}{2} \qquad [2.33]$$

The $\boldsymbol{B}_1$ field in the positively rotating reference frame is referred to as $\boldsymbol{B}_1^+$, and is useful in the consideration of the excitation of the magnetization. Equally useful is the $\boldsymbol{B}_1$ field in the negative rotating reference frame $\boldsymbol{B}_1^-$, which is used in the consideration of reception of signal from the precessing magnetization via the "principle of reciprocity" (8). In the case of $\boldsymbol{B}_1^-$, it is the oppositely polarized field that is important.

Another way of thinking about the rotating $\boldsymbol{B}_1$ field is by using complex values:

$$\boldsymbol{B}_1 = B_1 e^{i\omega t} \qquad [2.34]$$

where i = $\sqrt{-1}$. Using this "phasor" notation $\boldsymbol{B}_1$ can be decomposed into complex components along the orthogonal x, y, and z axes in the laboratory frame: $\boldsymbol{B}_{1\mathrm{x}}$, $\boldsymbol{B}_{1\mathrm{y}}$, and $\boldsymbol{B}_{1\mathrm{z}}$. Using this notation, the $\boldsymbol{B}_1^+$ and $\boldsymbol{B}_1^-$ fields are given by (8):

$$\boldsymbol{B}_1^+ = \frac{\boldsymbol{B}_{1\mathrm{x}} + i\boldsymbol{B}_{1\mathrm{y}}}{2} \qquad [2.35]$$

$$\boldsymbol{B}_1^- = \frac{(\boldsymbol{B}_{1\mathrm{x}} - i\boldsymbol{B}_{1\mathrm{y}})^*}{2} = \frac{\boldsymbol{B}_{1\mathrm{x}}^* + i\boldsymbol{B}_{1\mathrm{y}}^*}{2} \qquad [2.36]$$

where the factor of 2 arises from Eq. [2.33]. As both $\boldsymbol{B}_{1\mathrm{x}}$ and $\boldsymbol{B}_{1\mathrm{y}}$ are usually complex, $\boldsymbol{B}_1^+$ and $\boldsymbol{B}_1^-$ are not equivalent.

To calculate the effect of $\boldsymbol{B}_1$ on the total magnetization, Eq. [2.25] can be expanded in three dimensions by defining $\boldsymbol{B}$ as a combination of a B_0 field in the z-direction and the x- and y-components of a $\boldsymbol{B}_1$ field in the other dimensions (as the contribution of $\boldsymbol{B}_1$ in the z-direction can be neglected). This leaves us with the three Bloch equations:

$$\frac{\mathrm{d}M_\mathrm{x}}{\mathrm{d}t} = \gamma\,(M_\mathrm{y}B_0 - M_\mathrm{z}B_{1\mathrm{y}})$$

$$\frac{\mathrm{d}M_\mathrm{y}}{\mathrm{d}t} = \gamma\,(M_\mathrm{z}B_{1\mathrm{x}} - M_\mathrm{x}B_0) \qquad [2.37]$$

$$\frac{\mathrm{d}M_\mathrm{z}}{\mathrm{d}t} = \gamma\,(M_\mathrm{x}B_{1\mathrm{y}} - M_\mathrm{y}B_{1\mathrm{x}})$$

Substituting Eq. [2.30] into Eq. [2.37], and remembering to convert the components of the overall magnetization in the same way as the unit vectors, we can rewrite the Bloch equations in the rotating frame:

$$\frac{\mathrm{d}M'_\mathrm{x}}{\mathrm{d}t} = -(\omega_0 - \omega)M'_\mathrm{y} - \gamma M'_\mathrm{z}\,B'_{1\mathrm{y}}$$

$$\frac{\mathrm{d}M'_\mathrm{y}}{\mathrm{d}t} = \gamma M'_\mathrm{z}\,B'_{1\mathrm{x}} - (\omega_0 - \omega)M'_\mathrm{x} \qquad [2.38]$$

$$\frac{\mathrm{d}M'_\mathrm{z}}{\mathrm{d}t} = \gamma\,(M'_\mathrm{x}\,B'_{1\mathrm{y}} - M'_\mathrm{y}\,B'_{1\mathrm{x}})$$

From these equations, it can be seen that *frequency* of the RF field has an effect, as well as its magnitude and orientation. A convenient way to consider the effect of off-resonance RF is to treat the off-resonance term as an additional (fictitious) magnetic field i.e. $(\omega_0 - \omega)/\gamma$. We can then define an effective magnetic field $\boldsymbol{B}_e$ as the vector sum of $\boldsymbol{B}_1$ and this off-resonance 'field' (see Fig 2.2). In this way, we can see that as the RF becomes increasingly off-resonance, $\boldsymbol{B}_e$ tilts away from the xy plane towards the z-axis. This introduces a complicated movement to the magnetization.

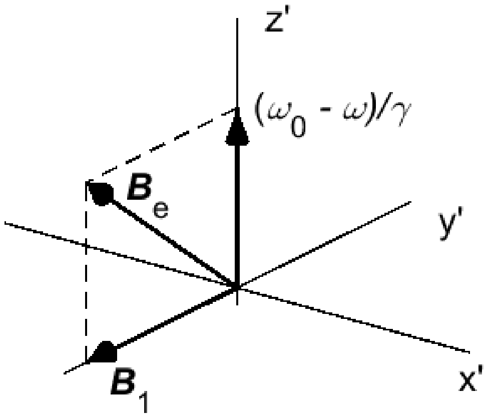

Fig 2.2. Effective magnetic field. Off-resonance, $\boldsymbol{B}_1$ is combined with $(\omega_0 - \omega)/\gamma$ to give the effective magnetic field $\boldsymbol{B}_e$.

$\boldsymbol{B}_1$ fields are normally applied for brief moments only, and are often termed a 'pulse'. These RF pulses can have many forms, depending on the requirements for the MR experiment. The basic pulse is a constant amplitude pulse (described as 'hard' or 'square'). The off-resonance characteristics of a hard pulse are shown in Fig 2.3a-b. The excitation can be made more uniform in the frequency domain by using a shorter, more intense, pulse as this makes the $\boldsymbol{B}_1$ a greater component of $\boldsymbol{B}_e$. The bandwidth of a hard pulse excitation is approximately given by:

$$\mathrm{BW} = \frac{1}{4\tau} \qquad [2.39]$$

where τ is the duration of the hard pulse.

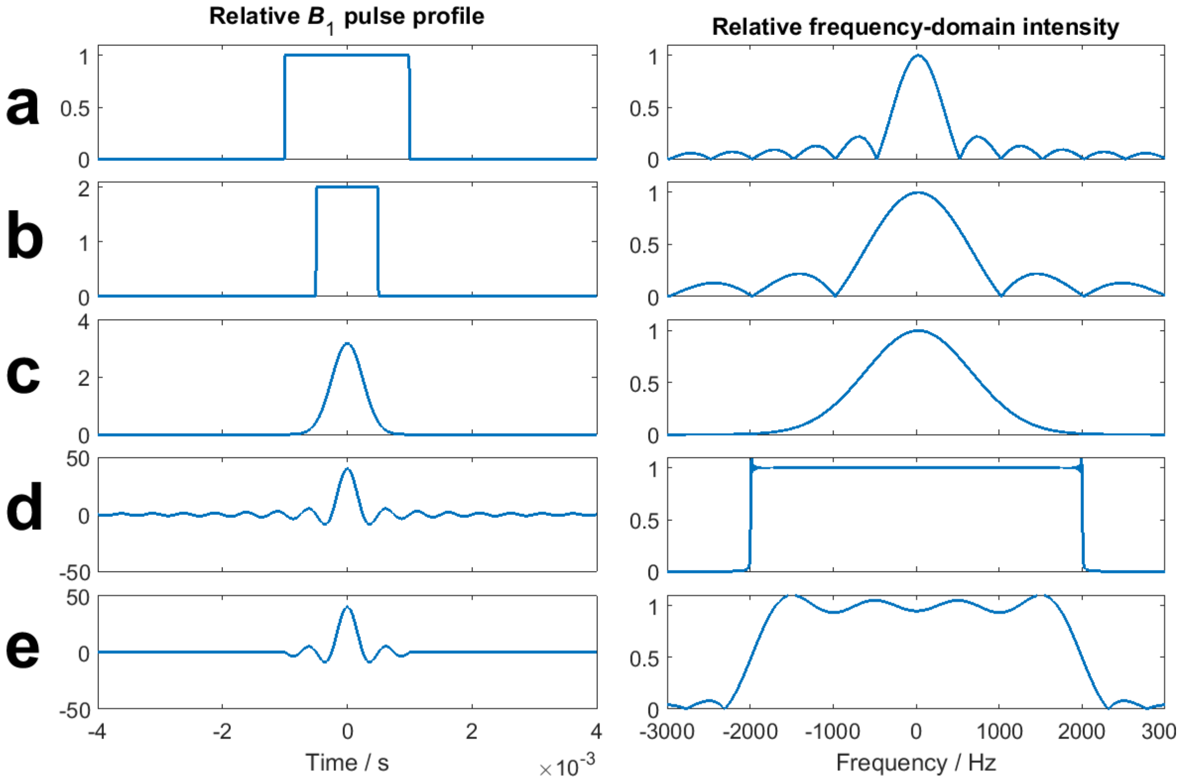

Fig 2.3. RF Pulses. Each pulse is shown in the time-dimension, as well as the characteristics of the resonance in the frequency-dimension. (a) shows a 2 ms hard pulse. (b) shows a 1 ms hard pulse of twice the intensity of the pulse in (a). (c) shows a Gaussian pulse with the same integral as (a). (d) shows an infinite sinc pulse. (e) shows a sinc pulse truncated to seven lobes.

RF pulses can be shaped to give more well-defined frequency profiles. For example, a Gaussian pulse gives a Gaussian profile (Fig 2.3c). The most desirable profile is one that is constant for the frequencies of interest, and zero elsewhere. This is given by a sinc pulse (Fig 2.3d). As the sinc function is infinite, it must be shortened for practical use (Fig 2.3e).

An extra consideration in RF pulse design in vivo is the deposition of energy within the body. The majority of this comes from induced electric fields which produce heat through Ohmic heating. This can reach unsafe levels, and so must be measured and controlled. It is quantified by determining the specific absorption rate (SAR), a time- and mass-normalized rate at which energy is deposited. SAR is expressed in units of W.kg^{-1}, and is calculated as the power over the mass in which the energy is being deposited. The exact calculation is complicated by variations in tissue properties, as power deposition is a property of the $\boldsymbol{E}$ field rather than the $\boldsymbol{B}$ field. However, power P is approximately related to $\boldsymbol{B}_1$ and ω_0 by:

$$P \propto \omega_0^2 \int \boldsymbol{B}_1^2(t)\mathrm{d}t \qquad [2.40]$$

As only signal in the xy plane can be measured, received signal depends on the amount the magnetization is 'tipped' away from the z-axis. This is known as the tip angle or flip angle θ. If the pulse duration is short (i.e. for small flip angles) and when the frequency of the RF field matches the resonant frequency it is given in radians by:

$$\theta = 2\pi\gamma \int B_1^+(t)\mathrm{d}t \qquad [2.41]$$

Signal detection can be calculated using the principle of reciprocity. This states that if the field at a sample were to be measured after unit direct current was applied to a receiving coil, the electromotive force *emf* induced in the coil by the precessing nuclear magnetic moment would be proportional to the field (from Eq [2.26]). This can be written as (8):

$$emf = 2\omega \boldsymbol{M}^+ \cdot \boldsymbol{B}_1^{-*} \qquad [2.42]$$

where $\boldsymbol{M}^+$ is the magnetization in the positive rotating frame. In other words, knowledge about the $\boldsymbol{B}_1$ field during a hypothetical transmission gives direct information about induced *emf* during reception. To be more precise, the voltage induced in the coil by the sample magnetization is proportional to $\boldsymbol{B}_1^{-*}$ (8). A dependence on $\boldsymbol{B}_1^+$ is implicit in the dependence on $\boldsymbol{M}$. The exact signal depends on the manner of excitation and reception of the signal, but from Eq. [2.24] M_0 is proportional to $\gamma^2 B_0$, and an extra dependence on resonant frequency (i.e. γB_0) is introduced in Eq. [2.42]. This means:

$$\text{signal} \propto \gamma^3 B_0^2 \qquad [2.43]$$

For an in vivo experiment with $\boldsymbol{B}_0 > 0.5 - 1$ T, received noise is dominated by noise from the sample, rather than from the electronics or the coil. Sample noise varies with ω_0, so the signal-to-noise ratio (SNR) can be written as:

$$\text{SNR} \propto \gamma^2 B_0 \qquad [2.44]$$

2.1.7. Chemical shift

In Eq. [2.17], the resonant frequency was solely based on γ and B_0. This means that the resonant frequencies should be the same for a single type of nucleus. The length of the excitation leads to bandwidths that do not excite two different nuclei simultaneously, and so sharp frequency boundaries should not be necessary. However, Eq. [2.17] is only strictly true for a bare nucleus in a magnetic field. In reality, electrons surround the nuclei, shielding them and reducing the effect of B_0:

$$\omega = -\gamma B_0 (1 - \sigma) \qquad [2.45]$$

In general, the more electron density there is around a nucleus, the greater the shielding, σ. But in molecules, the complex arrangement of electron density within electronic orbitals means that the overall effect is more challenging to determine. Fortunately, the effect is beneficial – nuclei in different chemical environments have slightly different resonance frequencies. In order to compare results, it is useful to have a method of describing the resonance frequency that will not change with B_0. Chemical shift is the relative shift in frequency from a reference standard. It is given in parts per million (ppm):

$$\delta = 10^6 \frac{\omega - \omega_{\text{ref}}}{\omega_{\text{ref}}} \qquad [2.46]$$

For in vitro experiments, the reference can be selected to give a strong signal well separated from other resonant frequencies that is invariant under a wide range of conditions.

Unfortunately this is not possible in vivo, and an alternative must be used, which is discussed in Chapter 3.

Another important effect is spin-spin coupling. This arises from interactions between nearby nuclei that give a splitting of energy levels. Coupling can be through-space (i.e. dipolar) or through-bond (i.e. scalar). For most molecules, dipolar coupling averages out due to rotation. Scalar coupling quickly drops off as the number of bonds between nuclei increases. For in vivo ^{31}P-MRS, phosphorus nuclei tend to be directly bonded to oxygen or nitrogen atoms. Oxygen (^{16}O) has a nuclear spin of zero and therefore does not couple, and nitrogen (^{14}N) has spin-1 and coupling is not visible due to relaxation effects. The predominant scalar coupling therefore comes from the two bond coupling to other phosphorus nuclei. There is also long distance coupling to ^{1}H nuclei, but the splitting is so fine that in vivo it is only seen as a line broadening.

This line broadening due to long-range ^{1}H coupling essentially reduces SNR, and it is therefore useful to remove it. This removal can be achieved by irradiating the sample at ^{1}H frequencies during ^{31}P signal acquisition, which 'flips' the ^{1}H spins rapidly, causing only an average state to be seen and removing the spin-spin interactions. The spins are said to be "decoupled".

A related phenomenon is the nuclear Overhauser effect (NOE), which arises from dipolar interactions. It occurs due to cross-relaxation which causes a transfer of magnetization from nearby nuclei. So if ^{1}H frequencies are saturated, there will be an increase in the signal for nearby ^{31}P nuclei. The selection of whether only NOE enhancement or ^{1}H decoupling is applied can be controlled to some degree by the timing and intensity of the ^{1}H saturation. In general, it is possible to have NOE without decoupling, but it is impossible to achieve decoupling without some NOE. This is because decoupling only occurs when the ^{1}H frequency is saturated during acquisition, whereas NOE enhancement can occur whether the ^{1}H frequency is saturated during acquisitions or in the gap between acquisitions.

As both ^{1}H-decoupling and NOE require long, high B_1 pulses to continuously saturate the ^{1}H spins, they naturally come at a cost of high SAR. Due to the proportionality of SAR and the square of the frequency (see Eq. [2.40]), this is more of a problem at higher field strengths.

2.1.8. Relaxation

With equations [2.38], the effect of the external RF excitation field can be fully described. And once the spins have been excited, they naturally relax into the ground state. However, if this relaxation occurred solely due to spontaneous thermal emission, there would be a very long wait for thermal equilibrium to be restored (on the order of 10^{15} s (9)). In vivo metabolites tend to become almost fully relaxed within about 10^0 – 10^2 s. There must therefore be other relaxation mechanisms in place.

These relaxation mechanisms are all based on changes that occur within the MR timescale. The most important mechanisms are caused by the motion and rotation of molecules. Although the direct effects of rotation are averaged out over an MR acquisition, indirect relaxation effects are vital to an MR experiment. Molecular rotation is described by τ_c, the rotation correlation time, which is (for random molecular tumbling) the average time required for a molecule to rotate over 1 rad. For spins in solution, τ_c is short (10^{-12} – 10^{-10} s), whereas for immobile spins τ_c is longer (10^{-8} – 10^{-6} s).

There are two distinct relaxation processes: spin-lattice relaxation and spin-spin relaxation. The first describes how spins return into equilibrium with the surroundings (the “lattice”), and is characterized by time constant T_1. After a 90° flip angle excitation pulse, the relaxation due to T_1 is given by:

$$\frac{\mathrm{d}M_z}{\mathrm{d}t} = -\frac{M_z - M_0}{T_1} \qquad [2.47]$$

Spin-spin relaxation describes how spins return into equilibrium with each other. This manifests as a gradual dephasing of spins in the xy plane. Once the spins are fully dephased, the overall xy magnetization returns to zero. The rate of recovery is given by the relaxation time constant T_2. Again, after a 90° pulse this is given as:

$$\frac{\mathrm{d}M_x}{\mathrm{d}t} = -\frac{M_x}{T_2} \qquad [2.48]$$

$$\frac{\mathrm{d}M_y}{\mathrm{d}t} = -\frac{M_y}{T_2} \qquad [2.49]$$

There are five common mechanisms for MR relaxation.

Dipolar relaxation is caused by direct through-space dipolar interactions. The charge density on molecules is anisotropic. If there is charge separation in one dimension, the molecule has a dipole. The motion and rotation of dipoles give rise to a locally varying magnetic field, which cause relaxation of individual spins. Dipolar relaxation is described by the Bloembergen-Purcell-Pound (BPP) theory (9). According to this theory, for very short τ_c (i.e. mobile liquids), $T_1 \approx T_2$, and both are long. For very long τ_c (i.e. solids), $T_1 \gg T_2$. Both T_1 and T_2 are dependent on viscosity. Dipolar interaction tends to be the dominant source of relaxation in vivo.

Quadrupolar relaxation is caused by the interaction of the electric quadrupole of the nucleus with the local electric field gradient. If a nucleus has a spin greater than ½, it will have a non-spherical charge distribution. However, because it is still symmetrical, it does not have an associated dipole (or only a very small one (10, 11)), but instead a quadrupole. Because it interacts directly with the electric field, any rotation of a nucleus with non-zero electric quadrupole moment induces rapid relaxation of the nuclear spin.

Chemical shift anisotropy is caused by the local variation in electron density around a nucleus, which means that the resonant frequency of the nucleus changes with orientation. For a solution, fast molecular tumbling averages away the chemical shift anisotropy over the MR timescale. However, this causes fluctuations in the local magnetic field which reduces the relaxation time. For ^{31}P, dipolar relaxation and chemical shift anisotropy relaxation both contribute significantly to observed relaxation times. These effects will be discussed further in Section 3.2.

Spin rotation relaxation arises from coupling due to the coherent rotation of entire molecules. The disruption of the coupling by, for example, collisions provides the relaxation mechanism. This is most important for small, symmetric molecules, or for similar parts of molecules. While this has little effect for most in vivo metabolites, it contributes appreciably to the relaxation of inorganic phosphate (12).

Scalar coupling is the indirect interaction of two spins through electrons in a chemical bond. Relaxation occurs if the coupling changes within the MR timescale. For example, if one of the nuclei is in fast exchange, or if it is quadrupolar and therefore has a much faster relaxation rate. This interaction mostly affects T_2 relaxation.

Including the relaxation terms (Eqs [2.47] – [2.49]) into the Bloch equations in the rotating frame (Eq. [2.38]) gives us:

$$\frac{\mathrm{d}M'_\mathrm{x}}{\mathrm{d}t} = -(\omega_0 - \omega)M'_\mathrm{y} - \gamma M'_\mathrm{z} B'_{1\mathrm{y}} - \frac{M'_\mathrm{x}}{T_2}$$

$$\frac{\mathrm{d}M'_\mathrm{y}}{\mathrm{d}t} = \gamma M'_\mathrm{z} B'_{1\mathrm{x}} - (\omega_0 - \omega)M'_\mathrm{x} - \frac{M'_\mathrm{y}}{T_2} \qquad [2.50]$$

$$\frac{\mathrm{d}M'_z}{\mathrm{d}t} = \gamma(M'_x B'_{1y} - M'_y B'_{1x}) - \frac{M'_z - M_0}{T_1}$$

In an MR experiment, signal is usually acquired after excitation has ended. At this point, the terms containing B_1 become zero, and we are left with a precession back to equilibrium magnetization. This gives rise to the characteristic signal called a free induction decay (FID) (see Fig 2.4).

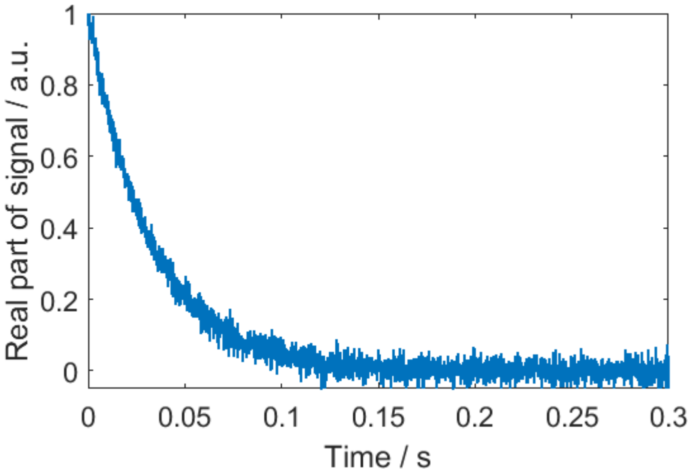

Fig 2.4. A free induction decay (FID). A FID from a simulated on resonance singlet with added noise.

One further addition to the Bloch equations is the effect of small variations (i.e. inhomogeneity) in the $\boldsymbol{B}_0$ field. These give rise to an effective reduction in the T_2 to give an apparent relaxation time T_2^*. The intrinsic T_2 and the additional term due to inhomogeneity dephasing effects are combined in the following way:

$$\frac{1}{T_2^*} = \frac{1}{T_2} + \frac{1}{T_2^{*'}} \qquad [2.51]$$

2.1.9. Localization

In vivo tissue is inhomogeneous. It is therefore useful to localize the signal to a smaller, defined volume, commonly called a voxel. The simplest method of spectral localization is to employ the variation in $\boldsymbol{B}_1$ associated with a surface loop coil. As the $\boldsymbol{B}_1$ naturally drops off further away from the coil, signal can only come from a nearby region. However, this is not precise, and would not allow differentiation between e.g. muscle in the chest wall and liver tissue.

A better method is to apply spatially varying magnetic fields to define regions with different excitation frequency. These magnetic field gradients $\boldsymbol{G}$ can be applied at various times during the acquisition process, with varying effects.

The first possibility is to apply a gradient during the excitation pulse. Only a specific portion of spins will be excited, dependant on the bandwidth of the pulse. This is called frequency-encoded localization. All frequency-encoded methods suffer from chemical shift displacement artefacts. This is because information about signal location is mixed with information about chemical shift.

Another possibility is to apply a gradient between excitation and signal acquisition. This is called phase-encoding. The FID is given by:

$$\mathrm{FID}(t) = \iint \rho(\boldsymbol{r}, \omega) e^{-i\omega t} \mathrm{d}\omega \; e^{-i\boldsymbol{k}\cdot\boldsymbol{r}} \mathrm{d}\boldsymbol{r} \qquad [2.52]$$

where ρ is the spin density, and r is the position. k is given by:

$$\boldsymbol{k} = \gamma \int \boldsymbol{G}(\tau) \mathrm{d}\tau \qquad [2.53]$$

where τ is the time of the gradient. For Cartesian sampling, the relationship between field of view (FOV) and k is given by:

$$\Delta k = \frac{1}{\mathrm{FOV}} \qquad [2.54]$$

One disadvantage of phase-encoding methods is that signal from outside the FOV is not fully localized, and becomes wrapped in because of the periodic nature of the localization.

However, unlike frequency-encoding, phase-encoding collects information from multiple places simultaneously. This opens up the way for imaging methods, as resolution is fundamentally limited only by signal and the peak strength and slew rate of the scanner's gradient hardware.

These two localization types do not overcome the $\boldsymbol{B}_1$ inhomogeneity inherent to surface coils, and so signal intensity will naturally drop off even in well localized images. This can be partially bypassed by a specific type of excitation pulse called an adiabatic pulse. The pulses are designed such that $\boldsymbol{B}_\mathrm{e}$ gradually sweeps towards the desired flip angle, which slowly affects the orientation of the precessing spins. Adiabatic pulses are amplitude and frequency- or phase-modulated and above a threshold $\boldsymbol{B}_1$ amplitude they provide a relatively uniform flip angle independent of $\boldsymbol{B}_1$. The signal is then only dependent on the receive sensitivity. A full description of a variety of adiabatic pulses is given by Tannus and Garwood (13).

An additional tool in signal localization is outer volume suppression (OVS). This uses frequency-encoding to place a slab over a certain region and saturate the signal. This is often combined with phase-encoding methods to eliminate unwanted signal from e.g. skeletal muscle.

Inhomogeneity in the $\boldsymbol{B}_0$ field not only gives rise to T_2^* (see Eq. [2.51]), but also has unwanted effects on localization. To overcome this, the field can be "shimmed". Shimming uses shim coils to correct harmonics in the field in each dimensions, as well as more complex harmonics. As the $\boldsymbol{B}_0$ changes every time an object is placed within the scanner, shimming should ideally be performed each time a scan session is started.

2.1.10. Sequences

Combining RF pulses, gradients and localization techniques allows us complete control in the design of an MR experiment. A particular arrangement of the timing and intensity of each of these components is called a pulse sequence.

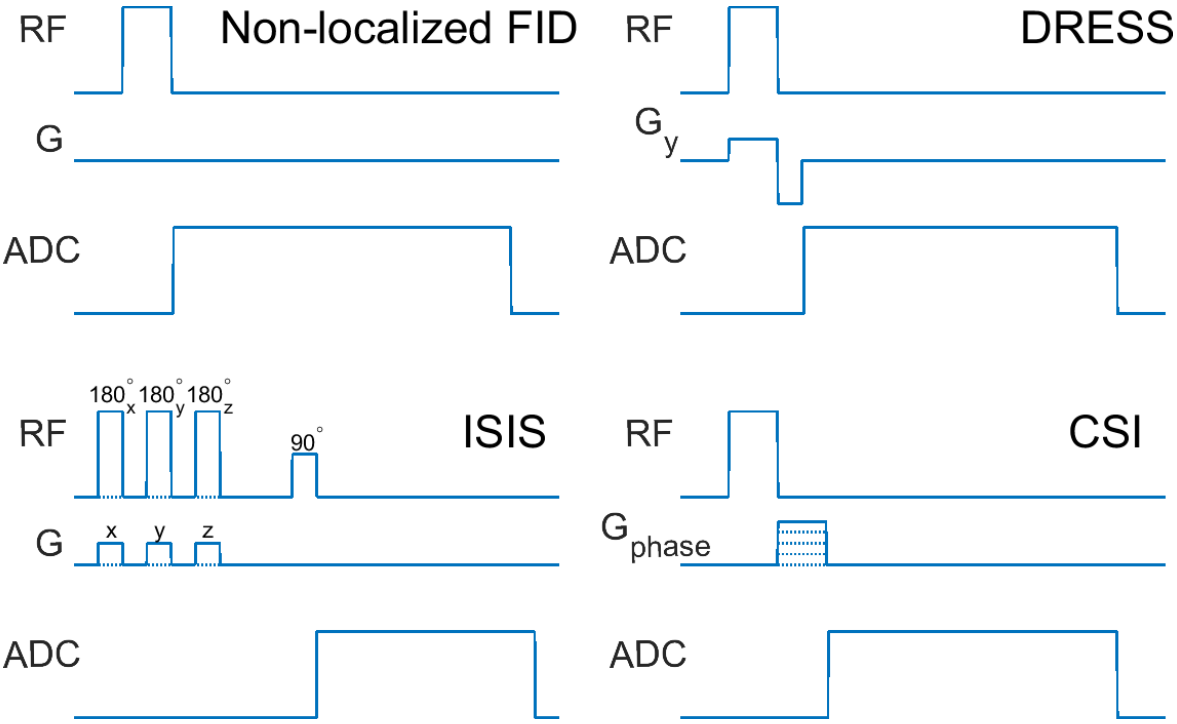

Fig 2.5. Pulse sequences. Each sequence shows the RF, gradient, and analog-to-digital conversion (ADC, i.e. signal acquisition) pulse diagram. For the ISIS sequence, each of the three 180° pulses is turned on or off according to Table 2.1. For the CSI sequence, the phase-encoding gradient can be applied in 1, 2 or 3 dimensions simultaneously.

The simplest pulse sequence is a non-localized pulse-acquire. For this, a single pulse is used to excite the signal and the FID is observed (see Fig 2.5). The next step is to combine this with a localization method.

Depth-resolved surface-coil spectroscopy (DRESS) uses a frequency-encoded slab parallel to the coil, and uses the $\boldsymbol{B}_1$ profile of the coil in the other two dimensions to localize the signal to a single volume (see Fig 2.5) (14).

Image-selected in vivo spectroscopy (ISIS) uses the addition and subtraction of multiple experiments to localize the signal in one, two or three-dimensions (15). Each experiment uses frequency-selective inversion pulses in each dimension (see Fig 2.5 and Table 2.1). This technique is sensitive to motion as multiple acquisitions are required for localization – two for 1D, four for 2D, and eight for 3D.

Table 2.1. ISIS experimental sequence. Frequency-selective inversion pulses are used for each experiment. The x, y and z columns denote in which dimensions the pulses are used. 1 indicates the pulse is switched on, and 0 indicates it was switched off. The next column shows the way in which the experiments must be summed in order to achieve the desired localization. For 1D localization, only the first two experiments are required. For 2D, the first four should be used, and for 3D all the experiments must be combined.

Experiment	x	y	z	Contribution	1D	2D	3D
1	0	0	0	+	■	■	■
2	1	0	0	-	■	■	■
3	0	1	0	-	░	■	■
4	1	1	0	+	░	■	■
5	0	0	1	-			■
6	1	0	1	+			■
7	0	1	1	+			■
8	1	1	1	-			■

Chemical shift imaging (CSI) uses phase-encoding in each required spatial dimension to localize the signal to multiple voxels (see Fig 2.5) (16). The nominal resolution in each dimension is given by:

$$\Delta x = \frac{\mathrm{FOV_x}}{N} \tag*{[2.55]}$$

where N is the number of phase-encoding steps in that dimension. As mentioned in the previous section, signal from outside the FOV can wrap in, and so the FOV must be large enough to cover the sensitive volume of the coil. For fully sampled CSI, this means that the number of acquisitions required to give a reasonable resolution quickly adds up. Even a low resolution (e.g eight phase-encoding steps in each dimension) requires eight acquisitions for 1D, 64 for 2D, and 512 for 3D. This means that CSI sequences often require very long total acquisition times (T_A).

In standard CSI, the signal is acquired at a uniform echo time (TE) across k-space. This TE is limited by the time required for the gradients to reach the far edges of k-space. The minimum TE for the CSI product sequence supplied as standard to Siemens MRI devices is 2.3 ms. In vivo, ^{31}P metabolites have T_2^* values between 0.002 and 0.02 s, which means that between 10 and 70 % of the signal is lost to T_2^* decay. Ultra-short echo time CSI (UTE-CSI) minimizes the echo time at each point of k-space to increase the SNR (17).

Imaging sequences ignore chemical shift information, and so do not need to sample the whole of the FID. This time can be used to sample part of the FID in several parts of k-space in a row before the signal has decayed to zero. This is achieved by creating an echo in the FID. Echoes can be created by using gradients (gradient-recalled echo, GRE), or they can use 180° RF pulses to refocus dephasing due to inhomogeneity (spin echo, SE). One of the standard Siemens imaging sequences is fast low angle shot (FLASH) MRI (18). It is a GRE sequence that uses low flip angles and short T_R to allow rapid imaging.

2.1.11. Multiple acquisitions

Often, signal averaging is used to improve SNR. The signal increases with the number of averages, n, and the noise increases with the square root, $\sqrt{n}$, giving an overall increase of $\sqrt{n}$.

An additional consideration when acquiring multiple times is the effect of residual magnetization from the previous acquisition. As a rule of thumb, the acquisition can be considered fully relaxed if the time between acquisitions (known as the repetition time, T_R) is greater than five times the T_1. From the relaxation equations, this gives a recovery of more than 99% of the magnetization for a 90 degree pulse. In practise, this will lead to an unreasonably long T_A, especially for ^{31}P metabolites which have long T_1 values. Instead, a shorter T_R is used, and the magnetization settles into a steady-state.

For simple pulse-acquire sequences such as CSI, steady-state magnetization is given by (19):

$$M = M_0 \frac{\sin\theta \times (1 - e^{-\frac{T_R}{T_1}})}{1 - \cos\theta \cdot e^{-\frac{T_R}{T_1}}} \qquad [2.56]$$

The flip angle giving the optimal SNR for such a steady-state is called the Ernst angle (19):

$$\theta_E = \arccos(e^{-\frac{T_R}{T_1}}) \qquad [2.57]$$

2.2. Pre-processing

After acquiring the data, some pre-processing is required before analysis can be performed. The exact pre-processing steps vary from sequence to sequence. For Siemens scanners, any pre-processing can be achieved on the scanner using ICE (Image Calculation Environment). Equally, the pre-processing could be achieved offline, e.g. in the MATLAB (Mathworks, Natick, USA) programming environment.

Averaging is performed by summing spectra together. For an ISIS sequence, the phase of the data is considered and a certain sign is assigned to each acquisition to get the required localization.

2.2.1. Fourier transform

Any phase-encoded method will require processing to return the data to real space. Reconsidering Eq. [2.52], it can be seen that there is a specific relationship between the acquired data and the spin density.

This relationship is called a Fourier transform, and converts from one space to a different ("inverse") space. For example, the Fourier transform of time is frequency. The Fourier transform of position is spatial wavelength ("k-space").

Any complicated periodic function can be represented as a sum of simple sines and cosines. Using Euler's formula, it is therefore possible to represent the function with a sum of complex exponentials of differing frequencies. The Fourier transform gives the amplitudes of each exponential in terms of frequency. One way of considering this is that the function to transform should be multiplied by a certain test function $e^{-i\omega t}$ (where ω is the angular frequency, and t is the time). The combination of these functions is then integrated over all space. Where the test function is approximately correct, the integral will be large. On the other hand, if the test function is off-frequency, the integral will tend to zero.

The one-dimensional Fourier transform (FT) is given mathematically by:

$$S(k) = \int \rho(x) e^{-2i\pi kx} \mathrm{d}x \qquad [2.58]$$

It is also possible to transform from k-space back into real space. This is given by the inverse FT:

$$\rho(x) = \int S(k) e^{+2i\pi kx} \mathrm{d}k \qquad [2.59]$$

2.2.2. Point spread function

The acquisition of data in k-space requires a Fourier transform back to real space before the spectra can be usefully analysed. However, artefacts are introduced due to the limited number of points acquired. The transformed signal is the true signal convolved with the point spread function – the signal that would be received from a point source.

$$\rho_{\text{rec}} = \rho_{\text{true}} \otimes \text{PSF} \qquad [2.60]$$

which can also be written as:

$$\rho_{\text{rec}} = \int \rho(s)\text{PSF}(r-s)\text{d}s \qquad [2.61]$$

The PSF is simply the FT of the k-space sampling pattern. It is present in all discrete Fourier transforms (DFTs), but in the case of a FID it is much narrower than the T_2^*-dominated linewidths. This is due to the reasonable number of sampling points (usually 2048), and also the fact that the signal has normally decayed to zero by the end of the FID. In the case of the spatial dimensions in CSI, the number of samples is much smaller (typically fewer than 64 voxels in each dimension), and the signal might not reach zero at the edges of k-space.

In three dimensions, the PSF can be defined analytically by taking the DFT of the k-space weighting:

$$\text{PSF}(\boldsymbol{r}) = \text{DFT}(w) = \sum_{n=0}^{N-1} w(n) e^{-i2\pi \boldsymbol{k}(n)\cdot \boldsymbol{r}} \qquad [2.62]$$

where $w(n)$ is the sampling weight at each point.

The PSF has a dependence on both the field of view and the resolution. This PSF has a “ringing” form known as the Gibbs phenomenon (see Fig 2.6). This means that there is a negative contribution from some parts of the sample. However, as the PSF is the FT of the k-space sampling pattern, we can apply a more reasonable form (i.e. with no or fewer negative side lobes) by changing the method of sampling k-space (20) (see Fig 2.6). For example, a Hamming function can be applied:

$$w(n) = \alpha - \beta \cos \frac{2\pi n}{N-1} \qquad [2.63]$$

With $\alpha = 0.54$ and $\beta = 0.46$. This collects more points in the centre of k-space, and fewer from the edges. A fortuitous side effect of this weighting is that the whole of k-space need not be collected, which drastically reduces the minimum number of points to acquire, and hence the acquisition time. For example, a fully-encoded 16 × 16 × 8 CSI matrix with 10 averages would take 5 hours and 41 minutes to acquire with a 1 s T_R. In contrast, the same CSI matrix size with a Hamming filtered acquisition scheme could be acquired in 28 minutes. However, although the Hamming filtering reduces side lobes and acquisition time, it also increases the effective size of the voxel.

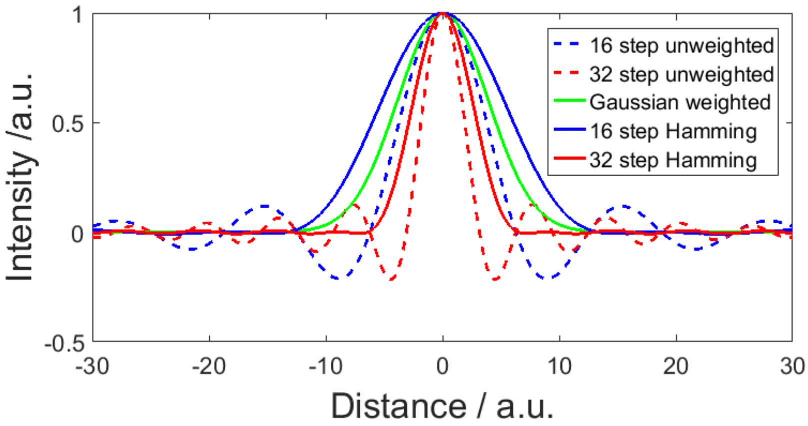

Fig 2.6. The Fourier Transforms of various 1D CSI weighting schemes. A 16 step unweighted acquisition is shown with a blue dashed line, and the 32 step equivalent is in red. The Gaussian weighting scheme is in green. The 16 and 32 step Hamming-weighed acquisitions are in solid blue and red.

Although the analytical PSF can be calculated, the sum of Fourier terms is often very long for more complex functions. Instead, it is easier to calculate the PSF by numerically evaluating the weighting function in k-space, zero-padding, and applying the DFT.

2.2.3. Coil combination

Our data is acquired using a receive array. At this point in processing, there are separate, localized signals for each of the elements. The problem of the optimal method of combining these signals before further processing e.g. fitting then arises. There are two common aims for coil combination: uniform noise or uniform sensitivity (21).

The uniform noise combination gives the combination of signal that is really “seen” by the individual elements. That is to say, the farther from the elements the lower the signal will be. This is the most common type of combination, as it assumes no knowledge of the receive fields of the coils.

Uniform sensitivity combination is the alternate aim for array combination. Rather than give the spectra that correspond to the reality of how much signal was excited and detected, it gives spectra that are normalized to give signal proportional to the concentrations within the voxel. The uniform sensitivity combination of array coils will be discussed more in Chapter 8.

2.3. Analysis

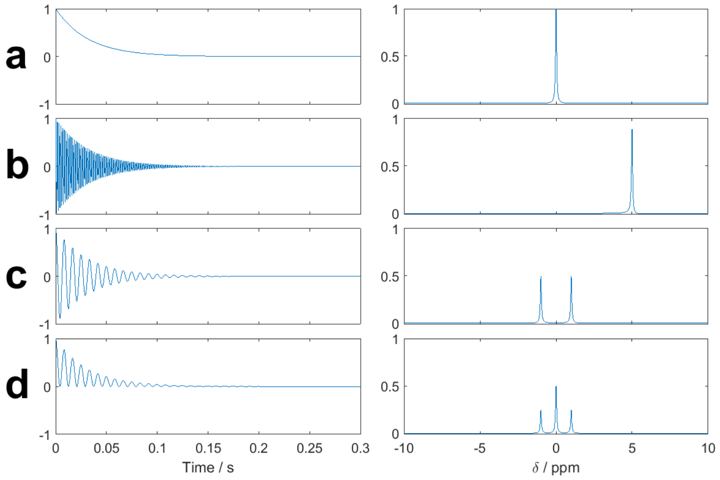

Fig 2.7. FIDs and spectra. (a) shows a 120.3MHz singlet FID, and the equivalent spectrum plotted with a 120.3MHz reference frequency, i.e. chemical shift of 0 ppm. (b) shows a FID and equivalent spectrum with a 5 ppm offset from (a). (c) shows a doublet, and (d) shows a triplet.

The time-domain signal is difficult to inspect and analyse intuitively. So a Fourier transform is used to transform to the frequency domain to see the spectrum (see Fig 2.7a). This allows straightforward differentiation between signals of different frequencies, such as those arising from molecules with different chemical shifts (Fig 2.7a vs b).

Signals of single frequency appear as delta functions in the frequency domain (i.e. they have a value at that frequency and are zero elsewhere). However, because the signal decays, idealised MR signals appear as a Lorentzian centred at the resonance frequency. Their width is based on the rate of decay, i.e. the T_2^* of the nuclei. For a Lorentzian peak, the linewidth is commonly defined as the full width at half maximum (FWHM), and is given by:

$$\text{Linewidth} = \frac{1}{\pi T_2^*} \qquad [2.64]$$

In reality, peaks tend to have a Gaussian component. This is because the environment of each of the nuclei is not identical, and there is an approximately normal distribution of values around the mean (which is explained by the central limit theorem (22)). The standard deviation of the Gaussian component depends on the homogeneity of the material. In vivo there will naturally be more heterogeneity than in phantoms (i.e. in vitro).

In the frequency domain, the effect of coupling can be more clearly seen. Coupling to one other spin-1/2 nuclei changes the peak from a singlet to a doublet (Fig 2.7c). Coupling to two others changes the peak to a triplet, and so on (Fig 2.7d).

Viewing spectra introduces another complication that has been ignored so far – phasing. Signal acquired in quadrature has a real component from the x-direction and an imaginary component from the y-direction. This means that the total signal is complex, and it remains complex after Fourier transformation. The manner in which the signal is split between the real and imaginary axes is known as its phase.

There are two types of phase that arise in an MR experiment – zero order and first order (see Fig 2.8). Zero order phase affects the whole spectrum equally, whereas first order phase is frequency-dependent. There are several possible causes for changes in phase. Zero order phase can be caused by the receiver reference phase not matching the phase of the MR signal. This occurs because of $\boldsymbol{B}_0$ inhomogeneity or, in single voxel spectroscopy, because of motion effects. First order phase can arises due to any delay before the beginning of acquisition. If signal were acquired directly after excitation, all the magnetization vectors would have identical phase. After a short amount of time, the magnetization will have evolved according to its frequency, and so the phases will become offset. Other possible sources of phase include adiabatic pulses and Bloch-Siegert phase shifts (4, 23).

A commonly used technique for easing the viewing of spectra is apodization. This involves convolving the spectrum with a Lorentzian peak in order to smooth out some of the noise.

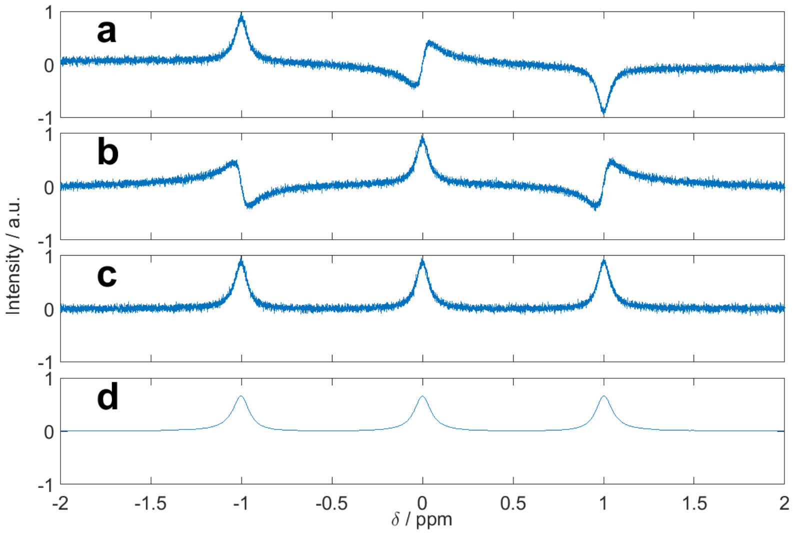

Fig 2.8. Phasing and apodization of spectra. (a) shows a frequency-domain spectrum with three singlet peaks, before it has been phased or apodized. (b) shows the same spectrum after zero-order phase correction (i.e. a single phase has been applied across the whole spectrum). (c) shows (b) after first-order (i.e. frequency-dependent) phase correction. (d) shows (c) after apodization.

Usually this is applied by multiplying the signal with an exponential decay in the time domain, using the properties of the FT.

After the spectrum is phased and apodized, it can be intuitively analysed, and any artefacts will be easily visible. This is useful for manual quality assurance.

A simple measure of the quality of a spectrum is the signal-to-noise ratio (SNR). The gain of the scanner receive chain is typically not calibrated, and can vary due to coil loading or changes in pre-amplifier gain. SNR is therefore used to distinguish a simple increase in signal and an actual increase in quality. There are several ways to define SNR. In the frequency domain, SNR of a metabolite is commonly defined as the height of a metabolite peak divided by the standard deviation of the noise (23). In the time domain, SNR is defined as the first point (or mean of the first few points) of the FID divided by the noise at the end of the FID where the signal has decayed (23).

Another method of manually assuring the quality of spectra is the shape of the peaks. Very large linewidths or clearly non-Lorentzian lineshapes are a sign of poorly shimmed voxel. Overlapping peaks are can be difficult to analyse. It is also easy to see contaminating signal, from metabolites that are not expected to arise from the region of interest.

While these methods are useful in acquiring a qualitative understanding of the peaks within a spectrum and the quality of the signal, solid numbers are required in order to compare spectra – they need to be quantified. The model-based fitting used in this work is described in Chapter 5.

2.4. References

1. Levitt MH. Spin dynamics : basics of nuclear magnetic resonance. 2nd ed. Chichester, England ; Hoboken, NJ: John Wiley & Sons; 2008.
2. Slichter CP. Principles of magnetic resonance. Berlin ; New York: Springer-Verlag; 1990.
3. Haacke EM. Magnetic resonance imaging : physical principles and sequence design. New York ; Chichester: Wiley-Liss; 1999. xxvii, 914 p. p.
4. De Graaf RA. In vivo NMR spectroscopy: principles and techniques. 2nd ed. Chichester: John Wiley & Sons; 2007.
5. Varshalovich DA, Moskalev AN, Khersonskiĭ VK. Quantum Theory of Angular Momentum: World Scientific Pub.; 1988.
6. Abragam A. The Principles of Nuclear Magnetism: Clarendon Press; 1961.
7. Bloch F, Siegert A. Magnetic Resonance for Nonrotating Fields. Phys Rev. 1940; 57(6):522-7.
8. Hoult DI. The principle of reciprocity in signal strength calculations - A mathematical guide. Concepts in Magnetic Resonance. 2000; 12(4):173-87.
9. Bloembergen N, Purcell EM, Pound RV. Relaxation Effects in Nuclear Magnetic Resonance Absorption. Phys Rev. 1948; 73(7):679-712.
10. Purcell EM, Ramsey NF. On the Possibility of Electric Dipole Moments for Elementary Particles and Nuclei. Phys Rev. 1950; 78(6):807-.
11. Wirzba A. Electric dipole moments of the nucleon and light nuclei. Nucl Phys A. 2014; 928:116-27.
12. Gaspar R, Andrew ER. P-31 Magnetic-Relaxation of Inorganic Orthophosphate in Solution. Chem Phys Lett. 1990; 170(2-3):171-4.
13. Tannus A, Garwood M. Adiabatic pulses. NMR Biomed. 1997; 10(8):423-34.
14. Bottomley PA, Foster TB, Darrow RD. Depth-Resolved Surface-Coil Spectroscopy (DRESS) for Invivo H-1, P-31, and C-13 NMR. J Magn Reson. 1984; 59(2):338-42.
15. Ordidge RJ, Connelly A, Lohman JAB. Image-Selected Invivo Spectroscopy (ISIS) - a New Technique for Spatially Selective NMR-Spectroscopy. J Magn Reson. 1986; 66(2):283-94.
16. Brown TR, Kincaid BM, Ugurbil K. NMR chemical shift imaging in three dimensions. Proc Natl Acad Sci USA. 1982; 79(11):3523-6.
17. Robson MD, Tyler DJ, Neubauer S. Ultrashort TE chemical shift imaging (UTE-CSI). Magn Reson Med. 2005; 53(2):267-74.
18. Haase A, Frahm J, Matthaei D, Hanicke W, Merboldt KD. Flash Imaging - Rapid Nmr Imaging Using Low Flip-Angle Pulses. J Magn Reson. 1986; 67(2):258-66.
19. Ernst RR, Anderson WA. Application of Fourier Transform Spectroscopy to Magnetic Resonance. Rev Sci Instrum. 1966; 37(1):93-+.
20. Pohmann R, von Kienlin M. Accurate phosphorus metabolite images of the human heart by 3D acquisition-weighted CSI. Magn Reson Med. 2001; 45(5):817-26.
21. Roemer PB, Edelstein WA, Hayes CE, Souza SP, Mueller OM. The NMR Phased Array. Magn Reson Med. 1990; 16(2):192-225.
22. Cam LL. The Central Limit Theorem Around 1935. Statist Sci. 1986; 1(1):78-91.
23. Kreis R. Issues of spectral quality in clinical H-1-magnetic resonance spectroscopy and a gallery of artifacts. NMR Biomed. 2004; 17(6):361-81.

3. ^{31}P-MRS in the liver

In this chapter, the context of hepatic ^{31}P-MRS studies will be explored. First, we summarise liver metabolism that involves ^{31}P-containing metabolites. Second, we detail the signal expected from those metabolites. Third, we summarise in vivo ^{31}P-MRS methods that have been used to study the human liver, and report the normal parameter ranges from those studies. Finally, we discuss the changes in ^{31}P metabolism that have been seen in various diseases.

3.1. ^{31}P metabolism in liver

Metabolism within the liver is complex, and plays a central role in the metabolism of the human body as a whole (1). The function of the liver is linked to the overall homeostasis of the body by hormonal, neuronal, and nutrient-based signalling.

Unless otherwise indicated, the basic background information in this section is taken from Berg et al.'s textbook "Biochemistry" (2).

3.1.1. Liver energetics

3.1.1.1. Glycolysis and gluconeogenesis

Glycolysis and gluconeogenesis are opposing metabolic processes in the liver (see Fig 3.1). Glycolysis is the conversion of glucose to pyruvate, which can then be used in the Krebs cycle (described in Section 3.1.1.3). The overall reaction is:

$$\mathrm{Glucose} + 2\,\mathrm{NAD}^+ + 2\,\mathrm{ADP} + 2\,\mathrm{P_i} + 2\,\mathrm{ATP} \rightarrow 2\,\mathrm{Pyruvate} + 2\,\mathrm{NADH} + 2\,\mathrm{H}^+ + 4\,\mathrm{ATP} + 2\,\mathrm{H_2O} \quad [3.1]$$

NAD^+ is the oxidised form of nicotinamide adenine dinucleotide, and NADH is the reduced form. ADP is adenosine diphosphate, which gains a terminal inorganic phosphate group (P_i) to form adenosine triphosphate (ATP).

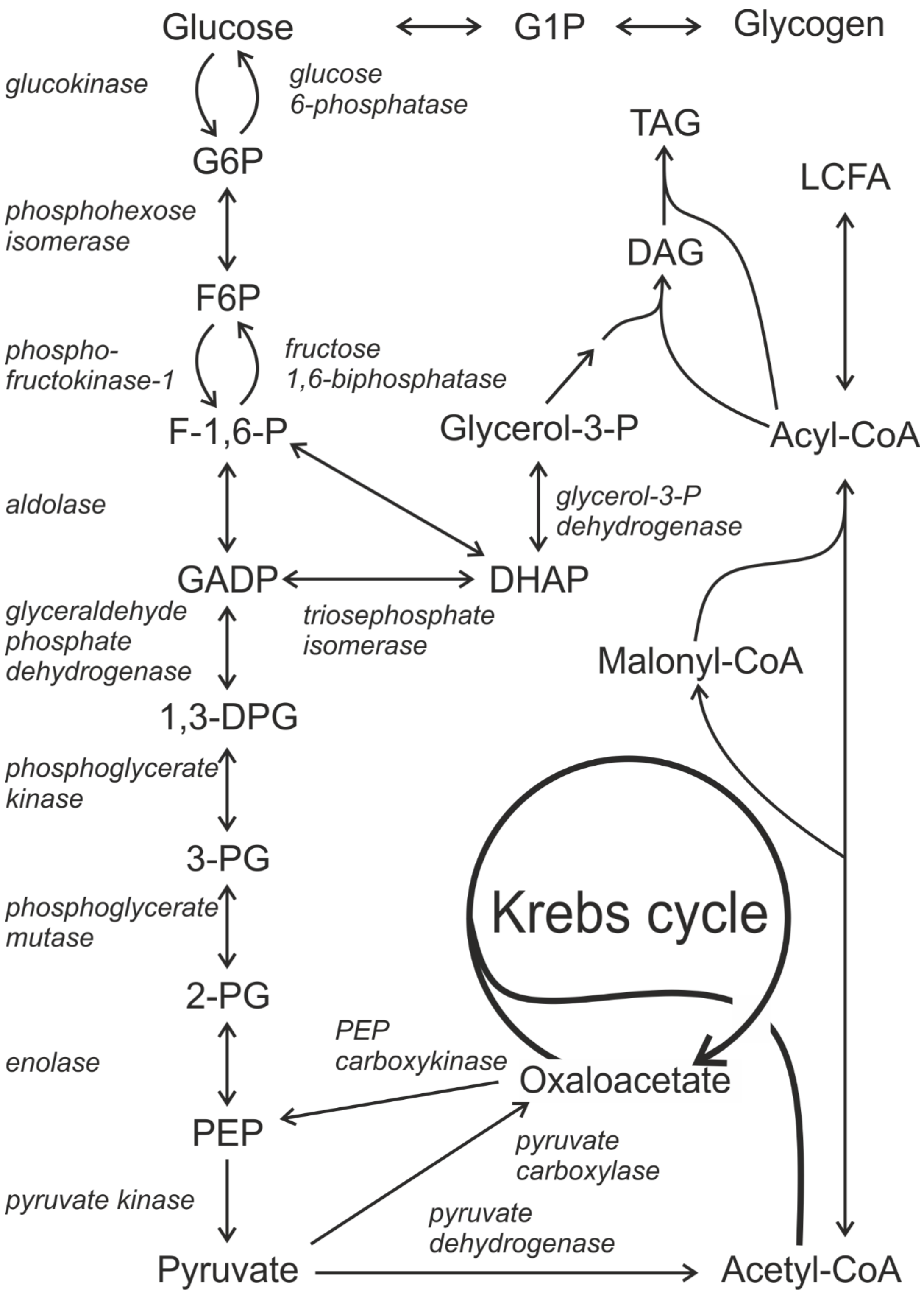

Fig 3.1. Liver energetics pathways. Enzymes are given in *italics*. Abbreviations are: glucose-1-phosphate (G1P), glucose-6-phosphate (G6P), fructose-6-phosphate (F6P), fructose-1,6-biphosphate (F-1,6-P), glyceraldehyde-3-phosphate (GADP), dihydroxyacetone phosphate (DHAP), diphosphoglycerate (DPG), phosphoglycerate (PG), phosphoenolpyruvate (PEP), coenzyme-A (CoA), long chain fatty acid (LCFA), diacylglycerate (DAG), and triacylglycerate (TAG).

As can be seen from Eq. [3.1], glycolysis is a net producer of ATP. Fig 3.1 shows in greater detail how glycolysis proceeds. Two ATP molecules are converted to ADP in order to form fructose-1,6-biphosphate (F-1,6-P) from glucose. F-1,6-P is then broken down to form glyceraldehyde-3-phosphate (GADP) and dihydroxyacetone phosphate (DHAP). DHAP can then isomerise to form GADP. In the following stages, each GADP molecule produces two ATP molecules as they are converted to pyruvate.

Gluconeogenesis is the formation of glucose from substrates such as pyruvate, glycerol, or amino acids:

$$2\,\mathrm{Pyruvate} + 2\,\mathrm{NADH} + 4\,\mathrm{ATP} + 2\,\mathrm{GTP} \rightarrow \mathrm{Glucose} + 2\,\mathrm{NAD}^{+} + 2\,\mathrm{ADP} + 2\,\mathrm{GDP} + 6\,\mathrm{P_i} \quad [3.2]$$

GTP and GDP are the guanidine equivalents of ATP and ADP.

Most of the reactions in glycolysis are reversible, except the reactions catalysed by glucokinase, phosphofructokinase, and pyruvate kinase. These are bypassed in gluconeogenesis, but additional ATP/GTP is required. Each of these three reactions is a rate-limiting step in glycolysis.

Glucokinase phosphorylates glucose to form glucose-6-phosphate (G6P), requiring the transfer of a terminal phosphate from ATP and creating ADP as a by-product. In gluconeogenesis, there is an alternate pathway which is catalysed by glucose-6-phosphatase and produces P_i as a by-product. The dephosphorylation of G6P is a rate-limiting step.

Phosphofructokinase reacts with fructose-6-phosphate (F6P) to form fructose-1,6-biphosphate (F-1,6-P). The reverse reaction of F-1,6-P to F6P is also a rate-limiting step in the gluconeogenesis pathway. However, in gluconeogenesis, the concentrations of these two metabolites tend to be much lower than in glycolysis. These metabolic pathways are reciprocally regulated, and so only one of them is activated at a time. Whether the overall effect is to form glucose, or to break it down, depends on the nutritional state of the body and hormonal control. Postprandially, there is a high level of plasma glucose, and glycolysis is the dominant pathway. In the fasted state, gluconeogenesis is the dominant pathway. As the length of the fast increases, the substrate used to form pyruvate (and hence glucose) becomes predominantly lactate provided from the muscle by the Cori cycle (3).

Pyruvate kinase catalyses the phosphorylation of ADP using the phosphate group from phosphoenolpyruvate (PEP), forming pyruvate and ATP. The related rate-limiting step in gluconeogenesis is the decarboxylation of oxaloacetate to form PEP, which is catalysed by the PEP carboxykinase (PEPCK) enzyme.

Glycogenesis is the addition of glucose subunits to the end of glycogen chains for storage. Before glucose can be added, it forms a unit with uridine diphosphate (UDP) to form uridine diphosphoglucose (UDPG). UDPG is then used as a substrate for glucosyltransferase enzymes, which attaches the glucosyl group to the growing glycogen chain.

Glycogenolysis is the reverse process – the breakdown of glycogen by phosphorolysis to form glucose-1-phosphate (G-1-P), which is then converted to glucose. The overall reversible reaction is given by:

$$\text{Glycogen}_{(n\ \text{residues})} + \text{P}_\text{i} \rightleftharpoons \text{glycogen}_{(n-2\ \text{residues})} + \text{G-1-P} \qquad [3.3]$$

3.1.1.2. Pentose phosphate pathway

The pentose phosphate pathway converts glucose-6-phosphate to ribose-5-phosphate, used in DNA and RNA, and generates NADPH from NADP^+ in the process. These reactions occur at low concentration.

3.1.1.3. Krebs cycle

The Krebs cycle is also known as the tricarboxylic acid (TCA) cycle, or the citric acid cycle. The cycle oxidises acetyl coenzyme A (acetyl-CoA), producing ATP, CO_2, and NADH. The NADH is then oxidized further in the oxidative phosphorylation process to produce more ATP. For each cycle, the sum of all the reactions is:

$$\text{Acetyl-CoA} + 3\,\text{NAD}^+ + \text{Q} + \text{P}_\text{i} + 2\,\text{H}_2\text{O} \rightarrow \text{CoA-SH} + \text{NADH} + \text{QH}_2 + 3\,\text{H}^+ + \text{GTP/ATP} + 2\,\text{CO}_2 \quad [3.4]$$

In this reaction, Q, ubiquinone (the fully oxidized form of coenzyme Q_{10}), is reduced to QH_2, ubiquinol. Because two acetyl-CoA molecules are created per glucose, two turns of the Krebs cycle occur for each glucose. This produces another two GTP or ATP molecules.

3.1.1.4. Oxidative phosphorylation

ATP decays quickly in vivo and is used in many different processes, so it must be continuously regenerated. Although glycolysis produces ATP directly, its products can also be utilized to form additional ATP from ADP by oxidative phosphorylation. Five different complexes in the inner membrane of the mitochondria take part in this process. During oxidative phosphorylation, ubiquinone is reduced to ubiquinol and NADH is oxidized to NAD^+. Direct production of ATP through glycolysis yields two ATP per glucose, and the Krebs cycle produce another two. Through oxidative phosphorylation, up to 34 additional ATP molecules can be produced per glucose. In reality, inefficiencies in the oxidative phosphorylation process usually reduce this number to about 26, making a total of 30 ATP per glucose.

3.1.1.5. Fatty acid oxidation (*"β-oxidation"*)

Long chain fatty acids are converted into acyl-CoA and then β-oxidized to acetyl-CoA. The overall reaction for β-oxidation is given by:

$$C_n\text{-acyl-CoA} + NAD^+ + FAD + CoA + H_2O \rightarrow C_{n-2}\text{-acyl-CoA} + FADH_2 + H^+ + \text{acetyl-CoA} \quad [3.5]$$

This results in increased formation of ATP via the Krebs cycle and oxidative phosphorylation in the mitochondria, and hence an influx in P_i from the cytosol.

3.1.1.6. Change in energetics in cirrhosis

Liver disease can occur through many different mechanisms; it could be due to viral infection, alcohol consumption, or the metabolic syndrome causing non-alcoholic fatty liver disease (NAFLD). In each case, the effect on the liver is similar. First, there is inflammation and a build-up of fatty deposits may occur, called steatosis (the order in which these occur depending on the disease) (4). Then scarring starts to occur, which is called “fibrosis”. When this fibrosis has built up to a certain severity, the liver is referred to as cirrhotic, and may cease to function properly. Changes in metabolism have been proposed as a potential cause for increased endoplasmic reticulum (ER) stress, which causes inflammation, and hence leads to steatosis (5).

As the hepatocyte undergoes increased stress, mitochondrial dysfunction starts to occur (6). In the early stages of chronic liver disease, mitochondrial energy production is maintained, but in order to achieve this ATP production switches predominantly to glycolysis, rather than oxidative phosphorylation (7). In late stage liver disease, this compensatory strategy starts to fail (7).

In cirrhosis, glycogenolysis is reduced and gluconeogenesis is increased (8). In addition, there is a reduced hepatic glycogen storage capacity (9). These effects are increased after an overnight fast, where the changes match what is seen in the normal liver in more advanced stages of starvation (10). It has been argued that the reduced hepatic glycogen may induce an increase in glucagon, and hence gluconeogenesis (11), but this was disproved in a study directly investigating the effect of levels of glycogen on gluconeogenesis (12).

As insulin is a regulator for gluconeogenesis (13), a possible cause for increased gluconeogenesis is the progressive glucose intolerance and insulin resistance seen in cirrhosis (14).

In keeping with the idea of the metabolism of the cirrhotic liver being similar to a starved healthy liver, there is an increased used of fat as an energy source (10, 15). In some cases, this corresponds with an increase in resting energy expenditure (16). However, this hypermetabolism does not correlate with type, duration, or severity of liver disease, and is likely to be influenced by extrahepatic factors such as portal hypertension (17).

3.1.2. De novo lipogenesis

De novo lipogenesis (DNL), the synthesis of fat within the liver and adipose tissue, is mainly provided with substrate via glycolysis and carbohydrate metabolism. The process starts with acetyl-CoA, and builds up fatty acids two carbon atoms at a time. Individual fatty acid chains are combined by bonding to glycerol backbones, forming monoacylglycerol, diacylglycerol (DAG), or triacylglycerol (TAG). DNL is stimulated by insulin, and is suspected to increase in NAFLD (18). It has been suggested as a contributor to hepatic steatosis and insulin resistance (19).

3.1.3. The cell cycle

3.1.3.1. Phospholipid metabolism

Phospholipids are the major components of cell membranes, because their amphiphilic nature causes them to naturally form bilayers. The predominant phospholipid within mammalian membranes is phosphatidylcholine (PtdC, also known as lecithin), making up

44% of phospholipids in the liver (20). The second most prevalent component is phosphatidylethanolamine (PtdE, also known as cephalin) at 28% (20).

These two lipids are formed de novo via the Kennedy pathway (see Fig 3.2) (21). Choline kinase catalyses the transfer of the terminal phosphate group from ATP onto choline to form phosphocholine (PC). The rate-limiting step is then the formation of cytidine diphosphate choline (CDP-choline) from PC and CDP, catalysed by cytidine triphosphate (CTP) phosphocholine cytidylyltransferase (22, 23). The activated CDP-choline then reacts with DAG to form PtdC. The process for PtdE is analogous, starting from ethanolamine, via phosphoethanolamine (PE). The Kennedy pathway is essential in proliferating cells (24).

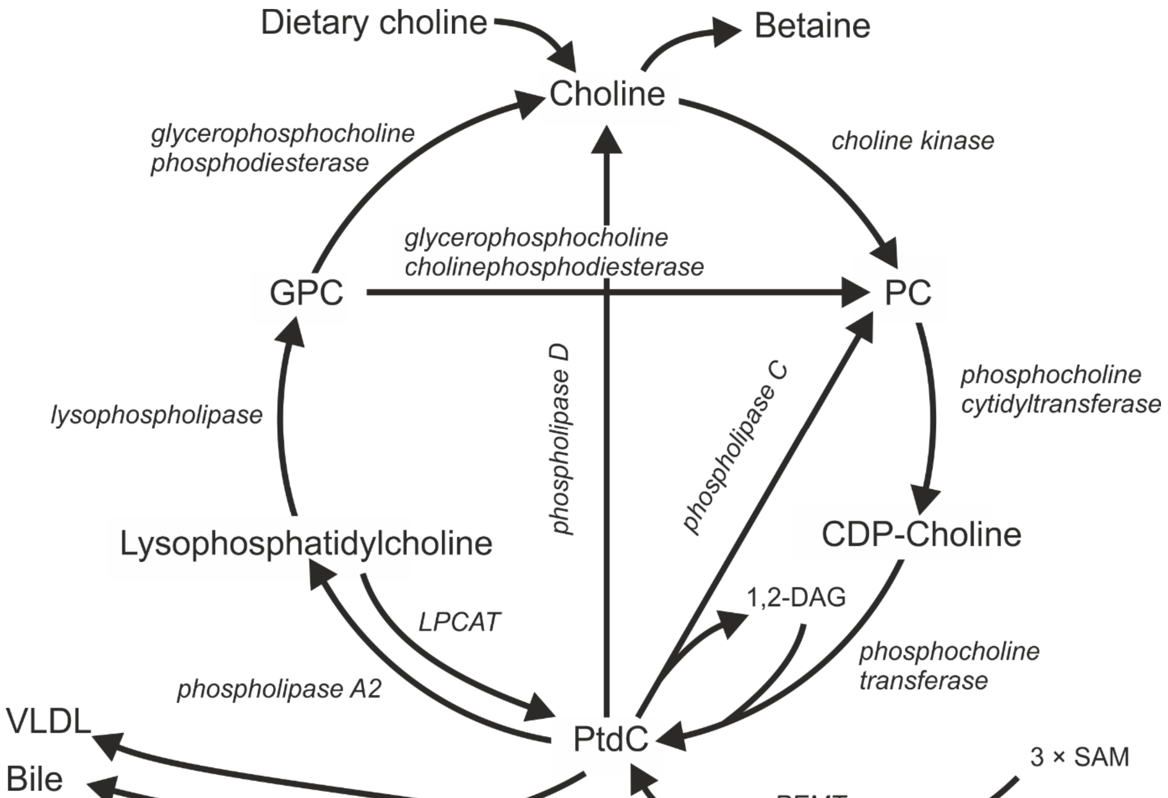

Fig 3.2. Simplified pathways of phosphatidylcholine anabolism and catabolism. Enzymes are given in italics. Central reactions are equivalent in phosphatidylethanolamine metabolism. Abbreviations are: phosphocholine (PC), cytidine diphosphate (CDP), S-adenosyl methionine (SAM), phosphatidylethanolamine N-methyltransferase (PEMT), diacylglycerate (DAG), phosphatidylcholine (PtdC), lysophosphatidylcholine acyltransferase (LPCAT), very low density lipoprotein (VLDL), and high density lipoprotein (HDL).

Within the endoplasmic reticulum, another pathway for the formation of PtdC is the sequential transfer of three methyl groups onto PtdE from S-adenosyl methionine (SAM). This reaction is catalysed by phosphatidylethanolamine N-methyltransferase (PEMT). The PEMT pathway accounts for 30% of PtdC biosynthesis, and the direct choline Kennedy pathway accounts for the other 70% (25).

A process for the renewal of PtdC is the Land cycle. Phospholipase A2 (PLA2) removes fatty acids at the *sn*-2 position to form lysophosphatidylcholine (lyso-PtdC) (26). Various lysophosphatidylcholine acyltransferases (LPCATs) can catalyse the reverse reaction, completing the Land cycle.

Lyso-PtdC has a disruptive effect on cell membranes (27, 28), but if it is not reformed into PtdC, it can be broken down by lysophospholipase to form glycerophosphocholine (GPC). GPC is then catalaysed by GPC phosphodiesterase to form glycerophosphate and choline. The PtdE catabolism pathway is the same, going via lysophosotidylethanolamine (lyso-PtdE) and glycerophosphoethanolamine (GPE). One alternative route of hydrolysis involves phospholipase D, which produces choline and phosphotidate (29, 30). Another involves phospholipase C, producing PC and DAG (30).

PtdC accounts for 95% of the total choline pool (31). In the liver, the majority of PtdC is either secreted into bile, into very low density lipoproteins (VLDLs), or used in high density lipoproteins (HPLs) which are secreted into plasma (32).

3.1.3.2. Cell cycle phases

Eukaryote cells which are actively dividing go through four phases – two gap phases (G_1 and G_2), a synthesis phase (S) and a mitosis phases (M). In G_1, all the cell contents except chromosomes are duplicated. In the S phase, DNA synthesis occurs and each of the chromosomes is copied. In G_2, any errors in the chromosomes are fixed. Then in the M phase, mitosis (nuclear division) occurs before cytokinesis (cell division) happens.

The membrane turnover rate changes in the different phases of cell growth cycle (33). In the G_1 phase there is a high membrane turnover rate. PtdC degradation is decreased in S phase, leading to a net accumulation of up to double the number of phospholipids (33). Less is known about the G_2 and M phase, but they are much shorter (2-4 h compared to 6-12 h). So, the build-up of phospholipids and their precursors is periodic. Average changes in concentration are dependent on the number of cells in each phase (34).

Some cells are no longer in the actively dividing state. There is a branching point within the G_1 phase where cells can enter a new phase, G_0, which does not then proceed to the S phase. The change to G_0 phase can be reversible, such as in mature hepatocytes, or irreversible, such as in senescent cells.

3.1.3.3. Changes in disease

Senescence of cells within the liver drives hepatic steatosis (35). It has been shown in cirrhotic livers independent of aetiology, and has even been shown in the livers of children with end stage liver disease (36). The inflammatory response of the liver to cirrhosis, and the presence of senescent cells has been proposed as a reason for the high prevalence of hepatocellular carcinoma (HCC) arising from cirrhosis (37).

In a variety of cancers, cell membrane precursors have been found to increase and degradation products to decrease (38). The reduction in GPC could potentially be due to GPC-phosphodiesterase activity increase in differentiated cells (39). An increase in phospholipase C activity has been suggested as a reason for PE/PC increase (40). However, ethanolamine is not a known inhibitor of phospholipase C, and the reduction of PC by introduction of ethanolamine was over 90% (41). Alternatively, the concentration of PC in tumours correlates strongly with number of cells in S-phase, and GPC and GPE are inversely correlated (42). The concentration of PE is not correlated, but this is attributed to having high enough concentration at all times to support PtdE synthesis.

The lipid composition of cell membranes (i.e. the ratio of PtdC to PtdE) is generally tightly regulated even in the diseased cell (43), with no relationship to the level of their precursors. Any changes in the ratio of PtdC to PtdE affects cell membrane integrity (44), and can cause the release of pro-inflammatory cytokines (45). In NAFLD, a reduced PtdC concentration has been found (46), and the changes in the PtdC to PtdE ratio are associated with an increase in steatosis (47). This might be caused by a change in SAM concentration and hence in the PEMT pathway (48).

An increase in PtdE and PtdC is seen in the regenerating liver (49-52). Their precursors also increase, but PE increases more than PC (53). After a resection, a limited supply of PtdC does not stop the liver from regenerating (54), but it does affect survival rate (55), possibly due to changes in membrane fluidity (56).

Cells respond to an increase in PtdC production by increasing degradation (57). While the major product is GPC, the concentrations of choline and PC are also increased through alternate degradation pathways (57). A by-product of this is an increase in DAG, and thereby an increase in DNL, which can cause steatosis.

There are also changes in phospholipid metabolism due to nutritional state. A 48 h fast produces sharp decrease in PtdC and PC, whereas there are only minor decreases in PtdE and PE (58). This is consistent with an increase in GPC in serum starved cells (which are assumed to be in G_0), whereas stimulated cells increase in PC (59).

3.2. In vivo hepatic ^{31}P-MRS

3.2.1. MR-visibility of some ^{31}P metabolites

Some proportion of ^{31}P metabolites are invisible to MR techniques, and the exact reasons for this are as yet unknown.

Apart from low concentrations, the main possible causes of metabolites being invisible to MR techniques are a shortening of T_1 by either macromolecular binding, association with paramagnetic ions (such as Mg^{2+} or Ca^{2+}), or being compartmentalized within a region of high viscosity. In the liver, ^{31}P metabolites can either be found in the cytosol or within the mitochondria, and it is those within the mitochondria that might be expected to be MR-invisible.

ADP has been found to be either completely MR-invisible (60-62), or to be 73 – 85% invisible (63-66). As the ex vivo concentration of ADP is about 1 – 1.5 mmol/L wet tissue (60, 67, 68), up to 0.15 – 0.4 mmol/L wet tissue may be MR visible. This poor visibility has been attributed to mitochondrial ADP being invisible due to the effects mentioned above (61, 69). Yet this may not be the whole story, because only 50 – 58% of ADP is mitochondrial (70-72).

Both intra and extra-mitochondrial ATP is visible (61, 69), but although some groups have claimed to see concentrations of ATP matching ex vivo measures (60, 73), others have seen a discrepancy of up to 24% (74, 75), which would match the 16 – 28% of ATP that is found in mitochondria (70-72).

Between 25 and 60% of P_i is invisible to MR methods (60, 64-66), which is comparable to the reported 34 and 54% of P_i found within mitochondria (70-72). This would also agree with the finding that the pH of P_i is consistent with cytosolic pH (76). However, P_i is MR visible in isolated mitochondria (75), and in some cases two peaks can be seen, which have been attributed to cytosolic and mitochondrial P_i (77, 78). So the hypothesis that any metabolites within mitochondria are not MR-visible is attractive, but does not seem to tell the entire story.

Nevertheless, it is clearly the case that some proportion of ^{31}P metabolites are not visible to MR methods, and it is likely that this holds equally true for less well investigated metabolites as it does for ATP, ADP and P_i.

3.2.2. The ^{31}P hepatic spectrum

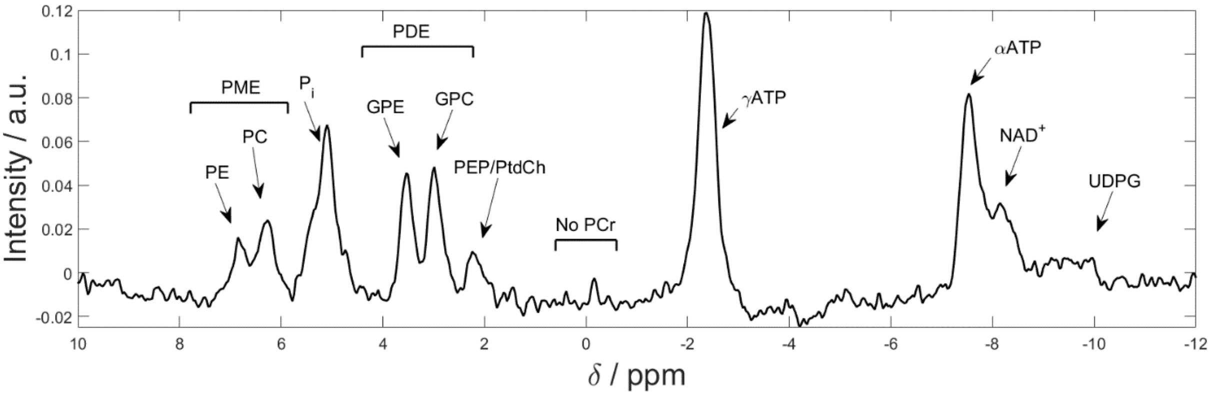

Fig 3.3. Typical in vivo ^{31}P-MRS liver spectrum acquired at 7T. Each of the peaks is labelled with its attributed metabolite. The β-ATP peak is at -16ppm, and is not shown here.

Phosphocreatine (PCr) is usually used as a reference for in vivo ^{31}P spectra. This is because in most tissues it is the dominant signal. PCr is a buffer for ATP, which explains its high concentration in muscle and brain. However, in the liver, ATP usage is mostly constant, and a buffer is not required. So, PCr is not seen in healthy liver tissue. Despite this, the frequency of PCr is still defined as 0 ppm for consistency with other in vivo studies.

The dominant signal in the liver spectrum comes from ATP (see Fig 3.3). As ATP has three phosphorus atoms, it has three peaks: γ-ATP (at -2.2 ppm), α-ATP (at -7.4 ppm), and β-ATP (at -16 ppm, not shown in Fig 3.3). The chemical shifts of γ- and β-ATP are sensitive to

Mg^{2+} concentrations, so α-ATP is often used as the reference to determine 0 ppm. These peaks will have some contributions from other nucleotide triphosphates (NTP), including up to 10% GTP (60).

Also contributing to these peaks is any signal that arises from ADP. The β-ADP resonance lies close to γ-ATP, and α-ADP lies close to α-ATP. The ratio of ATP to ADP is 0.9 – 2 in the mitochondria and 6 – 8.8 in the cytosole (70-72, 79), and a greater proportion of ADP is invisible, so the ADP peaks will amount to at most 7% of the ATP signal.

Overlapping α-ATP is a signal that is predominantly from NAD^+. The reduced form of NAD^+, NADH, is formed in several metabolic processes, and NADPH and $NADP^+$ are involved in the pentose phosphate pathway (80). As the phosphorus in these four compounds have very similar chemical shifts, it is difficult to distinguish them by ^{31}P-MRS. The combined NAD concentration is significantly higher than that of NADP under physiological conditions (81). The concentration of NAD^+ is 700 times that of NADH in the cytosole and 7 – 8 times NADH in the mitochondria (82). Mitochondrial membranes are impermeable to NAD^+, leading to a difference in concentration in the two pools. The relative levels change depending on cell type; the NAD^+ pool is 70% mitochondrial in cardiac myocytes (83), 50% in neurons (83) and 30 – 40% in hepatocytes (84). It has been proposed that the different NAD^+ pools, as well as NAD, NADPH and $NADP^+$, are visible in muscle in vivo (85).

Close to α-ATP and NAD^+, there is a small peak that corresponds to UDPG. There are no other metabolites that are likely to be in the same region. As it is low in SNR, it has been challenging to investigate.

The positive chemical shift region is more complicated than the negative region, and there are many overlapping peaks. It is simple to attribute the peak at 5.4 ppm to P_i, as it has a high concentration, despite some proportion of P_i being MR-invisible. Although all metabolites have small chemical shift changes due to pH, P_i changes the most (86). In fact, pH within the cell can be measured by comparing the chemical shift of P_i to that of PCr (when it is present) or ATP, which change very little within physiological ranges (87). This characteristic allows the differentiation between cytosolic and mitochondrial P_i (77, 78).

Phosphodiester (PDE) metabolites also have high signal peaks. These can be resolved to two peaks that mainly come from GPC and GPE (88), although it is possible that the GPC peak has some contribution from PtdE (89). Overlapping these is a third resonance, which has often been assigned to PEP (90-94). However, recent studies have shown that it is likely that biliary PtdC is the major component of this signal (95-97).

In the PDE region and extending towards higher ppm, there is also a broad baseline resonance from the ER (98). In vitro, the phospholipid bilayer broadens from 210 Hz at 1.9 T to 7000 Hz at 7 T and shifts towards lower ppm (98). This broadening was observed in vivo in rats at 8.5 T (99).

The most complicated part of the ^{31}P spectrum of the liver is the phosphomonoester (PME) region. In ex vivo tissue, more than ten peaks have been assigned: G6P, glycerol-3-phosphate, G1P, 3-PG, PE, CoA, ribose 5-phosphate, AMP, 2,3-diphosphoglycerate (2,3-DPG), and PC (100). However, the method of acquiring in vitro samples causes changes in the levels of several metabolites including: ATP, ADP, AMP, P_i, and any phosphorylated metabolites including G6P, 3-PG, and G1P (101). High resolution in vivo spectra resolve the PME peak into two separate components. In cancer, PC and PE are undoubtedly major components of those two peaks (88, 102, 103). In healthy tissue, it is more difficult to assign these peaks to any single compound, and it is likely that the contributors depend on the state of the tissue. For example, when fructose or glucose is taken orally or infused, a time-varying fructose-6-phosphate (F-6-P) peak is clearly visible (104-107). Or if there is a lot of contamination from the blood pool, the 2,3-DPG peak will be particularly evident (108, 109).

In this thesis, I refer to these two PME peaks as “PC” and “PE”, acknowledging that they are likely to also contain signal from other metabolites. It may be possible to validate this assignment using the known variation in PC and PE chemical shift for changes in pH (87).

3.3. ^{31}P-MRS methods

3.3.1. Acquisition

3.3.1.1. Localization

Highly localized spectra require more time to acquire and have lower SNR. There is therefore a trade-off to be made in the choice of localization methods. Where scan time or temporal resolution is the major concern, depth-resolved spectroscopy (DRESS) can be used (110). Methods such as 1D chemical shift imaging (CSI) (111), or 1D image-selected in vivo spectroscopy (ISIS) (112) are similarly swift. Fully 3D localized methods limit contamination better; 3D-ISIS is faster than 3D-CSI, and is therefore commonly used (91, 113-116). But the additional spatial information gained from 3D-CSI means that it is often preferred when time allows (117-121). 2D-CSI is sometimes used to compromise localization with time (122-124). Chmelik et al. compared a variety of localization methods at 7 T (125).

3.3.1.2. ^{1}H-decoupling and nuclear Overhauser effect (NOE) enhancement

^{1}H-decoupling suppresses J-coupling between ^{31}P nuclei and ^{1}H nuclei, which reduces the apparent peak linewidths of these ^{1}H-coupled metabolites, giving better spectral resolution. In the liver, this is especially useful, as there are multiple overlapping peaks. However it requires additional hardware, and demands high SAR. Its use is more common in recent studies, as these problems have largely been overcome (115-117, 126).

NOE enhancement uses ^{1}H magnetization to give a 1.4 – 1.8 times signal enhancement in the ^{31}P signal. Its use can be challenging as it adds an additional correction to quantification. It appears to be impossible to perform ^{1}H-decoupling without some additional NOE effect (127). Like ^{1}H-decoupling, NOE enhancement requires a dual-tuned coil hardware, but can be less power-demanding and does not require high performance RF filtering on the receive chain to prevent ^{1}H transmit from corrupting the ^{31}P signal.

3.3.1.3. Field strength

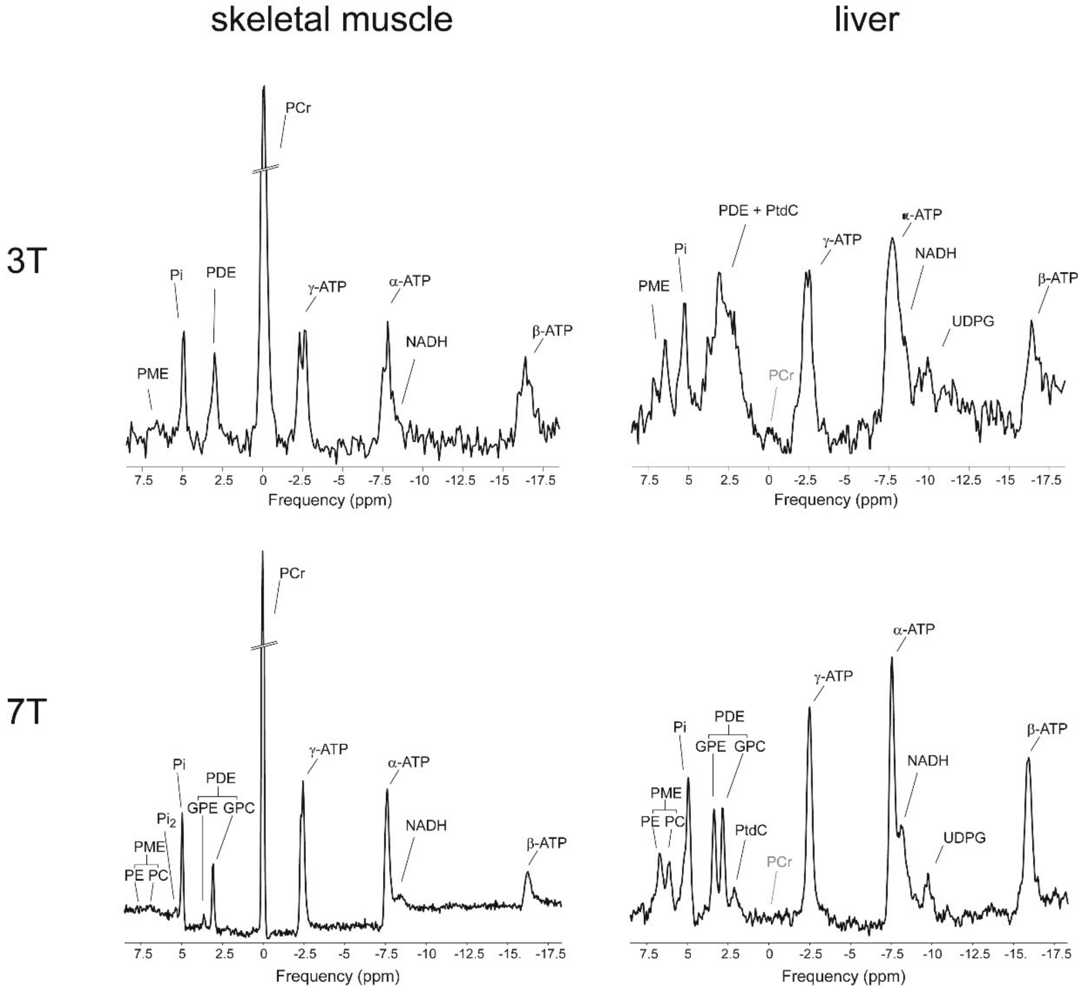

Fig 3.4. Typical ^{31}P-MR spectra acquired at 3 T (top) and 7 T (bottom), at rest, in skeletal muscle (left) and liver tissue (right). All spectra are depicted relative to the resonance frequency of phosphocreatine (PCr), although this is not present in healthy human liver tissue. Phosphorus metabolites common to both tissues include resonance lines of adenosine-triphosphate (ATP), nicotinamide adenine dinucleotide (NADH), phosphodiesters (PDEs) – glycerol-phosphocholine (GPC) and glycerol-phosphoethanolamine (GPE), inorganic phosphate (Pi) and phosphomonoesters (PMEs) – phosphocholine (PC) and phosphoethanolamine (PE). From Valkovič et al. (128).

^{31}P-MRS is a signal-to-noise-limited technique. As SNR is proportional to B_0 (see Eq [2.44]), there is a drive to increasing field strength despite the technical challenges that imposes. The general availability of lower field strength scanners has meant that 1.5 T has been the most common field strength for ^{31}P experiments (110, 113, 114, 118, 122, 123, 129-131). Now 3 T scanners have become more prevalent, many experiments have utilized their increased SNR (91, 112, 115, 116, 119-121). And recently whole-body 7 T MR scanners have become available for ^{31}P-MRS (124, 125).

The improvement in SNR at 7 T makes fully 3D-resolved localization methods feasible in a clinically-relevant scan time. In addition to SNR, there are other benefits. The increase in field strength from 3 T to 7 T allows resolution of the PME and PDE peaks without ^{1}H-decoupling (see Fig 3.4) (95, 125). And the underlying ER resonance broadens as field strength increases, which is expected to make it indistinguishable from baseline noise in vivo.

Resolution of individual metabolites can allow more subtle metabolite changes to be visible. For example at 7 T, PC and PE have been reported to have opposing changes in human breast cancer, which was not visible in the combined PME peak seen at lower fields (132).

3.3.1.4. Coils

Predominantly, single loop surface coils have been used for ^{31}P-MRS of the liver. They are simple to make and tune, have high $\boldsymbol{B}_1^+$ efficiency, and naturally enhance localization. Some of the coils are tuned only to ^{31}P frequencies (110, 115, 130), but the majority are also tuned to ^{1}H (112, 113, 122, 125, 129). Double-tuning the coils allows ^{1}H localizers and shimming to be achieved in the same session as ^{31}P acquisition without having to swap a coil, which can be challenging to achieve without moving the subject. The size of the coil is chosen to optimize sensitivity and $\boldsymbol{B}_1^+$, depending on the depth and size of the target anatomy. The sizes range from 6.5 cm diameter (130), to 16 cm diameter (111). There have been some more complex coils: an 8-channel array coil has been developed for ^{31}P-MRS at 3 T (133, 134) and a quadrature coil has been used at 7 T (124).

3.3.2. Analysis

A variety of methods are used for analysis in the literature, including simple peak integration (113) and frequency-domain Lorentzian (122) or Gaussian fitting (111, 130). However, after the Magnetic Resonance User Interface (MRUI) was developed, it became commonly used (135). Initially, the Variable projection (VARPRO) algorithm was used (129, 136), but it was only when the algorithm was extended in the *advanced method for accurate, robust and efficient spectral fitting* (AMARES) that it became truly popular (115, 116, 118-121). AMARES is now predominantly used in the Java interface of MRUI (jMRUI) (137).

3.3.3. Normalization and Calibration

In some studies, saturation-correction was deemed infeasible, and all other normalization and calibration corrections were bypassed by taking ratios (91, 111, 113, 114, 122). In other studies, ratios were taken, but the peaks were corrected for T_1 effects (138). These ratios could either be to the summed phosphate signal (113, 122), the sum of the PME and PDE signal (115), or ATP (139). In other studies, saturation-correction was performed, and sensitivity-correction and calibration was achieved by the phantom replacement method (121), with care taken to account for coil loading differences between the phantom and the subject. The most rigorous methods account for each of the corrections separately, allowing error analysis of each separate part (117).

3.4. Literature normal values

3.4.1. Relaxation times

Relaxation in ^{1}H metabolites is dominated by dipolar interactions, and so their T_1 times typically increase with B_0. In contrast, ^{31}P metabolites have significant relaxation from two mechanisms: dipolar interaction and chemical shift anisotropy (CSA). ^{31}P metabolites generally have long T_1 and short T_2. In the extreme narrowing limit, when τ_c is short (as it is in liquids), CSA relaxation dominated T_1 and T_2 values are proportional to $1/B_0^2$. It can therefore be expected that CSA relaxation will have an increasingly predominant effect as B_0 increases. Indeed, studies have indicated that CSA is the dominant relaxation mechanism for ATP at high field strengths, whereas dipolar interactions dominate relaxation at lower field strengths (140). Metabolites with more isotropic chemical shift, such as P_i, PME, and PCr, are always in the dipolar relaxation regime at field strengths relevant to human MRI (140). When relaxation is CSA-dominated, the linewidth ($1/T_2$) increases with B_0^2, but the frequency separation between peaks only increases with B_0. This means that it is possible for spectral resolution to *decrease* at higher field strengths in some situations.

In vivo, other interactions also need to be considered. Binding with enzymes may increase T_1 and reduce T_2 by restricting metabolite mobility. Dipolar interactions between ATP and magnesium (Mg^{2+}) could reduce relaxation times. Any deposition of iron in the liver will also shorten relaxation times.

In the liver, ATP has very short T_1 values (0.35 – 0.56 s for 1.5 – 7 T) (117, 125). This is in stark contrast to other organs, where ATP T_1 values are between 1 and 5 s (141-144). The difference in values is attributed to the interaction between ATP and paramagnetic ions in the liver. Because of these interactions, ATP T_1 relaxation times are not seen to change significantly with field strength (see Fig 3.5). A similar effect is seen for P_i, with values between 0.41 and 1.6 s in the liver (145, 146), and between 1.45 and 6.9 s in other organs (141, 143).

The PME peaks have longer T_1 values than ATP or P_i, between 0.84 and 4.41 s (112, 125, 147), compared to 1.42 to 8.1 s in other organs (143, 148). There is also potentially a trend to an increase in T_1 with field strength, although more studies would be needed to confirm this.

The PDE peaks have longer T_1 values again, between 1.36 and 6.6 s (117, 147), which are similar to the T_1 values for other tissues (143, 148).

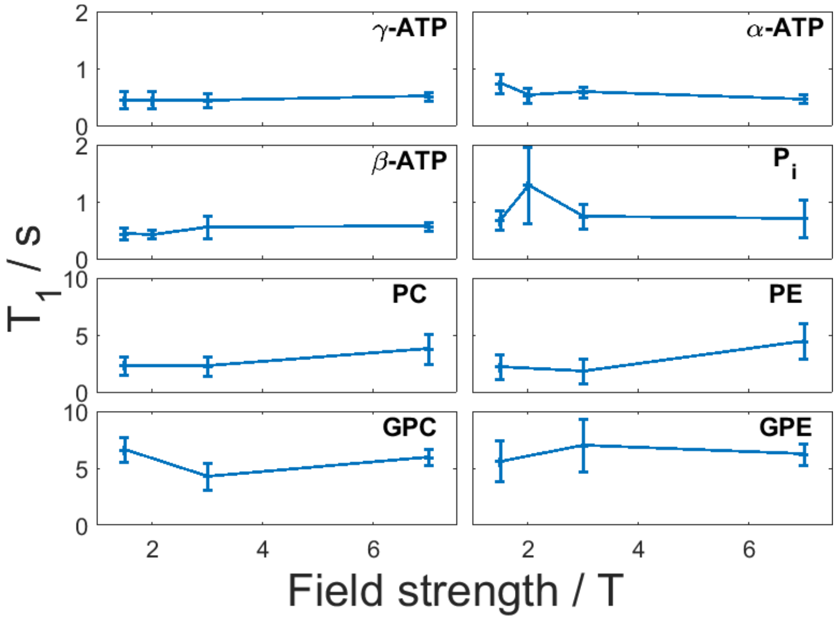

Fig 3.5. Variation of T_1 with field strength. Mean ± SD of literature T_1 values acquired at 1.5 (117, 145, 149), 2 (146, 147), 3 (112) and 7 T (125). Where more than one value was available at a single field strength the mean was taken, and the SD is the mean of the individual SDs.

The other peaks have lower SNR, which makes it challenging to measure their relaxation times. The NAD^+ T_1 time has been determined to be 2.6 ± 1.4 s at 1.5 T (117). The PEP/PtdC peak has been measured as 2.0 ± 1.0 s at 1.5 T (117), and 0.97 ± 0.30 s at 3 T (97).

True T_2 relaxation times, rather than T_2^* times, are difficult to measure, and their exact values have little impact on experimental design or normalization unlike T_1 values. Because of this, they are not often measured. At 7 T, the β-ATP peak was found to have a T_2 of 18.18 ± 0.37 ms, the P_i peak was 46.37 ± 1.08 ms, and the PME and PDE peaks were between 44 and 65 ms (124).

In some pilot studies, ^{31}P relaxation times have been shown to change in liver disease (150). In part, this could be due to changes in iron concentrations, as has been seen for the ^1H T_1 values (151). Changes in T_2^* will only change the linewidth, which should not significantly change quantification results. But changes in T_1 will affect saturation-correction of CSI spectra according to Eq. 2.56. Depending on normal T_1 and scan parameters, the bias in the final concentration is expected to be between about 1 – 46% of the bias between the T_1 value used for correction compared to the actual T_1 value.

3.4.2. Concentrations

Due to the variety of normalization and calibration methods described in Section 3.3.3, there are large discrepancies in reported concentrations. Data from a selection of studies that accounted for saturation- and sensitivity-correction, coil loading and volume effects, are given in Table 3.1. The only one of these studies to determine the concentrations of the PME and PDE peaks separately was Li et al. (117). They found the concentration of PC to be 1.1 ± 0.10 mmol/L wet volume, PE 1.2 ± 0.40 mmol/L wet volume, GPC 3.5 ± 0.60 mmol/L wet volume, and GPE 2.8 ± 0.70 mmol/L wet volume.

Table 3.1. ^{31}P metabolite concentrations in the liver. In each case, the values were corrected for volume, PSF and loading. Only Li et al used proton decoupling or NOE, and the NOE was corrected.

PME / mmol L^{-1} wet tissue	PDE / mmol L^{-1} wet tissue	P_i / mmol L^{-1} wet tissue	γ-ATP / mmol L^{-1} wet tissue	Localization	Nominal Volume / mL	B_0 / T	Saturation correction	Sensitivity correction	n	Reference
3.77 ± 0.68	10.85 ± 1.71	2.35 ± 0.53	4.29 ± 0.64 (β-ATP)	DRESS	30mm slice thickness	1.5	Single correction measurement	Single correction measurement	13	Noren et al. 2008 (3)
3.09 ± 1.45	10.83 ± 2.68	1.63 ± 0.55	3.72 ± 0.99	2D CSI	36	1.5	Same T_R/T_1 used in reference scan	Phantom replacement	11	Dezortova et al. 2005 (5)
3.8 ± 0.7	9.7 ± 1.5	2.9 ± 0.3	2.9 ± 0.4	3D ISIS	216	1.5	Adiabatic + fully relaxed (10 s T_R)	Phantom replacement	12	Buchli et al. 1994 (8)
2.4 ± 0.40	7.6 ± 1.67	2.8 ± 0.50	3.7 ± 0.60	3D CSI	27-64	1.5	Biot-Savart and previously measured T_1	Biot-Savart and phantom reference	6	Li et al. 1996 (9)
0.92 ± 0.41	5.36 ± 1.43	0.97 ± 0.25	2.02 ± 0.13	3D ISIS	53-150	1.5 / 2	Biot-Savart and previously measured T_1	Phantom replacement	13	Meyerhoff et al. 1990 (12)
2.24 ± 0.32	11.40 ± 3.04	1.37 ± 0.22	2.14± 0.32	3D CSI	3.64	3	Adiabatic excitation and literature T_1	Phantom replacement	10	Chmelik et al. 2008 (1)
1.98 ± 0.58	8.01 ± 2.17	1.99 ± 0.51	2.74 ± 0.55	3D ISIS	216	3	Adiabatic excitation and literature T_1	Correction measurement + phantom reference	85	Laufs et al. 2013 (116)

3.5. Human liver metabolism investigated using in vivo ^{31}P-MRS

The centres publishing work on in vivo liver ^{31}P-MRS between 2010 and 2018 are in Table 3.2, and the changes seen in various disease states are given in Table 3.3.

Several studies have shown a decrease in ATP due to various causes (118, 120, 123, 152, 153). In the early stages of liver disease only limited ATP reduction is seen; the extent of ATP depletion depends on fibrosis stage (110). In the regenerating liver (118, 152), the ATP reduction is explained by increased gluconeogenesis and reduced glycolysis (154, 155). However other processes (cirrhosis (123), type-2 diabetes mellitus (T2DM) (120), and HCC (153)) have a common theme – insulin resistance. As most of these scans were performed on subjects in the fasted state, the insulin resistance could lead to preferential gluconeogenesis over glycogenolysis, which requires more ATP. To my knowledge, no studies have thus far shown an increase in ATP concentration due to disease or dietary stimulus.

In the regenerating liver, an increase in P_i is seen along with the reduction in ATP (118, 152), whereas a decrease is seen in all the fibrosis stages and disease aetiologies apart from NAFLD and some cases of cancer (102, 110, 119, 120, 123, 153) . A reduction in P_i has been explicitly associated with increased β-oxidation of fatty acids and gluconeogenesis in hepatic steatosis (156), and with a reduced ATP synthesis rate in T2DM (119). An inverse correlation of P_i with hepatic inflammation has been found (113, 157, 158).

Several infusions have been used to actively challenge hepatic metabolism. L-alanine increases gluconeogenic rates after it is converted to pyruvate, and it has been used in studies in healthy volunteers and patients with cirrhosis to find an increase in gluconeogenesis in cirrhosis (122, 159). In order to investigate glycolysis, both glucose and fructose infusions have been used (104-107).

Table 3.2. **List of currently or recently active research centres in the field of human in vivo hepatic ^{31}P-MRS.**

Centre name	PIs	Selected references
Medical University of Vienna, Austira	Martin Krššák	(95, 125, 160)
China-Japan Union Hospital Affiliated to Jilin University, China	Hai-Shan Yang	(161)
The Chinese University of Hong Kong	Winnie C.W. Chu, Henry L.W. Chan	(115, 162)
University Medical Center Utrecht, Netherlands	Dennis W.J. Klomp	(124)
German Diabetes Center, Germany	Jong-Hee Hwang, Michael Roden	(97, 116, 163, 164)
University of Nottingham, UK	Penny Gowland	(104)
University of Edinburgh, UK	Scott Semple	Macrophage therapy study underway
Linkoping University, Sweden	Peter Lundberg	(110)
Imperial University, UK	Simon Taylor-Robinson	(126, 165-167)
Institute for Clinical and Experimental Medicine, Czech Republic	Monika Dezortová, Milan Hájek	(123, 131, 168)
Washington University School of Medicine, USA	Joseph Ackerman	(169)
Purdue University / Indiana University School of Medicine, USA	Ulrike Dydak	(133)
University of Bern, Switzerland	Chris Boesch	(170)
The Second Military Medical University, China	Shi-Yuan Liu	(171)
University of Oxford	Christopher T. Rodgers	(172)

NADH has not been extensively studied, but has been found as a potential biomarker for NAFLD (91). This corroborates the hypothesis of deranged metabolism within NAFLD.

The peak height of PME in tumours has been associated with nutritional state (173). PME decreases as time after feeding increases (and the opposite is seen for PDE, although the response is smaller).

In a variety of disease states, it has been shown that a decrease in PDE peaks is associated with an increase in PME peaks (118, 123, 152, 153). However, this does not seem to be the case for T2DM, where both PME and PDE decrease (120). These changes probably depend on the dominant signal within the "PME" peak. In cancer, the increase in signal has been shown to be due mainly to increases in PC and PE (43). This change is attributed to an increased rate of cell turnover (43).

Intracellular pH has also been studied in several disease states, with a significant increase visible in certain cancer cells (102).

3.6. Other methods for the investigation of human in vivo liver metabolism

A complete understanding of liver metabolism is impossible using ^{31}P-MRS alone. In this section, I will briefly discuss a few other methods for the investigation of human in vivo liver metabolism.

The first method is biopsy. Biopsy allows detailed investigation of hepatocyte structure and cell composition. However biopsy is invasive, and suffers from high sampling variability (174-177).

Closely connected to ^{31}P-MRS are proton (^{1}H) and carbon (^{13}C) MRS (90). With the exception of P_i, all of the metabolites containing ^{31}P also contain both ^{1}H and $^{12/13}$C. However, both of these methods have limitations. In ^{1}H-MRS, water and lipid resonances can overwhelm the signal arising from less abundant metabolites. In addition, the ^{1}H-MRS chemical shift range is very narrow (< 10 ppm), which makes the separation of the numerous visible metabolites challenging. In contrast, ^{13}C-MRS has a large spectral range (>200 ppm), but it is limited by the low natural abundance and gyromagnetic ratio of ^{13}C. One method for overcoming this limitation is hyperpolarization.

Hyperpolarization using the dynamic nuclear polarization technique can increase the SNR of ^{13}C by more than 10,000 times (178). Although this SNR boost only lasts for a few minutes, imaging methods can be used to trace the metabolism of the tracer e.g. pyruvate (179). Another technique which follows tracer metabolism is positron emission tomography (PET) (180). With this technique, an increase in focal glucose uptake can be found by imaging ^{18}F-fluoro-2-deoxy-D-glucose. This is mainly used to detect glucose-avid tumours but the naturally high glucose uptake in liver tissue makes the detection of small tumours challenging (181).

Unless they are target a particular metabolite, imaging methods are not useful for the direct investigation of metabolism. However, they may be useful for measuring secondary markers, such as fibrosis (182). For this purpose, liver stiffness measures are also useful (182). There are also other methods that measure the metabolism of the whole body, from which the metabolism of the liver may be inferred. These include the measurement of serum biomarkers (182), or the measurement of e.g. the level of ^{13}C in breath CO_2 after a ^{13}C enriched meal (183).

My work has been focused on the development of ^{31}P-MRS methods, and so I will not discuss these techniques further. However, any study investigating the liver should consider using multiple methods to aid a greater understanding of the underlying metabolism.

Table 3.3. List of ^{31}P metabolite changes in hepatic disease.

Metabolite	Fibrosis	Cirrhosis	Cancer	NAFLD	Liver regeneration	T2DM	Reflects	Other comments
ATP	- or ↓	↓	↓	-	↓	↓	ATP is primary cellular energy supply.	
PtdC	?	?	?	?	?	?	Present in bile.	Distinguishable from PDE with ^{1}H decoupling or at 7 T
PDE	↓	↓	↓	↓ or -	↓	↓	Cell membrane degradation products	Glycerophosphocholine (GPC) and glycerophosphoethanolamine (GPE) distinguishable with ^{1}H decoupling or at 7 T
P_i	↓	↓	↑ or ↓	-	- or ↑	↓	P_i is produced (net) when ATP hydrolysis exceeds ATP synthesis.	
PME	- or ↑	- or ↑	↑	↑	↑	↓	Cell membrane precursors	Two peaks, assigned to phosphocholine (PC) and phosphoethanolamine (PE) distinguishable with ^{1}H decoupling or at 7 T
NAD^+	?	?	?	↑	?	?	Energy shuttle in oxidative phosphorylation	Visible at 7 T or with ^{1}H-decoupling and NOE enhancement
UDPG	?	?	?	?	?	?	Glycogen precursor	Visible at 7 T or with ^{1}H-decoupling and NOE enhancement
Intracellular pH	-	-	↑	-	-	?	In hypoxic conditions, myocytes respire more anaerobically, building up lactic acid and lowering pH.	Derived from P_i chemical shift
References	(110)	(110, 123)	(102, 184)	(91, 110)	(118, 152)	(120)		

3.7. Summary

1. MR-visible ^{31}P metabolites take part in both liver energetics (ATP, P_i, NAD^+, UDPG), and the cell cycle (PC, PE, GPC, GPE, PtdC).
2. The diseased liver has changes in both energetics and the cell cycle.
3. ^{31}P metabolites are not all fully visible using ^{31}P-MRS due to macromolecular binding, association with paramagnetic ions, or being compartmentalized within regions of high viscosity.
4. Many methods have been developed for ^{31}P-MRS in the liver, using a variety of localization techniques, coils and field strengths.
5. There are large discrepancies in reported concentrations of liver metabolites.
6. Liver ^{31}P metabolites often have shorter T_1 times than other organs.
7. Changes in ^{31}P metabolites are visible using ^{31}P-MRS in the diseased liver.
8. Whole-body 7 T scanners allow higher SNR and better spectral resolution than at 3 T.
9. Multimodal investigation may allow a greater understanding of underlying metabolism.

3.8. References

1. Boyer TD, Manns MP, Sanyal AJ, Zakim D. Zakim and Boyer's Hepatology: A Textbook of Liver Disease: Elsevier Health Sciences; 2012.
2. Berg JM, Tymoczko JL, Stryer L. Biochemistry. Fifth Edition ed: W.H. Freeman; 2002.
3. Katz J, Tayek JA. Gluconeogenesis and the Cori cycle in 12-, 20-, and 40-h-fasted humans. American Journal of Physiology - Endocrinology And Metabolism. 1998; 275(3):E537-E42.
4. Tilg H, Moschen AR. Evolution of Inflammation in Nonalcoholic Fatty Liver Disease: The Multiple Parallel Hits Hypothesis. Hepatology. 2010; 52(5):1836-46.
5. Hotamisligil GS. Endoplasmic Reticulum Stress and the Inflammatory Basis of Metabolic Disease. Cell. 2010; 140(6):900-17.
6. Hassanein T. Mitochondrial dysfunction in liver disease and organ transplantation. Mitochondrion. 2004; 4(5):609-20.
7. Nishikawa T, Bellance N, Damm A, Bing H, Zhu Z, Handa K, Yovchev MI, Sehgal V, Moss TJ, Oertel M, Ram PT, Pipinos II, Soto-Gutierrez A, Fox IJ, Nagrath D. A switch in the source of ATP production and a loss in capacity to perform glycolysis are hallmarks of hepatocyte failure in advance liver disease. J Hepatol. 2014; 60(6):1203-11.
8. Petersen KF, Krssak M, Navarro V, Chandramouli V, Hundal P, Schumann WC, Landau BR, Shulman GI. Contributions of net hepatic glycogenolysis and gluconeogenesis to glucose production in cirrhosis. Am J Physiol-Endoc M. 1999; 276(3):E529-E35.
9. Mccullough AJ, Tavill AS. Disordered Energy and Protein-Metabolism in Liver-Disease. Semin Liver Dis. 1991; 11(4):265-77.
10. Owen OE, Reichle FA, Mozzoli MA, Kreulen T, Patel MS, Elfenbein IB, Golsorkhi M, Chang KHY, Rao NS, Sue HS, Boden G. Hepatic, Gut, and Renal Substrate Flux Rates in Patients with Hepatic Cirrhosis. J Clin Invest. 1981; 68(1):240-52.
11. Kabadi UM. Is Hepatic Glycogen-Content a Regulator of Glucagon-Secretion. Metabolism-Clinical and Experimental. 1992; 41(2):113-5.
12. Bugianesi E, Kalhan S, Burkett E, Marchesini G, McCullough A. Quantification of gluconeogenesis in cirrhosis: Response to glucagon. Gastroenterology. 1998; 115(6):1530-40.
13. Michael MD, Kulkarni RN, Postic C, Previs SF, Shulman GI, Magnuson MA, Kahn CR. Loss of Insulin Signaling in Hepatocytes Leads to Severe Insulin Resistance and Progressive Hepatic Dysfunction. Mol Cell. 2000; 6(1):87-97.
14. Cavalloperin P, Cassader M, Bozzo C, Bruno A, Nuccio P, Dallomo AM, Marucci M, Pagano G. Mechanism of Insulin Resistance in Human-Liver Cirrhosis - Evidence of a Combined Receptor and Postreceptor Defect. J Clin Invest. 1985; 75(5):1659-65.
15. Muller MJ, Lautz HU, Plogmann B, Burger M, Korber J, Schmidt FW. Energy-Expenditure and Substrate Oxidation in Patients with Cirrhosis - the Impact of Cause, Clinical Staging and Nutritional State. Hepatology. 1992; 15(5):782-94.
16. Schneeweiss B, Graninger W, Ferenci P, Eichinger S, Grimm G, Schneider B, Laggner AN, Lenz K, Kleinberger G. Energy-Metabolism in Patients with Acute and Chronic Liver-Disease. Hepatology. 1990; 11(3):387-93.
17. Müller MJ, Böttcher J, Selberg O, Weselmann S, Böker KH, Schwarze M, von zur Mühlen A, Manns MP. Hypermetabolism in clinically stable patients with liver cirrhosis. The American Journal of Clinical Nutrition. 1999; 69(6):1194-201.
18. Donnelly KL, Smith CI, Schwarzenberg SJ, Jessurun J, Boldt MD, Parks EJ. Sources of fatty acids stored in liver and secreted via lipoproteins in patients with nonalcoholic fatty liver disease. J Clin Invest. 2005; 115(5):1343-51.
19. Postic C, Girard J. Contribution of de novo fatty acid synthesis to hepatic steatosis and insulin resistance: lessons from genetically engineered mice. The Journal of Clinical Investigation. 2008; 118(3):829-38.
20. Ansell GB, Spanner S. Chapter 1 Phosphatidylserine, phosphatidylethanolamine and phosphatidylcholine. In: Hawthorne JN, Ansell GB, editors. New Compr Biochem. 4: Elsevier; 1982. p. 1-49.

21. Gibellini F, Smith TK. The Kennedy Pathway-De Novo Synthesis of Phosphatidylethanolamine and Phosphatidylcholine. Iubmb Life. 2010; 62(6):414-28.
22. Sundler R, Akesson B. Regulation of Phospholipid Biosynthesis in Isolated Rat Hepatocytes - Effect of Different Substrates. J Biol Chem. 1975; 250(9):3359-67.
23. Kennedy EP, Weiss SB. Cytidine Diphosphate Choline - a New Intermediate in Lecithin Biosynthesis. J Am Chem Soc. 1955; 77(1):250-1.
24. Fagone P, Jackowski S. Phosphatidylcholine and the CDP–choline cycle. Biochimica et Biophysica Acta (BBA) - Molecular and Cell Biology of Lipids. 2013; 1831(3):523-32.
25. Vance DE. Phospholipid methylation in mammals: from biochemistry to physiological function. Biochimica et Biophysica Acta (BBA) - Biomembranes. 2014; 1838(6):1477-87.
26. van den Bosch H. Phosphoglyceride Metabolism. Annu Rev Biochem. 1974; 43:243-77.
27. Masamune A, Sakai Y, Satoh A, Fujita M, Yoshida M, Shimosegawa T. Lysophosphatidylcholine induces apoptosis in AR42J cells. Pancreas. 2001; 22(1):75-83.
28. Takahashi M, Okazaki H, Ogata Y, Takeuchi K, Ikeda U, Shimada K. Lysophosphatidylcholine induces apoptosis in human endothelial cells through a p38-mitogen-activated protein kinase-dependent mechanism. Atherosclerosis. 2002; 161(2):387-94.
29. Exton JH. New developments in phospholipase D. J Biol Chem. 1997; 272(25):15579-82.
30. Hodgkin MN, Pettitt TR, Martin A, Michell RH, Pemberton AJ, Wakelam MJO. Diacylglycerols and phosphatidates: which molecular species are intracellular messengers? Trends Biochem Sci. 1998; 23(6):200-4.
31. Li ZY, Agellon LB, Vance DE. Phosphatidylcholine homeostasis and liver failure. J Biol Chem. 2005; 280(45):37798-802.
32. Li Z, Vance DE. Thematic Review Series: Glycerolipids. Phosphatidylcholine and choline homeostasis. J Lipid Res. 2008; 49(6):1187-94.
33. Jackowski S. Cell Cycle Regulation of Membrane Phospholipid Metabolism. J Biol Chem. 1996; 271(34):20219-22.
34. Sanchez-Alvarez M, Zhang Q, Finger F, Wakelam MJO, Bakal C. Cell cycle progression is an essential regulatory component of phospholipid metabolism and membrane homeostasis. Open Biology. 2015; 5(9):150093.
35. Ogrodnik M, Miwa S, Tchkonia T, Tiniakos D, Wilson CL, Lahat A, Day CP, Burt A, Palmer A, Anstee QM, Grellscheid SN, Hoeijmakers JHJ, Barnhoorn S, Mann DA, Bird TG, Vermeij WP, Kirkland JL, Passos JF, von Zglinicki T, Jurk D. Cellular senescence drives age-dependent hepatic steatosis. 2017; 8:15691.
36. Gutierrez-Reyes G, Garcia de Leon MdC, Varela-Fascinetto G, Valencia P, Pérez Tamayo R, Rosado CG, Labonne BF, Rochilin NM, Garcia RM, Valadez JA, Latour GT, Corona DL, Diaz GR, Zlotnik A, Kershenobich D. Cellular Senescence in Livers from Children with End Stage Liver Disease. Plos One. 2010; 5(4):e10231.
37. Ramakrishna G, Rastogi A, Trehanpati N, Sen B, Khosla R, Sarin SK. From Cirrhosis to Hepatocellular Carcinoma: New Molecular Insights on Inflammation and Cellular Senescence. Liver Cancer. 2013; 2(3-4):367-83.
38. Negendank W. Studies of Human Tumors by MRS - a Review. NMR Biomed. 1992; 5(5):303-24.
39. Podo F, Carpinelli G, Ferretti A, Borghi P, Proietti E, Belardelli F. Activation of Glycerophosphocholine Phosphodiesterase in Friend Leukemia Cells Upon In-Vitro Induced Erythroid Differentiation. 31P and 1H NMR Studies. Isr J Chem. 1992; 32(2-3):291-8.
40. Radda GK, Dixon RM, Wood CA. N.m.r. studies of phospholipid metabolism and cell proliferation. Biochem Soc Trans. 1991; 19(4):995-6.
41. Daly PF, Lyon RC, Faustino PJ, Cohen JS. Phospholipid-Metabolism in Cancer-Cells Monitored by P-31 Nmr-Spectroscopy. J Biol Chem. 1987; 262(31):14875-8.
42. Smith TAD, Glaholm J, Leach MO, Machin L, McCready VR. The effect of intra-tumour heterogeneity on the distribution of phosphorus-containing metabolites within human breast tumours: An In Vitro study using 31P NMR spectroscopy. NMR Biomed. 1991; 4(6):262-7.
43. Podo F. Tumour phospholipid metabolism. NMR Biomed. 1999; 12(7):413-39.

44. Li ZY, Agellon LB, Allen TM, Umeda M, Jewel L, Mason A, Vance DE. The ratio of phosphatidylcholine to phosphatidylethanolamine influences membrane integrity and steatohepatitis. Cell Metab. 2006; 3(5):321-31.

45. Caballero F, Fernández A, Matías N, Martínez L, Fucho R, Elena M, Caballeria J, Morales A, Fernández-Checa JC, García-Ruiz C. Specific contribution of methionine and choline in nutritional nonalcoholic steatohepatitis: impact on mitochondrial S-adenosyl-L-methionine and glutathione. J Biol Chem. 2010; 285(24):18528-36.

46. Puri P, Baillie RA, Wiest MM, Mirshahi F, Choudhury J, Cheung O, Sargeant C, Contos MJ, Sanyal AJ. A lipidomic analysis of nonalcoholic fatty liver disease. Hepatology. 2007; 46(4):1081-90.

47. Arendt BM, Ma DWL, Simons B, Noureldin SA, Therapondos G, Guindi M, Sherman M, Allard JP. Nonalcoholic fatty liver disease is associated with lower hepatic and erythrocyte ratios of phosphatidylcholine to phosphatidylethanolamine. Applied Physiology, Nutrition, and Metabolism. 2012; 38(3):334-40.

48. Jacobs RL, van der Veen JN, Vance DE. Finding the balance: The role of S-adenosylmethionine and phosphatidylcholine metabolism in development of nonalcoholic fatty liver disease. Hepatology. 2013; 58(4):1207-9.

49. Fex G. Phospholipid Metabolism during Regeneration of Rat Liver. Biochem J. 1970; 119(4):743.

50. Tata JR. Co-Ordination between Membrane Phospholipid Synthesis and Accelerated Biosynthesis of Cytoplasmic Ribonucleic Acid and Protein. Biochem J. 1970; 116(4):617.

51. Johnson RM, Levin E, Albert S. Lipide Metabolism during Cell Division. Arch Biochem Biophys. 1954; 51(1):170-5.

52. Levin E, Johnson RM, Albert S. Phospholipide Metabolism in Cell Fractions of Regenerating Liver. Arch Biochem Biophys. 1958; 73(1):247-54.

53. Murphy EJ, Brindle KM, Rorison CJ, Dixon RM, Rajagopalan B, Radda GK. Changes in Phosphatidylethanolamine Metabolism in Regenerating Rat-Liver as Measured by P-31-Nmr. Biochim Biophys Acta. 1992; 1135(1):27-34.

54. Ling J, Zhu LF, Vance DE, Jacobs RL. Impaired phosphatidylcholine biosynthesis does not attenuate liver regeneration after 70% partial hepatectomy in hepatic CTP:phosphocholine cytidylyltransferase-alpha deficient mice. Can J Physiol Pharmacol. 2012; 90(10):1403-12.

55. Ling J, Chaba T, Zhu LF, Jacobs RL, Vance DE. Hepatic ratio of phosphatidylcholine to phosphatidylethanolamine predicts survival after partial hepatectomy in mice. Hepatology. 2012; 55(4):1094-102.

56. Dawaliby R, Trubbia C, Delporte C, Noyon C, Ruysschaert J-M, Van Antwerpen P, Govaerts C. Phosphatidylethanolamine is a Key Regulator of Membrane Fluidity in Eukaryotic Cells. J Biol Chem. 2015.

57. Baburina I, Jackowski S. Cellular responses to excess phospholipid. J Biol Chem. 1999; 274(14):9400-8.

58. Tijburg LBM, Houweling M, Geelen MJH, Vangolde LMG. Effects of Dietary Conditions on the Pool Sizes of Precursors of Phosphatidylcholine and Phosphatidylethanolamine Synthesis in Rat-Liver. Biochim Biophys Acta. 1988; 959(1):1-8.

59. Aiken NR, Szwergold BS, Kappler F, Stoyanova R, Kuesel AC, Shaller C, Brown TR. Metabolism of phosphonium choline by Rat-2 fibroblasts: Effects of mitogenic stimulation studied using P-31 NMR spectroscopy. Anticancer Res. 1996; 16(3B):1357-63.

60. Iles RA, Stevens AN, Griffiths JR, Morris PG. Phosphorylation status of liver by 31P-n.m.r. spectroscopy, and its implications for metabolic control. A comparison of 31P-n.m.r. spectroscopy (in vivo and in vitro) with chemical and enzymic determinations of ATP, ADP and Pi. Biochem J. 1985; 229(1):141-51.

61. Murphy E, Gabel SA, Funk A, London RE. NMR observability of ATP: preferential depletion of cytosolic ATP during ischemia in perfused rat liver. Biochemistry (Mosc). 1988; 27(2):526-8.

62. Taylor DJ, Bore PJ, Styles P, Gadian DG, Radda GK. Bioenergetics of intact human muscle. A 31P nuclear magnetic resonance study. Mol Biol Med. 1983; 1(1):77-94.

63. Malloy CR, Cunningham CC, Radda GK. The Metabolic State of the Rat-Liver Invivo Measured by P-31-Nmr Spectroscopy. Biochim Biophys Acta. 1986; 885(1):1-11.

64. Cunningham CC, Malloy CR, Radda GK. Effect of fasting and acute ethanol administration on the energy state of in vivo liver as measured by 31P-NMR spectroscopy. Biochimica et Biophysica Acta (BBA) - Molecular Cell Research. 1986; 885(1):12-22.
65. Tanaka A, Chance B, Quistorff B. A Possible Role of Inorganic-Phosphate as a Regulator of Oxidative-Phosphorylation in Combined Urea Synthesis and Gluconeogenesis in Perfused Rat-Liver - a Phosphorus Magnetic-Resonance Spectroscopy Study. J Biol Chem. 1989; 264(17):10034-40.
66. Desmoulin F, Cozzone PJ, Canioni P. P-31 Nmr-Study of Phosphorylated Metabolites Compartmentation, Intracellular Ph and Phosphorylation State during Normoxia, Hypoxia and Ethanol Perfusion, in the Perfused-Rat-Liver. Eur J Biochem. 1987; 162(1):151-9.
67. Veech RL, Lawson JWR, Cornell NW, Krebs HA. Cytosolic Phosphorylation Potential. J Biol Chem. 1979; 254(14):6538-47.
68. Veech RL, Veloso D, Guynn R. Time-Course of Effects of Ethanol on Redox and Phosphorylation States of Rat-Liver. Biochem J. 1972; 127(2):387-&.
69. Hutson SM, Williams GD, Berkich DA, Lanoue KF, Briggs RW. A P-31 Nmr-Study of Mitochondrial Inorganic-Phosphate Visibility - Effects of Ca^{2+}, Mn^{2+}, and the Ph Gradient. Biochemistry (Mosc). 1992; 31(5):1322-30.
70. Akerboom TPM, Bookelman H, Zuurendonk PF, Vandermeer R, Tager JM. Intra-Mitochondrial and Extra-Mitochondrial Concentrations of Adenine-Nucleotides and Inorganic-Phosphate in Isolated Hepatocytes from Fasted Rats. Eur J Biochem. 1978; 84(2):413-20.
71. Siess EA, Wieland OH. Phosphorylation State of Cytosolic and Mitochondrial Adenine-Nucleotides and of Pyruvate-Dehydrogenase in Isolated Rat-Liver Cells. Biochem J. 1976; 156(1):91-&.
72. Aw TY, Andersson BS, Jones DP. Mitochondrial Transmembrane Ion Distribution during Anoxia. Am J Physiol. 1987; 252(4):C356-C61.
73. Desmoulin F, Canioni P, Crotte C, Gerolami A, Cozzone PJ. Hepatic-Metabolism during Acute Ethanol Administration - a P-31 Nuclear-Magnetic-Resonance Study on the Perfused-Rat-Liver under Normoxic or Hypoxic Conditions. Hepatology. 1987; 7(2):315-23.
74. Ikai I, Okuda M, Doliba N, Chance B. Visibility of Atp and Adp in Freeze-Trapped Tissue from Perfused-Rat-Liver during Normoxia and Ischemia Using P-31-Cryo-Nmr. Biochim Biophys Acta. 1991; 1074(2):289-93.
75. Ogawa S, Rottenberg H, Brown TR, Shulman RG, Castillo CL, Glynn P. High-Resolution P-31 Nuclear Magnetic-Resonance Study of Rat-Liver Mitochondria. Proc Natl Acad Sci U S A. 1978; 75(4):1796-800.
76. Iles RA, Griffiths JR, Stevens AN, Gadian DG, Porteous R. Effects of Fructose on the Energy-Metabolism and Acid-Base Status of the Perfused Starved-Rat Liver - a P-31 Nuclear Magnetic-Resonance Study. Biochem J. 1980; 192(1):191-202.
77. Garlick PB, Brown TR, Sullivan RH, Ugurbil K. Observation of a 2nd Phosphate Pool in the Perfused Heart by P-31 Nmr - Is This the Mitochondrial Phosphate? J Mol Cell Cardiol. 1983; 15(12):855-8.
78. Kan HE, Klomp DWJ, Wong CS, Boer VO, Webb AG, Luijten PR, Jeneson JA. In vivo P-31 MRS detection of an alkaline inorganic phosphate pool with short T1 in human resting skeletal muscle. NMR Biomed. 2010; 23(8):995-1000.
79. Schwenke WD, Soboll S, Seitz HJ, Sies H. Mitochondrial and Cytosolic Atp-Adp Ratios in Rat-Liver Invivo. Biochem J. 1981; 200(2):405-8.
80. Ying W. NAD+/NADH and NADP+/NADPH in cellular functions and cell death: regulation and biological consequences. Antioxid Redox Signal. 2008; 10(2):179-206.
81. Pollak N, Dölle C, Ziegler M. The power to reduce: pyridine nucleotides – small molecules with a multitude of functions. Biochem J. 2007; 402(Pt 2):205-18.
82. Stubbs M, Veech RL, Krebs HA. Control of the redox state of the nicotinamide-adenine dinucleotide couple in rat liver cytoplasm. Biochem J. 1972; 126(1):59-65.
83. Alano CC, Tran A, Tao R, Ying W, Karliner JS, Swanson RA. Differences among cell types in NAD(+) compartmentalization: a comparison of neurons, astrocytes, and cardiac myocytes. J Neurosci Res. 2007; 85(15):3378-85.
84. Sauve AA. NAD+ and vitamin B3: from metabolism to therapies. J Pharmacol Exp Ther. 2008; 324(3):883-93.

85. Conley KE, Ali AS, Flores B, Jubrias SA, Shankland EG. Mitochondrial NAD(P)H In vivo: Identifying Natural Indicators of Oxidative Phosphorylation in the P-31 Magnetic Resonance Spectrum. Front Physiol. 2016; 7.
86. Moon RB, Richards JH. Determination of Intracellular Ph by P-31 Magnetic-Resonance. J Biol Chem. 1973; 248(20):7276-8.
87. Ackerman JJH, Soto GE, Spees WM, Zhu ZH, Evelhoch JL. The NMR chemical shift pH measurement revisited: Analysis of error and modeling of a pH dependent reference. Magn Reson Med. 1996; 36(5):674-83.
88. Ruiz-Cabello J, Cohen JS. Phospholipid Metabolites as Indicators of Cancer Cell-Function. NMR Biomed. 1992; 5(5):226-33.
89. van der Kemp WJM, Stehouwer BL, Runge JH, Wijnen JP, Nederveen AJ, Luijten PR, Klomp DWJ. Glycerophosphocholine and Glycerophosphoethanolamine Are Not the Main Sources of the In Vivo P-31 MRS Phosphodiester Signals from Healthy Fibroglandular Breast Tissue at 7 T. Front Oncol. 2016; 6.
90. De Graaf RA. In vivo NMR spectroscopy: principles and techniques. 2nd ed. Chichester: John Wiley & Sons; 2007.
91. Sevastianova K, Hakkarainen A, Kotronen A, Cornér A, Arkkila P, Arola J, Westerbacka J, Bergholm R, Lundbom J, Lundbom N, Yki-Järvinen H. Nonalcoholic Fatty Liver Disease: Detection of Elevated Nicotinamide Adenine Dinucleotide Phosphate with in Vivo 3.0-T 31P MR Spectroscopy with Proton Decoupling. Radiology. 2010; 256(2):466-73.
92. Pollesello P, Eriksson O, Vittur F, Paoletti S, Geimonen E, Toffanin R. Detection and quantitation of phosphorus metabolites in crude tissue extracts by H-1 and P-31 NMR: Use of gradient assisted H-1-P-31 HMQC experiments, with selective pulses, for the assignment of less abundant metabolites. NMR Biomed. 1995; 8(5):190-6.
93. Changani KK, Barnard ML, Bell JD, Thomas EL, Williams SCR, Bloom SR, Iles RA. In vivo assessment of metabolic perturbations following alanine and glucagon administration using P-31-MRS in the rat. Bba-Gen Subjects. 1997; 1335(3):290-304.
94. Shulman RG, Brown TR, Ugurbil K, Ogawa S, Cohen SM, Hollander JAD. Cellular Applications of P-31 and C-13 Nuclear Magnetic-Resonance. Science. 1979; 205(4402):160-6.
95. Chmelík M, Valkovič L, Wolf P, Bogner W, Gajdošík M, Halilbasic E, Gruber S, Trauner M, Krebs M, Trattnig S, Krššák M. Phosphatidylcholine contributes to in vivo 31P MRS signal from the human liver. Eur Radiol. 2015:1-8.
96. Small DM, Bourges M, Dervichian DG. Ternary and Quaternary Aqueous Systems Containing Bile Salt, Lecithin, and Cholesterol. Nature. 1966; 211(5051):816-8.
97. Bierwagen A, Begovatz P, Nowotny P, Markgraf D, Nowotny B, Koliaki C, Giani G, Kluppelholz B, Lundbom J, Roden M. Characterization of the peak at 2.06ppm in P-31 magnetic resonance spectroscopy of human liver: phosphoenolpyruvate or phosphatidylcholine? NMR Biomed. 2015; 28(7):898-905.
98. Murphy EJ, Bates TE, Williams SR, Watson T, Brindle KM, Rajagopalan B, Radda GK. Endoplasmic-Reticulum - the Major Contributor to the Pde Peak in Hepatic P-31-Nmr Spectra at Low Magnetic-Field Strengths. Biochim Biophys Acta. 1992; 1111(1):51-8.
99. Bates TE, Williams SR, Gadian DG. Phosphodiesters in the Liver: The Effect of Field Strength on the 31P Signal. Magn Reson Med. 1989; 12(1):145-50.
100. Bell JD, Jane Cox I, Sargentoni J, Peden CJ, Menon DK, Foster CS, Watanapa P, Ales RA, Urenjak J. A 31P and 1H-NMR investigation in vitro of normal and abnormal human liver. Biochimica et Biophysica Acta (BBA) - Molecular Basis of Disease. 1993; 1225(1):71-7.
101. Taylor-Robinson SD, Sargentoni J, Bell JD, Saeed N, Changani KK, Davidson BR, Rolles K, Burroughs AK, Hodgson HJF, Foster CS, Cox IJ. In vivo and in vitro hepatic P-31 magnetic resonance spectroscopy and electron microscopy of the cirrhotic liver. Liver. 1997; 17(4):198-209.
102. Bell JD, Bhakoo KK. Metabolic changes underlying P-31 MR spectral alterations in human hepatic tumours. NMR Biomed. 1998; 11(7):354-9.
103. Maris JM, Evans AE, McLaughlin AC, D'Angio GJ, Bolinger L, Manos H, Chance B. 31P Nuclear Magnetic Resonance Spectroscopic Investigation of Human Neuroblastoma in Situ. N Engl J Med. 1985; 312(23):1500-5.

104. Bawden SJ, Stephenson MC, Ciampi E, Hunter K, Marciani L, Macdonald IA, Aithal GP, Morris PG, Gowland PA. Investigating the effects of an oral fructose challenge on hepatic ATP reserves in healthy volunteers: A P-31 MRS study. Clin Nutr. 2016; 35(3):645-9.

105. Boesch C, Elsing C, Wegmüller H, Felblinger J, Vock P, Reichen J. Effect of ethanol and fructose on liver metabolism: A dynamic 31Phosphorus magnetic resonance spectroscopy study in normal volunteers. Magn Reson Imaging. 1997; 15(9):1067-77.

106. Dufour J-F, Stoupis C, Lazeyras F, Vock P, Terrier F, Reichen J. Alterations in hepatic fructose metabolism in cirrhotic patients demonstrated by dynamic 31phosphorus spectroscopy. Hepatology. 1992; 15(5):835-42.

107. Terrier F, Vock P, Cotting J, Ladebeck R, Reichen J, Hentschel D. Effect of intravenous fructose on the P-31 MR spectrum of the liver: dose response in healthy volunteers. Radiology. 1989; 171(2):557-63.

108. Labotka RJ, Glonek T, Hruby MA, Honig GR. P-31 Spectroscopic Determinations of Phosphorus Metabolite Profiles of Blood Components - Erythrocytes, Reticulocytes, and Platelets. Biochem Med. 1976; 15(3):311-29.

109. Henderson TO, Costello AJ, Omachi A. Phosphate-Metabolism in Intact Human Erythrocytes - Determination by Phosphorus-31 Nuclear Magnetic-Resonance Spectroscopy. Proc Natl Acad Sci U S A. 1974; 71(6):2487-90.

110. Noren B, Dahlqvist O, Lundberg P, Almer S, Kechagias S, Ekstedt M, Franzén L, Wirell S, Smedby Ö. Separation of advanced from mild fibrosis in diffuse liver disease using 31P magnetic resonance spectroscopy. Eur J Radiol. 2008; 66(2):313-20.

111. Leij-Halfwerk S, Agteresch HJ, Sijens PE, Dagnelie PC. Adenosine triphosphate infusion increases liver energy status in advanced lung cancer patients: an in vivo ^{31}P magnetic resonance spectroscopy study. Hepatology. 2002; 35(2):421-4.

112. Schmid AI, Chmelík M, Szendroedi J, Krššák M, Brehm A, Moser E, Roden M. Quantitative ATP synthesis in human liver measured by localized 31P spectroscopy using the magnetization transfer experiment. NMR Biomed. 2008; 21(5):437-43.

113. van Wassenaer-van Hall HN, van der Grond J, van Hattum J, Kooijman C, Hoogenraad TU, Mali WP. 31P magnetic resonance spectroscopy of the liver: correlation with standardized serum, clinical, and histological changes in diffuse liver disease. Hepatology. 1995; 21(2):443-9.

114. Lim AKP, Patel N, Hamilton G, Hajnal JV, Goldin RD, Taylor-Robinson SD. The relationship of in vivo ^{31}P MR spectroscopy to histology in chronic hepatitis C. Hepatology. 2003; 37(4):788-94.

115. Abrigo JM, Shen J, Wong VWS, Yeung DKW, Wong GLH, Chim AML, Chan AWH, Choi PCL, Chan FKL, Chan HLY, Chu WCW. Non-alcoholic fatty liver disease: Spectral patterns observed from an in vivo phosphorus magnetic resonance spectroscopy study. J Hepatol. 2014; 60(4):809-15.

116. Laufs A, Livingstone R, Nowotny B, Nowotny P, Wickrath F, Giani G, Bunke J, Roden M, Hwang J-H. Quantitative liver 31P magnetic resonance spectroscopy at 3T on a clinical scanner. Magn Reson Med. 2014; 71(5):1670-5.

117. Li CW, Negendank WG, Murphy-Boesch J, Padavic-Shaller K, Brown TR. Molar Quantitation of Hepatic Metabolites In Vivo in Proton-decoupled, Nuclear Overhauser Effect Enhanced 31P NMR Spectra Localized by Three-dimensional Chemical Shift Imaging. NMR Biomed. 1996; 9(4):141-55.

118. Zakian KL, Koutcher JA, Malhotra S, Thaler H, Jarnagin W, Schwartz L, Fong Y. Liver regeneration in humans is characterized by significant changes in cellular phosphorus metabolism: Assessment using proton-decoupled 31P- magnetic resonance spectroscopic imaging. Magn Reson Med. 2005; 54(2):264-71.

119. Schmid AI, Szendroedi J, Chmelik M, Krššák M, Moser E, Roden M. Liver ATP Synthesis Is Lower and Relates to Insulin Sensitivity in Patients With Type 2 Diabetes. Diabetes Care. 2011; 34(2):448-53.

120. Szendroedi J, Chmelik M, Schmid AI, Nowotny P, Brehm A, Krssak M, Moser E, Roden M. Abnormal hepatic energy homeostasis in type 2 diabetes. Hepatology. 2009; 50(4):1079-86.

121. Chmelik M, Schmid AI, Gruber S, Szendroedi J, Krssak M, Trattnig S, Moser E, Roden M. Three-dimensional high-resolution magnetic resonance spectroscopic imaging for absolute quantification of P-31 metabolites in human liver. Magn Reson Med. 2008; 60(4):796-802.

122. Changani KK, Jalan R, Cox IJ, Ala-Korpela M, Bhakoo K, Taylor-Robinson SD, Bell JD. Evidence for altered hepatic gluconeogenesis in patients with cirrhosis using in vivo 31-phosphorus magnetic resonance spectroscopy. Gut. 2001; 49(4):557-64.
123. Dezortova M, Taimr P, Skoch A, Spicak J, Hajek M. Etiology and functional status of liver cirrhosis by 31P MR spectroscopy. World J Gastroenterol. 2005; 11(44):6926-31.
124. Runge JH, van der Kemp WJM, Klomp DWJ, Luijten PR, Nederveen AJ, Stoker J. 2D AMESING multi-echo P-31-MRSI of the liver at 7T allows transverse relaxation assessment and T-2-weighted averaging for improved SNR. Magn Reson Imaging. 2016; 34(2):219-26.
125. Chmelik M, Považan M, Krššák M, Gruber S, Tkačov M, Trattnig S, Bogner W. In vivo 31P magnetic resonance spectroscopy of the human liver at 7 T: an initial experience. NMR Biomed. 2014; 27(4):478-85.
126. Wylezinska M, Cobbold JFL, Fitzpatrick J, McPhail MJW, Crossey MME, Thomas HC, Hajnal JV, Vennart W, Cox IJ, Taylor-Robinson SD. A comparison of single-voxel clinical in vivo hepatic 31P MR spectra acquired at 1.5 and 3.0 Tesla in health and diseased states. NMR Biomed. 2011; 24(3):231-7.
127. Van Uden MJ, Peeters TH, Scheenen TWJ, Heerschap A, editors. ^{31}P spectroscopic imaging of the human brain at 3T: effect of NOE and ^{1}H-decoupling. 24th Annual Meeting of ISMRM; 2017; Hawaii, USA.
128. Valkovic L, Chmelik M, Krssak M. In-vivo P-31-MRS of skeletal muscle and liver: A way for non-invasive assessment of their metabolism. Anal Biochem. 2017; 529:193-215.
129. Mann DV, Lam WW, Magnus Hjelm N, So NM, Yeung DK, Metreweli C, Lau WY. Biliary drainage for obstructive jaundice enhances hepatic energy status in humans: a 31-phosphorus magnetic resonance spectroscopy study. Gut. 2002; 50(1):118-22.
130. Nair S, V PC, Arnold C, Diehl AM. Hepatic ATP reserve and efficiency of replenishing: comparison between obese and nonobese normal individuals. Am J Gastroenterol. 2003; 98(2):466-70.
131. Tosner Z, Dezortova M, Tintera J, Hajek M. Application of two-dimensional CSI for absolute quantification of phosphorus metabolites in the human liver. Magn Reson Mater Phy. 2001; 13(1):40-6.
132. Klomp DWJ, van de Bank BL, Raaijmakers A, Korteweg MA, Possanzini C, Boer VO, de Berg CATv, van de Bosch MAAJ, Luijten PR. (31)P MRSI and (1)H MRS at 7T: initial results in human breast cancer. NMR Biomed. 2011; 24(10):1337-42.
133. Panda A, Jones S, Stark H, Raghavan RS, Sandrasegaran K, Bansal N, Dydak U. Phosphorus liver MRSI at 3 T using a novel dual-tuned eight-channel 31P/1H coil. Magn Reson Med. 2012; 68(5):1346-56.
134. Rodgers CT, Robson MD. Receive Array Magnetic Resonance Spectroscopy: Whitened Singular Value Decomposition (WSVD) Gives Optimal Bayesian Solution. Magn Reson Med. 2010; 63(4):881-91.
135. van den Boogaart A. Quantitative data analysis of in vivo MRS data sets. Magn Reson Chem. 1997; 35:S146-S52.
136. van der Veen JW, de Beer R, Luyten PR, van Ormondt D. Accurate quantification of in vivo 31P NMR signals using the variable projection method and prior knowledge. Magn Reson Med. 1988; 6(1):92-8.
137. Stefan D, Di Cesare F, Andrasescu A, Popa E, Lazariev A, Vescovo E, Strbak O, Williams S, Starcuk Z, Cabanas M, van Ormondt D, Graveron-Demilly D. Quantitation of magnetic resonance spectroscopy signals: the jMRUI software package. Meas Sci Technol. 2009; 20(10):104035.
138. Traussnigg S, Kienbacher C, Gajdošík M, Valkovič L, Halilbasic E, Stift J, Rechling C, Hofer H, Steindl-Munda P, Ferenci P, Wrba F, Trattnig S, Krššák M, Trauner M. Ultra-high-field magnetic resonance spectroscopy in non-alcoholic fatty liver disease: Novel mechanistic and diagnostic insights of energy metabolism in non-alcoholic steatohepatitis and advanced fibrosis. Liver Int. 2017; 37(10):1544-53.
139. Sijens PE, Dagnelie PC, Halfwerk S, van Dijk P, Wicklow K, Oudkerk M. Understanding the Discrepancies Between 31P MR Spectroscopy Assessed Liver Metabolite Concentrations from Different Institutions. Magn Reson Imaging. 1998; 16(2):205-11.
140. Andrew ER, Gaspar R. Mechanisms of P-31 relaxation in phosphorus metabolites. Magn Reson Mater Phy. 1994; 2(3):421-3.

141. Luyten PR, Groen JP, Vermeulen JWAH, Denhollander JA. Experimental Approaches to Image Localized Human P-31 Nmr-Spectroscopy. Magn Reson Med. 1989; 11(1):1-21.

142. Lei H, Zhu XH, Zhang XL, Ugurbil K, Chen W. In vivo P-31 magnetic resonance spectroscopy of human brain at 7 T: An initial experience. Magn Reson Med. 2003; 49(2):199-205.

143. Bogner W, Chmelik M, Schmid AI, Moser E, Trattnig S, Gruber S. Assessment of (31)P Relaxation Times in the Human Calf Muscle: A Comparison between 3 T and 7 T In Vivo. Magn Reson Med. 2009; 62(3):574-82.

144. Rodgers CT, Clarke WT, Snyder C, Vaughan JT, Neubauer S, Robson MD. Human cardiac 31P magnetic resonance spectroscopy at 7 Tesla. Magn Reson Med. 2014; 72(2):304-15.

145. Buchthal SD, Thoma WJ, Taylor JS, Nelson SJ, Brown TR. In vivo T1 values of phosphorus metabolites in human liver and muscle determined at 1.5 T by chemical shift imaging. NMR Biomed. 1989; 2(5-6):298-304.

146. Bottomley PA, Ouwerkerk R. The Dual-Angle Method for Fast, Sensitive T-1 Measurement in-Vivo with Low-Angle Adiabatic Pulses. J Magn Reson, Ser B. 1994; 104(2):159-67.

147. Meyerhoff DJ, Karczmar GS, Matson GB, Boska MD, Weiner MW. Non-invasive quantitation of human liver metabolites using image-guided 31p magnetic resonance spectroscopy. NMR Biomed. 1990; 3(1):17-22.

148. Roth K, Hubesch B, Meyerhoff DJ, Naruse S, Gober JR, Lawry TJ, Boska MD, Matson GB, Weiner MW. Noninvasive Quantitation of Phosphorus Metabolites in Human-Tissue by Nmr-Spectroscopy. J Magn Reson. 1989; 81(2):299-311.

149. Buchli R, Meier D, Martin E, Boesiger P. Assessment of absolute metabolite concentrations in human tissue by 31P MRS in vivo. Part II: Muscle, liver, kidney. Magn Reson Med. 1994; 32(4):453-8.

150. Cox IJ, Coutts GA, Gadian DG, Ghosh P, Sargentoni J, Young IR. Saturation effects in phosphorus-31 magnetic resonance spectra of the human liver. Magn Reson Med. 1991; 17(1):53-61.

151. Banerjee R, Pavlides M, Tunnicliffe EM, Piechnik SK, Sarania N, Philips R, Collier JD, Booth JC, Schneider JE, Wang LM, Delaney DW, Fleming KA, Robson MD, Barnes E, Neubauer S. Multiparametric magnetic resonance for the non-invasive diagnosis of liver disease. J Hepatol. 2014; 60(1):69-77.

152. Mann DV, Lam WW, Hjelm NM, So NM, Yeung DK, Metreweli C, Lau WY. Human liver regeneration: hepatic energy economy is less efficient when the organ is diseased. Hepatology. 2001; 34(3):557-65.

153. Meyerhoff DJ, Karczmar GS, Valone F, Venook A, Matson GB, Weiner MW. Hepatic Cancers and Their Response to Chemoembolization Therapy - Quantitative Image-Guided P-31 Magnetic-Resonance Spectroscopy. Invest Radiol. 1992; 27(6):456-64.

154. Katz N. Correlation between Rates and Enzyme Levels of Increased Gluconeogenesis in Rat-Liver and Kidney after Partial-Hepatectomy. Eur J Biochem. 1979; 98(2):535-42.

155. Rosa JL, Bartrons R, Tauler A. Gene-Expression of Regulatory Enzymes of Glycolysis Gluconeogenesis in Regenerating Rat-Liver. Biochem J. 1992; 287:113-6.

156. Seery JP, Bryant DJ, Jenkinson G, Schwieso JE, Houlden HJ, Changani KK, Hodgson HJF, Taylor-Robinson SD. Intravenous intralipid infusion in hepatic steatosis: an in vivo hepatic phosphorus-31 magnetic resonance spectroscopy study. Hepatol Res. 1998; 12(1):50-8.

157. Jalan R, Sargentoni J, Coutts GA, Bell JD, Rolles K, Burroughs AK, Taylor Robinson SD. Hepatic phosphorus-31 magnetic resonance spectroscopy in primary biliary cirrhosis and its relation to prognostic models. Gut. 1996; 39(1):141-6.

158. Taylor-Robinson SD, Sargentoni J, Bell JD, Thomas EL, Marcus CD, Changani KK, Saeed N, Hodgson HJF, Davidson BR, Burroughs AK, Rolles K, Foster CS, Cox IJ. In vivo and in vitro hepatic phosphorus-31 magnetic resonance spectroscopy and electron microscopy in chronic ductopenic rejection of human liver allografts. Gut. 1998; 42(5):735-43.

159. Dagnelie PC, Menon DK, Cox IJ, Bell JD, Sargentoni J, Coutts GA, Urenjak J, Iles RA. Effect of L-Alanine Infusion on P-31 Nuclear-Magnetic-Resonance Spectra of Normal Human Liver - Towards Biochemical Pathology Invivo. Clin Sci. 1992; 83(2):183-90.

160. Valkovič L, Gajdošík M, Traussnigg S, Wolf P, Chmelík M, Kienbacher C, Bogner W, Krebs M, Trauner M, Trattnig S, Krššák M. Application of localized 31P MRS saturation transfer at 7 T for

measurement of ATP metabolism in the liver: reproducibility and initial clinical application in patients with non-alcoholic fatty liver disease. Eur Radiol. 2014; 24(7):1602-9.

161. Zhang CY, Zhang Q, Zhang HM, Yang HS. 3.0T 31P MR spectroscopy in assessment of response to antiviral therapy for chronic hepatitis C. World J Gastroentero. 2014; 20(8):2107-12.

162. Jeon MJ, Lee Y, Ahn S, Lee C, Kim OH, Oh BC, Yu U, Kim H. High resolution in vivo 31P-MRS of the liver: potential advantages in the assessment of non-alcoholic fatty liver disease. Acta Radiol. 2015; 56(9):1051-60.

163. Fritsch M, Koliaki C, Livingstone R, Phielix E, Bierwagen A, Meisinger M, Jelenik T, Strassburger K, Zimmermann S, Brockmann K, Wolff C, Hwang JH, Szendroedi J, Roden M. Time course of postprandial hepatic phosphorus metabolites in lean, obese, and type 2 diabetes patients. Am J Clin Nutr. 2015; 102(5):1051-8.

164. Gancheva S, Bierwagen A, Begovatz P, Olof J, Lundbom J, Kahl S, Nowotny P, Giani G, Hoffmann B, Szendroedi J, Roden M. Hepatic ATP Content Is Lower and Relates to Glycemic Control in Type 1 Diabetes. Diabetes. 2015; 64:A502-A.

165. Lim AK, Patel N, Hamilton G, Forton D, Hajnal JV, Taylor-Robinson S. Characterisation of the severity of diffuse liver disease in patients with hepatitis C using 31P-magnetic resonance spectroscopy. Radiology. 2002; 225:539-40.

166. Taylor-Robinson SD, Sargentoni J, Bell JD, Thomas EL, Marcus CD, Changani KK, Saeed N, Hodgson HJ, Davidson BR, Burroughs AK, Rolles K, Foster CS, Cox IJ. In vivo and in vitro hepatic phosphorus-31 magnetic resonance spectroscopy and electron microscopy in chronic ductopenic rejection of human liver allografts. Gut. 1998; 42(5):735-43.

167. Menon DK, Sargentoni J, Taylor-Robinson SD, Bell JD, Cox IJ, Bryant DJ, Coutts GA, Rolles K, Burroughs AK, Morgan MY. Effect of functional grade and etiology on in vivo hepatic phosphorus-31 magnetic resonance spectroscopy in cirrhosis: biochemical basis of spectral appearances. Hepatology. 1995; 21(2):417-27.

168. Chmelik M, Povazan M, Jiru F, Kukurova IJ, Dezortova M, Krssak M, Bogner W, Hajek M, Trattnig S, Valkovic L. Flip-Angle Mapping of P-31 Coils by Steady-State MR Spectroscopic Imaging. J Magn Reson Imaging. 2014; 40(2):391-7.

169. Bashir A, Gropler R, Ackerman J. Absolute Quantification of Human Liver Phosphorus-Containing Metabolites In Vivo Using an Inhomogeneous Spoiling Magnetic Field Gradient. Plos One. 2015; 10(12).

170. Buehler T, Kreis R, Boesch C. Comparison of 31P saturation and inversion magnetization transfer in human liver and skeletal muscle using a clinical MR system and surface coils. NMR Biomed. 2015; 28(2):188-99.

171. Jiang T, Liu S, Xiao X, Tao X, Liu G, Wang J. Diagnosis of rejection after liver transplantation: use of phosphorus-31 magnetic resonance spectroscopy (31P-MRS). Abdom Imaging. 2012; 37(5):788-94.

172. Purvis LAB, Clarke WT, Valkovič L, Levick C, Pavlides M, Barnes E, Cobbold JF, Robson MD, Rodgers CT. Phosphodiester content measured in human liver by in vivo 31P MR spectroscopy at 7 tesla. Magn Reson Med. 2017; 78(6):2095-105.

173. Miceli MV, Kan L-s, Newsome DA. Phosphorus-31 nuclear magnetic resonance spectroscopy of human retinoblastoma cells: correlations with metabolic indices. Biochimica et Biophysica Acta (BBA) - Molecular Cell Research. 1988; 970(3):262-9.

174. Rockey DC, Caldwell SH, Goodman ZD, Nelson RC, Smith AD. Liver biopsy. Hepatology. 2009; 49(3):1017-44.

175. Maharaj B, Leary WP, Naran AD, Maharaj RJ, Cooppan RM, Pirie D, Pudifin DJ. Sampling variability and its influence on the diagnostic yield of percutaneous needle biopsy of the liver. The Lancet. 1986; 327(8480):523-5.

176. Baunsgaard P, Sanchez GC, Lundborg CJ. The variation of pathological changes in the liver evaluated by double biopsies. Acta Pathol Microbiol Scand A. 1979; 87(1):51-7.

177. Abdi W, Millan JC, Mezey E. Sampling variability on percutaneous liver biopsy. Arch Intern Med. 1979; 139(6):667-9.

178. Ardenkjaer-Larsen JH, Fridlund B, Gram A, Hansson G, Hansson L, Lerche MH, Servin R, Thaning M, Golman K. Increase in signal-to-noise ratio of > 10,000 times in liquid-state NMR. Proc Natl Acad Sci U S A. 2003; 100(18):10158-63.

179. Tyler DJ, Neubauer S. Science to Practice: Hyperpolarized Metabolic MR Imaging-The Light at the End of the Tunnel for Clinical C-13 MR Spectroscopy? Radiology. 2016; 278(3):639-41.
180. Sahani DV, Kalva SP. Imaging the liver. Oncologist. 2004; 9(4):385-97.
181. Sharma B, Martin A, Zerizer L. Positron Emission Tomography-Computed Tomography in Liver Imaging. Semin Ultrasound Ct. 2013; 34(1):66-80.
182. EASL-ALEH Clinical Practice Guidelines: Non-invasive tests for evaluation of liver disease severity and prognosis. J Hepatol. 63(1):237-64.
183. Hodson L, McQuaid SE, Humphreys SM, Milne R, Fielding BA, Frayn KN, Karpe F. Greater dietary fat oxidation in obese compared with lean men: an adaptive mechanism to prevent liver fat accumulation? Am J Physiol-Endoc M. 2010; 299(4):E584-E92.
184. ter Voert EG, Heijmen L, van Laarhoven HW, Heerschap A. In vivo magnetic resonance spectroscopy of liver tumors and metastases. World J Gastroenterol. 2011; 17(47):5133-49.

4. Acquisition

In this chapter, the rationale behind my choices of acquisition parameters is given. Then data from ten healthy subjects and eleven patients with liver cirrhosis is acquired. This initial in vivo data is used in the development of an improved processing pipeline. The repeatability of the full processing pipeline will be examined in Chapter 9, and the final results from the data acquired in this chapter will be given in Chapter 10.

4.1. Hardware

Fig 4.1. Siemens Magnetom 7 T system.

Different scanners have been developed with several competing features, such as bore size or gradient strength and speed. But for an SNR limited regime, such as ^{31}P-MRS, the most important choice to make is field strength. Higher field scanners are inherently more expensive, and their use brings other technical difficulties. However, there is an invaluable increase of SNR with $\boldsymbol{B}_0$. Scanners with a field strength of 1.5 or 3 T are now widely available. This work was performed using a research-only whole-body Magnetom 7 T system (Siemens, Erlangen, Germany) (see Fig 4.1).

At the start of the project, there were no coils capable of both ^{1}H and ^{31}P acquisition on the 7 T, so a 10 cm ^{1}H loop coil (see Fig 4.2) and 16 channel ^{31}P array were used (see Fig 4.3). The ^{31}P array consisted of a single 28 × 27 cm^{2} transmit loop and a 4 × 4 matrix of 8 × 5.5 cm^{2} diameter flexible receive loops (1).

Fig 4.2. 10 cm ^{1}H transceive loop.

Fig 4.3. 16 channel ^{31}P receive array. The rectangular transmit loop is above the blue housing of the 16 receive channels. The five white boxes contain phenylphosphonic acid fiducials.

4.2. ^{1}H localization and $\boldsymbol{B}_0$ shimming

As there were only single-tuned coils available, ^{1}H images were acquired separately from the main ^{31}P scan. Transverse, sagittal and coronal ^{1}H fast low angle shot (FLASH) stacks of images for localization were acquired using the 10 cm ^{1}H loop (see Fig 4.4a). Dual-echo gradient-recalled echo (GRE) field maps were then acquired for $\boldsymbol{B}_0$ shimming. Shims were optimised over a region of interest covering the entire liver (2). Each FLASH stack and GRE field map was acquired in a single 20 s breath-hold, without cardiac gating.

After localizer images were acquired and shimming was performed, each subject was removed from the magnet to swap coils to the ^{31}P array. The subject remained in the same position on the patient table at all times, and so was able to be returned to an identical location within the magnet for the ^{31}P scans.

4.3. Coil loading and positioning

The 16 channel array had five spherical fiducials mounted on its rear housing (one in the centre, one in each corner, see Fig 4.3). The fiducials were polypropylene spheres, filled with a solution of phenylphosphonic acid and doped with chromium (III) acetylacetonate to give short (~100 ms) ^{31}P T_1 values. The solvent used in the central fiducial was ethanol, whereas the solvent for the outer fiducials was acetone, giving rise to a small difference in frequency. To calculate transmit efficiency, a series of inversion-recovery FIDs were run, using only the data from a single, central receive element to localize the signal to the central fiducial. Three orthogonal ^{31}P FLASH images were then acquired to localize all five fiducials. The fiducial coordinates were used to calculate the coil position, orientation and flexion (3).

4.4. Main acquisition protocol

An ideal protocol should give high SNR, be well-localized in both spatial and spectral dimensions, and be quickly acquired. However, in reality there is a trade-off between these requirements. Section 3.3 describes the different methods used in previous studies. As ^{31}P-MRS is a signal-to-noise-ratio-limited technique, SNR must not be compromised, and so localization and speed must be sacrificed. Increasing the field strength from 3 T to 7 T allows improvements in these two areas without reducing SNR. However, two limitations of scanning at 7 T are relatively poorer $\boldsymbol{B}_1$ and $\boldsymbol{B}_0$ homogeneity.

$\boldsymbol{B}_1$ inhomogeneity means that peak $\boldsymbol{B}_1$ is limited further into the liver. This restricted the use of adiabatic excitation pulses with the hardware available at the time of protocol development. Instead, a shaped excitation pulse was used. This consisted of a short hard pulse preceded by a numerically-optimized portion to flatten the pulse's frequency response, giving a uniform bandwidth (3). Initially a 1.015 ms pulse length was used, giving a ~ 4000 Hz bandwidth such that all metabolites were covered. However, this limited the potential excitation and reduced flip angles, and the pulse duration was lengthened to a 2.4 ms total length (of which the final 0.5 ms was a hard pulse), giving a ~ 2000 Hz bandwidth. Although this shorter pulse did not excite the β-ATP peak, it increased the maximum flip angle from 20° for the 1.015 ms pulse to 40° for the 2.4 ms pulse. The mean flip angle within the liver of a typical subject was 31 ± 3° for the 2.4 ms pulse, and the mean interquartile range was 6°. In the heart, Rodgers et al. had found that using a very short T_R (300 – 500 ms) introduced errors into quantitation because of exchange effects (personal communication). Therefore, a 1 s T_R was chosen for use in the liver. At that T_R, the Ernst angle (see Eq. [2.57]) for the metabolite with the longest T_1 (GPE) is ~ 37° and the Ernst angle for the metabolite with the shortest T_1 (α-ATP) is ~ 80°. The flip angles for the 2.4 ms pulse were therefore slightly less than the optimal values, but they were the maximum possible for this coil while maintaining a uniform 2000 Hz bandwidth covering all metabolites from UDPG to PC (-9.5 to 7 ppm). In the future, it may be possible to design a better excitation using alternative hardware. For example, consistent adiabatic excitation has been demonstrated for cardiac ^{31}P-MRS at 7 T using a quadrature coil built by our group (4), and theory predicts the same should be possible using a 7 T ^{31}P body coil, which we are currently helping to develop (5, 6).

$\boldsymbol{B}_0$ inhomogeneity means that large voxels will give poor spectral resolution. This means that good localization is important, even if it incurs an additional time penalty. High resolution CSI is therefore preferable to single voxel spectroscopy methods (such as ISIS), which tend to use much larger voxels. Using the 16-channel array increases coverage compared to a 10 cm ^{31}P loop as well as increasing the SNR. This has a side effect of increasing the contamination when using 1D or 2D-localized methods. Therefore, 3D CSI is preferable to 1D or 2D CSI.

Rather than conventional CSI, a 3D ultra-short echo time (UTE) CSI sequence was used (7). UTE-CSI minimizes the echo time at each point of k-space to increase the SNR. The minimum TE is set to 100 μs, allowing time for the coil to fully stop transmitting as it switches from transmit to receive mode. The TE at the edge of k-space, where the gradients are on for longest, was 200 μs.

This UTE-CSI matrix is both acquisition-weighted and filtered in post-processing using a Hamming filter (8, 9). This leads to a point spread function (PSF) that is much larger than the nominal voxel at the full width half maximum (FWHM), but has reduced sidebands (see Fig. 2.6 in Section 2.2.2). The acquisition-weighting also reduces scan time by preferentially collecting more points in the centre of k-space.

The field of view was set to 270 × 240 × 200 mm^3, so that it covered the whole sensitive volume of the coil, with some space for phase-encoding artefacts.

The resolution and number of averages of the CSI matrix was largely determined by measurement time. Two possibilities were considered: a long protocol (limited by reasonable scan time), and a short protocol (limited by maintaining a reasonable resolution). The standard scan slot was one hour. Once each subject had arrived, been positioned and made comfortable, localization and shimming has been run, and the coils have been swapped over, half an hour remained. Thus, the long protocol resolution was set to 16 × 16 × 8, with the lower resolution in the head-foot direction, and 10 averages were taken, giving a 28 min 10 s total scan time. The short protocol was 12 × 12 × 8 (interpolated to 16 × 16 × 8) with

6 averages giving a 10 minute scan time. These two protocols were tested for data quality and repeatability (see Chapter 9).

In each case, a $\boldsymbol{B}_1$-insensitive train to obliterate signal (BISTRO) saturation band was used to suppress overlying skeletal muscle (10). No ^{1}H-decoupling or nuclear Overhauser effect (NOE) enhancement was used.

4.5. In vivo acquisition

Ten volunteers (six males and four females, 27 ± 5 years, BMI 22.5 ± 1.5 kg.m^{-2}) were scanned using both the long and the short CSI protocols. To test the repeatability of both protocols, each healthy volunteer was measured a second time in the same session, after full repositioning and reshimming. Example spectra acquired using the long CSI protocol are shown in Fig 4.4.

Eleven patients with cirrhosis of the liver (seven males and four females, 61 ± 6 years, BMI 29.5 ± 6.9 kg.m^{-2}, Child-Pugh score 5 or 6) were scanned with the long UTE-CSI protocol. The patients were recruited by Drs Michael Pavlides and Christina Levick based on cirrhosis established using clinical, biochemical or radiological criteria, as part of the larger NICOLA (Non-Invasive Comprehensive Liver Assessment) study. Patient recruitment to the study was granted ethical approval from the UK National Research Ethics Service (13/SC/0243) and was conducted according to the principles of the 1975 Declaration of Helsinki. Five of these patients had been previously diagnosed with hepatitis C, three with non-alcoholic fatty liver disease, two with alcoholic steatohepatitis, and one with autoimmune hepatitis.

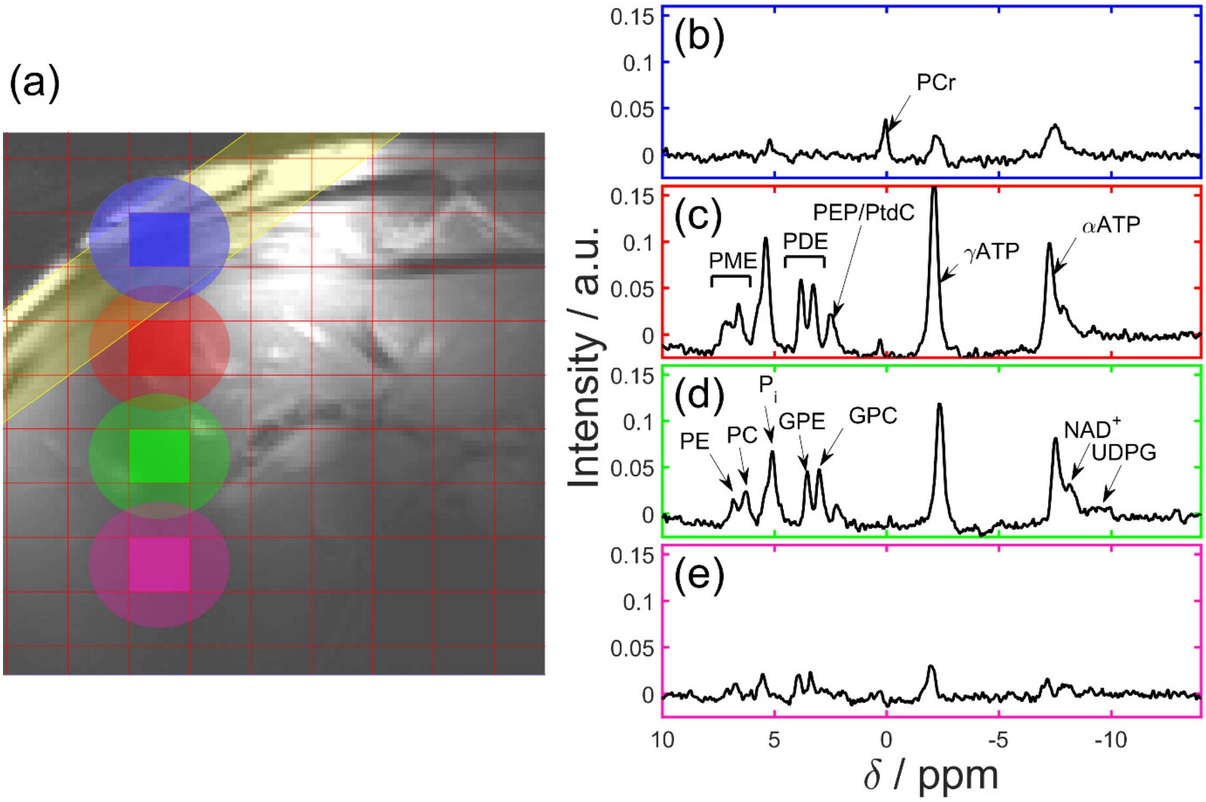

Fig 4.4. Typical liver ^{31}P-MRS spectra acquired at 7 T in the right lobe of the liver using our 3D UTE-CSI protocol. (a) shows a ^{1}H FLASH localizer. The red lines mark the CSI grid, the yellow band marks the outer volume BISTRO suppression. The spectrum for each coloured voxel is given on the right side. The ellipses show the extent of the full width at half maximum of the point spread function for each voxel. (b) is taken from the blue voxel and shows a suppressed muscle spectrum, and (c)-(e) are taken from the red, green and pink voxels, and show the change in the liver spectra as they are taken from deeper in the liver. From Purvis et al. (11).

To calculate the true volume of the CSI voxels, the FWHM of the theoretical PSF (5, 8) was used in each dimension to form an ellipsoid for each voxel (see Fig 4.4a). When several voxels were used, the contribution from any overlapping volumes was considered only once.

The liver volume of each subject in mL was approximated by using Eq. [4.1] (from (12)) and Eq. [4.2] (from (13)). This volume was then used to calculate the coverage achieved in this study.

$$\text{Body surface area (BSA)/m}^2 = 0.007184 \times (\text{mass/kg})^{0.425} \times (\text{height/m})^{0.725} \quad [4.1]$$

$$\text{Liver volume / mL} = 1072.8 \times (\text{BSA / m}^2) - 347.5 \quad [4.2]$$

4.5.1. Voxel selection

The variable quality of voxels acquired using this protocol can be seen in Fig 4.4. Therefore some method of excluding low quality voxels must be used. Although the voxels could be selected manually, a more automatic quality assurance (QA) approach reduces selection bias and the need for post-processing by experts. In each case, the general procedure is the same:

1. I manually drew a region of interest (ROI) on a single transverse localizer which was then propagated through each of the CSI slices. The ROI was drawn such that obvious skeletal muscle was excluded, and so that the analysis did not include voxels far from the coil.

2. Voxels with low time-domain (FID) SNR were excluded to reduce the number that should be analysed.

3. After fitting, spectra with low γ-ATP SNR or with poor fit were excluded.

4. Finally, contaminated spectra were excluded based on high PCr amplitude or concentration (for skeletal muscle contamination), or high PME or PDE coefficient of variance (CoV) (for blood or bile contamination).

For time-domain SNR, the noise was taken from the last 100 points of the FID. For frequency-domain SNR, the noise was taken from the chemical shift region between -20 and -25 ppm.

The exact selection criteria are described in later chapters, and the final pipeline is given in detail in Chapter 9.

4.6. Summary

1. Localization and $\boldsymbol{B}_0$ shimming was acquired with 10 cm ^{1}H loop.
2. The 16-channel ^{31}P array consisted of a single 28 × 27 cm^2 transmit loop and a 4 × 4 matrix of 8 × 5.5 cm^2 diameter flexible receive loops.
3. The ^{31}P acquisition protocol was Hamming-weighted UTE-CSI with 1s T_R, a 2.4 ms shaped excitation pulse, and a 270 × 240 × 200 mm^3 FOV.
4. The matrix size was either 16 × 16 × 8 (long protocol) or 12 × 12 × 8 (short protocol).
5. 10 healthy volunteers were scanned twice with each matrix size.
6. 11 patients with liver cirrhosis were scanned with the 16 × 16 × 8 protocol.
7. Voxel selection was performed using a manually-drawn ROI and automatic QA.

4.7. References

1. Rodgers CT, Clarke WT, Berthel D, Neubauer S, Robson MD. A 16-element receive array for human cardiac ^{31}P MR spectroscopy at 7T. In the Proceedings of the 22rd Annual Meeting of ISMRM, Milan, Italy, 2014. p. 2896.
2. DelaBarre L, Neubauer S, Robson MD, Vaughan JT, Rodgers CT. B_0 shimming further improves human cardiac ^{31}P-MRS at 7 tesla. In the Proceedings of the 23rd Annual Meeting of ISMRM, Toronto, Canada, 2015. p. 3152.
3. Rodgers CT, Clarke WT, Snyder C, Vaughan JT, Neubauer S, Robson MD. Human cardiac 31P magnetic resonance spectroscopy at 7 tesla. Magn Reson Med. 2014; 72(2):304-15.
4. Valkovič L, Clarke WT, Purvis LAB, Schaller B, Robson MD, Rodgers CT. Adiabatic excitation for 31P MR spectroscopy in the human heart at 7 T: A feasibility study. Magn Reson Med. 2016; 78(5):1667-73.
5. Valkovič L, Dragonu I, Wicklow K, Fontius U, Almujayyaz S, Young L, Purvis LAB, Clarke WT, Wichmann T, Lanz T, Neubauer S, Robson MD, Klomp D, Rodgers CT. Initial experiences with a whole-body birdcage transmit coil and 16-element receive array for cardiac 31P-MRS at 7T. In the Proceedings of the 24th Annual Meeting of ISMRM, Hawaii, USA, 2017. p. 6594.
6. Loring J, van der Kemp WJM, Almujayyaz S, van Oorschot JWM, Luijten PR, Klomp DWJ. Whole-body radiofrequency coil for P-31 MRSI at 7T. NMR Biomed. 2016; 29(6):709-20.
7. Robson MD, Tyler DJ, Neubauer S. Ultrashort TE chemical shift imaging (UTE-CSI). Magn Reson Med. 2005; 53(2):267-74.
8. Pohmann R, von Kienlin M. Accurate phosphorus metabolite images of the human heart by 3D acquisition-weighted CSI. Magn Reson Med. 2001; 45(5):817-26.
9. Harris FJ. Use of Windows for Harmonic-Analysis with Discrete Fourier-Transform. P Ieee. 1978; 66(1):51-83.
10. Luo Y, de Graaf RA, DelaBarre L, Tannus A, Garwood M. BISTRO: An outer-volume suppression method that tolerates RF field inhomogeneity. Magn Reson Med. 2001; 45(6):1095-102.
11. Purvis LAB, Clarke WT, Valkovič L, Levick C, Pavlides M, Barnes E, Cobbold JF, Robson MD, Rodgers CT. Phosphodiester content measured in human liver by in vivo 31P MR spectroscopy at 7 tesla. Magn Reson Med. 2017; 78(6):2095-105.
12. Du Bois D, Du Bois EF. Clinical calorimetry: Tenth paper a formula to estimate the approximate surface area if height and weight be known. Arch Intern Med. 1916; 17(6_2):863-71.
13. Heinemann A, Wischhusen F, Püschel K, Rogiers X. Standard liver volume in the caucasian population. Liver Transpl Surg. 1999; 5(5):366-8.

5. Analysis

5.1. Fitting algorithms

Fitting can be performed in either the frequency domain or the time domain. Frequency domain fitting is well-suited to the naturally frequency-dependent nature of MR. On the other hand, time domain fitting allows more flexibility in the choice of model. In theory, both types of fitting should give similar results (1).

Another option that must be considered is whether to use prior knowledge. Additional prior knowledge often reduces the variation between fits, but could also introduce bias into the results. The trade-off between bias and variance must be considered.

The fitting algorithm used in this work is based on the *advanced method for accurate, robust and efficient spectral fitting* (AMARES), which is a popular time-domain fitting algorithm that incorporates flexible prior knowledge to improve the accuracy and precision of fitting in-vivo magnetic resonance spectra (2). AMARES has been used for fitting phosphorus (^{31}P) (3), proton (^{1}H) (4) and carbon (^{13}C) (5) MRS data.

The AMARES algorithm fits data in a linear least-squares sense to the following model function (2):

$$y_n = \hat{y}_n + e_n = \sum_{k=1}^{K} a_k e^{i\varphi_k} e^{-d_k(1-g_k+g_k t_n)t_n} e^{i2\pi f_k t_n} + e_n \qquad [5.1]$$

Where $n = 0$ to N-1, N is the number of measured points, y_n is a sum of exponentially damped sinusoids, $i = \sqrt{-1}$, a_k is the amplitude, φ_k is the phase, d_k is the damping factor, and f_k is the frequency of the k^{th} sinusoid. K is the total number of sinusoids, including one for each component of multiplet peaks. $t_n = n\Delta t + t_0$ with Δt sampling interval, and t_0 time before the first data point. e_n is complex white Gaussian noise. The caret on $\hat{y}$ indicates that this quantity represents the model function rather than actual measurements. g_k denotes whether the lineshape for each peak is Gaussian ($g_k = 1$) or Lorentzian ($g_k = 0$).

The model function variables are chemical shift, linewidth, amplitude (i.e. area) and phase for each peak. They are constrained by prior knowledge comprising the initial values, upper and lower bounds and intrinsic relationships between the peaks. For example, with broadband excitation and after first-order phase correction to compensate for the receiver dead-time, the spectral peaks often all have the same phase. Multiplet peaks are another example of an intrinsic relationship, as they have a fixed difference in chemical shift based on literature J-couplings and fixed amplitude ratios.

The first step of the AMARES algorithm is to solve the linear least-squares problem for amplitudes and phases using the starting values provided for the frequencies and dampings. The resulting amplitudes and phases are then used as the starting values for the main non-linear fitting step. The prior knowledge is applied using a linearized constraint matrix. As well as the fitted parameters, their uncertainty is estimated using their estimated Cramér-Rao lower bounds (CRLBs) (6).

5.2. OXSA toolbox

5.2.1. Background

The Oxford Spectroscopy Analysis (OXSA) toolbox was originally written by Prof. Rodgers to facilitate debugging of his Whitened Singular Value Decomposition (WSVD) coil combination algorithm (7). It allowed the loading of Siemens Digital Imaging and Communications in Medicine (DICOM) data into MATLAB and the presentation of spectra. However, it rapidly became clear that the ability to process data within MATLAB allowed the construction of more effective processing pipelines. The utility of the toolbox was expanded with the implementation of the advanced method for accurate, robust and efficient spectral fitting (AMARES) algorithm directly in MATLAB by Dr Biasiolli and Dr Clarke (2, 8).

The current version of the toolbox was designed to simplify the tailored development of fully automated or semi-automated processing pipelines by:

1. Being easy to install and use;

2. Seamlessly importing Siemens DICOM standard data, including all of the measurement headers;

3. Allowing visualisation of 1, 2 and 3D-resolved spectroscopy data volumes of interest (VOIs) overlaid on anatomical localizer images;

4. Offering a robust time-domain analysis (i.e. fitting) routine (an implementation of the AMARES algorithm);

5. Flexibly and dynamically specifying prior knowledge when fitting; and

6. Allowing batch processing of spectra.

Over the last few years, the toolbox code has also been distributed for use at various sites with links to the OCMR Spectroscopy group including: the University of Edinburgh, the University of Minnesota, Auburn University, Raboud University, McMaster University and the Medical University of Vienna. And, by compiling tools created using the OXSA toolbox, clinical fellows in OCMR have been able to process various datasets leading to multiple publications (9-13).

5.2.2. Distribution

As the code was used by an increasing number of groups, it became desirable to have a reference to bring together the various uses of the toolbox. In addition, it was decided that the code should be updated to a form that allowed simpler distribution to a wider audience, without the requirement of hands-on installation and training by a member of the group.

In order to achieve this, a paper was published detailing the design and uses of OXSA (14), and the code was made available on https://github.com/OXSAtoolbox/OXSA/. Github was chosen as it encourages contributions to the code from the wider scientific community, rather than only from the OCMR Spectroscopy group. In addition, several supplementary files were included in the package.

5.2.2.1. Documentation

Software documentation is required if the software is used by more than a single person, and recommended even if the software is only ever used by the creator (15, 16). Documentation can either be used to help improve the code (e.g. planning / versioning), or to explain the code to a new user. Documentation of the first type already existed, but the group had still mainly relied on being able to explain the code face to face to new members. Therefore for distribution, the latter type of documentation had to be written.

The three areas that a potential user is interested in are: the purpose of the package; the limitations on the use of the package; and the methods for using the package. These were covered in the paper, the license, and several user guides. The license allows all use or modification of the code for non-commercial use. The user guides explained the two main parts of the toolbox: loading DICOM data and fitting it using AMARES.

5.2.2.2. Examples

The examples included within the toolbox aimed to showcase the six points mentioned in the first section. The first example showed three different methods of importing DICOM data into MATLAB, as well as the visualization of the spectra. Two others showed the different methods of fitting multiple spectra, including using different prior knowledge files.

5.2.2.3. Testing

The aim of testing the code was to ensure that it was easy to install and use, and that there were no dependencies that were hidden within the internal MATLAB repository used by the group. The first step was to remove all the code within the tree that was unnecessary for running the OXSA toolbox. Then, a clean Windows 7 virtual machine was created with a fresh installation of MATLAB R2014a and R2017a with the MATLAB Optimization, Image Processing and Symbolic Maths toolboxes. The example scripts from the previous section were then run. These tests can be re-run any time the code is changed.

5.2.3. Updating the OXSA code

The OXSA toolbox was developed over several years, and naturally gained some redundancy and complicated code relationships. In order to ease development of additional prior knowledge within the AMARES algorithm, the code required some refactoring. During this process, certain parts of the implementation were changed completely. To ensure that this did not substantially change the output, tests were defined to compare the old and new functionality.

5.2.3.1. Code changes

The aim of this code update was to simplify the implementation of additional prior knowledge in the AMARES algorithm. This requires minimizing the number of functions that must be changed by consolidating existing functions and removing redundant code. The major changes are detailed below.

The two parts of the AMARES implementation are the model itself and the prior knowledge.

The model input was consolidated from three functions (`makeSyntheticData`, `makeModelFid`, and `makeModelFidAndJacobianReIm`) into `makeModelFid`, which can then be called by various functions based on specific requirements e.g `makeModelFidAndJacobianReIm` for fitting.

If any changes are made to the fitting model, the analytical Jacobians must be determined to pass to `lsqcurvefit`, and to allow calculation of CRLBs. These derivatives were hard coded into various functions, and so were consolidated into `compute_Jacobian`.

If the model is changed, the prior knowledge files must apply to the new model. This is achieved in `createModelConstraints`. This loops through all the compounds and peaks to create functions that describe the relationship between each of the components. There is no option except to hard code in all the possible relationships, which means that this code can be quite confusing. To try and simplify it, indices were relabelled, and additional comments were added.

These functions are then applied in various locations, such as `applyModelConstraints` or `compute_P_Matrix`. In each case, explicit knowledge of the names of each of the variables (e.g. amplitudes or linewidths) is not required, so the code was updated to avoid this. However, the knowledge of how the different parameters are combined into matrices is needed. This is now given in `getCanonicalOrdering`.

In some cases, additional prior knowledge will have an effect on the initial values. These can be accounted for through careful writing of the prior knowledge file, but can also be included as check in `initializePriorKnowledge`, which updates the initial values based on a linear least squares fit of the spectrum.

Another piece of code that affects the prior knowledge is the offset determination in `amares`. Both this and `initializePriorKnowledge` require a model spectrum to fit. Previously, this was achieved by `makeSyntheticSpectra`. However, this function does not include all the prior knowledge information, and so `makeInitialValuesModelFid` was written to more closely match the final model constraints. This leads to some concrete differences between the updated code and the original, rather than just a refactoring.

To summarise, the steps for adding additional prior knowledge are:

1. Include prior knowledge in a PK file
2. Update createModelConstraints
3. Update initializePriorKnowledge
4. Update makeInitialValuesModelFid

And the steps for updating the fitting model are now:

1. Decide the form of the new model
2. Update the model in `makeModelFid`
3. Calculate analytical derivatives and implement in `compute_Jacobian`

4. Update createModelConstraints

5. Update getCanonicalOrdering

6. Update Results structure naming in `amares`

5.2.3.2. Testing of the updated code

The tests for changing the code should be simple to run and be possible to include in the distribution. Therefore the code for testing was based on the example code (in `/examples/`) and sample data (in `/sample-data/`). Monte Carlo simulation are run by adding random noise to two types of high SNR spectra: simulated (in `/test/MonteCarlo/test_simSpec_MonteCarlo`) and phantom data (in `/test/MonteCarlo/test_phantom_MonteCarlo`).

For the simulated spectra, noise of twelve variances was added to the perfect example cardiac spectrum. This was repeated 2000 times and each fit was timed. To make this repeatable, the top and bottom 0.1% based on absolute values of each variable, and the top 1% based on absolute CRLBs was excluded, and the remaining data was split into twelve bins of 1143 points based on SNR. The bias and standard deviation were calculated as percentages using the input simulation parameters. These were combined to give the root mean square error (RMSE) using Eq. [5.2] (17):

$$\mathrm{RMSE} = \sqrt{\mathrm{SD}^2 + \mathrm{Bias}^2} \qquad [5.2]$$

Using RMSE gives a measure of total error for the model at each step and noise level.

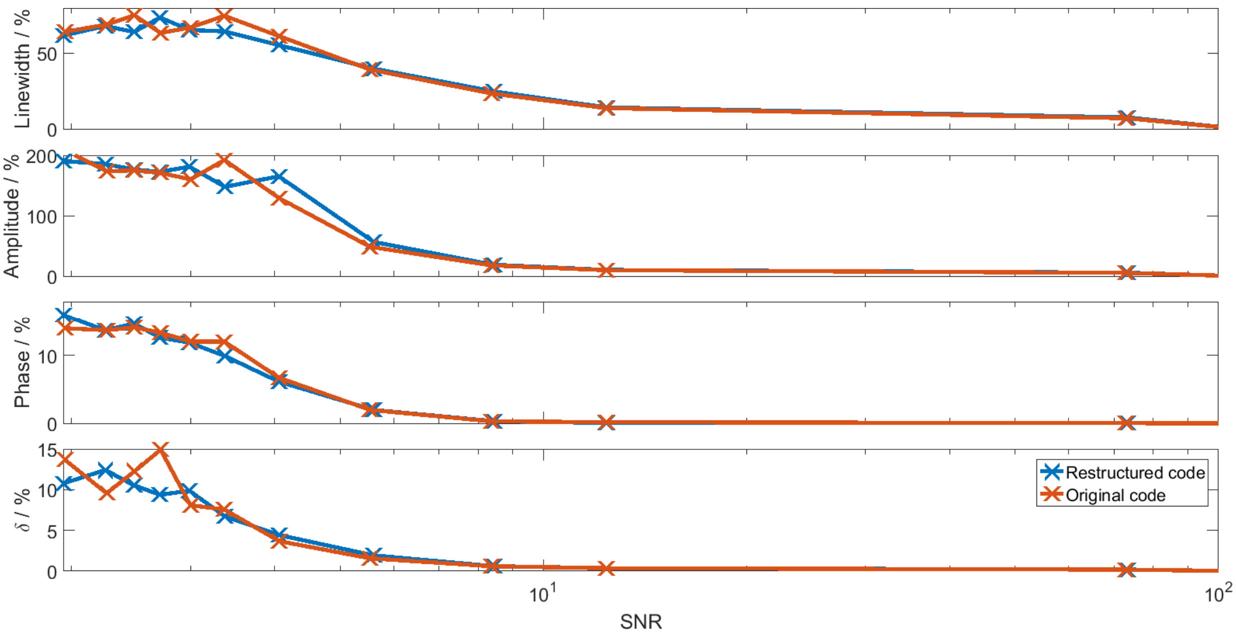

Fig 5.1. RMSE (%) of PCr fit parameters in Monte Carlo simulation of cardiac spectra. Linewidth, amplitude, phase and chemical shift (δ) RMSE are all given as percentages of the simulation input parameters. The restructured code is in blue, and the original code is given in orange. The lines are drawn only to guide the eye.

The RMSE for the PCr peak is given in Fig 5.1. The average time to fit each spectrum was reduced by 21% for the restructured code.

Five voxels were selected from phantom data containing a single phosphate resonance. For each of twelve variances, random Gaussian noise was added to every voxel 1000 times. The extreme values were excluded in the same way as for the simulated data leaving 4764 points per SNR bin. The bias and percentages were calculated from the fit values when no additional noise was added to the spectra. The phosphate peak RMSE is given in Fig 5.2. Chemical shift is not included, as it is approximately zero except when fitting fails at very low SNR. The average time to fit each spectrum was reduced by 12% for the updated code.

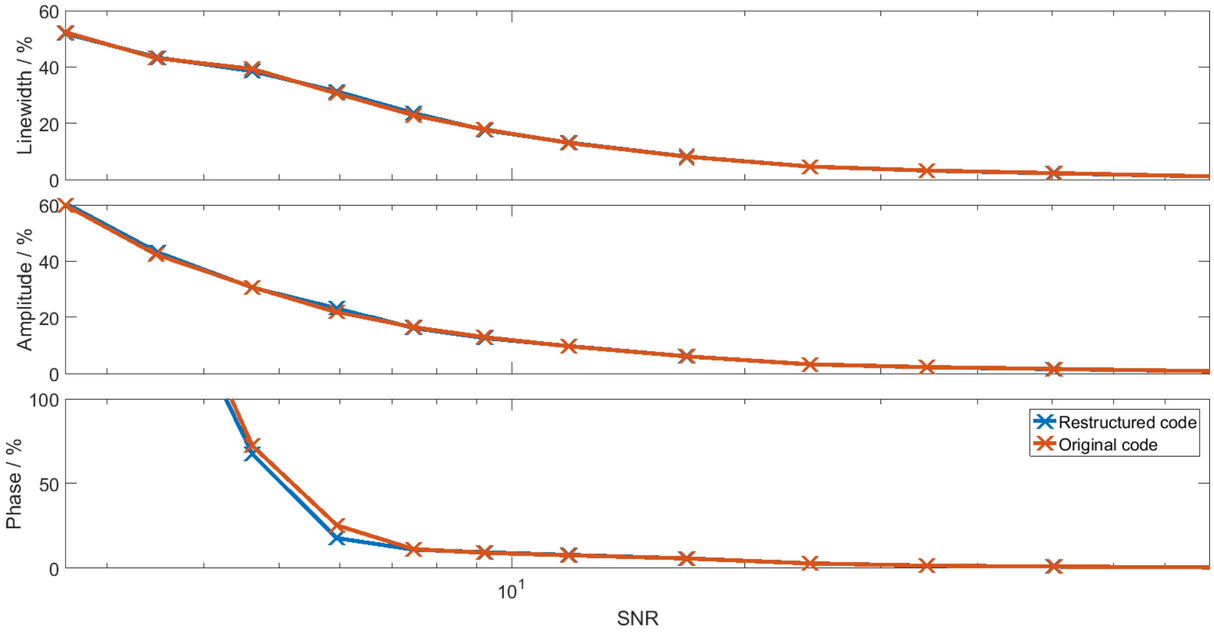

Fig 5.2. RMSE (%) of fit parameters in Monte Carlo simulation of phantom spectra. Linewidth, amplitude, and phase RMSE are all given as percentages of the fit values when no additional noise is added to each voxel. The restructured code is depicted in blue, and the original code is given in orange.

For both of these tests, the results of the restructured code only differ from the original code at low SNR, where the initial value determination has a greater effect and the fitting has multiple local minima.

This testing code is included with the distribution, as well as reference results to allow the determination of the effect of changes to the fitting algorithm (in `/test/MonteCarlo/data/`).

5.3. Voigt lineshapes

The form of a signal peak in the frequency-domain is called its lineshape. The signal arising from a homogenous group of excited spins has a Lorentzian lineshape, as its FID will show pure exponential decay. In practise, no group of spins is completely homogenous and there will be some broadening of the lineshape due to a distribution of different local field strengths for each spin isochromat. In other words, there will be a Gaussian component to the lineshape. This combination can be described as a convolution of a Gaussian and a Lorentzian, which is called the Voigt lineshape.

Both the OXSA toolbox and the implementation of AMARES in the java Magnetic Resonance User interface (jMRUI (8)) use a pure Lorentzian lineshape, and assume that the error introduced because of this is negligible. The aim of the following section is to test that assumption and to examine the possible improvements using Voigt lineshapes.

First, Voigt lineshapes are implemented into the OXSA toolbox. Then Lorentzian prior knowledge is used to fit Voigt and Gaussian lineshapes and the errors are determined. This is then compared to using Lorentzian, Voigt or Gaussian prior knowledge to fit the same models to determine theoretical improvements. Finally, Gaussian contributions to lineshapes are measured in phantoms and in vivo.

5.3.1. Implementation

In this work, analysis is performed using the AMARES algorithm implemented in MATLAB as part of the OXSA toolbox (2, 14) . The algorithm uses the model function given in Eq. [5.1] and repeated here:

$$y_n = \hat{y}_n + e_n = \sum_{k=1}^{K} a_k e^{i\varphi_k} e^{-d_k(1-g_k+g_k t_n)t_n} e^{i2\pi f_k t_n} + e_n$$

where $g_k = 1$ for a Gaussian and $g_k = 0$ for a Lorentzian.

In theory, any combination of Lorentzian and Gaussian could be achieved by rewriting this model function as:

$$\hat{y}_n = \sum_{k=1}^{K} a_k e^{i\varphi_k} e^{-(\alpha_k+\beta_k t_n)t_n} e^{i2\pi f_k t_n} \qquad [5.3]$$

where α and β are the Lorentzian and Gaussian decay factors.

In the OXSA toolbox, only the Lorentzian model function was originally implemented, i.e. $g_k = 0$ in Eq. [5.1] or $\beta_k = 0$ in Eq. [5.3]. The damping term α_k was replaced by a linewidth term Γ_k which, for a pure Lorentzian, is π times α_k. In addition the phase ϕ_k is given in degrees, and the offset is given as a chemical shift δ_k multiplied by the imaging frequency f_I. The Lorentzian model function is therefore:

$$\hat{y}_n = \sum_{k=1}^{K} a_k e^{i\varphi_k \cdot \frac{\pi}{180}} e^{-\pi \Gamma_k t_n} e^{i2\pi\delta_k f_I t_n} \qquad [5.4]$$

With this model function, there are four fitting parameters per peak: amplitude, phase, linewidth and chemical shift.

A Voigt or Gaussian lineshape can be included by allowing $\beta_k > 0$ in Eq. [5.3]. A frequency-space Gaussian centred at zero and with a standard deviation σ is defined as:

$$g(x) = ae^{-\frac{f^2}{2\sigma^2}} \qquad [5.5]$$

In the time domain, this becomes:

$$G(\mathrm{t}) = Ae^{-2\pi^2\sigma^2 t^2} \qquad [5.6]$$

Therefore,

$$\beta_k = 2\pi^2\sigma_k^2 \qquad [5.7]$$

The full Voigt model function is then:

$$\hat{y}_n = \sum_{k=1}^{K} a_k e^{i\varphi_k \cdot \frac{\pi}{180}} e^{-\pi \Gamma_k t_n} e^{-2\pi^2 \sigma_k^2 t_n^2} e^{i2\pi\delta_k f_I t_n} \qquad [5.8]$$

An extra fitting term is added to the model function – the standard deviation of the frequency-domain Gaussian σ_k.

An important feature of a lineshape profile is its full width at half maximum (FWHM) or linewidth. The Lorentzian linewidth is included in Eq. [5.8] as Γ. The linewidth of a Gaussian in terms of the standard deviation σ is:

$$LW_G = 2\sqrt{2\ln 2} \times \sigma \qquad [5.9]$$

It is not possible to define the linewidth of a Voigt profile analytically, but many approximations have been developed (18). A first approximation of the Voigt linewidth was given by Danos and Geschwind (19):

$$LW_V = \sqrt{\Gamma^2 + LW_G^2} \qquad [5.10]$$

However, a closer approximation was proposed by Olivero and Longbothum (18):

$$LW_V = \frac{1+0.099\ln 2}{2}\Gamma + \sqrt{\frac{(1-0.099\ln 2)^2}{4}\Gamma^2 + LW_G^2 \cdot \ln 2} \qquad [5.11]$$

In general, the linewidth of a Voigt profile is greater than the linewidth of either the Gaussian or Lorentzian profile that have been convolved.

In the following sections, several simulations are described using different models and prior knowledge. In each case, the linewidths of the Gaussian and Lorentzian that are being compared are equal, and the Voigt profile is the combination of those two lineshapes. The Voigt profile is described using "% Gaussian", which is defined:

$$\%\ \text{Gaussian} = \frac{LW_G}{LW_G + \Gamma} \qquad [5.12]$$

5.3.2. Limitations of pure Lorenztian lineshapes

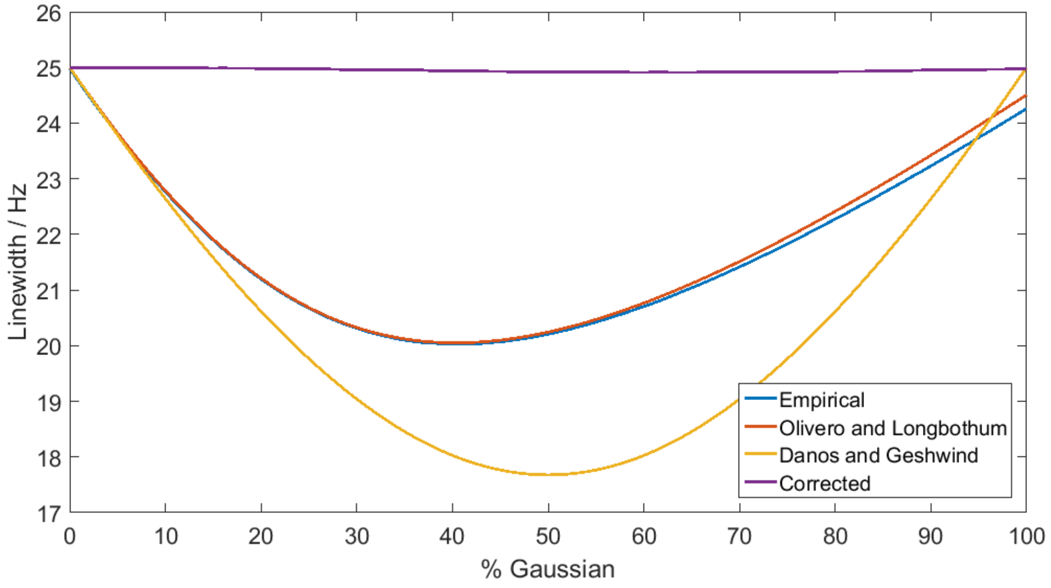

Fig 5.3. Voigt linewidths. The blue, orange, and yellow lines were determined using uncorrected Γ and σ from Eqs [5.13] and [5.14] (i.e. the linewidth correction was set to one). The blue line was measured numerically from the Fourier transformed spectrum from a noise-less FID. The orange line was determined from Eq. [5.10], and the yellow line was determined from Eq. [5.11]. The purple line shows the empirically determined linewidth when Γ and σ were corrected according to Eqs [5.13] and [5.14] using the uncorrected empirical data i.e. the blue line.

Simulated "perfect" single peak spectra were created for ten different Gaussian contributions, with maximum Lorentzian and Gaussian linewidths of 25 Hz. The Lorentzian linewidth input for the model was:

$$\Gamma = 25 \times (1 - \%\ \text{Gaussian}) \times \text{linewidth correction} \qquad [5.13]$$

And the Gaussian SD was:

$$\sigma = \frac{25}{2\sqrt{2\ln 2}} \times \%\ \text{Gaussian} \times \text{linewidth correction} \qquad [5.14]$$

The linewidth correction was the maximum linewidth (i.e. 25 Hz) divided by the empirically determined Voigt linewidth (i.e. the linewidth measured numerically from the Fourier transformed spectrum). Without this correction, the peak linewidth would become narrower for the Voigt lineshape (see Fig 5.3).

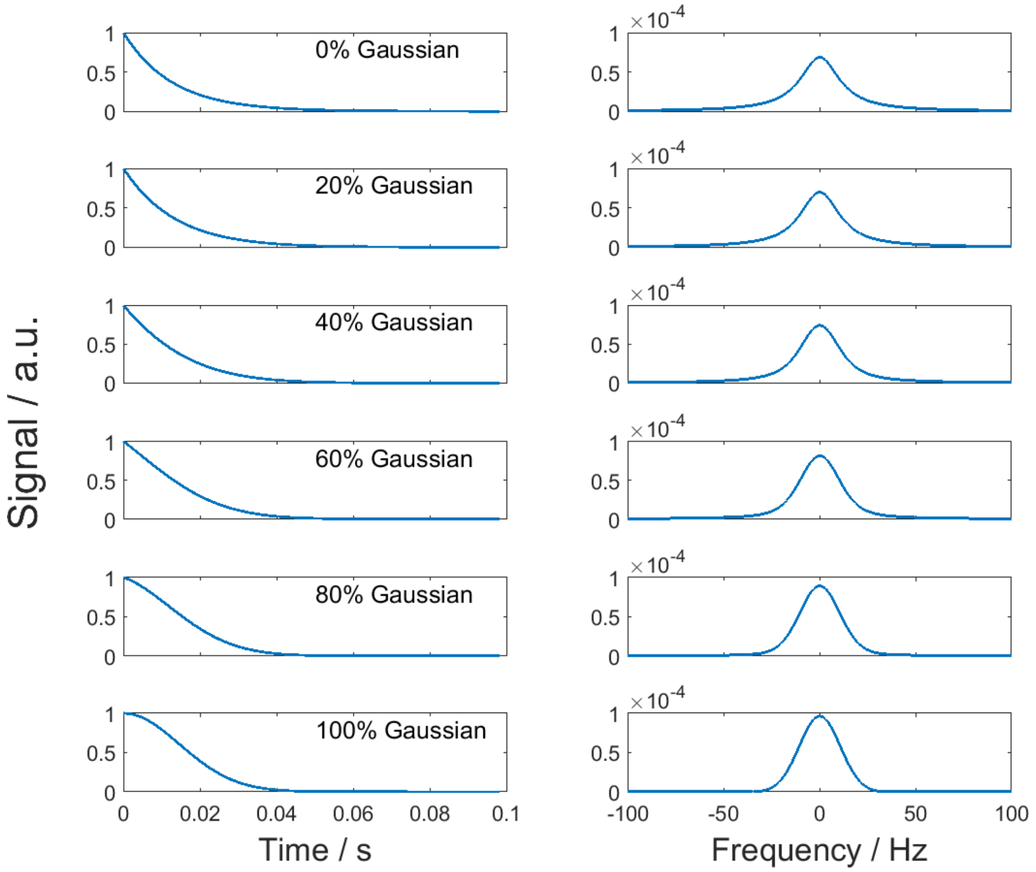

Fig 5.4. Typical FIDs and spectra of various Voigt lineshapes. The amplitude for each peak was 1 a.u., the chemical shift was 0 Hz, and the phase was 0°. Γ and σ were determined for each peak according to Eqs [5.13] and [5.14], corrected to give equal linewidths.

To each of these spectra (see examples in Fig 5.4), 1000 repetitions of random noise of twelve variances was added, and the resulting spectra were fitted using a single peak Lorentzian prior knowledge. Bias, SD and RMSE was determined for the fitted amplitude compared to the model amplitude. The results for five of the lineshapes at different SNR are shown in Fig 5.5. As the model becomes increasingly Gaussian, the bias in the result also increases. However, the SD decreases. This means that at low SNR, where SD becomes comparable to bias, the RMSE of fitting more Gaussian spectra is reduced compared to fitting purely Lorentzian spectra. These results are shown for varying % Gaussian in Fig 5.6. At low SNR, the RMSE error remains stable until the spectrum is 50% Gaussian. At this point, the increase in bias overcomes the reduction in SD, and the overall fitting error increases.

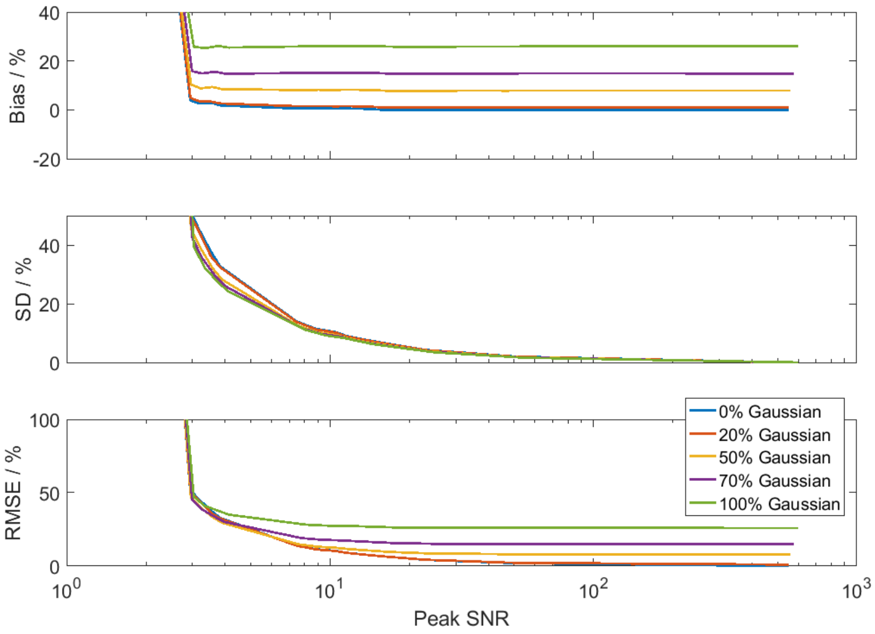

Fig 5.5. Monte Carlo simulations of five single peaks of different lineshapes, fitted with a Lorentzian. Bias, SD and RMSE of amplitudes of Lorenztian fitting of models with lineshapes ranging from fully Lorentzian to fully Gaussian. Each variable is plotted against the mean SNR at that noise variance.

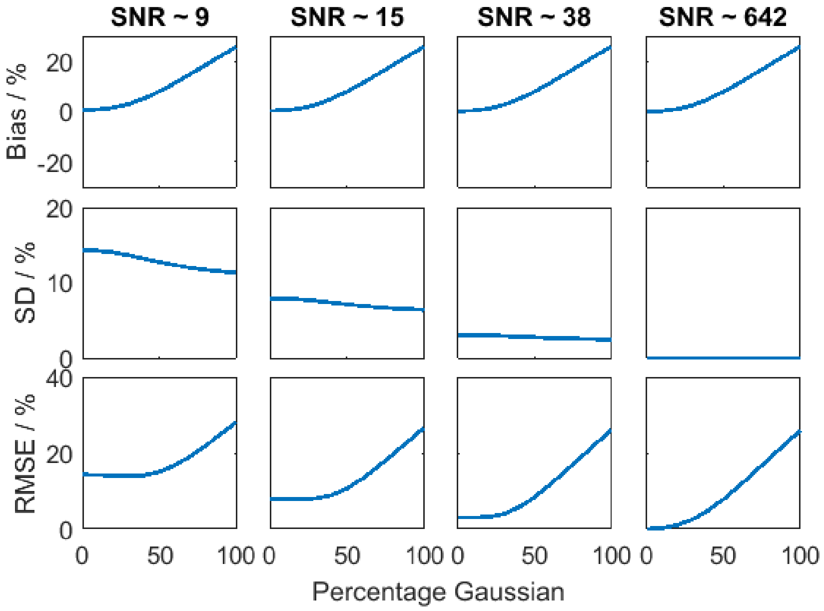

Fig 5.6. Monte Carlo simulations of single peaks with Voigt lineshapes at four SNR values, fitted with a Lorentzian. Bias, SD and RMSE of amplitudes of Lorenztian fitting of models with lineshapes ranging from fully Lorentzian to fully Gaussian. Each variable is plotted against the percentage of Gaussian lineshape at a single noise variance.

5.3.3. Theoretical benefits of Voigt lineshapes

Five models and five different prior knowledge sets were used (see Table 5.1). These range from fully Lorentzian (L) to fully Gaussian (G), with three mixed lineshapes in between: Lorentzian-dominated Voigt (V_L), Gaussian-dominated Voigt (V_G) and one with approximately equal contributions from Lorentzian and Gaussian lineshapes (V_e).

Table 5.1. Model and prior knowledge values for different lineshapes. The models are: fully Lorentzian (L), Lorentzian-dominated Voigt (V_L), equal contribution Voigt (V_e), Gaussian-dominated Voigt (V_G) and fully Gaussian (G).

Name	Model		Prior Knowledge initial values	
	Lorentzian linewidth / Hz	Gaussian linewidth / Hz	Lorentzian linewidth / Hz	Gaussian sigma / Hz
L	25	0	20	n/a
V_L	15	5	20	0
V_e	12.5	12.5	20	20
V_G	5	15	0	20
G	0	25	n/a	20

For each model, 100 repetitions of twelve variances of random noise were added and each spectrum was fitted by every prior knowledge in turn. This gave 25 results per SNR. The mean bias, SD and RMSE were calculated at each SNR, and are depicted for three SNR in Fig 5.7.

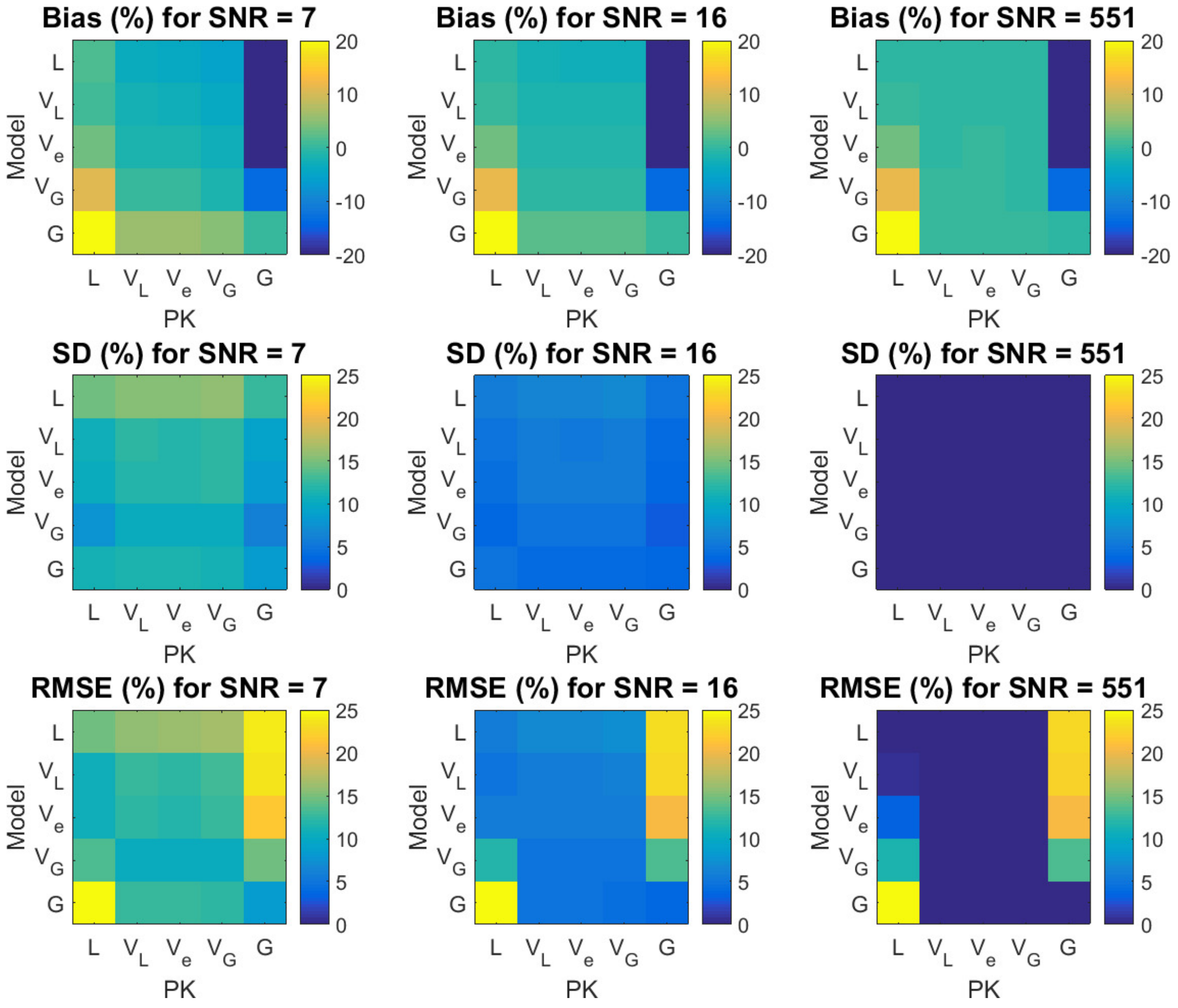

Fig 5.7. Single peak Monte Carlo simulation of lineshape models. Simulated amplitude bias, mean and RMSE are given as percentage of true value for three SNR: 5, 20 and 207. For each plot, the row denotes the model used to create the spectrum, and the column denotes the prior knowledge used for fitting. L and G denote Lorentzian and Gaussian. V denotes Voigt, with the subscripts describing the major component of the lineshape. V_e has approximately equal contributions from Lorentzian and Gaussian.

As expected, the pure Lorentzian and pure Gaussian models and prior knowledge give extreme values, with the Voigt lineshapes falling in between. At high SNR, the bias dominates the total error, whereas at low SNR there are contributions from both bias and SD. The SD for the Voigt lineshapes are higher than for either the Lorentzian or Gaussian. This is common when increasing the complexity of the model, as the additional fitting term reduces bias but adds variability to the result.

The bias is up to 25% for Lorentzian fitting Gaussian or vice versa. For the Voigt prior knowledge, the bias is up to 6% at low SNR, and the SD is up to 4% worse than the pure lineshapes.

5.3.4. Lineshape analysis in phantoms and in vivo

An analysis of lineshapes in phantoms was achieved by fitting eight phantom UTE-CSI datasets of varying resolution and matrix size. The phantoms themselves were of different sizes and concentrations of phosphate ($K_2HPO_{4(aq)}$). One phantom contained triphenylphosphite (TPP). $\boldsymbol{B}_0$ shimming was performed on each of the phantoms before the CSI acquisition. The data were fitted using Voigt prior knowledge with 5 Hz Lorentzian and Gaussian initial linewidths. Mean % Gaussian values were determined for each of the datasets.

The results varied between 57 and 87% Gaussian lineshapes. This indicates that fitting with Lorentzian prior knowledge would result in a large bias (6 – 20%). Although there is a possible reduction in SD (3 – 7%) , the overall RMSE is higher for pure Lorenztian prior knowledge than for Voigt prior knowledge except at very low SNR (< 7) and with about 50% Gaussian linewidths contribution.

Five shimmed UTE-CSI scans acquired in vivo in the liver were fitted using equal contribution Voigt prior knowledge. The average Gaussian contribution was determined to be 60%. This is similar to the phantom datasets, and so Voigt prior knowledge would be expected to reduce the overall RMSE.

5.4. Linewidth-constraints

In my Master's thesis, I explored the idea of constraining linewidths using additional prior knowledge in order to improve fitting of ^{31}P-MR spectra (20, 21). This concept is based on the additional contribution to apparent T_2^* from $\boldsymbol{B}_0$ inhomogeneity (Eq. 2.51, repeated here):

$$\frac{1}{T_2^*} = \frac{1}{T_2} + \frac{1}{T_2^{*'}} \qquad [5.15]$$

For a Lorentzian:

$$LW = \frac{1}{\pi T_2^*} \qquad [5.16]$$

For a given metabolite A, Eq. 2.51 can then be rewritten as:

$$\begin{aligned} \mathrm{LW(A)} &= \mathrm{LW_{intrinsic}(A) + LW_{\Delta B0}} \\ &= \mathrm{LW_{intrinsic}(A) + (LW(\gamma\text{-ATP}) - LW_{intrinsic}(\gamma\text{-ATP}))} \\ &= \mathrm{LW(\gamma\text{-ATP}) + (LW_{intrinsic}(A) - LW_{intrinsic}(\gamma\text{-ATP}))} \\ &= \mathrm{LW(\gamma\text{-ATP}) + \Delta LW_{intrinsic}\ (A)} \qquad [5.17] \end{aligned}$$

Each peak can be fitted a sum of its intrinsic (previously determined) linewidth and additional linewidth which is common to all peaks, thus reducing the total number of fit parameters. This was shown to increase fitting accuracy by reducing the SD of the fit without significantly increasing the bias (20, 21).

However, the assumption in Eq. 2.51 that $\boldsymbol{B}_0$ inhomogeneity only causes a T_2^* linewidth broadening is only true when considering inhomogeneity on a microscale. On the other hand, two groups of spins experiencing different, homogenous, $\boldsymbol{B}_0$ will be seen as two separate peaks within a spectrum. When averaging over a voxel this will give rise to a normal distribution of chemical shifts, i.e. a Voigt profile with an intrinsic Lorentzian and extrinsic

Gaussian. In reality, inhomogeneity will cause both of these two effects. This can be modelled by assuming that the intrinsic component is purely Lorentzian, but that the additional component is a Voigt combination of Lorentzian and Gaussian.

5.4.1. Testing the inclusion of constrained Voigt lineshapes

In Section 5.3.4 the Gaussian contribution in the liver in vivo was determined to be 60%. Therefore, a perfect liver spectrum with 60% Gaussian contribution was simulated with linewidths equal to an arbitrary intrinsic value plus a common Voigt profile. 1000 repetitions of random noise with 12 variances was added to give 12000 spectra of various SNR. These spectra were fitted with four prior knowledge files: Voigt lineshapes with unconstrained linewidths, and Voigt lineshapes constrained according to Eq. [5.17], unconstrained Lorentzian linewidths, and constrained Lorentzian linewidths. The prior knowledge for chemical shifts and amplitudes was based on literature values (22, 23).

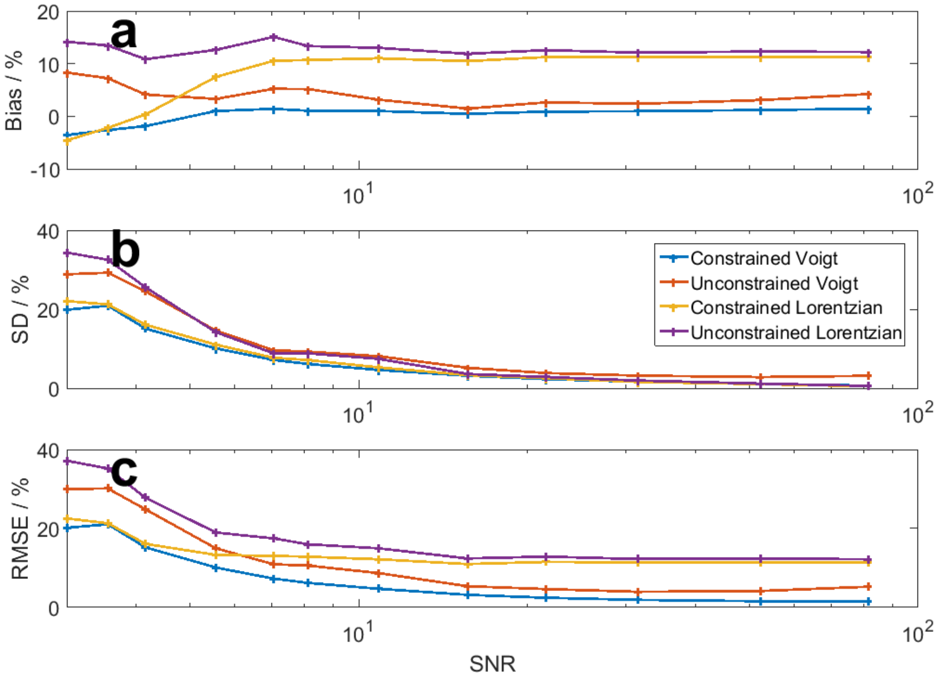

Fig 5.8. γ-ATP error in Monte-Carlo simulation of linewidth-constraint models. The bias (a), SD (b) and RMSE (c) of the γ-ATP amplitudes, fitted using four different prior knowledge files, were plotted against γ-ATP SNR. Values are given as a percentage of the simulation input amplitude. Each variance was repeated 1000 times. Lines are drawn only to guide the eye.

The results for the γ-ATP peak are shown in Fig 5.8. The results for the other peaks are similar: the error for the Lorentzian fitting is dominated by the bias, and at very low SNR the models with the fewest fitting parameters have lower SD and so tend to have lower RMSE. The amount of bias depends on the overlap between neighbouring peaks. For Lorentzian fitting, a greater overlap leads to a lower bias. In contrast, for Voigt fitting greater overlap leads to a larger bias. In all cases except SNR < 3, the constrained Voigt model has the lowest overall error.

Averaging across all peaks, unconstrained Voigt fitting does not give perfect fits even at high SNR, due to overlapping peaks (see Fig 5.9). This introduces some bias, and there is only a 10% improvement compared to Lorentzian fitting (compared to 25% for the single peak, γ-ATP, shown in Fig 5.8). Constrained Voigt fitting does not give bias (in this simulation) and so provides up to 10% further improvement in fitting error (i.e. up to 20% improvement over pure Lorentzian fitting).

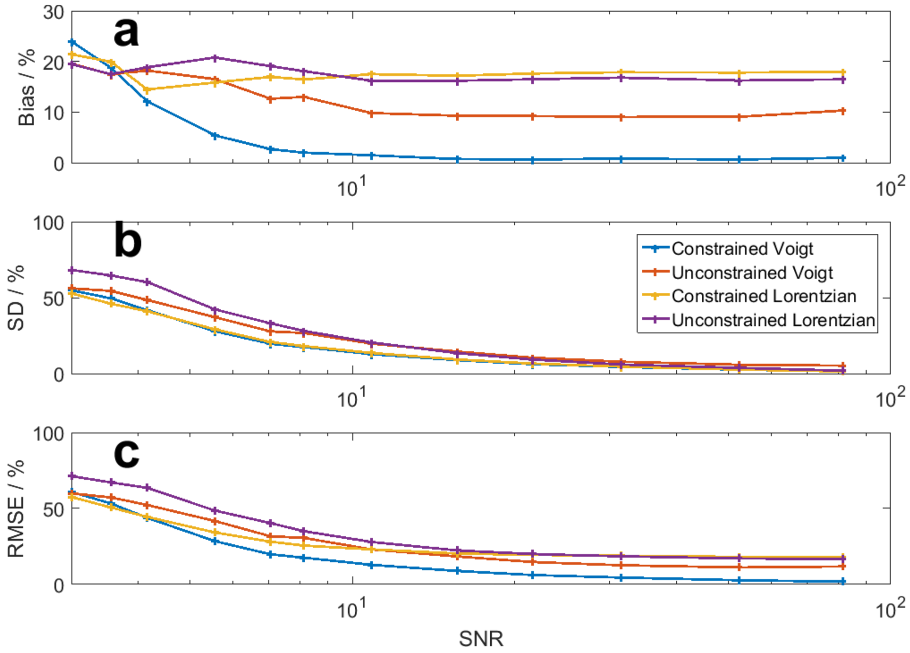

Fig 5.9. Mean peak error in Monte-Carlo simulation of linewidth-constraint models. The mean absolute bias (a), SD (b) and RMSE (c) of all peak amplitudes, fitted using four different prior knowledge files, were plotted against γ-ATP SNR. Values are given as a percentage of the simulation input amplitude. Each variance was repeated 1000 times. Lines are drawn only to guide the eye.

5.4.2. Determination of constraints

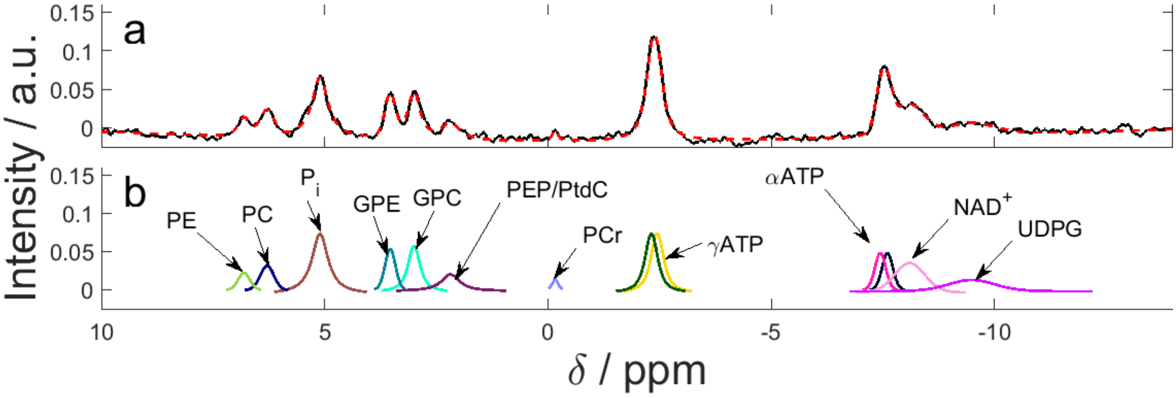

Fig 5.10. **An example of Voigt fitting.** (a) shows a typical ^{31}P-MRS 7 T liver spectrum (in black) overlaid with the model function fitted by using the unconstrained Voigt prior knowledge set (in red). (b) shows the model function split into individual peaks.

Voigt fitting with unconstrained linewidths was run on five UTE-CSI datasets acquired in the liver at 7 T (as described in Section 4.5). An example of the fitting is given in Fig 5.10. Data were excluded if: the voxel was outside a manually drawn region of interest (ROI); the peak amplitudes had greater than 50% CRLB; the linewidth or Gaussian SD CRLB were over 150 Hz; or the γ-ATP SNR was less than 30. Total Voigt linewidths were approximated using Eq. [5.11]. The remaining data for each peak were plotted against the γ-ATP Voigt linewidth (see Fig 5.11). The data were fitted to a straight line of unit slope using the Matlab robust bisquares-weighted fitting function `fit`. The intercept defines the additional linewidth of the peak compared to that of γ-ATP i.e. $\Delta LW_{intrinsic}$.

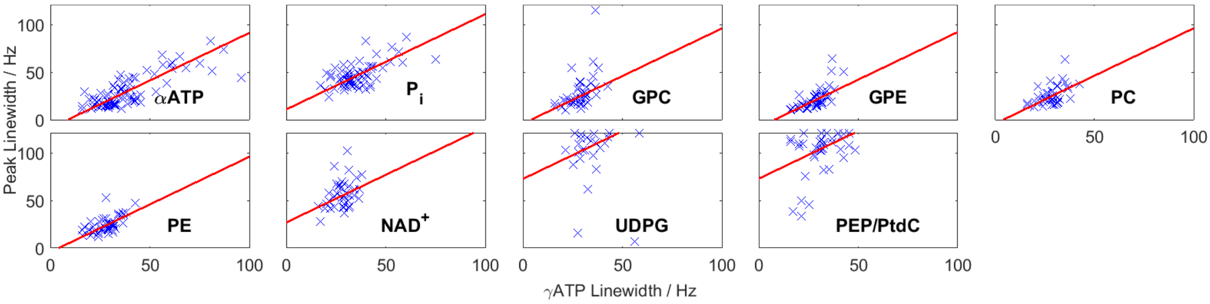

Fig 5.11. **Metabolite Voigt linewidths in the human liver at 7 T.** Each blue 'x' marks a single spectrum, and the red line shows the bisquares fit. Intercepts show $\Delta LW_{intrinsic}$ relative to γ-ATP

Table 5.2. Intrinsic differences in linewidth relative to γ-ATP. $\Delta LW_{intrinsic}$ are given in Hz ± 95% confidence intervals.

Metabolite name	**$\Delta LW_{intrinsic}$ / Hz**	**R^2**
α-ATP	-8.79 ± 1.95	0.65
GPC	-4.1 ± 2.58	0.78
GPE	-7.9 ± 1.73	0.73
P_i	10.8 ± 2.29	0.24
PC	-3.92 ± 2.23	0.42
PE	-4.21 ± 1.81	0.46
PtdC	72.8 ± 6.17	0.28
NAD^+	26.8 ± 4.03	0.27
UDPG	72.5 ± 6.69	0.71

The intercepts ± 95% confidence intervals for α-ATP, GPC, GPE, Pi, PC, PE, PtdC, NAD+ and UDPG are -8.79 ± 1.95 Hz, -4.1 ± 2.58 Hz, -7.9 ± 1.73 Hz, 10.8 ± 2.29 Hz, -3.92 ± 2.23 Hz, -4.21 ± 1.81 Hz, 72.8 ± 6.17 Hz, 26.8 ± 4.03 Hz, and 72.5 ± 6.69 Hz respectively. The corresponding R^2 for the robust fits, as derived from the bisquares-weighted residual sum of square and total sum of squares, are 0.65, 0.78, 0.73, 0.24, 0.42, 0.46, 0.28, 0.27, and 0.71 (see Table 5.2).

The 95% confidence intervals of the intercepts of the liver linewidth plots are only a few Hz for all metabolites. However, some R^2 values for the linewidths of γ-ATP against individual metabolites are relatively low. There are several possible reasons for low correlation. For example, noise has a large effect in liver ^{31}P spectra, and although the γ-ATP SNR in the spectra used for the determination is greater than 20, this is not true for the other peaks. Restraining the smaller peaks in such a way would limit the number of available data, and potentially make fitting impossible. The $\boldsymbol{B}_0$ inhomogeneity may not be the same for all peaks, for example if the local micro-environment of the metabolites differs.

The PtdC, NAD$^+$ and UDPG linewidths have visibly poor fits and either had low R^2 or high confidence intervals. The simulation from Section 5.4.1 was rerun to test the largest expected error introduced by setting $\Delta LW_{intrinsic}$ incorrectly for those three peaks. The constrained prior knowledge was set to have $\Delta LW_{intrinsic}$ equal to the values in Table 5.2, but the model FID had $\Delta LW_{intrinsic}$ set to zero for PtdC, NAD$^+$ and UDPG. Both the constrained and unconstrained prior knowledge files were used, with the addition of a third set of prior knowledge where all peaks except PtdC, NAD$^+$ and UDPG were constrained. As expected, a large bias was introduced for the constrained fitting, averaging 16% across all the peaks. This bias was not present when using the semi-constrained prior knowledge, and so it gave the lowest average RMSE.

The reproducibility of the constrained and semi-constrained prior knowledge will be compared in vivo in Chapter 9. If the constrained prior knowledge does not give considerable improvement in the reproducibility of the results, the semi-constrained prior knowledge should be used instead in order to avoid the inclusion of unnecessary bias.

The determination of $\Delta LW_{intrinsic}$ need only be performed once for each set of prior knowledge. To perform linewidth-constrained fitting in e.g. the brain the $\Delta LW_{intrinsic}$ would need to be determined anew, but for future work, linewidth-constrained fitting of 7 T liver ^{31}P spectra the $\Delta LW_{intrinsic}$ determined here can be reused.

5.5. Summary

1. The OXSA toolbox allows inclusion of varied prior knowledge.

2. Voigt lineshape fitting was implemented.

3. Voigt lineshapes improve the fitting of simulated single peaks by up to 25%, and by 5 – 10% for the lineshapes and SNR seen in standard phosphate phantom scans

4. Similarly, Voigt lineshapes improve the fitting of liver spectra with in vivo lineshapes by up to 10%.

5. Constrained Voigt lineshapes can improve the fitting of liver spectra by another 10% (i.e. 20% compared to Lorentzian fitting).

6. The addition of bias due to the incorrect determination of per peak $\Delta LW_{intrinsic}$ may reduce the potential improvements.

7. The full prior knowledge used for constrained Voigt fitting is given in Table 5.3.

8. The reproducibility of constrained and semi-constrained Voigt fitting needs to be compared in vivo. This is presented in Chapter 9.

Table 5.3. List of prior knowledge used for fitting the standard protocol. The phases of all peaks were additionally constrained to be the same as all the other peaks.

	β-ATP	**α-ATP**	**γ-ATP**	**PCr**	**P_i**	**GPC**	**GPE**	**PC**	**PE**	**NAD^+**	**UDPG**	**PEP/PtdC**
Multiplet												
Ratio	1:2:1	1:1	1:1	-	-	-	-	-	-	-	-	-
Splitting (Hz)	15	16	15	-	-	-	-	-	-	-	-	-
Additional linewidth	-	-8.79	0	-	10.8	-4.1	-7.9	-3.92	-4.21	26.8	72.5	72.8
Initial Values (Bounds)												
Chemical shift / ppm	-16.00 (-inf ,-10)	-7.40 (-inf, inf)	-2.21 (-inf, -0.5)	0.00 (-0.5, 0.5)	5.37 (0, 10)	3.19 (3,6)	3.71 (3, 6)	6.70 (6,8)	7.30 (6.3, 9)	-8.25 (-15,-5)	-9.48 (-15,-5)	2.20 (2,5)
Linewidth / Hz	35 (0, 40)	35 (0, inf)	30 (0, inf)	12 (0, 20)	40 (0, 50)	25 (0, 50)	25 (0, 50)	25 (0, 50)	20 (0, 50)	25 (0, 50)	25 (0, 50)	25 (0, 50)
Amplitude / a.u.	3 (0, inf)	3 (0, inf)	3 (0, inf)	0.5 (0, inf)	2 (0, inf)	2.5 (0, inf)	2.5 (0, inf)	1 (0, inf)	1 (0, inf)	0.5 (0, inf)	0.6 (0, inf)	0.6 (0, inf)
Phase / degrees	0 (0, 360)	0 (0, 360)	0 (0, 360)	0 (0, 360)	0 (0, 360)	0 (0, 360)	0 (0, 360)	0 (0, 360)	0 (0, 360)	0 (0, 360)	0 (0, 360)	0 (0, 360)
Sigma / Hz	14.9 (0, 100)	14.9 (0, inf)	12.7 (0, inf)	5.1 (0, 15)	17.0 (0, 100)	10.6 (0, 100)	10.6 (0, 100)	10.6 (0, 100)	8.5 (0, 100)	10.6 (0, 100)	10.6 (0, 100)	10.6 (0, 100)

5.6. References

1. Poullet J-B, Sima DM, Van Huffel S. MRS signal quantitation: A review of time- and frequency-domain methods. J Magn Reson. 2008; 195(2):134-44.
2. Vanhamme L, van den Boogaart A, Van Huffel S. Improved method for accurate and efficient quantification of MRS data with use of prior knowledge. J Magn Reson. 1997; 129(1):35-43.
3. Rodgers CT, Clarke WT, Snyder C, Vaughan JT, Neubauer S, Robson MD. Human cardiac 31P magnetic resonance spectroscopy at 7 tesla. Magn Reson Med. 2014; 72(2):304-15.
4. Kanowski M, Kaufmann J, Braun J, Bernarding J, Tempelmann C. Quantitation of simulated short echo time H-1 human brain spectra by LCModel and AMARES. Magn Reson Med. 2004; 51(5):904-12.
5. Lanz B, Duarte JMN, Kunz N, Mlynarik V, Gruetter R, Cudalbu C. Which prior knowledge? Quantification of in vivo brain 13C MR spectra following 13C glucose infusion using AMARES. Magn Reson Med. 2013; 69(6):1512-22.
6. Cavassila S, Deval S, Huegen C, van Ormondt D, Graveron-Demilly D. Cramér-Rao bounds: an evaluation tool for quantitation. NMR Biomed. 2001; 14(4):278-83.
7. Rodgers CT, Robson MD. Receive Array Magnetic Resonance Spectroscopy: Whitened Singular Value Decomposition (WSVD) Gives Optimal Bayesian Solution. Magn Reson Med. 2010; 63(4):881-91.
8. Stefan D, Di Cesare F, Andrasescu A, Popa E, Lazariev A, Vescovo E, Strbak O, Williams S, Starcuk Z, Cabanas M, van Ormondt D, Graveron-Demilly D. Quantitation of magnetic resonance spectroscopy signals: the jMRUI software package. Meas Sci Technol. 2009; 20(10):104035.
9. Stoll VM, Clarke WT, Levelt E, Liu A, Myerson SG, Robson MD, Neubauer S, Rodgers CT. Dilated Cardiomyopathy: Phosphorus 31 MR Spectroscopy at 7 T. Radiology. 2016; 281(2):409-17.
10. Clarke WT, Robson MD, Neubauer S, Rodgers CT. Creatine kinase rate constant in the human heart measured with 3D-localization at 7 tesla. Magn Reson Med. 2017; 78(1):20-32.
11. Wijesurendra RS, Liu A, Eichhorn C, Ariga R, Levelt E, Clarke WT, Rodgers CT, Karamitsos TD, Bashir Y, Ginks M, Rajappan K, Betts T, Ferreira VM, Neubauer S, Casadei B. Lone Atrial Fibrillation Is Associated With Impaired Left Ventricular Energetics That Persists Despite Successful Catheter Ablation. Circulation. 2016; 134(15):1068-81.
12. Levelt E, Mahmod M, Piechnik SK, Ariga R, Francis JM, Rodgers CT, Clarke WT, Sabharwal N, Schneider JE, Karamitsos TD, Clarke K, Rider OJ, Neubauer S. Relationship Between Left Ventricular Structural and Metabolic Remodeling in Type 2 Diabetes. Diabetes. 2016; 65(1):44-52.
13. Levelt E, Rodgers CT, Clarke WT, Mahmod M, Ariga R, Francis JM, Liu A, Wijesurendra RS, Dass S, Sabharwal N, Robson MD, Holloway CJ, Rider OJ, Clarke K, Karamitsos TD, Neubauer S. Cardiac energetics, oxygenation, and perfusion during increased workload in patients with type 2 diabetes mellitus. Eur Heart J. 2016; 37(46):3461-9A.
14. Purvis LAB, Clarke WT, Biasiolli L, Valkovic L, Robson MD, Rodgers CT. OXSA: An open-source magnetic resonance spectroscopy analysis toolbox in MATLAB. Plos One. 2017; 12(9):e0185356.
15. Wilson G, Bryan J, Cranston K, Kitzes J, Nederbragt L, Teal TK. Good enough practices in scientific computing. Plos Comput Biol. 2017; 13(6):e1005510.
16. Wilson G, Aruliah DA, Brown CT, Chue Hong NP, Davis M, Guy RT, Haddock SHD, Huff KD, Mitchell IM, Plumbley MD, Waugh B, White EP, Wilson P. Best Practices for Scientific Computing. Plos Biol. 2014; 12(1):e1001745.
17. Hastie T, Tibshirani R, Friedman J. The elements of statistical learning: Springer; 2001.
18. Olivero JJ, Longbothum RL. Empirical fits to the Voigt line width: A brief review. J Quant Spectrosc Radiat Transfer. 1977; 17(2):233-6.

19. Danos M, Geschwind S. Broadening of Microwave Absorption Lines Due to Wall Collisions. Phys Rev. 1953; 91(5):1159-62.
20. Purvis LAB. Dynamic Human Cardiac 31P MRS at 7T [MChem]: University of Oxford; 2015.
21. Purvis LAB, Clarke WT, Biasiolli L, Robson MD, Rodgers CT. Linewidth Constraints in Matlab AMARES using per-Metabolite T2 and per-Voxel Delta B0. In the Proceedings of the 22nd Annual Meeting of ISMRM, Milan, Italy, 2014. p. 2885.
22. Schmid AI, Chmelík M, Szendroedi J, Krššák M, Brehm A, Moser E, Roden M. Quantitative ATP synthesis in human liver measured by localized 31P spectroscopy using the magnetization transfer experiment. NMR Biomed. 2008; 21(5):437-43.
23. Chmelik M, Považan M, Krššák M, Gruber S, Tkačov M, Trattnig S, Bogner W. In vivo 31P magnetic resonance spectroscopy of the human liver at 7 T: an initial experience. NMR Biomed. 2014; 27(4):478-85.

6. ^{31}P liver metabolite T_1 values at 7 T

6.1. Introduction

As was shown in Section 2.1.11, peak areas must be corrected for saturation effects when the spectrum is not acquired under fully relaxed conditions (i.e. $T_R > 5 \times T_1$). The correction of longitudinal relaxation in the steady state can be derived from Eq. [2.56]:

$$\text{Saturation factor} = \frac{\sin\theta \times (1 - e^{-\frac{T_R}{T_1}})}{1 - \cos\theta \cdot e^{-\frac{T_R}{T_1}}}$$

The T_R is known, and there are several possible methods to estimate the flip angle. Therefore, the only unknown is the relaxation times (T_1).

Several liver metabolite T_1 values at 7 T were determined by Chmelik et al. (1), but these did not include the phosphatidylcholine (PtdC), nicotinamide adenine dinucleotide (NAD$^+$), or uridine diphosphoglycerate (UDPG) peaks.

In order to quantify the concentrations of these metabolites in vivo, their T_1 values must be known. The 'gold-standard' method for T_1 determination is inversion recovery (IR) (2). This involves inverting the magnetization with a 180° pulse, waiting for a set amount of time (the TI or inversion time), and then exciting the magnetization into the transverse plane and recording an FID. This must be repeated several times with different TI values to give a recovery curve. In vivo, signal must be localized to avoid contamination from unwanted tissue e.g. skeletal muscle. There are several possible methods, such as 1D-ISIS (1), or CSI (3). For consistency with the protocol described in Chapter 4, a 3D-CSI based localization method was used.

Part of this chapter has been published in Purvis LAB, Clarke WT, Valkovič L, Levick C, Pavlides M, Barnes E, Cobbold JF, Robson MD, Rodgers CT. Phosphodiester content measured in human liver by in vivo ^{31}P MR spectroscopy at 7 tesla. Magn Reson Med. 2017; 78(6):2095-105.

6.2. Methods

6.2.1. Acquisition

The data was collected using a Look-Locker chemical shift imaging (LL-CSI) pulse sequence (3). The sequence diagram is detailed in Fig 6.1.

A 29.696 ms full passage hyperbolic secant (HS8) pulse with time-bandwidth product R = 24 was used for inversion, as described in Tannus and Garwood (4). This inversion pulse was followed by excitations and readouts at an inversion times (TIs) of 50 – 10050 ms at 500 ms intervals. After a 5.2 s gap, there were three further excitations and readouts. Both the inversion and excitations used maximal $\boldsymbol{B}_1^+$. The signals were localized to a $6 \times 6 \times 4$ acquisition-weighted CSI grid (interpolated to 8 x 8 x 8 by zero-padding of k-space) over a $200 \times 240 \times 270$ mm^3 FOV. The LL-CSI sequence was run twice in each subject, first with inversion at +666 Hz (relative to skeletal phosphocreatine (PCr)) and second at -584 Hz (relative to PCr). The inversion pulse bandwidth of 1020 Hz ensured that every metabolite of interest was inverted in at least one data set.

Each of the two acquisitions took 34 min 12 s. A BISTRO saturation band was placed over the skeletal muscle at the maximum voltage possible within SAR limits (5).

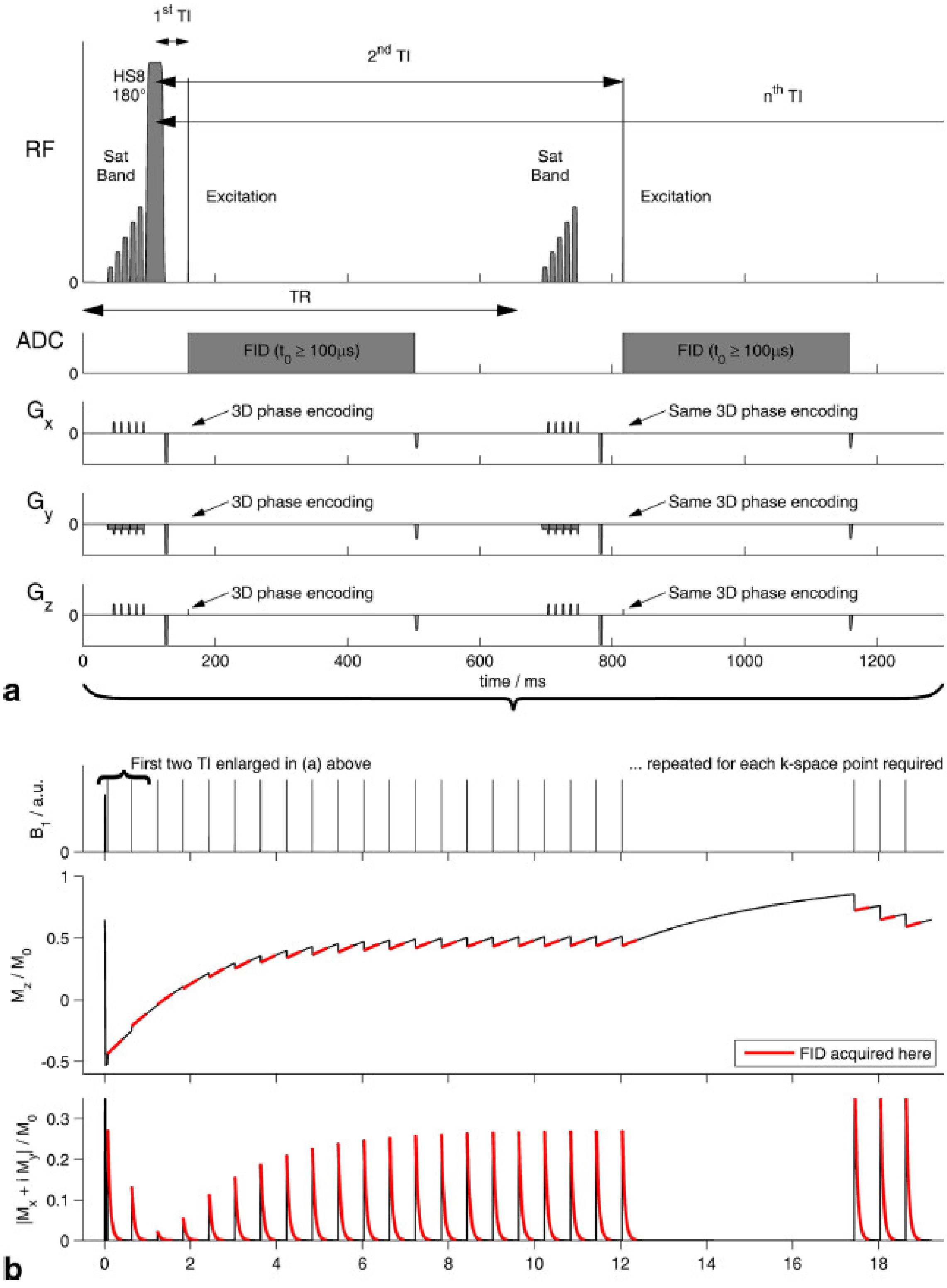

Fig 6.1. Look-Locker CSI sequence. (a) Look-locker chemical shift imaging (LL-CSI) pulse sequence diagram showing the first two T_I. **(b)** Simulated evolution of magnetization during a single T_R interval. From Rodgers et al. (3).

6.2.2. Analysis

For each voxel manually chosen for analysis, frequency-domain spectra were simulated for every TI and both inversions. The exact RF pulse waveforms and RF and ADC event timings for both inversion and excitation were used. Perfect spoiling after inversion and readout was assumed. A $T_2^{*'}$ term due to B_0 inhomogeneity was combined with individual T_2 values to give independent T_2^* terms for each peak. A Bloch simulation for each peak was separately performed in the time-domain and the results were summed. Multiplets were modelled with separate peaks with relative amplitude and frequency offset. The resultant FIDs were Fourier transformed to the frequency-domain and zero-order phase was applied.

These model spectra were fitted to the experimental spectra using the MATLAB function `lsqcurvefit`. Both model and experimental spectra were apodized to stabilize the fit. Bounds were applied to avoid unphysical fit variables, e.g. negative relaxation times and initial magnetization (M_0).

Table 6.1. List of Bloch simulation fitting steps for T_1 analysis.

Step	Fitting variables	MOLLI step	Inversion frequency relative to PCr
1	Voxel M_0 scaling factor and all peak T_2	Fully relaxed	+666Hz
2	All peaks M_0, acquisition phase.	Fully relaxed	+666Hz
3	RF scaling factor	All acquisitions	+666 and -584 Hz
4	All peaks M_0 and T_2	Fully relaxed	+666Hz
5	All peak T_1 and M_0	All acquisitions	+666 and -584 Hz
6	All peak parameters, RF scaling factor, and global zero order phase	All acquisitions	+666 and -584 Hz

Each fitting step used specific TIs, inversions, and fitting variables (see Table 6.1). The initial values for frequency, T_2 and zero-order phase were supplied by fitting the fully-relaxed spectrum from the +666 Hz experiment using unconstrained Lorentzian AMARES fitting, as described in the previous chapter. The initial M_0 of each voxel was manually matched to the spectrum.

At each step, Cramér-Rao lower bounds were calculated for the fitted variables (6).

6.2.3. Simulation

The accuracy and precision of the fitting method was investigated by simulation. The Bloch simulation described above was used to create model spectra at each TI. The simulation's experimental parameters matched the acquisition protocol, and typical values were used for each peak's frequency, T_2^*, and M_0. The T_1 values were taken from the literature (1). For PtdC, NAD$^+$, and UPDG, the T_1 values were 1.0, 2.0 and 2.5 s respectively.

To these perfect spectra, random normally distributed noise was added with ten different standard deviations logarithmically spaced between 0.1 and 100.

Metabolite frequency and T_2^*, and overall phase starting values were provided by AMARES fits. Metabolite M_0 and T_1, voxel M_0, and RF scaling starting values were taken from a normal distribution around the true value with a ten percent standard deviation. These values were chosen to simulate the errors that might be introduced for in vivo fitting.

At each fitting step and noise level, the bias from the true value, and standard deviation were calculated. The RMSE was then determined using Eq. [5.2].

The simulation was run for a lone singlet, a doublet, two overlapping peaks, and with the full spectrum.

The P_i peak was used to simulate a singlet, γ-ATP was used to simulate a doublet and PC and PE were chosen to simulate overlapping peaks. For each simulation, the M_0 of all other peaks was set to zero. In each fitting step, only the parameters that affected the peak or peaks of interest were allowed to vary. To speed up the simulation, at each step any peak with an M_0 of zero was not simulated. There were 100 repetitions at each of the ten noise levels.

The full simulation was only run with thirty repetitions at each noise level, as it took several times longer than the three other simulations. The begin time, i.e. the delay between excitation and acquisition used for the AMARES fit, was manually optimized to empirically fit the model fully-relaxed spectrum.

6.2.4. In vivo T_1 determination

Five male volunteers (28 ± 6 years, body mass index (BMI) 21.3 ± 2.9 $kg.m^{-2}$) were scanned. One voxel that was fully localized to the liver was manually selected per subject, considering the following criteria: resolution of the PtdC, PDE and PME regions, skeletal muscle contamination and SNR. Data were fitted as described above. The final step of each fit was manually inspected to ensure a high quality result.

6.3. Results

6.3.1. Simulation

6.3.1.1. Singlet

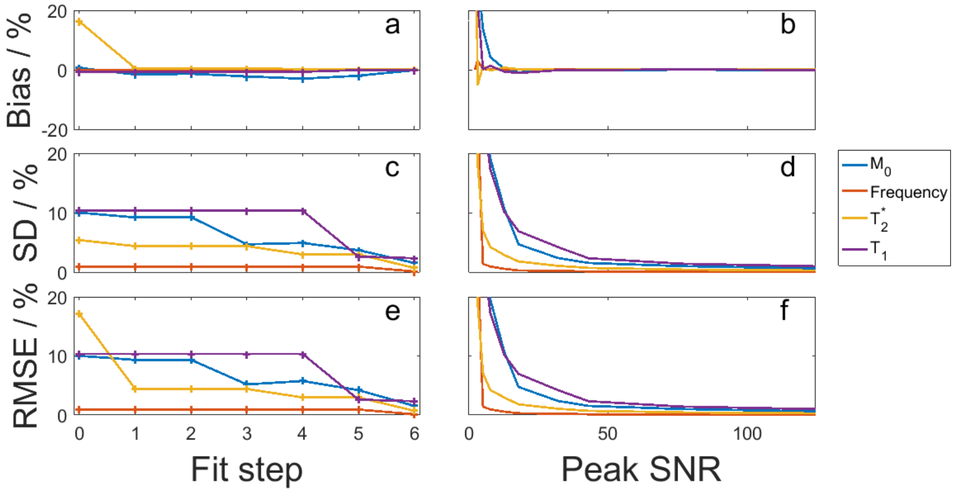

Fig 6.2. Singlet fitting error. (**a,c,e**) show variation with fitting step at an in vivo SNR (20-50), and (**b,d,f**) show variation with SNR after the final fitting step.

The bias, SD and RMSE error for a singlet are shown in Fig 6.2. In the in vivo SNR range (20 – 50), the bias in T_1 was -0.47%, the SD was 4.47% and the overall RMSE was 4.50%.

6.3.1.2. Doublet

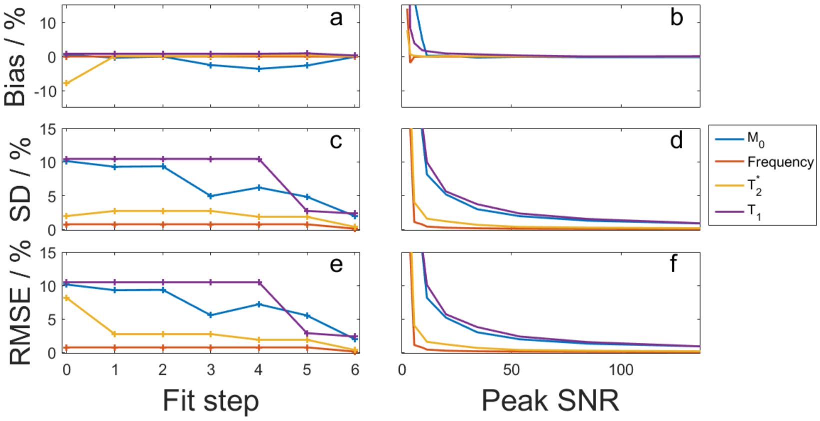

Fig 6.3. Doublet fitting error. (**a,c,e**) show variation with fitting step at an in vivo SNR (20-50), and (**b,d,f**) show variation with SNR after the final fitting step.

Fig 6.3 shows the fitting error for a doublet. In the in vivo SNR range, the bias was 0.61%, the SD was 5.03% and the overall RMSE was 5.07% for the T_1.

6.3.1.3. Overlapping peaks

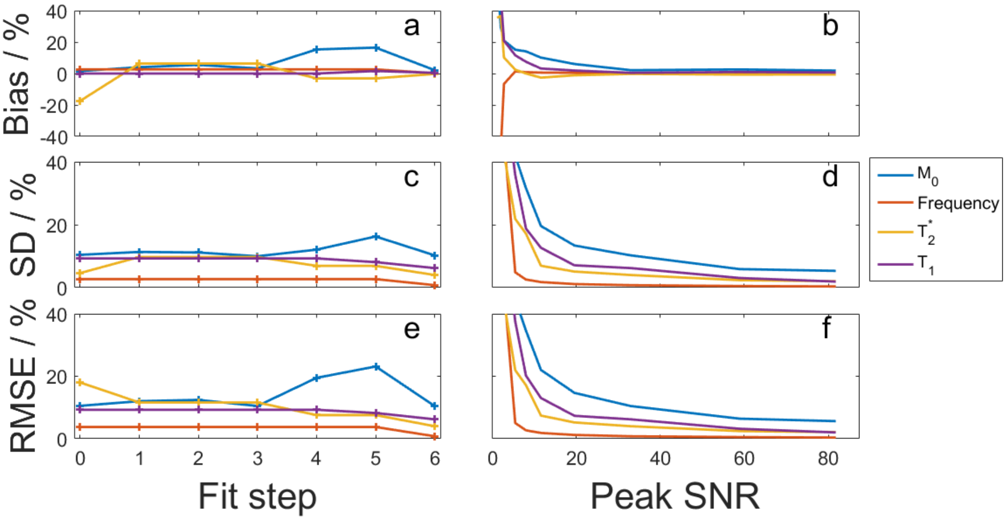

Fig 6.4. Fitting error for PC when overlapping with PE. (**a,c,e**) show variation with fitting step at an in vivo SNR (20-50), and (**b,d,f**) show variation with SNR after the final fitting step.

Fig 6.4 and Fig 6.5 show the fit error for two overlapping peaks PC and PE. In the in vivo SNR range, the bias in T_1 for PC was 0.97%, the SD was 6.82% and the overall RMSE was 6.92%. The bias for PE was -0.57%, the SD was 5.45% and the RMSE was 5.50%.

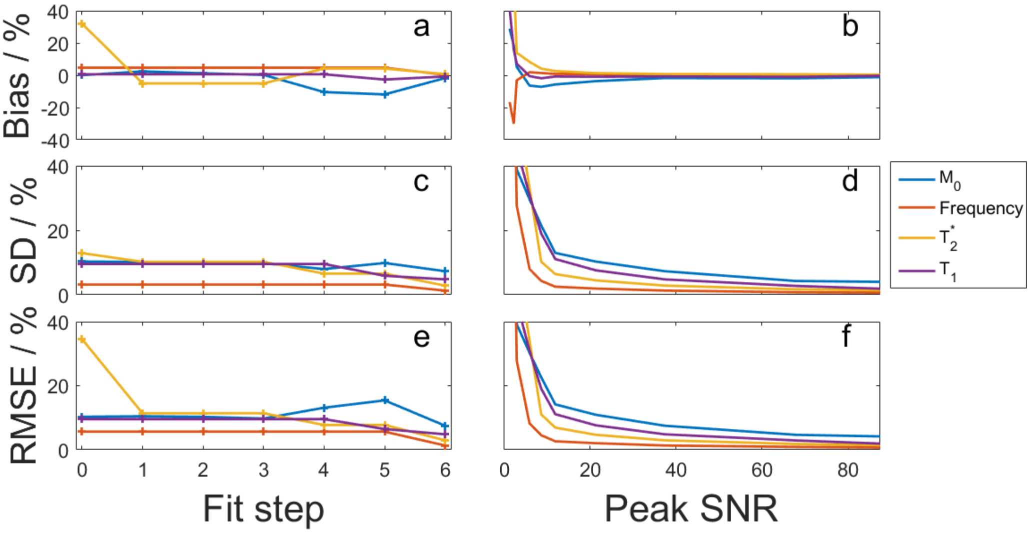

Fig 6.5. Fitting error for PE when overlapping with PC. (**a,c,e**) show variation with fitting step at an in vivo SNR (20-50), and (**b,d,f**) show variation with SNR after the final fitting step.

6.3.1.4. Full simulation

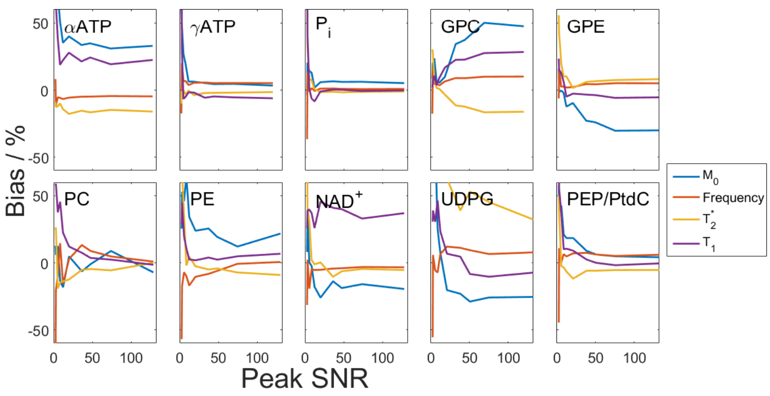

Fig 6.6. Full spectrum fitting bias. Peak parameter fit bias across SNR after the final fitting step.

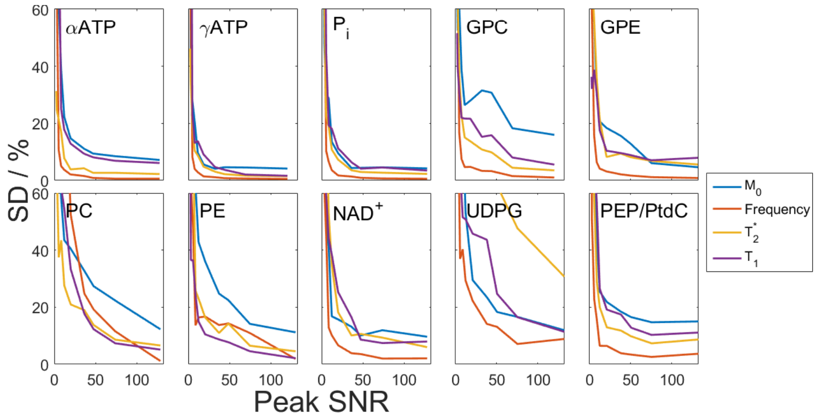

Fig 6.7. Full spectrum fitting SD. Peak parameter fit SD across SNR after the final fitting step.

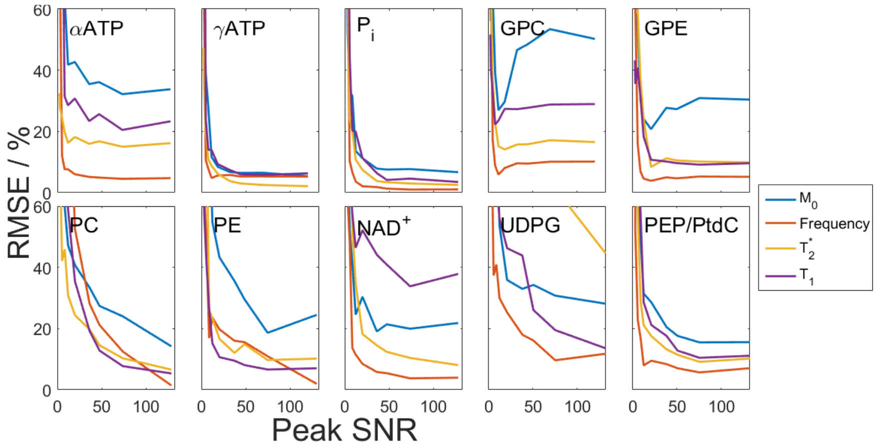

Fig 6.8. Full spectrum fitting RMSE. Peak parameter fit RMSE across SNR after the final fitting step.

Fig 6.6-8 show the bias, SD and RMSE for each peak after the final fitting step for every SNR. The mean values for the SNR range 20 to 50 (approximately in vivo values) are given in Table 6.2.

Table 6.2. Fitting error for simulated liver spectra in the in vivo SNR range

Metabolite	T_1 bias / %	T_1 SD / %	T_1 RMSE / %
α-ATP	8.29	7.17	11.00
γ-ATP	-2.60	3.90	4.72
P_i	0.54	5.44	5.57
GPC	7.12	10.70	13.03
GPE	-1.53	6.47	6.77
PC	5.92	10.19	11.92
PE	-1.81	8.84	9.09
PtdC	-3.25	13.57	14.05
NAD^+	-3.31	8.95	9.57
UDPG	5.03	28.28	29.14

6.3.2. In vivo

An illustration of the T_1 fitting method is given in Fig 6.9. Healthy human liver metabolite T_1 values from this study and the literature are reported in Table 6.3.

The full width half maximum PSF size of a single LL-CSI protocol voxel was 377 mL. The newly determined T_1 means ± standard deviations were: PtdC 1.05 ± 0.28 s, NAD^+ 2.0 ± 1.0 s, UDPG 3.3 ± 1.4 s. The T_1 for P_i was 1.34 ± 0.15 s, GPC was 3.9 ± 1.3 s, and GPE was 4.4 ± 1.1 s.

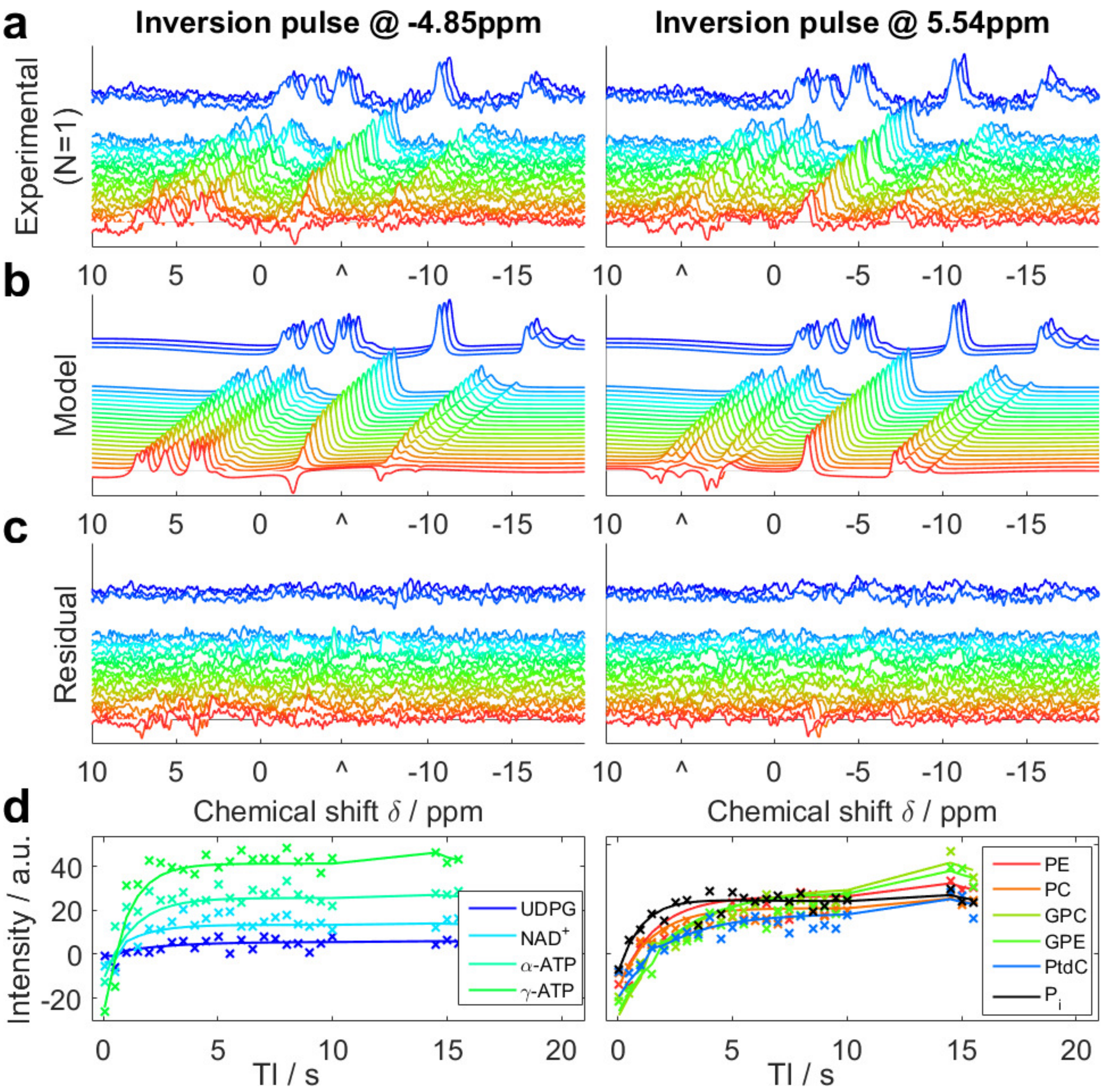

Fig 6.9. Illustration of ^{31}P Look-Locker CSI fitting for a typical set of liver data. (a) shows raw spectra from single voxel of a single subject. Each line shows a different TI, with a gap to indicate the break for magnetization recovery in the pulse sequence. (b) shows the model spectra that were fitted simultaneously to the experimental data. (c) shows the residual error after fitting. Panels (a)-(c) are plotted with the same scaling. '^' marks the central frequency of the inversion pulse. (d) shows the absolute intensity sampled at the fitted frequency of each metabolite. Each 'x' marks an experimental TI, and the lines show the simulated data. These panels are drawn to help interpret the spectra in (a)-(c), but were not used in the T_1 analysis. From Purvis et al. (7).

Table 6.3. In vivo T_1 values. Values from each subject are given with Cramer-Rao lower bounds of the fit. The mean and literature values are given with SD. * 7 T values from Chmelik et al. (1). ** 3 T value from Bierwagen et al.(8). *** 1.5 T value from Li et al. (9).

Metabolite	**Subject 1**	**Subject 2**	**Subject 3**	**Subject 4**	**Subject 5**	**Mean ± SD**	**Literature values**
α-ATP / s	0.66 ± 0.04	0.42 ± 0.04	0.55 ± 0.07	0.62 ± 0.09	0.55 ± 0.05	0.56 ± 0.09	0.46 ± 0.07*
γ-ATP / s	0.52 ± 0.03	0.82 ± 0.03	0.62 ± 0.04	0.46 ± 0.04	0.44 ± 0.03	0.57 ± 0.15	0.50 ± 0.08*
P_i / s	1.32 ± 0.07	1.40 ± 0.06	1.11 ± 0.09	1.51 ± 0.14	1.34 ± 0.10	1.34 ± 0.15	0.70 ± 0.33*
GPC / s	3.5 ± 0.4	3.8 ± 0.3	6.0 ± 3.6	3.7 ± 0.3	2.5 ± 0.3	3.9 ± 1.3	5.94 ± 0.73*
GPE / s	4.4 ± 0.3	4.0 ± 0.3	6.2 ± 1.9	3.4 ± 0.4	3.9 ± 0.3	4.4 ± 1.1	6.19 ± 0.91*
PC / s	1.5 ± 0.3	2.0 ± 0.2	1.8 ± 0.3	3.1 ± 0.6	2.9 ± 0.7	2.3 ± 0.7	3.74 ± 1.31*
PE / s	3.4 ± 0.3	3.9 ± 0.5	4.4 ± 1.0	5.4 ± 0.5	2.4 ± 0.3	3.9 ± 1.1	4.41 ± 1.55*
PtdC/ s	1.37 ± 0.25	1.09 ± 0.04	0.70 ± 0.04	1.25 ± 0.17	0.86 ± 0.03	1.05 ± 0.28	0.97 ± 0.30**
NAD^+ / s	1.3 ± 0.2	1.6 ± 0.2	1.0 ± 0.3	3.1 ± 0.5	3.2 ± 0.4	2.0 ± 1.0	2.0 ± 1.0***
UDPG / s	1.9 ± 0.8	1.9 ± 0.6	3.7 ± 1.3	5.0 ± 1.7	4.0 ± 1.4	3.3 ± 1.4	-

The error in T_1 determination is given in Fig 6.10. The P_i peak has the smallest inter-subject SD. UDPG has almost 20% higher CRLBs than any other peak, but the inter-subject SD is lower than NAD^+.

The CRLBs for GPC, GPE, PC and NAD^+ are significantly larger than the simulated SDs (F-test, $P < 0.05$ for each metabolite). The inter-subject SDs for γ-ATP, GPE, PtdC and NAD^+ are significantly larger than the CRLBs (F-test, $P < 0.05$).

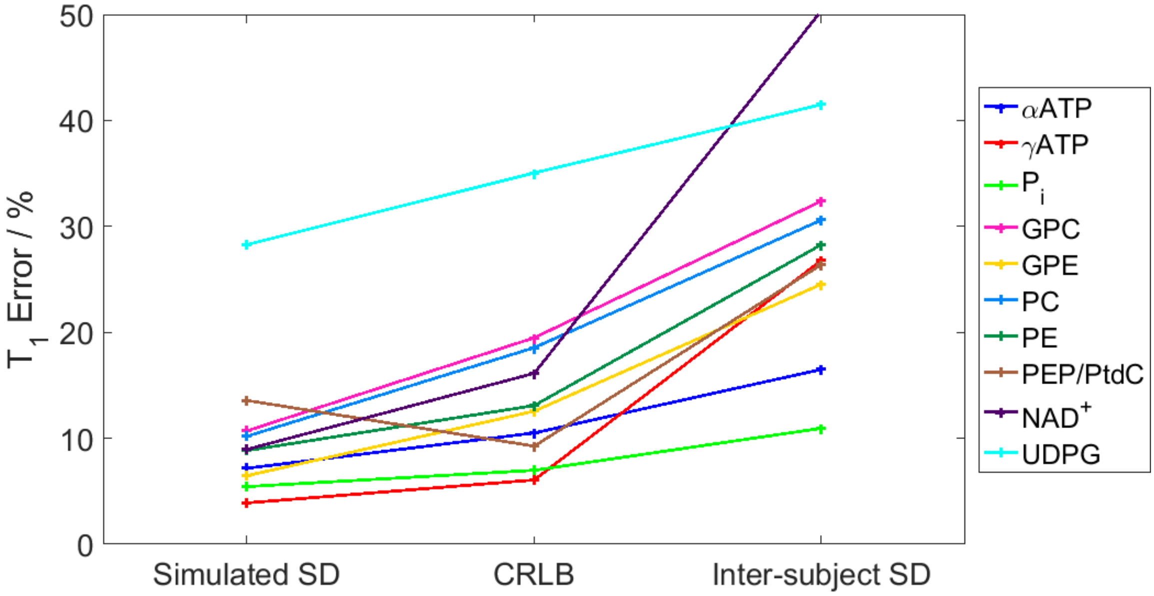

Fig 6.10. ***T_1* fitting error.** The SD from simulation was calculated from the 100 Monte-Carlo repetitions. The CRLB was calculated using the mean CRLB from the individual fits across subjects. The inter-subject SD was calculated from the final T_1 values for each of the 5 subjects.

6.4. Discussion

A LL-CSI protocol was used with a Bloch simulation fitting algorithm to fit the liver metabolite T_1 values of five subjects at 7 T. Monte Carlo simulation allowed investigation of the errors of the fitting method for single peaks, doublets, overlapping peaks and fully simulated liver spectra.

6.4.1. Simulation

Peak M_0, voxel M_0 scaling factor and RF scaling factor co-vary, which increased the overall M_0 error. The overall error is dominated by the SDs. These only increased at very low SNR; in the range of SNR seen in vivo, the overall RMSE for a singlet was only 4.50%. Due to long fitting times, it was not possible to run enough repetitions at each noise step for the initial SD to fully converge to 10% for each parameter. Some steps have little effect on the parameters, as the fitting is much simpler for a single peak than for many peaks.

The bias in the overlapping peaks are similar to each other, but mirrored. In order to compensate for the M_0 of one peak being slightly low, the other must be slightly higher. Overall, the fitting steps do well in reducing this error. In each step, the error is improved in at least one parameter. The RMSE was about the same for both peaks, 6.92% for PC, and 5.50% for PE.

Some of the differences in error between the three simulations in the in vivo SNR range can be attributed to differences in sampled SNRs. Although the noise levels are the same in the different simulations, the peaks have different M_0 values and linewidths.

The errors in the full simulation are larger than the independent simulations, as all peaks have some interaction with their neighbours. For example, while PE and PC overlap with each other in the same way as before, they also overlap with P_i, and their phase is dependent on all the other peaks. So the RMSE for PE is increased to 9.09% (from 5.50% in the independent simulation), and the RMSE of PC is increased to 11.92% (from 6.92%). These values are also affected by the difference in SNR, as in the full simulation the SNR of γ-ATP was used to calculate in vivo values, rather than SNR for individual peaks.

The in vivo CRLBs can be compared with the full simulation SDs. As the linewidths and chemical shifts are not significantly different between simulation and in vivo, the differences are largely from SNR. A slightly lower SNR in vivo would account for the general increase in CRLB compared to simulated SD. The relative difference in errors between metabolites is likely due to differences in relative SNR. For example, the fitted initial magnetization (and hence SNR) is higher for PtdC in vivo than in simulation (t-test, $P < 0.05$), which could account for the differences between simulated SD and CRLB seen for this peak.

Despite these differences in error between the in vivo and the simulated data, the simulations remain useful in optimizing both the acquisition and fitting parameters. In particular, the plots of error against SNR show that error quickly increases at lower SNRs. So although there may be benefits to improving the localization of the T_1 determination method, they are outweighed by the error the fitting introduces. On the other hand, using a larger voxel would not be feasible due to contamination from other tissue, despite the improved fitting with increased SNR.

6.4.2. In vivo

The volume calculated from the ellipsoid of the PSF at full width half maximum is 377 mL. This is similar to 3D ISIS volumes in the liver of 75 – 500 mL. Despite a time penalty compared to 3D ISIS, the 3D-CSI method was used to localize the T_1 measurements in order to be consistent with our main acquisition protocol.

The inter-subject SDs are all larger than the CRLBs, though the differences are only significant for γ-ATP, GPE, PtdC and NAD$^+$ (F-test, $P < 0.05$). This is likely to be due to a combination of two factors. First, the simulation did not perfectly match reality. There will be differences in e.g. chemical shift homogeneity and lineshape. And second, the T_1 values would be expected to have some normal range, even in healthy volunteers.

The 95% confidence intervals of our T_1 values and those in the literature overlapped for all metabolites except for P_i, GPE and GPC (1). The limited bandwidth of our inversion pulse meant that two inversions were required. Magnetization transfer could therefore have reduced the apparent T_1 of the P_i or ATP peaks. However, as the T_1 values were longer than those of Chmelik et al., this effect does not appear to be significant. Chmelik et al. performed two IR experiments, one optimized for short T_1 metabolites (eight TI values between 0.02-2 s) and the other for long T_1 metabolites (eight TI values between 0.1 – 20 s). The effective TI values in our study (twenty-four between 0.05 s and 15.55 s) are more optimally spaced for intermediate T_1 metabolites. This could be the cause of the differences seen in metabolite T_1 values. Valkovič et al. used eight TI values between 0.08 and 3 s, and reported an apparent T_1 of P_i with saturated γ-ATP of 0.77 ± 0.16 s (10). This is consistent with our result (P_i T_1 = 1.34 ± 0.15 s), as the true T_1 would be longer than the apparent T_1 under saturation. The three new metabolite T_1 values that we have measured all fall in the intermediate range, and our protocol should therefore give an accurate result. Furthermore, previously reported T_1 relaxation times at 1.5 T have shown shorter values for ATP, P_i, PME and PDE in human liver compared to those in calf muscle (11), and a similar effect can be seen at 3 T (12, 13). Extrapolating to 7 T, it could be expected that the average T_1 values for PDE should be shorter than 5.7 ± 1.5 s (13), which is consistent with our findings. Similarly, the T_1 of ATP should be shorter than 1.8 ± 0.1 s (13), and closer to the values seen in the liver at lower field strength (0.4 – 0.9 s) (9, 11, 12). It is perhaps surprising that T_1 values in the liver differ so much from those in skeletal muscle and prostate at 7 T. Further study will be required to determine the origins of this difference.

A Monte-Carlo simulation of propagation of error can be used to determine the effect of differences in T_1 or flip angle on saturation correction. For the flip angles expected in vivo, the SD on the T_1 values lead to a 2 – 15 % error on corrected amplitudes.

6.5. Summary

1. A 6 × 6 × 4 LL-CSI sequence was used to acquire inversion-recovery datasets for the determination of liver T_1 values.
2. Bloch simulations were used to analyse the data.
3. At in vivo SNR, the T_1 values are expected to have 5 – 29% fitting error.
4. In vivo T_1 CRLBs are 5 – 32%.
5. Inter-subject SDs were 11 – 50%.
6. The effect of error in T_1 on corrected amplitudes can be simulated each time saturation correction is calculated.
7. These errors are expected to contribute 2 – 15% of the error on the final corrected amplitudes.

6.6. References

1. Chmelik M, Považan M, Krššák M, Gruber S, Tkačov M, Trattnig S, Bogner W. In vivo 31P magnetic resonance spectroscopy of the human liver at 7 T: an initial experience. NMR Biomed. 2014; 27(4):478-85.
2. De Graaf RA. In vivo NMR spectroscopy: principles and techniques. 2nd ed. Chichester: John Wiley & Sons; 2007.
3. Rodgers CT, Clarke WT, Snyder C, Vaughan JT, Neubauer S, Robson MD. Human cardiac 31P magnetic resonance spectroscopy at 7 tesla. Magn Reson Med. 2014; 72(2):304-15.
4. Tannus A, Garwood M. Adiabatic pulses. NMR Biomed. 1997; 10(8):423-34.
5. Luo Y, de Graaf RA, DelaBarre L, Tannus A, Garwood M. BISTRO: An outer-volume suppression method that tolerates RF field inhomogeneity. Magn Reson Med. 2001; 45(6):1095-102.
6. Cavassila S, Deval S, Huegen C, van Ormondt D, Graveron-Demilly D. Cramér-Rao bounds: an evaluation tool for quantitation. NMR Biomed. 2001; 14(4):278-83.
7. Purvis LAB, Clarke WT, Valkovič L, Levick C, Pavlides M, Barnes E, Cobbold JF, Robson MD, Rodgers CT. Phosphodiester content measured in human liver by in vivo 31P MR spectroscopy at 7 tesla. Magn Reson Med. 2017; 78(6):2095-105.
8. Bierwagen A, Begovatz P, Nowotny P, Markgraf D, Nowotny B, Koliaki C, Giani G, Kluppelholz B, Lundbom J, Roden M. Characterization of the peak at 2.06ppm in P-31 magnetic resonance spectroscopy of human liver: phosphoenolpyruvate or phosphatidylcholine? NMR Biomed. 2015; 28(7):898-905.
9. Li CW, Negendank WG, Murphy-Boesch J, Padavic-Shaller K, Brown TR. Molar Quantitation of Hepatic Metabolites In Vivo in Proton-decoupled, Nuclear Overhauser Effect Enhanced 31P NMR Spectra Localized by Three-dimensional Chemical Shift Imaging. NMR Biomed. 1996; 9(4):141-55.
10. Valkovič L, Bogner W, Gajdošík M, Považan M, Kukurová IJ, Krššák M, Gruber S, Frollo I, Trattnig S, Chmelík M. One-dimensional image-selected in vivo spectroscopy localized phosphorus saturation transfer at 7T. Magn Reson Med. 2014; 72(6):1509-15.
11. Buchli R, Meier D, Martin E, Boesiger P. Assessment of absolute metabolite concentrations in human tissue by 31P MRS in vivo. Part II: Muscle, liver, kidney. Magn Reson Med. 1994; 32(4):453-8.
12. Schmid AI, Chmelík M, Szendroedi J, Krššák M, Brehm A, Moser E, Roden M. Quantitative ATP synthesis in human liver measured by localized 31P spectroscopy using the magnetization transfer experiment. NMR Biomed. 2008; 21(5):437-43.
13. Bogner W, Chmelik M, Schmid AI, Moser E, Trattnig S, Gruber S. Assessment of (31)P Relaxation Times in the Human Calf Muscle: A Comparison between 3 T and 7 T In Vivo. Magn Reson Med. 2009; 62(3):574-82.

7. Single loop absolute quantification

Absolute quantification requires the normalization and calibration of acquired and analysed signals. For array coils, this also involves careful consideration of the combination of signals from each of the receive channels. The problem involves the application of $\boldsymbol{B}_1^{\pm}$ field maps, which is complicated by the increasing $\boldsymbol{B}_1^{\pm}$ inhomogeneity at higher $\boldsymbol{B}_0$ (1).

In this chapter, the problem is simplified by considering the case of a 10 cm ^{31}P transceiver loop coil. Electromagnetic (EM) fields are simulated for the 10 cm loop to determine a set of requirements for a phantom for absolute quantification in the liver at 1.5 T, 3 T and 7 T. The simulations are validated in phosphate phantoms at 7 T, and field maps are acquired. Two methods that use phantom $\boldsymbol{B}_1^-$ maps for the correction of in vivo hepatic ^{31}P-MRS datasets are compared to phantom replacement (i.e. correcting for sensitivity using phantom CSI amplitudes).

7.1. Background

7.1.1. Normalization

The basic absolute quantification equation [1.2] is:

$$[\mathrm{m}] = n_\mathrm{m} c S_\mathrm{m} .$$

In this equation, for a metabolite m, n_m is a normalization constant, c is a calibration constant, and S_m is the amplitude from the analysed spectrum.

n_m can be broken down to:

$$n_\mathrm{m} = \frac{F\eta}{V} \qquad [7.1]$$

where F is the saturation-correction factor, η is the sensitivity-correction factor, and V is the voxel volume.

F is dependent on the T_R, T_1, and flip angle (i.e. the $\boldsymbol{B}_1^+$), and therefore varies between metabolites with different T_1 values. For a single loop, η is only dependent on the receive-sensitivity, i.e. $\boldsymbol{B}_1^-$, and does not vary between metabolites. V can be determined with a proper knowledge of the acquisition protocol. In other words, V can be calculated as the volume of the metabolite-containing tissue that falls within the acquisition volume (2).

Normalization therefore requires $\boldsymbol{B}_1^\pm$ maps. For X-nuclei, where SNR prohibits in vivo measurement of $\boldsymbol{B}_1^\pm$, the maps are typically acquired in phantoms. This assumes that the $\boldsymbol{B}_1^\pm$ is the same in the subject and in the phantom. At low field strengths, this assumption is only expected to introduce small errors for phantoms of approximately in vivo concentrations (3, 4). However, as field strength increases so does $\boldsymbol{B}_1^\pm$ inhomogeneity, so we would expect effect of material properties to become more important (1).

For a CSI acquisition, the application of the field map is complicated by the point spread function (PSF). This can be accounted for in three ways: a phantom replacement method could be used to account for the PSF inherently (Method 1); the $\boldsymbol{B}_1^\pm$ at the centre of each voxel could be used (Method 2); or a full PSF correction could be performed (Method 3). The background of these methods is described in the following sections, and they are applied in Section 7.3.3.

7.1.2. Calibration

To calculate calibration constant c from Eq [1.2], a reference is required. This reference can be either endogenous (internal), or exogenous (external). In either case, the signal must be normalized:

$$c = \frac{[\mathrm{R}]}{n_{\mathrm{R}} S_{\mathrm{R}}} = \frac{[\mathrm{R}]}{\frac{F_{\mathrm{R}} \eta_{\mathrm{R}}}{V_{\mathrm{R}}} S_{\mathrm{R}}} = \frac{V_{\mathrm{R}}}{F_{\mathrm{R}} \eta_{\mathrm{R}} S_{\mathrm{R}}} [\mathrm{R}] \qquad [7.2]$$

Substituting Eqs [7.1] and [7.2] back into Eq. [1.2] gives a full equation for calculating metabolite concentration (5, 6):

$$[\mathrm{m}] = \frac{S_{\mathrm{m}} F_{\mathrm{m}} V_{\mathrm{R}} \eta_{\mathrm{m}}}{S_{\mathrm{R}} F_{\mathrm{R}} V_{\mathrm{m}} \eta_{\mathrm{R}}} [\mathrm{R}] \qquad [7.3]$$

For an endogenous reference, V and η can be ignored, simplifying Eq. [7.3] to:

$$[\mathrm{m}] = \frac{S_{\mathrm{m}} F_{\mathrm{m}}}{S_{\mathrm{R}} F_{\mathrm{R}}} [\mathrm{R}] \qquad [7.4]$$

However, the concentration of an internal reference is typically unknown. This necessitates either assuming a normal value for the concentration, or reporting values as a direct ratio. An external reference concentration can be known precisely, and there is therefore no doubt about the source of the variation in reported metabolite concentrations.

7.1.3. Point spread function

Localization has several effects on the quantification of metabolite concentrations. The first is contamination; signal from an unwanted region (such as skeletal muscle) can be acquired with the desired signal from the liver. The second effect is related to the requirement for a volume-correction, which can be seen in Eq. [7.1]. If a sequence such as ISIS is used, the signal is equally localized to an entire voxel (ignoring chemical shift displacement artefacts), and the voxel boundaries are comparatively sharp (depending on the inversion pulse slice profile). However, for CSI the voxels are less sharply delineated. They are better described through the voxel point spread function (PSF). Although a simple volume correction can be applied if the sample is uniform, any inhomogeneity in spin density can make the correction much more challenging. Furthermore, $\boldsymbol{B}_1^{\pm}$ inhomogeneity means that even a uniform sample cannot be treated with a simple volume correction.

For inhomogeneous spin density, but uniform transmit and receive sensitivity, the reconstructed spin density ρ_{rec} is given by Eq. [2.61]:

$$\rho_{\mathrm{rec}}(r) = \int \rho_{\mathrm{true}}(s)\mathrm{PSF}(r-s)\mathrm{d}s \qquad [7.5]$$

where ρ is the spin density, r is each point in the reconstructed image and s is each point within the PSF.

If the spin density, coil transmit and receive profiles vary, the signal equation becomes:

$$\rho_{\mathrm{rec}}(r) = \int K_{\mathrm{sat}}(s)\boldsymbol{B}_1^{-}(s)\rho_{\mathrm{true}}(s)\mathrm{PSF}(r-s)\mathrm{d}s \qquad [7.6]$$

where K_{sat} is the saturation factor, i.e. $K_{\mathrm{sat}} = 1/F$.

Assuming ρ_{true} is constant, it can be determined by rewriting the equation:

$$\rho_{\mathrm{true}} = \frac{\rho_{\mathrm{rec}}(r)}{\int K_{\mathrm{sat}}(s)\boldsymbol{B}_1^{-}(s)\mathrm{PSF}(r-s)\mathrm{d}s} \qquad [7.7]$$

If the change in $\boldsymbol{B}_1^{\pm}$ at each point is much less than the change in the PSF, the equation reverts to a form comparable to Eq. [7.1]:

$$\rho_{\mathrm{true}} \approx \frac{F(r)\eta(r)\rho_{\mathrm{rec}}(r)}{V} \qquad [7.8]$$

where V is determined from the FWHM of the PSF. This assumption holds for small voxel sizes, or where $\boldsymbol{B}_1^{\pm}$ inhomogeneity is small. Neither of these is necessarily true for a ^{31}P CSI acquisition at 7 T.

7.2. Electromagnetic simulations

To explore the errors that are introduced due to material effects at different field strengths I used CST Studio Suite 2016 (CST AG, Darmstadt, Germany) to simulate $\boldsymbol{B}_1^{+}$ fields of a 10 cm loop coil centred above various phantoms (described below) and, separately, the livers and hearts of two "virtual human" voxel models, Laura and Gustav. In each case, the fields were simulated at 25.9, 49.9, and 120.3 MHz (i.e. 1.5, 3 and 7 T for ^{31}P). The coil was tuned to each frequency and matched to 50 Ω. The initial values were manually inputted based on the S-parameter and Smith charts, and then numerically optimized to minimize the S-parameter at the chosen frequencies. The $\boldsymbol{B}_1^{+}$ field was sampled along a line through the centre of the coil and phantom. These $\boldsymbol{B}_1^{+}$ profiles were normalized to a "reference fiducial" simulated 10 mm behind the face of the coil and then a ratio was taken compared to an average from the Laura and Gustav liver models. Finally the mean and standard deviation of the ratio values across the depth of the liver (40 – 120 mm) were calculated to give a single bias, standard deviation and RMSE for each simulation.

At 3 T, the difference between the human voxel models is small ($< 0.2\%$). At 7 T, it increases to 3.5%. These findings suggest that not only may it not be possible to use a simple phosphate phantom to correct for in vivo $\boldsymbol{B}_1^{\pm}$ inhomogeneity at > 7 T, but that $\boldsymbol{B}_1^{\pm}$ may have to be accounted for in a variety of representative body types, and perhaps even on a subject-by-subject basis.

7.2.1. Phantom size

The sharp boundary between phantom material and the surrounding air can cause edge effects, e.g. from reflected RF waves or dielectric resonances. Larger phantoms naturally reduce the relative importance of these effects (as less of the phantom is close to an edge). However, very large phantoms are unwieldy and are difficult to make and use. We therefore ran several simulations to determine the minimum phantom size necessary to avoid excessive edge effects. This was achieved by reducing the size of the phantom until the errors started to change from those found in a large phantom.

First, several simulations were run on a 300 × 300 × 150 mm^3 cuboidal phantom to select a conductivity to use for the following experiments. A conductivity of 0.45 Sm^{-1} was found to give minimal RMSE compared to the human voxel models at 7 T. Using this conductivity, a set of cylindrical phantoms were simulated, independently varying the depth (between 100 and 336 mm) and radius (between 125 and 350 mm). When varying depth, the radius was set to 350 mm, and when varying radius the depth was set to 336 mm.

The minimum depth with error matching (i.e. less than 1% change from) the 336 mm depth phantom was 200 mm (see Fig 7.1). The RMSE at 200mm depth was 2.4% for 1.5 T, 6.2% for 3 T, and 9.3% for 7 T. The minimum width with error matching the 350 mm width was 250 mm (see Fig 7.2). The RMSE at 250 mm depth was 1.7% for 1.5 T, 5.0% for 3 T, and 8.3% for 7 T.

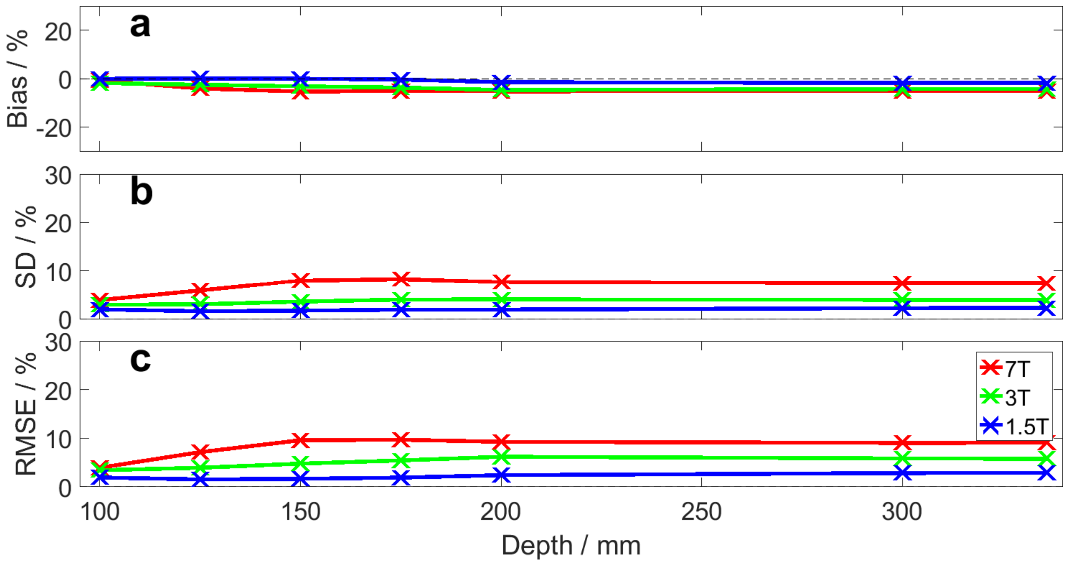

Fig 7.1. B_1^+ error for cylindrical phantoms of depths 100 – 336 mm. (a) shows the bias relative to the simulated human liver voxel models, (b) shows the SD, and (c) shows the RMSE.

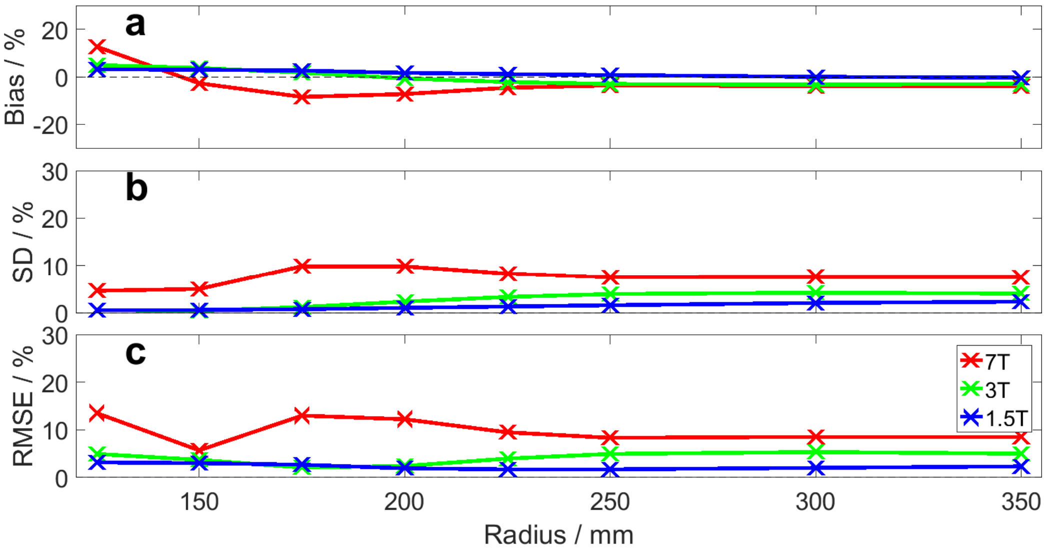

Fig 7.2. B_1^+ error for cylindrical phantoms of radii 125 – 250 mm. (a) shows the bias relative to the simulated human liver voxel models, (b) shows the SD, and (c) shows the RMSE.

The radius of the cylindrical phantom must be larger to have consistent errors than the depth. This is because the edges of the coil are 50 mm closer to the edge than the bottom. However, the error was lower for radius than for depth because the sides are curved, compared to the flat bottom of the phantom.

Based on the size simulations, a jerry can phantom of dimensions 280 × 280 × 450 mm^3 was selected. The size of the jerry can phantom was chosen to give consistent errors in simulation, rather than minimize errors. Ideally, there would be an iterative process across size and conductivity to find the perfect phantom. In practise, this is unreasonably time consuming, as a single simulation can take half a day to run, and relies on the simulations perfectly matching the “real world” results. It is easier to match conductivity than find a perfectly sized phantom. In addition, the perfect size varies from field strength to field strength. It is therefore better to choose a phantom size that gives consistent errors than to pick one that matches perfectly the in vivo values.

7.2.2. Phantom composition

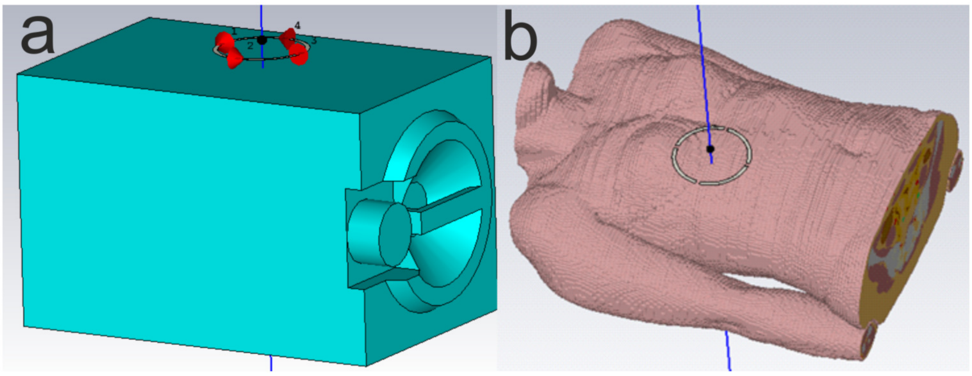

Fig 7.3. Setup of CST simulation. (a) shows the 10cm loop above the phantom. (b) shows the loop placement above the Laura voxel model.

A CST model of the selected jerry can phantom was made, and eleven conductivities between 0.02 and 2 Sm^{-1} were simulated. The setup in shown in Fig 7.3.

Table 7.1. Conductivities required at different field strengths, according to CST simulations.

Field strength	Conductivity for < 3% bias / Sm^{-1}	Conductivity for < 0.5% bias / Sm^{-1}	Crossing point / Sm^{-1}	Conductivity required to minimize RMSE / Sm^{-1}
1.5	0.23 - 0.86	0.57 - 0.66	0.62	0.6
3	0.39 - 0.58	0.47 - 0.50	0.48	0.45
7	0.34 - 0.42	0.37 - 0.38	0.38	0.35

Matching the phantom conductivity to liver tissue conductivity of 0.5 Sm^{-1} gives 1.5% error at 3 T and 10% error at 7 T, but it is possible to more closely match the in vivo values with slightly lower conductivities (see Table 7.1). This is likely due to the inhomogeneous nature of human tissue. The variation in $\boldsymbol{B}_1^+$ due to difference in conductivity and field strength is given in Fig 7.4.

Repeating the same analysis using the Laura and Gustav voxel models with the 10 cm loop placed above the heart as a reference, the required conductivities for minimal RMSE were slightly higher – 0.7 Sm^{-1} for 1.5 T, 0.6 Sm^{-1} for 3 T, and 0.5 for 7 T.

The permittivity of ionic solutions does not greatly vary from the permittivity of water at these concentrations (7). It may be possible to find an optimal combination of permittivity and conductivity, but this would further increase the complexity of the phantom. Different field strengths have different optimal conductivities. The difference between the field strengths could be due to the multiple different materials (e.g. muscle, fat and liver) within the in vivo model. For each field strength, both the bias and the SD are minimal at around the same conductivities, which means that there need be no trade-off between them.

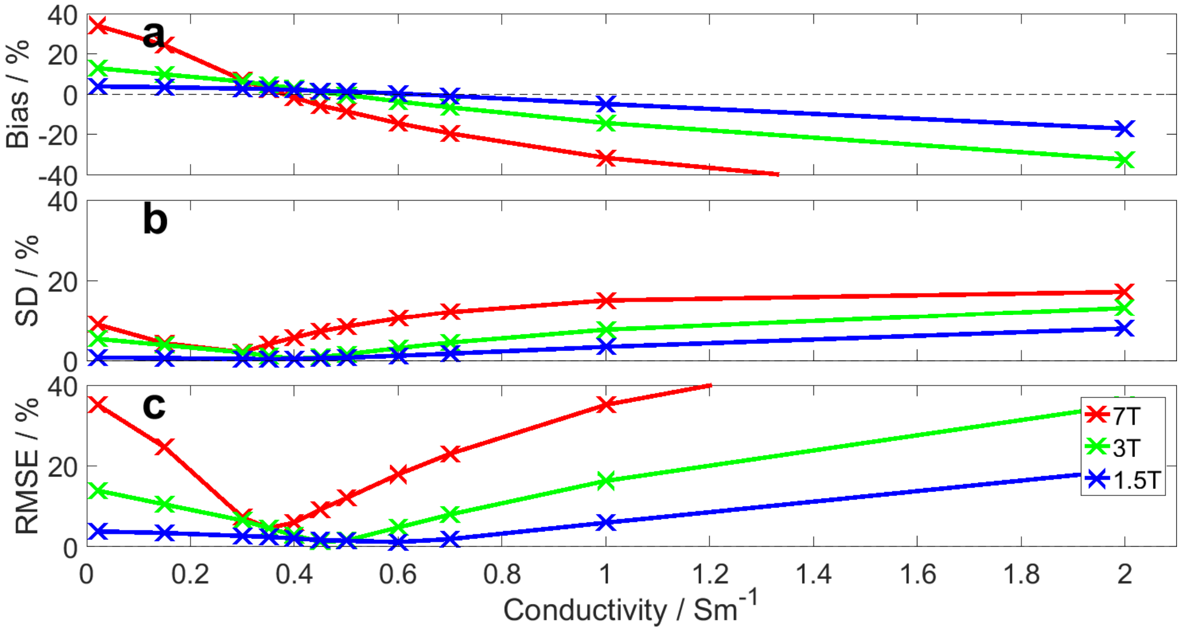

Fig 7.4. B_1^+ error vs human liver models for uniform phantoms of conductivity 0.02 – 2 Sm^{-1}. (a) shows the bias relative to the simulated human liver voxel models, (b) shows the SD, and (c) shows the RMSE.

7.3. Phantom

7.3.1. Conductivity determination

Six aqueous potassium phosphate ($K_2HPO_{4(aq)}$) phantoms were made up in 5.5 L cylindrical containers: 15, 18, 20, 30, 40 and 50 mM. For each phantom, a 10 cm loop was tuned and matched to 120.3 MHz (i.e. ^{31}P at 7 T). In a separate phantom of equal size, the concentration of a NaCl solution was increased until the S_{11} for the 10 cm loop matched that of one of the K_2HPO_4 solutions. The conductivity was then interpolated using data from Schwan et al. relating NaCl concentrations to RF conductivities (7). This procedure was repeated for each K_2HPO_4 solution. Static conductivities were calculated by interpolating data from Pethybridge et al. (8) and the CRC Handbook (9). The conductivity would be expected to increase at 120.3 MHz based on the Debye-Falkenhagen effect. Results are given in Table 7.2. Errors in the 120.3 MHz values were estimated based on the precision of matching the S-parameter using the K_2HPO_4 solution.

Table 7.2. Conductivities of various phosphate solutions. 120.3 MHz values are given with error based on estimated precision of matching the K_2HPO_4 solutions.

K_2HPO_4 concentration / mM	Static conductivity / Sm^{-1}	Conductivity at 120.3 MHz / Sm^{-1}
15	0.30	0.32 ± 0.02
18	0.35	0.36 ± 0.02
20	0.38	0.45 ± 0.02
30	0.54	0.52 ± 0.02
40	0.70	0.89 ± 0.02
50	0.86	1.09 ± 0.02

7.3.2. Field map determination

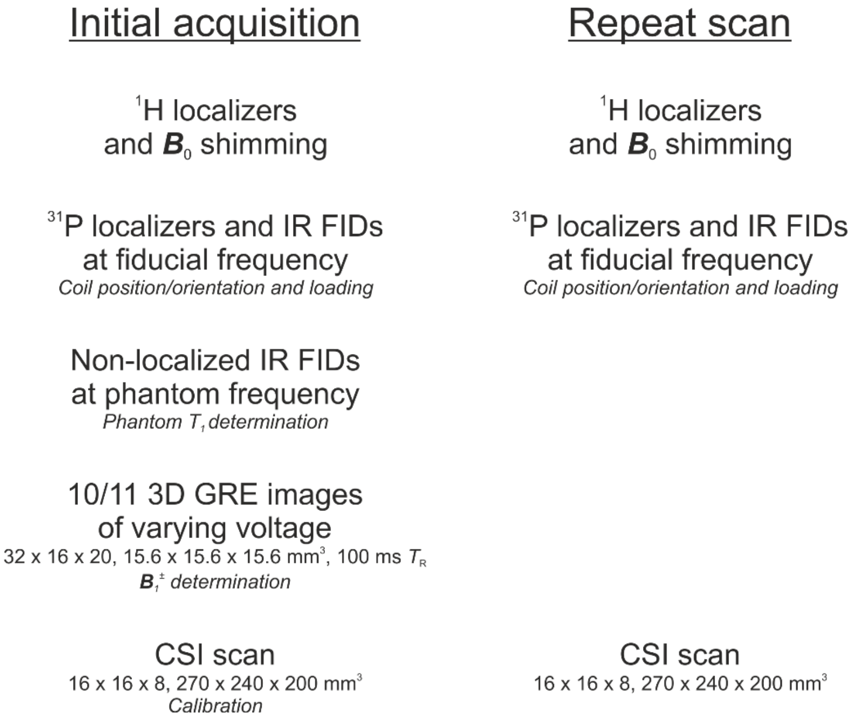

Fig 7.5. Full B_1 mapping protocol including repeat scan for testing.

7.3.2.1. Methods

Two phosphate phantom concentrations – 18 mM (0.36 $\mathrm{Sm^{-1}}$), and 40 mM (0.89 $\mathrm{Sm^{-1}}$) – were made up in 280 × 280 × 450 $\mathrm{mm^3}$ jerry cans.

The following data were acquired on a whole-body Siemens Magnetom 7 T system using a 10 cm ^{31}P loop coil following the protocol in Fig 7.5. The coil was placed on the centre of the jerry can phantom in the same way as in the CST simulations (see Fig 7.3). Coil location and loading was calculated using phenylphosphoric acid fiducials situated on the rear of the coil housing (10). The T_1 for each phantom was determined using non-localized inversion-recovery FID signals. Ten ^{31}P 3D gradient echo (GRE) images (32 × 16 × 20, 15.6 × 15.6 × 15.6 $\mathrm{mm^3}$, 100 ms T_R, 1 h 20 min total time scan per image) were acquired, each with a different transmit voltage between 2 and 270 V. Field maps were calculated using MATLAB's `lsqcurvefit` to fit the intensities acquired at various voltages to:

$$I(V) = \frac{a \sin bV \times (1 - e^{-\frac{T_R}{T_1}})}{1 - \cos bV \cdot e^{-\frac{T_R}{T_1}}} \quad [7.9]$$

Constant *a* is a complex number proportional to the receive sensitivity, and *b* is the number of degrees per volt at that pixel (i.e. the transmit field strength). Maps of *b* are then converted to $\boldsymbol{B}_1^+$ in Hz per volt by multiplication of the number of degrees flip angle per Hz calculated for the single-lobe sinc pulse used in the GRE acquisition.

7.3.2.2. Results and discussion

The T_1 mean ± fitting CRLB was 15.9 ± 1.19 s for the 18 mM phosphate phantom, and 7.8 ± 1.65 s for the 40 mM phosphate phantom.

The difference in the $\boldsymbol{B}_1^+$ field maps between 18 and 40 mM can be clearly seen in Fig 7.6, and the $\boldsymbol{B}_1^-$ field maps are depicted in Fig 7.7. The individual maps show the “twisting” that is expected of a $\boldsymbol{B}_1$ field in a conductive material at higher field strengths (1). The difference maps show that the error can be over 50% of the mean value. This would lead to significant errors if the wrong field map were applied during data processing.

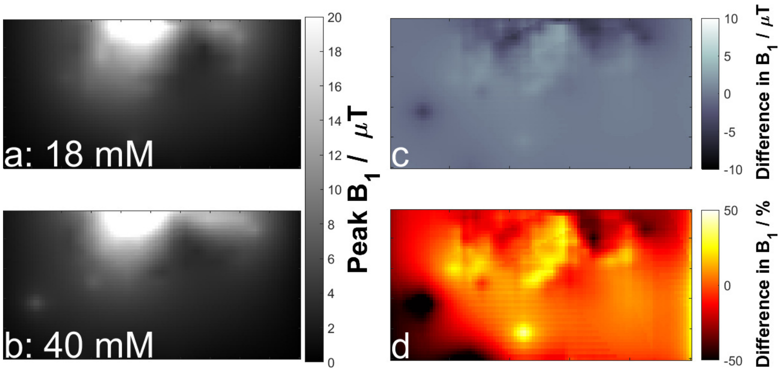

Fig 7.6. Phantom $\boldsymbol{B}_1^+$ Field maps. The field maps are sampled at a 4 × 4.5 mm^2 resolution over a 400 × 200 mm^2 field of view. (a) shows the $\boldsymbol{B}_1^+$ field map from the 18 mM phantom. (b) shows the field map from the 40 mM phantom. (c) shows the difference between the two maps in μT (i.e. (a) – (b)), and (d) shows the difference as a percentage of (a) at each pixel.

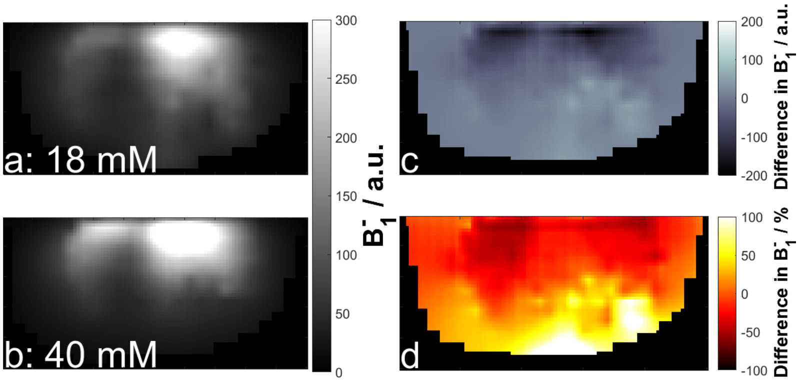

Fig 7.7. Phantom absolute B_1^- Field maps. The field maps are sampled at a 4 × 4.5 mm^2 resolution over a 400 × 200 mm^2 field of view. (a) shows the absolute B_1^- field map from the 18 mM phantom. (b) shows the field map from the 40 mM phantom. (c) shows the difference between the two maps in arbitrary units (i.e. (a) – (b)), and (d) shows the difference as a percentage of (a) at each pixel.

The B_1^+ profiles from the two phantoms are compared against CST simulations in Fig 7.8. For both the phantoms and the CST data, B_1^+ was averaged over a 1 × 1 cm^2 square at each depth and the B_1^+ for 270 V was determined (i.e. the maximum for the 10 cm loop). To account for loading, each profile was then scaled so that the reference voltage (i.e. B_1^+) at the position of the fiducial was identical.

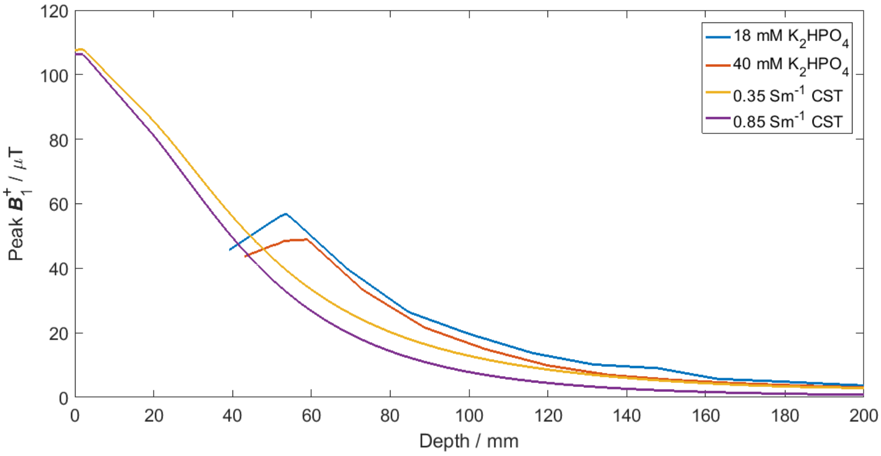

Fig 7.8. Simulated and phantom B_1^+ profiles. The profiles acquired in 18 mM and 40 mM K_2HPO_4 phantoms are plotted with the profiles from two CST simulations. The drop in phantom B_1^+ at the lowest depths is an artefact from the processing of the GRE images.

As is expected from simulation, the B_1^+ is lower in a higher conductivity medium, after loading is accounted for. Although the profiles do not perfectly match those in simulation, the 18 mM phantom would match the 0.35 Sm^{-1} profile if a scaling of 0.66 was used, thus the difference probably arises due to the differences in correcting simulated and phantom data. This would occur if, for example, the experimental fiducial is not in exactly the same relative position as in the CST simulation.

7.3.3. Field map application

Each queried coordinate is rotated and translated into the same coordinate system as the acquired field maps. Then, the field map is linearly interpolated onto the target coordinate. Coordinates outside the acquired field maps return NaNs (not-a-number). For the $\boldsymbol{B}_1^-$ maps, the magnitude and phases are interpolated separately. The CRLBs are also interpolated.

There are then two ways to apply the field maps: either correcting the data based on the $\boldsymbol{B}_1^\pm$ values at the centre of each voxel (i.e. assuming Eq. [7.8] holds), or by taking into account the full PSF (i.e. using Eq. [7.7]).

The flip angle can be determined by applying the $\boldsymbol{B}_1^+$ field map to simulated pulse profiles, and saturation correction can be worked out from Eq. [1.62]:

$$F = \frac{1}{K_{\text{sat}}} = \frac{1 - \cos\theta \cdot e^{-\frac{T_{\text{R}}}{T_1}}}{\sin\theta \times (1 - e^{-\frac{T_{\text{R}}}{T_1}})} \qquad [7.10]$$

The sensitivity correction, η, is given by:

$$\eta = \frac{1}{\sqrt{\boldsymbol{B}_1^{-*}\boldsymbol{B}_1^-}} \qquad [7.11]$$

After the CSI scan is acquired, each spectrum was analysed using the single peak Voigt lineshape AMARES fitting (as described in Chapter 5).

Three methods were used to correct the amplitudes (see Fig 7.9):

Method 1: Phantom replacement. The fitted amplitudes were corrected for saturation using the $\boldsymbol{B}_1^+$ at the central point of each voxel to calculate the flip angle, and then applying Eq. [7.10]. The corrected amplitudes were then divided by the corrected amplitude from the calibration scan, accounting for relative position and orientation of the coil, as well as coil loading.

Method 2: Central point $\boldsymbol{B}_1$ correction. The fitted amplitudes were corrected by using the $\boldsymbol{B}_1^+$ at the central point of each voxel to determine F (using Eq. [7.10]), the $\boldsymbol{B}_1^-$ at the central point of each voxel to determine η (using Eq. [7.11]), and then applying Eq. [7.8].

Method 3: PSF correction (i.e. using Eq. [7.7]).

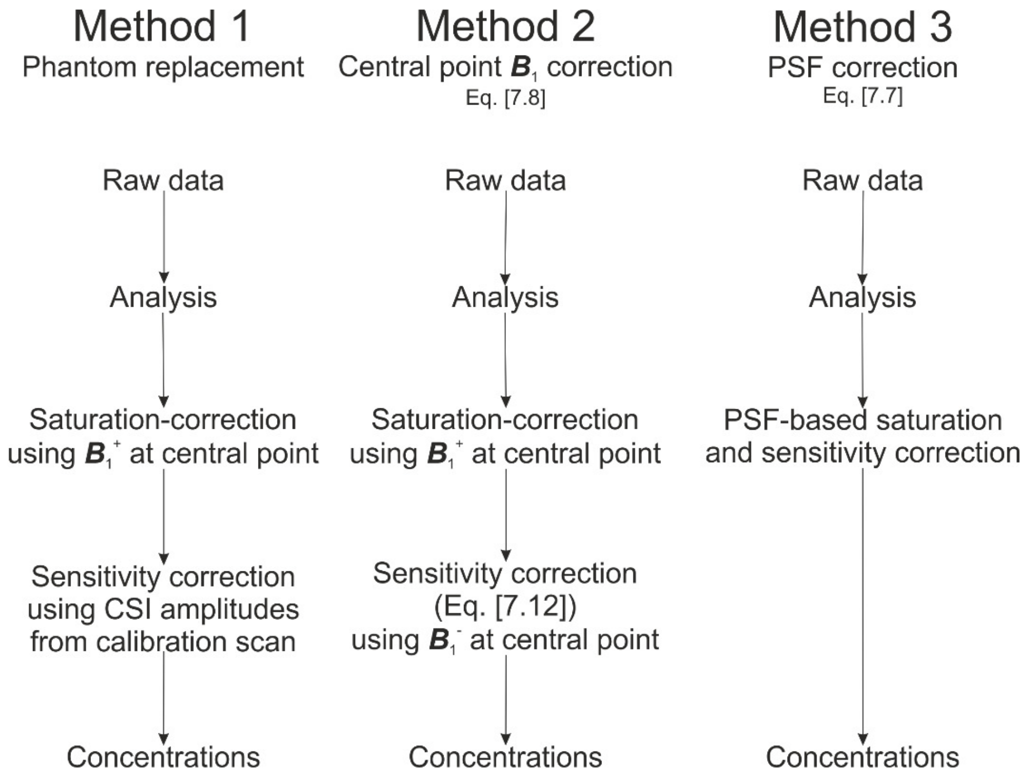

Fig 7.9. Three methods used for normalization and calibration of CSI data acquired using a 10 cm ^{31}P loop.

In each case, the resulting values were multiplied by the product of the CSI matrix size. This additional correction is required to undo an additional scaling from the Siemens Image Calculation Environment (ICE) online reconstruction software (in the `scale` function of `IceSpectro.cpp`), which is applied by the Siemens software so that the resulting intensities are similar for all matrix sizes. The concentration were then multiplied by the voxel volume, as calculated from the FWHM of the PSF.

7.3.4. Calibration and validation

To calibrate the sensitivity map, a 16 × 16 × 8 matrix of spectra over a 270 × 240 × 200 mm^3 field of view (i.e. matching the long in vivo protocol introduced in Chapter 4) was acquired in the same session as the GRE images (the "**calibration**" scan). The total time required for the acquisition of the field maps and data required for calibration was 20 hours. In a separate scan, a second 16 × 16 × 8 CSI matrix was acquired on the 18 mM phantom (the "**repeat**" scan, see Fig 7.5). Both scans were corrected using the three methods described in the previous section.

A calibration factor (*c* in Eq. [7.2]) was calculated for each method by scaling the mode of the corrected amplitudes from the initial scan to match the true concentration (i.e. 18 mM). These calibration factors were then applied to the second scans.

The top and bottom 10th percentiles were discarded. The bias, SD, and RMSE were then calculated, with the bias determined from the mean value (see Table 7.4 and Fig 7.10). A single transverse slice from the calibrated concentrations of each of the two scans corrected by three methods are shown in Fig 7.11.

Table 7.3. Error data from correction of UTE-CSI acquisitions of an 18 mM K_2HPO_4 phantom. The mean and SD of these data are plotted in Fig 7.10.

	Bias / mM	SD / mM	RMSE / mM
Method 1: phantom replacement			
Calibration scan	0 by definition		
Repeat scan	-1.85	2.16	2.85
Method 2: central point B_1 correction			
Calibration scan	1.02	4.07	4.20
Repeat scan	-1.35	4.20	4.41
Method 3: PSF correction			
Calibration scan	-0.41	3.98	4.00
Repeat scan	-2.15	3.87	4.43

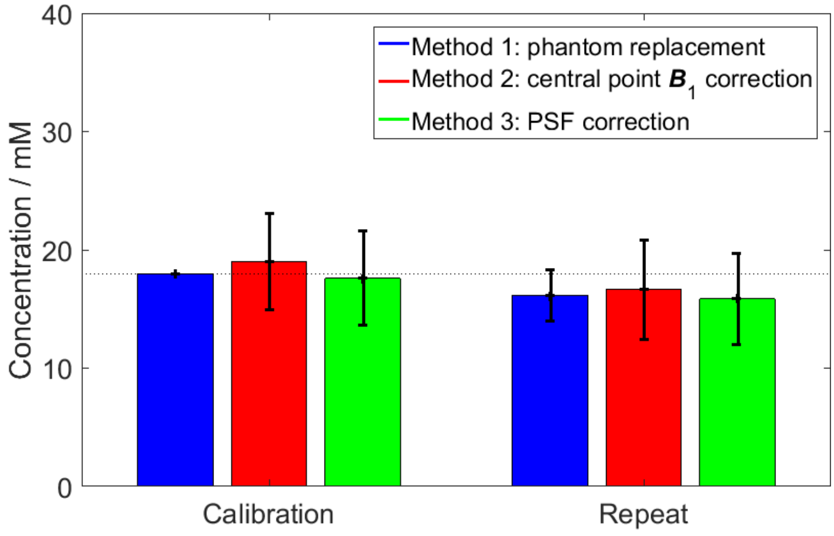

Fig 7.10. Mean and standard deviation of three correction methods (see Fig 7.9) for two UTE-CSI acquisitions. These data are also shown in Table 7.4.

There are clear differences between the two phantom replacement scans. There are two possible causes: either a difference in the transmit field map, or an error in the phantom replacement itself due to the small differences in scan setup. In Fig 7.11, it can be seen that the SD of 2.16 mM is spread over the phantom, rather than due to a few outlying points. For the transmit field map to cause this variation, there would need to be an average of 15% error in the calculated flip angles.

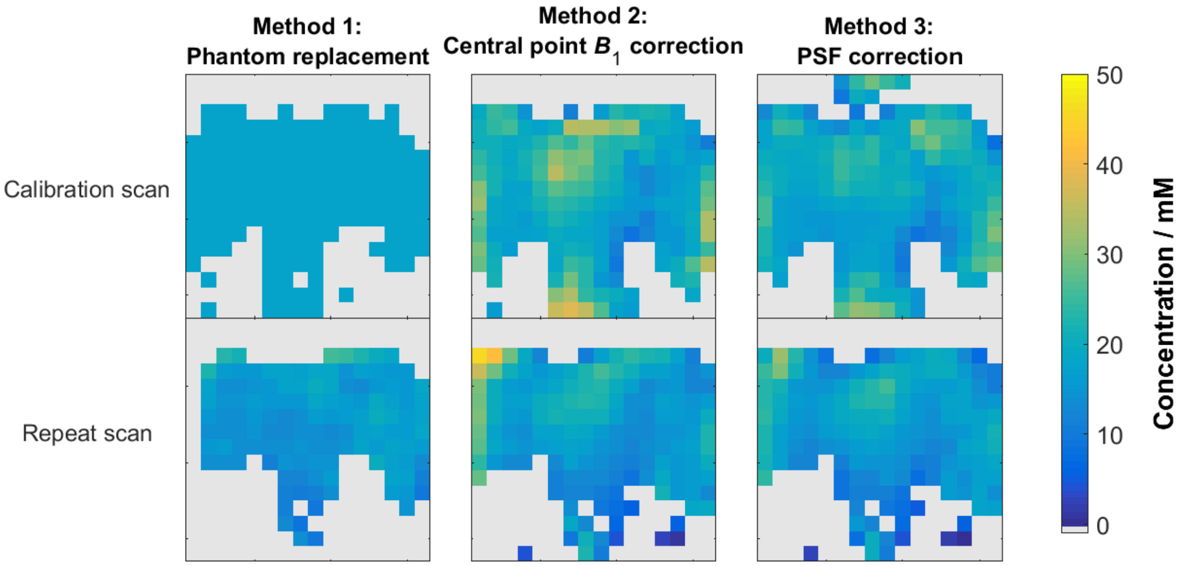

Fig 7.11. **The mid-transverse slice from two 16 × 16 × 8 UTE-CSI acquisitions of an 18 mM K_2HPO_4 phantom, with sensitivity-correction performed using three different methods.**

The difference between the mode and the mean of the scans causes apparent bias in the calibration scans themselves. This is particularly apparent in the central point correction. The PSF-corrected scans show slightly reduced SDs compared to the central point correction. However, they are not as low as the SDs for the phantom correction.

7.4. In vivo correction

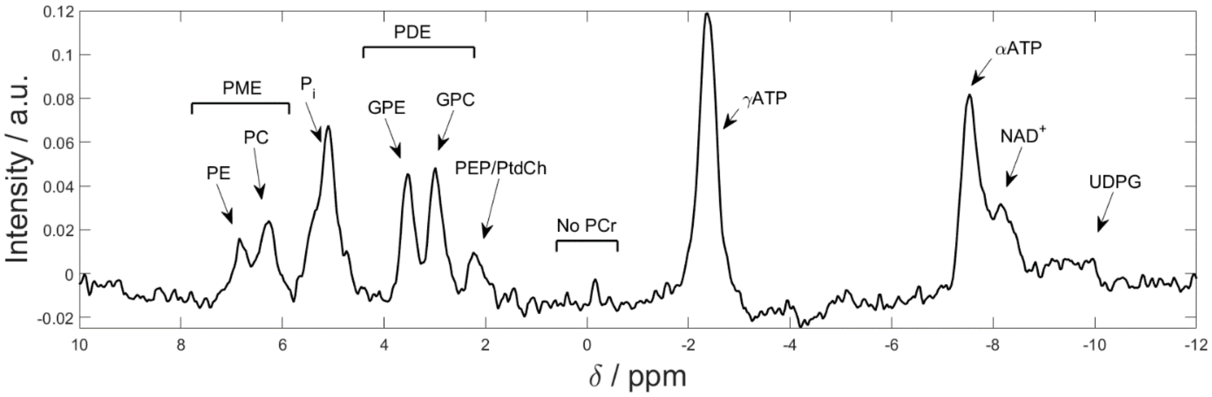

Fig 7.12. **Typical in vivo ^{31}P-MRS liver spectrum acquired at 7T.** Each of the peaks is labelled with its attributed metabolite. The β-ATP peak is at -16ppm, and is not shown here.

Four subjects (3M/1F, 26 ± 4 years, BMI 20.8 ± 3.2 kg.m^{-2}) were scanned at 7 T after an overnight fast, in accordance with guidelines from our local ethics committee. UTE-CSI spectra from within the liver were acquired with the long protocol described in Chapter 4, using the 10 cm ^{31}P loop for the main acquisition. In short: a 1s T_R, ten average acquisition-weighted UTE-CSI sequence was used to acquire a 16 × 16 × 8 matrix of liver spectra over a 270 × 240 × 200 mm^3 field of view in a total acquisition duration of 28 min.

Each spectrum (e.g. Fig 7.12) was analysed using the Voigt fitting with semi-constrained linewidths described in Chapter 5, and saturation- and sensitivity-corrected using field maps acquired using the 18 mM phosphate phantom. As in the phantom experiments, three correction methods were used: phantom replacement (Method 1), central point $\boldsymbol{B}_1$ correction (Method 2), and PSF correction (Method 3). A CRLB was calculated for each peak from the analysis of each spectrum and combined with the error arising from the normalization and calibration. The spectra were then processed to remove voxels with PCr concentration > 1 mmol/L wet tissue. The intra-subject standard deviation was calculated as the standard deviation of all the voxels used in the determination of the concentration.

The average corrected γ-ATP concentrations for the in vivo hepatic spectra are given in Table 7.4. The γ-ATP in vivo concentrations calculated using the 18 mM field map and calibration are at the low end (1.73 ± 0.32 mmol/L wet tissue) compared to literature values of 1.9 – 3.7 mmol/L wet tissue (3, 4, 11-14).

The mean CRLBs include the lowest bounds on all of the errors due to the analysis, normalization, and calibration of the signal. Correcting using the $\boldsymbol{B}_1$ at the central point (Method 2), the intra-subject SDs are not significantly different from the CRLBs ($P > 0.1$). This implies that the errors in the final concentrations are caused by a lack of precision in the field maps, as low accuracy in the field maps would increase the standard deviation in vivo.

Table 7.4. In vivo hepatic γ-ATP concentrations and errors. The concentrations are the mean from all subjects. The fitting CRLB and intrasubject SD are given as a mean ± SD across all subjects.

Method	γ-ATP intersubject mean ± SD / mmol/L wet tissue	γ-ATP mean CRLB / mmol/L wet tissue	γ-ATP intrasubject SD / mmol/L wet tissue
Method 1: phantom replacement	1.39 ± 0.30	0.12 ± 0.02	0.66 ± 0.21
Method 2: central point $\boldsymbol{B}_1$ correction	1.46 ± 0.23	0.43 ± 0.07	0.56 ± 0.06
Method 3: PSF correction	1.73 ± 0.35	0.13 ± 0.02	0.57 ± 0.16

There are several possible methods of improving the error on the final concentrations. For example, a more complex phantom may be used to more precisely match the in vivo $\boldsymbol{B}_1$ field. Or more time could be taken to acquire higher SNR data used for both the $\boldsymbol{B}_1^{\pm}$ maps and the calibration factor. However, the reduction in error for each individual improvement is marginal – 4 h additional time spent per voltage (i.e. 40 h for the whole acquisition) to double the SNR would only improve the error by 2%, according to Monte Carlo simulations. Similarly, higher resolution $\boldsymbol{B}_1^{\pm}$ data would reduce errors, but would again take significantly longer to acquire.

7.5. Summary

1. EM simulations predict a 3.5% difference between human voxel models at 7 T (an increase from 0.2% at 3 T), suggesting that this is a potentially significant source of error.

2. A jerry can phantom of dimensions 280 × 280 × 450 mm^3 was large enough to give good coverage of $\boldsymbol{B}_1^{\pm}$ maps, but was small enough to be easily usable while retaining errors matching larger phantoms in simulation.

3. Simulations determined that the uniform phosphate phantom that best matched in vivo $\boldsymbol{B}_1^{+}$ for human liver ^{31}P-MRS at 7T was a 0.35 Sm^{-1} phantom (18 mM $K_2HPO_{4(aq)}$).

4. In phantoms, full PSF $\boldsymbol{B}_1^{\pm}$ correction (Method 3) improves SDs by 1 – 2% compared to simply correcting for $\boldsymbol{B}_1^{\pm}$ at the central point (Method 2).

5. In phantoms, full PSF $\boldsymbol{B}_1^{\pm}$ correction (Method 3) gave 10% worse SD than phantom replacement (Method 1).

6. In vivo, the CRLB on the final concentration can be estimated by propagation of errors through each stage of the correction. Central point $\boldsymbol{B}_1^{\pm}$ correction (Method 2) gave significantly larger CRLB than full PSF correction (Method 3), matching the results in phantoms.

7.6. References

1. Vaidya MV, Collins CM, Sodickson DK, Brown R, Wiggins GC, Lattanzi R. Dependence of B1− and B1+ field patterns of surface coils on the electrical properties of the sample and the MR operating frequency. Concepts in Magnetic Resonance Part B: Magnetic Resonance Engineering. 2016; 46(1):25-40.
2. El-Sharkawy AM, Gabr RE, Schär M, Weiss RG, Bottomley PA. Quantification of human high-energy phosphate metabolite concentrations at 3 T with partial volume and sensitivity corrections. NMR Biomed. 2013; 26(11):1363-71.
3. Buchli R, Meier D, Martin E, Boesiger P. Assessment of absolute metabolite concentrations in human tissue by 31P MRS in vivo. Part II: Muscle, liver, kidney. Magn Reson Med. 1994; 32(4):453-8.
4. Chmelik M, Schmid AI, Gruber S, Szendroedi J, Krssak M, Trattnig S, Moser E, Roden M. Three-dimensional high-resolution magnetic resonance spectroscopic imaging for absolute quantification of P-31 metabolites in human liver. Magn Reson Med. 2008; 60(4):796-802.
5. Bottomley PA. NMR Spectroscopy of the Human Heart. In: Harris RK, Wasylishen RE, editors. Encyclopaedia of Magnetic Resonance. Chichester: John Wiley; 2009.
6. Bottomley PA, Hardy CJ, Roemer PB. Phosphate metabolite imaging and concentration measeurements in human heart by nucler magnetic resonance. Magn Reson Med. 1990; 14(3):425-34.
7. Schwan HP. Electrical Properties of Tissue and Cell Suspensions. In: John H L, Cornelius A T, editors. Adv Biol Med Phys. Volume 5: Elsevier; 1957. p. 147-209.
8. Pethybridge AD, Talbot JDR, House WA. Precise Conductance Measurements on Dilute Aqueous Solutions of Sodium and Potassium Hydrogenphosphate and Dihydrogenphosphate. J Solution Chem. 2006; 35(3):381-93.
9. CRC Handbook of Chemistry and Physics. 70th ed. Boca Raton, FL: CRC Press; 1989.
10. Rodgers CT, Clarke WT, Snyder C, Vaughan JT, Neubauer S, Robson MD. Human cardiac 31P magnetic resonance spectroscopy at 7 tesla. Magn Reson Med. 2014; 72(2):304-15.
11. Laufs A, Livingstone R, Nowotny B, Nowotny P, Wickrath F, Giani G, Bunke J, Roden M, Hwang J-H. Quantitative liver 31P magnetic resonance spectroscopy at 3T on a clinical scanner. Magn Reson Med. 2014; 71(5):1670-5.
12. Meyerhoff DJ, Karczmar GS, Matson GB, Boska MD, Weiner MW. Non-invasive quantitation of human liver metabolites using image-guided 31p magnetic resonance spectroscopy. NMR Biomed. 1990; 3(1):17-22.
13. Li CW, Negendank WG, Murphy-Boesch J, Padavic-Shaller K, Brown TR. Molar Quantitation of Hepatic Metabolites In Vivo in Proton-decoupled, Nuclear Overhauser Effect Enhanced 31P NMR Spectra Localized by Three-dimensional Chemical Shift Imaging. NMR Biomed. 1996; 9(4):141-55.
14. Rajanayagam V, Lee RR, Ackerman Z, Bradley WG, Ross BD. Quantitative P-31 MR spectroscopy of the liver in alcoholic cirrhosis. J Magn Reson Imaging. 1992; 2(2):183-90.

8. Phased array absolute quantification

In this chapter, absolute quantification will be considered in the context of phased arrays. Although $\boldsymbol{B}_1^{\pm}$ maps can be acquired as I showed for the 10 cm loop in Chapter 7, coil combination requires proper phasing of the spectra from individual channels. Therefore, we will start by discussing the problem of determining the $\boldsymbol{B}_1^{-}$ phase.

Once the $\boldsymbol{B}_1^{\pm}$ has been determined, potential coil combination and normalization methods will be selected. First, methods using $\boldsymbol{B}_1^{\pm}$ at the central point of each voxel are considered. Then methods correcting for the PSF will be proposed. Finally, the limitations on the use of phantom replacement for phased arrays are discussed.

Four different data-processing methods are tested in phantoms, and one is selected for testing in the full in vivo processing pipeline. The results of the in vivo comparison to an endogenous γ-ATP reference will be given in Chapter 9.

8.1. $\boldsymbol{B}_1$ determination for arrays

As in the case for a single loop which was considered in Chapter 7, the $\boldsymbol{B}_1^{+}$ from the transmit loop of our ^{31}P array coil can be computed from a series of ^{31}P GRE images of the 18 mM jerry can phosphate phantom using Eq. [7.6]. $\boldsymbol{B}_1^{-}$ magnitude can be determined using the series of GRE images for each receive coil. However, the determination of the phase of $\boldsymbol{B}_1^{-}$ for each receive channel is more complicated.

8.1.1. $\boldsymbol{B}_1$ phases

To combine spectra from different channels using $\boldsymbol{B}_1^{-}$ (as described in Section 8.2), the relative phase at each voxel must be known. However, the phase in the GRE images has contributions from several other factors, such as $\boldsymbol{B}_0$ inhomogeneity and the $\boldsymbol{B}_1^{+}$ from the transmit loop. For a head or knee coil, several assumptions can be made using e.g. symmetry arguments, which allow the cancellation of individual phase terms, and leaving the relative phase (1). However, these assumptions are not possible with a flexible 16 channel array, as the channels are not symmetrical in the same way as for a head coil.

Another route to the determination of the $\boldsymbol{B}_1$ phase would be to fit it by assuming that the channel specific phase is identical, after rotation and repositioning. However, this requires fitting the whole phase map simultaneously, rather than pixel by pixel as is done for the $\boldsymbol{B}_1^+$ maps. This method of fitting would be computationally expensive, and impractical to implement.

We are therefore unable to correctly compute the relative phases of the $\boldsymbol{B}_1^-$ for each channel, and the combination method must be chosen accordingly.

8.1.2. $\boldsymbol{B}_1$ map acquisition

Data from the 280 × 280 × 450 mm^3, 18 mM $KH_2PO_{4(aq)}$ jerry can phantom were acquired on the whole-body Siemens Magnetom 7 T system using the ^{31}P 16 channel array in the same fashion as for the 10 cm loop (described in Chapter 7). Coil position and loading was calculated using phenylphosphoric acid fiducials (7). The T_1 for the phantom was determined using non-localized inversion-recovery FID signals. Eleven ^{31}P 3D GRE images (32 × 16 × 20, 15.6 × 15.6 × 15.6 mm^3, 100 ms T_R, 1 h 20 min total time per image) were acquired with varying voltages between 1 and 530 V. Field maps were calculated using MATLAB's `lsqcurvefit` to fit the intensities acquired at various voltages to:

$$I(V) = \frac{a \sin bV \times (1 - e^{-\frac{T_R}{T_1}})}{1 - \cos bV \cdot e^{-\frac{T_R}{T_1}}} \qquad [8.1]$$

Constant *a* is a complex number proportional to the combined receive sensitivity, and *b* is the number of degrees per volt at that pixel (i.e. the transmit field map). The maps are then converted to $\boldsymbol{B}_1^+$ in Hz per volt by multiplication of the number of degrees flip angle per Hz calculated for the specific pulse used in the GRE acquisition. Receive sensitivity maps were calculated for each channel by fitting Eq. [8.1] to the uncombined GRE images, and fixing *b* to match the value determined using the combined images.

The $\boldsymbol{B}_1^+$ profiles through the centre of the coil are shown in Fig 8.1 in comparison to the profile for the 10 cm ^{31}P loop. As expected, the array has lower peak $\boldsymbol{B}_1^+$, but remains fairly constant over the depths measured.

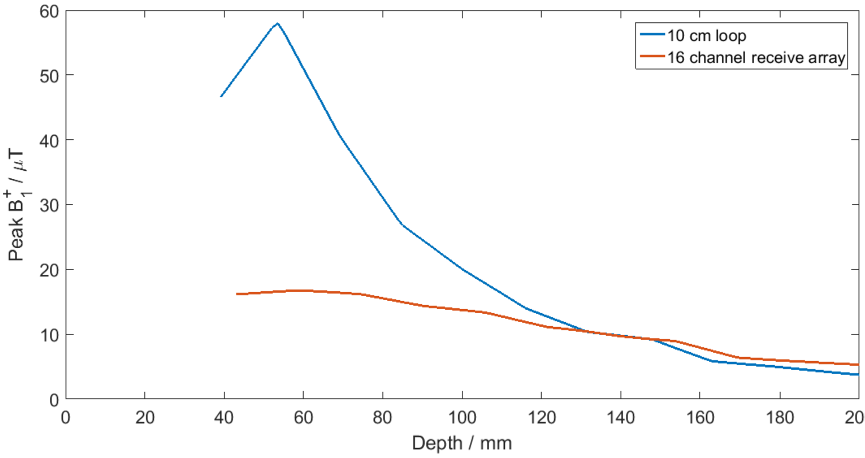

Fig 8.1. Phantom $\boldsymbol{B}_1^+$ profiles. The profiles acquired in an 18 mM $KH_2PO_{4(aq)}$ phantom for the 16 channel receive array (in blue) are plotted with for the 10 cm loop (in red).

The receive profiles for each channel are shown in Fig 8.2. The figure shows a central, transverse slice. The $\boldsymbol{B}_1^-$ is localized to a small region, and drops away quickly further from the coil.

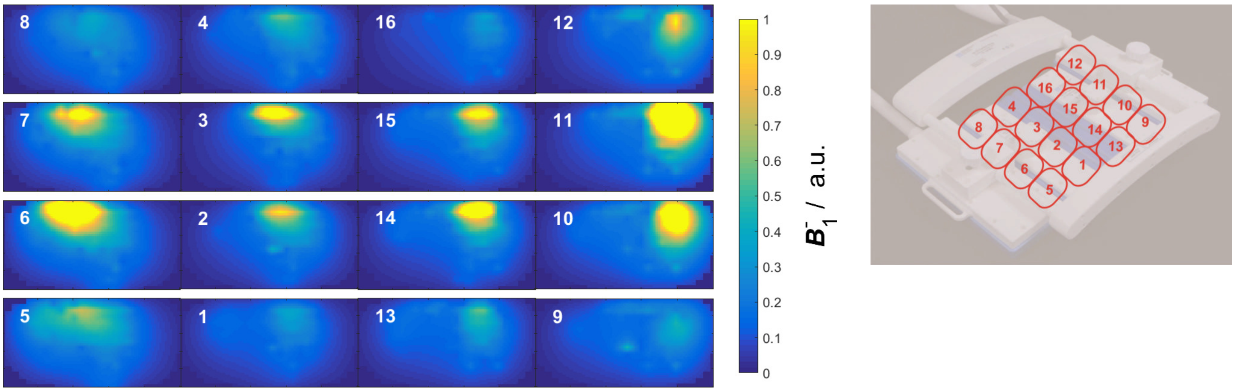

Fig 8.2. Array B_1^- profiles. Receive sensitivity profiles acquired in an 18 mM $KH_2PO_{4(aq)}$ phantom for the 16 channel receive array. Each subplot shows the transverse slice through the centre of the phantom for a single receive channel. The plots have been ordered to match the arrangement of channels within the array (see photo on the right).

8.2. Coil combination using central point B_1^-

In general, there are two types of coil combination: uniform noise and uniform sensitivity (2). Using a form of the Roemer formula (2), extended for spectroscopy (3), the uniform noise spectrum with maximal SNR is given by:

$$P(\boldsymbol{r},\delta)=C\frac{\hat{\boldsymbol{p}}(\boldsymbol{r},\delta)^{\mathrm{T}}(\boldsymbol{\Psi}^{-1})^{*}\hat{\boldsymbol{b}}(\boldsymbol{r})^{*}}{\sqrt{\hat{\boldsymbol{b}}(\boldsymbol{r})^{\dagger}(\boldsymbol{\Psi}^{-1})^{*}\hat{\boldsymbol{b}}(\boldsymbol{r})}} \tag*{[8.2]}$$

Where P is the combined complex-valued point in voxel $\boldsymbol{r}$ at chemical shift δ, C is an arbitrary constant, $\hat{\boldsymbol{p}}$ is the column vector of points from each element, $\boldsymbol{\Psi}$ is the noise covariance matrix, and $\hat{\boldsymbol{b}}$ is the column vector of the receive field $\boldsymbol{B}_1^-$ for each element. $^{\mathrm{T}}$ denotes the transpose, * the conjugate, and † the conjugate transpose.

$$\boldsymbol{\Psi}=\left\langle\left(\hat{\boldsymbol{n}}-\langle\hat{\boldsymbol{n}}\rangle_{\mathrm{time}}\right)\left(\hat{\boldsymbol{n}}-\langle\hat{\boldsymbol{n}}\rangle_{\mathrm{time}}\right)^{\dagger}\right\rangle_{\mathrm{time}} \tag*{[8.3]}$$

can be measured robustly for a 16 element array from $> 10^5$ noise samples $\hat{\boldsymbol{n}}$.

Uniform noise combination methods are commonly used in X-nuclear spectroscopy as no prior knowledge of coil $\boldsymbol{B}_1^-$ is required (3). But the amplitudes that are determined by analysing uniform noise spectra have an unknown scaling relative to metabolite concentrations. To quantify metabolite concentrations ("absolute quantification") the uniform sensitivity scaling must be used instead. The uniform sensitivity formula is given by:

$$P(\boldsymbol{r},\delta_l) = C\frac{\hat{\boldsymbol{p}}(\boldsymbol{r},\delta_l)^{\mathrm{T}}(\boldsymbol{\Psi}^{-1})^{*}\hat{\boldsymbol{b}}(\boldsymbol{r})^{*}}{\hat{\boldsymbol{b}}(\boldsymbol{r})^{\dagger}(\boldsymbol{\Psi}^{-1})^{*}\hat{\boldsymbol{b}}(\boldsymbol{r})} \qquad [8.4]$$

In order to split up this problem, Eq. [8.4] can be rewritten as:

$$P(\boldsymbol{r},\delta) = \hat{\boldsymbol{p}}(\boldsymbol{r},\delta)^{\mathrm{T}}\boldsymbol{W}(\boldsymbol{r})\boldsymbol{\eta}(\boldsymbol{r}) \qquad [8.5]$$

where

$$\boldsymbol{W}(\boldsymbol{r}) = C\frac{(\boldsymbol{\Psi}^{-1})^{*}\hat{\boldsymbol{b}}(\boldsymbol{r})^{*}}{\sqrt{\hat{\boldsymbol{b}}(\boldsymbol{r})^{\dagger}(\boldsymbol{\Psi}^{-1})^{*}\hat{\boldsymbol{b}}(\boldsymbol{r})}} \qquad [8.6]$$

is the vector of the weightings $w(\boldsymbol{r},k)$ of each element k and

$$\boldsymbol{\eta}(\boldsymbol{r}) = \frac{1}{\sqrt{\hat{\boldsymbol{b}}(\boldsymbol{r})^{\dagger}(\boldsymbol{\Psi}^{-1})^{*}\hat{\boldsymbol{b}}(\boldsymbol{r})}} \qquad [8.7]$$

represents the vector of per-voxel sensitivity correction.

Splitting up the problem in this way allows the opportunity for using a uniform noise method to calculate $\boldsymbol{W}$, and a separate method for calculating $\boldsymbol{\eta}$.

The optimal $\boldsymbol{W}$ should be given by the highest SNR uniform noise combination method. This was considered in simulation for an 8 channel cardiac array at 3 T by Rodgers and

Robson (3). They compared various data-driven and Roemer-based methods, including Whitened Singular Value Decomposition (WSVD (4)) and Roemer combination using simulated $\boldsymbol{B}_1^-$ maps from a 14 L of 73 mM $\mathrm{NaCl}_{(aq)}$ phantom. Rodgers and Robson found that, for reasonable SNR in the heart, data-driven methods outperformed the phantom-based combination.

In my master's thesis, I extended Rodgers and Robson's approach using their simulated 3 T array data and including the sensitivity correction $\boldsymbol{\eta}$ as well (5). I found that using WSVD for both the determination of $\boldsymbol{W}$ and $\boldsymbol{\eta}$ gave larger RMSE than using a uniform sensitivity Roemer combination with phantom $\boldsymbol{B}_1^-$. However, using WSVD to determine $\boldsymbol{W}$ and phantom $\boldsymbol{B}_1^-$ to determine $\boldsymbol{\eta}$ reduced this difference. As the $\boldsymbol{B}_1^-$ phase of each channel is unknown, using this mixed method will give better combination than performing a uniform sensitivity Roemer combination with phantom $\boldsymbol{B}_1^-$.

However, these combination methods assume that the PSF contribution is dominated by the central point. In the previous chapter it was found that this assumption leads to an increase in the error. So a correction for the entire PSF should be considered.

8.3. PSF correction

Rewriting Eq [6.3] for signal at each spectral point rather than spin density, and including noise and phase terms gives the formula for reconstructed signal S_{rec}:

$$S_{\mathrm{rec}}(\boldsymbol{r},\delta,k)=\int e^{i\phi(s,k)}K_{\mathrm{sat}}(\boldsymbol{s},\delta)\boldsymbol{B}_1^-(\boldsymbol{s},k)\mathrm{PSF}(\boldsymbol{r}-\boldsymbol{s}).\left[S_{\mathrm{true}}(\boldsymbol{s},\delta)+e(\boldsymbol{s},\delta,k)\right]\mathrm{d}\boldsymbol{s} \quad [8.8]$$

where δ is the chemical shift, k is the channel, and e is a noise term. Assuming uniform spin density, this can be rewritten as:

$$S_{\mathrm{rec}}(\boldsymbol{r},\delta,k)=[S_{\mathrm{true}}(\boldsymbol{r},\delta)+e(\delta,k)].I(\boldsymbol{r},k) \quad [8.9]$$

Where I is given by:

$$I(\boldsymbol{r},k)=\int e^{i\phi(s,k)}K_{\text{sat}}(\boldsymbol{s},\delta)\boldsymbol{B}_1^-(\boldsymbol{s},k)\text{PSF}(\boldsymbol{r}-\boldsymbol{s})\text{d}\boldsymbol{s} \qquad [8.10]$$

Therefore S_{true} is approximately given by:

$$S_{\text{true}}(\boldsymbol{r},\delta)\approx\sum_{k=1}^{N}w(\boldsymbol{r},k)\frac{S_{\text{rec}}(\boldsymbol{r},\delta,k)}{I(\boldsymbol{r},k)} \qquad [8.11]$$

where N is the number of channels, and the weights $w(\boldsymbol{r},k)$ are normalized:

$$w(\boldsymbol{r},k)=\frac{w(\boldsymbol{r},\text{k})}{\sum_{k=1}^{N}w(\boldsymbol{r},k)} \qquad [8.12]$$

The weights can then be chosen to maximize SNR. This is essentially the problem that was considered by Rodgers and Robson, as described above (3). They found that the WSVD method gave optimal SNR, except for very low SNR spectra. In the standard implementation of WSVD, the coil amplitudes α (i.e. the sensitivities multiplied by some unknown constant) are normalized such that $\Sigma|\alpha|^2 = 1$ (3). But it is simple to normalise the weights according to Eq. [8.12], so that $\Sigma|w| = 1$ instead.

As saturation-correction is metabolite-specific, either the combination must be repeated for each metabolite, or by assuming K_{sat} is approximately constant over the PSF it can be removed from the integral I in Eq. [8.10], giving:

$$S_{\text{true}}(\boldsymbol{r},\delta)\approx\frac{1}{K_{\text{sat}}(\boldsymbol{r},\delta)}\sum_{k=1}^{N}w(\boldsymbol{r},k)\frac{S_{\text{rec}}(\boldsymbol{r},\delta,k)}{I_{\text{sense}}(\boldsymbol{r},k)} \qquad [8.13]$$

Correcting the signals using Eq. [8.13] is an intermediate between using only the central point $\boldsymbol{B}_1$ and fully-correcting for the PSF.

8.4. Phantom replacement for phased arrays

In Chapter 7, we found that phantom replacement gave a 10% reduced SD for the 10 cm loop in phantoms compared to the full PSF correction. However, there are drawbacks to the phantom replacement method which limit its use for phased arrays. Phantom replacement implicitly assumes that the coil setup, $\boldsymbol{B}_1^{\pm}$ profile and acquisition protocol are identical between the phantom scan and the main scan. While this is possible with a single loop, it is much more challenging with a flexible array. This is because the coil sensitivities must *all* be identical in the target voxel such that the same weights can be used to combine the signal. The voxels must therefore be placed in an identical position relative to the coil, unlike for a single loop where interpolation can be used between voxel, and the array must be locked into a single position.

To determine whether this challenging scan setup is worthwhile, phantom replacement will be compared in phantoms against the other potential methods.

8.5. Absolute quantification methods in phantoms

Based on Sections 8.2 – 8.4, four methods for absolute quantification with arrays have been chosen for comparison in phantoms (see Fig 8.3).

Method 1: Phantom replacement. The fitted amplitudes were corrected for saturation using the $\boldsymbol{B}_1^+$ at the central point of each voxel to calculate the flip angle. The corrected amplitudes were then divided by the corrected amplitude from the calibration scan.

Method 2: Central point $\boldsymbol{B}_1$ correction. The spectra from each element were combined with WSVD followed by analysis and corrected for saturation using the $\boldsymbol{B}_1^+$ at the central point of each voxel to calculate the flip angle, and then applying Eq. [6.8]. Finally, a Roemer sensitivity correction (Eq. [8.7]) was applied using the $\boldsymbol{B}_1^-$ values at the central point of each voxel, as determined in an 18 mM phosphate phantom (i.e. Section 8.1.2).

Method 2.5: PSF sensitivity correction (i.e. using Eq. [8.13]). This method is an intermediate between only using the $\boldsymbol{B}_1^\pm$ at the central point, and correcting based on the PSF. The spectra from each element were corrected for sensitivity over the PSF. This was followed by WSVD combination, analysis and then saturation-correction using the $\boldsymbol{B}_1^+$ at the central point of each voxel.

Method 3: Full PSF correction (i.e. using Eq. [8.11]). The spectra from each element were corrected for both saturation and sensitivity over the PSF. They were then combined using WSVD combination, and the combined spectrum was analysed.

WSVD combination is used rather than phantom-based Roemer combination for two reasons. The first is that as the channel relative phase is unknown, Roemer combination is likely to have issues with phasing. The second is that the Roemer combination would rely on using the $\boldsymbol{B}_1$ values at the central point of the voxel, which would be contrary to the purpose of using the PSF-based correction (for Methods 2.5 and 3).

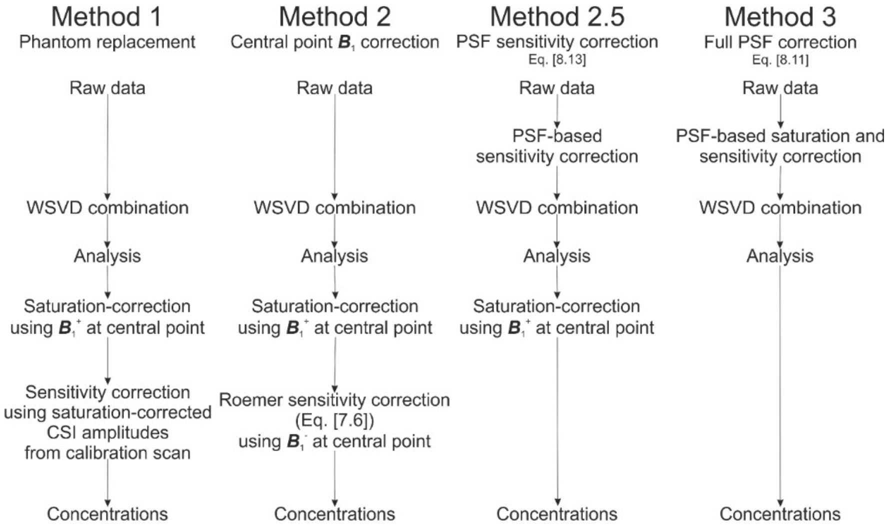

Fig 8.3. Array absolute quantification methods tested in phantoms.

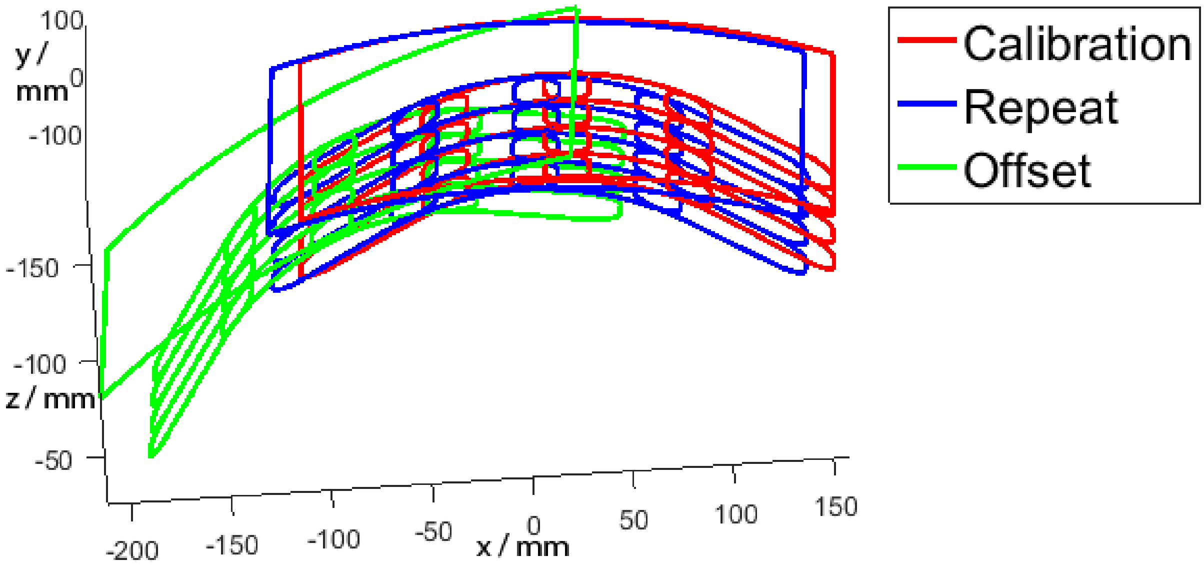

Fig 8.4. Array coil position for each of the phantom scans. Each array diagram shows the larger transmit loop above 16 overlapping coil elements.

Each method was used to process three 18 mM $KH_2PO_{4(aq)}$ phantom datasets, all consisting of a 16 × 16 × 8 matrix of spectra over a 270 × 240 × 200 mm^3 field of view. The first dataset (the "**calibration**" scan) was acquired in the same session as the $\boldsymbol{B}_1$ maps, and was used to calibrate the signal to 18 mM. The second and third datasets were acquired in separate sessions (see Section 7.3.4 and Fig. 7.7). The second dataset (the "**repeat**" scan) matched the array position and flexion in the calibration scan as closely as possible, using the laser alignment mechanism on the scanner to centre the coil. The third dataset (the "**offset**" scan) was offset by ~ 5 cm, which also involved a rotation around the phantom. The relative coil positions and orientations are shown in Fig 8.4. The figure shows the difficulty in perfectly matching the array position, even on the same phantom.

Analysis was performed using the single peak Voigt lineshape AMARES fitting (described in Chapter 5). For all methods, the resulting values were multiplied by the product of the CSI matrix size. This additional correction is required to undo an additional scaling from the Siemens ICE spectroscopy code (in the `scale` function of `IceSpectro.cpp`), which is applied by the Siemens software so that the resulting intensities are similar for all matrix sizes.

The top and bottom 10th percentiles were discarded to suppress imaging artefacts. The bias, SD, and RMSE were then calculated, with the bias determined from the mean value (see Table 8.1 and Fig 8.5).

Table 8.1. Error data from correction of a UTE-CSI acquisition of an 18 mM K_2HPO_4 phantom using a 16 channel array. The mean and SD of these data are plotted in Fig 8.5.

	Bias / mM	**SD / mM**	**RMSE / mM**
Method 1: phantom replacement			
Calibration scan	0.00	0.00	0.00
Repeat scan	-2.97	4.84	5.68
Offset scan	-5.82	5.00	7.67
Method 2: central point B_1 correction			
Calibration scan	2.51	4.66	5.29
Repeat scan	3.91	4.43	5.91
Offset scan	3.28	6.99	7.72
Method 2.5: PSF sensitivity correction			
Calibration scan	1.87	5.93	6.22
Repeat scan	7.43	9.65	12.18
Offset scan	8.49	10.75	13.70
Method 3: Full PSF correction			
Calibration scan	1.29	5.58	5.73
Repeat scan	6.59	8.37	10.65
Offset scan	8.27	12.27	14.79

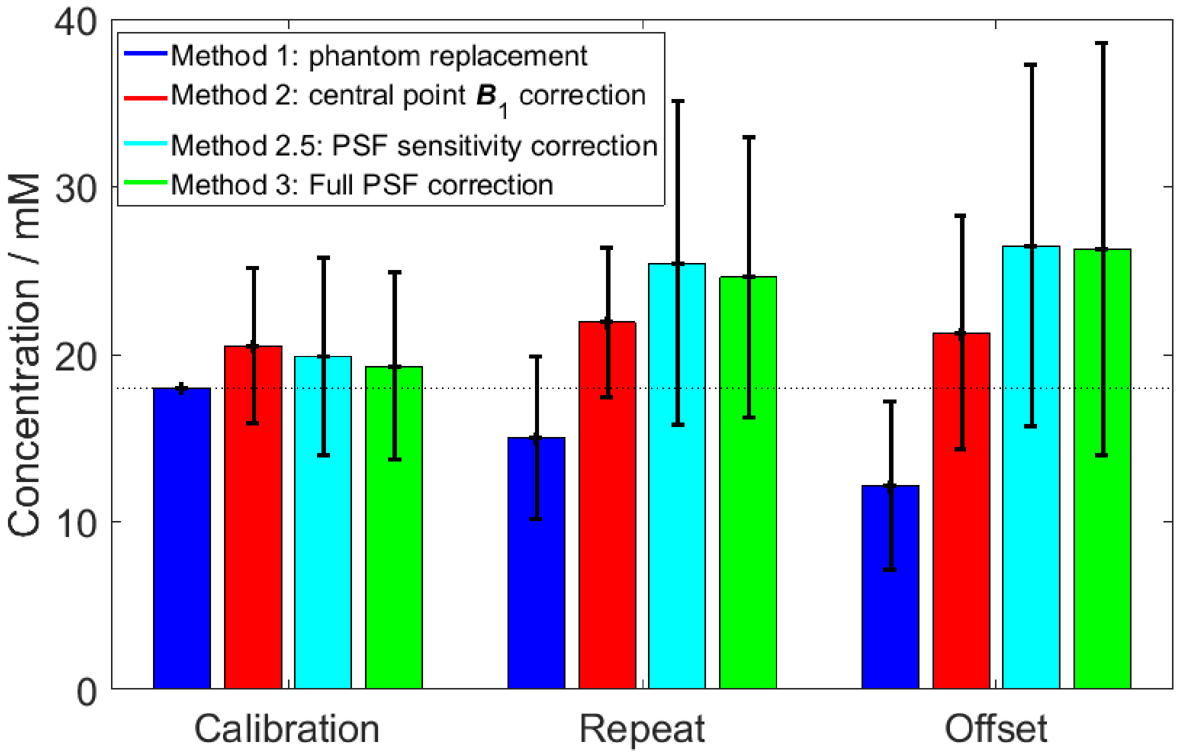

Fig 8.5. Mean and standard deviation of four correction methods (see Fig 8.3) for three CSI acquisitions. These data are also shown in Table 8.1.

The mid-transverse slice from the calibrated concentrations of each of the three scans corrected by four methods are shown in Fig 8.6.

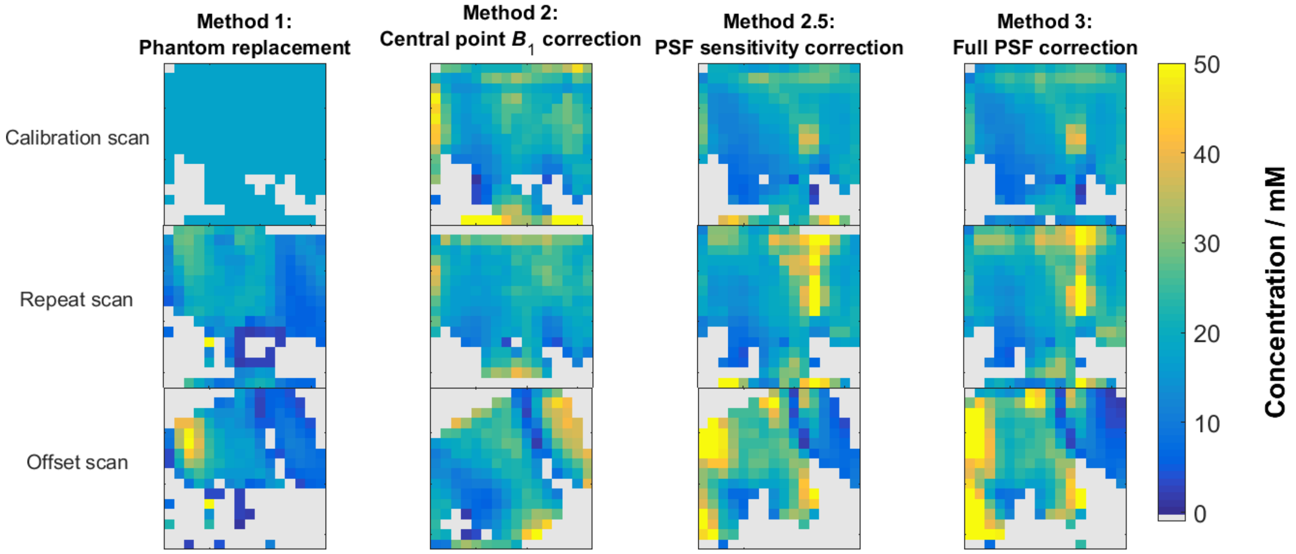

Fig 8.6. The mid-transverse slice from three UTE-CSI acquisition of an 18 mM K_2HPO_4 phantom, corrected using four different methods (see Fig 8.3).

For the central point correction (Method 2), the bias in the calibration scans is roughly equivalent to the bias seen for a single loop (2.51 mM vs 1.02 mM). This arises from the difference between the mode (used for calculating the calibration constant), and the mean (used for calculating the bias). The SD for the repeat scan using central point $\boldsymbol{B}_1^{\pm}$ correction is also similar for the array (4.43 mM) and for the single loop (4.20 mM).

However, unlike for the 10 cm loop, the central point correction (Method 2) gives lower SDs for both the calibration scan and the repeated scan compared to Methods 2.5 and 3. Although the PSF-based corrections have the potential to be more accurate than the central point correction, in this case the added difficulties of correcting each individual coil and then combining them leads to larger errors. This difference can be seen as the central point $\boldsymbol{B}_1^{\pm}$ correction errors are similar for both coils, but the PSF-based errors are significantly increased for the array.

Phantom replacement (Method 1) has very slightly smaller RMSE than central point $\boldsymbol{B}_1^{\pm}$ correction (Method 2). However, while the bias of Method 1 rises quickly with difference in coil position, Method 2 has a consistent, coil position indifferent, bias. Besides, Method 2 is easier to apply when processing the data.

Based on these results, the central point $\boldsymbol{B}_1^{\pm}$ correction method (Method 2) will be compared against calculating concentrations using an endogenous γ-ATP reference and phantom $\boldsymbol{B}_1^{+}$ for saturation correction in Chapter 9.

8.6. Summary

1. The exact phases for individual channel $\boldsymbol{B}_1^-$ maps can be challenging or even impossible to determine.
2. The limitation on determining the per-channel phase mean that the optimal uniform sensitivity combination in this case (and assuming $\boldsymbol{B}_1^\pm$ at the centre of each voxel can be used) is a uniform noise WSVD combination followed by Roemer sensitivity correction using phantom $\boldsymbol{B}_1^-$ values.
3. Uniform sensitivity combination can also be achieved by correcting each channel for sensitivity (and saturation) effects before uniform noise combination.
4. Central point $\boldsymbol{B}_1^\pm$ correction with WSVD combination gives similar errors for the 10 cm loop as for the 16 channel array.
5. For a 16 × 16 × 8 matrix over a 270 × 240 × 200 mm^3 FOV, the PSF-based correction of individual channels before combination gives 30 – 40 % larger errors than central point $\boldsymbol{B}_1^\pm$ correction.
6. In vivo quantification using endogenous and exogenous references will be compared in Chapter 9, after the optimal acquisition and analysis protocols have been selected.

8.7. References

1. Van De Moortele PF, Akgun C, Adriany G, Moeller S, Ritter J, Collins CM, Smith MB, Vaughan JT, Ugurbil K. B-1 destructive interferences and spatial phase patterns at 7 T with a head transceiver array coil. Magn Reson Med. 2005; 54(6):1503-18.
2. Roemer PB, Edelstein WA, Hayes CE, Souza SP, Mueller OM. The NMR Phased Array. Magn Reson Med. 1990; 16(2):192-225.
3. Rodgers CT, Robson MD. Coil combination for receive array spectroscopy: Are data-driven methods superior to methods using computed field maps? Magn Reson Med. 2016; 75(2):473-87.
4. Rodgers CT, Robson MD. Receive Array Magnetic Resonance Spectroscopy: Whitened Singular Value Decomposition (WSVD) Gives Optimal Bayesian Solution. Magn Reson Med. 2010; 63(4):881-91.
5. Purvis LAB. Dynamic Human Cardiac ^{31}P MRS at 7T [MChem]: University of Oxford; 2015.

9. Protocol quality and repeatability

In previous chapters, several options have been proposed for a complete processing pipeline for in vivo hepatic ^{31}P-MRS at 7 T. In this chapter, the quality and repeatability of each of these methods will be compared (see Fig 9.1). For acquisition, the choice is between a short protocol or a longer protocol with higher spatial resolution. For analysis, there is a choice whether to impose linewidth constraints on all the peaks, or only the higher SNR peaks. For saturation correction, I will use phantom-replacement $\boldsymbol{B}_1^+$ maps. For receive sensitivity correction, I will test two possible methods for sensitivity $\boldsymbol{B}_1^-$ correction: using γ-ATP as an endogenous reference or using a central point $\boldsymbol{B}_1^-$ method (i.e. Method 2 from Chapter 8).

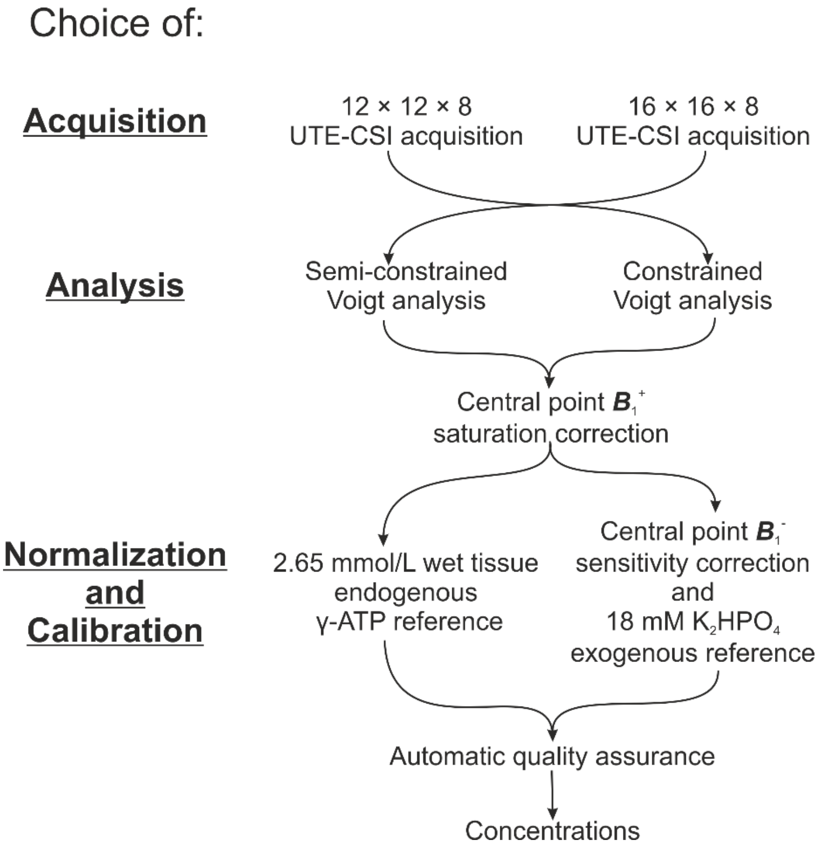

Fig 9.1. Flow chart of potential protocol pipelines.

Part of this chapter has been published in Purvis LAB et al. Phosphodiester content measured in human liver by in vivo ^{31}P MR spectroscopy at 7 tesla. Magn Reson Med. 2017; 78(6):2095-105.

To simplify this comparison, the full results will only be given for the final method. In every other case, I will focus on three representative peaks: α-ATP, GPC and PEP/PtdC.

In the last section, the full final protocol is summarized, and its superiority is discussed in comparison to methods published in the literature.

9.1. General pipeline

Ten volunteers were scanned twice in the same session, after full repositioning and reshimming (see Chapter 4). The data were analysed used the AMARES algorithm in the OXSA toolbox (see Chapter 5). Saturation correction was performed using T_1 values acquired as described in Chapter 6.

An endogenous γ-ATP reference can be used by assuming that the filling fraction and sensitivities of γ-ATP and each of the other metabolites were equal, and applying Eq. [1.85]. The concentration of γ-ATP is taken as 2.65 mmol/L wet volume based on a 2.51 ± 0.61 mmol/kg wet weight (1), and 1.054 kg/L specific gravity of the liver (2).

In each case, automatic quality assurance (QA) was used to ensure that the results only used voxels from within the liver. In short:

1. Voxels outside a manually drawn ROI were excluded
2. A pre-fit QA excluded spectra with time-domain (i.e. FID) SNR < 3
3. A post-fit QA excluded spectra with γ-ATP SNR < 5 or those with poor fit (residual 2-norm > 80%)
4. A final QA excluded contaminated spectra after quantification using PCr amplitudes or concentrations, as well as PME and PDE CRLBs.

The exact cutoffs used for the final QA were consistent in the first two comparison, but changed for the comparison of quantification methods (see Table 9.1). In each case, reasonable cutoff values were determined using histograms to select the PCr amplitudes or concentrations below the normal distribution (to exclude skeletal muscle contamination) and PME or PDE CRLBs more than two SD above the mean (to exclude contamination from the blood or bile).

Any voxels remaining after this automatic quality assurance procedure are referred to below as “high quality” voxels.

The mean and SD for each subject was calculated from the high quality voxels. The within-subject SDs were calculated using the SDs between the mean values for the repeated volunteer scans. The coefficients of repeatability (CoRs) were calculated as $1.96 \times \sqrt{2} \times$ the within-subject SD. The mean absolute difference between two repeated scans should be less than the CoR in 95% of cases.

Bland-Altman plots were used to further analyse the repeatability of the protocol. Welch’s t-test was used to compare means, allowing for unequal variances (5). An F-test was used to compare variances.

Table 9.1. A summary of the protocols used in each method comparison. Parameters that are being compared at each stage are given in bold.

Quantification stage comparison	Acquisition matrix size	Analysis prior knowledge	Normalization and calibration	Final QA exclusion criteria
Acquisition	**12 × 12 × 8**	Semi-constrained Voigt	γ-ATP endogenous reference	PCr amplitude > 5, PME CoV > 20%, PDE CoV > 10%
	16 × 16 × 8	Semi-constrained Voigt	γ-ATP endogenous reference	PCr amplitude > 5, PME CoV > 20%, PDE CoV > 10%
Analysis	16 × 16 × 8	**Semi-constrained Voigt**	γ-ATP endogenous reference	PCr amplitude > 5, PME CoV > 20%, PDE CoV > 10%
	16 × 16 × 8	**Constrained Voigt**	γ-ATP endogenous reference	PCr amplitude > 5, PME CoV > 20%, PDE CoV > 10%
Normalization and calibration	16 × 16 × 8	Constrained Voigt	**γ-ATP endogenous reference**	PCr amplitude > 5, PME CoV > 20%, PDE CoV > 10%
	16 × 16 × 8	Constrained Voigt	**Central point B_1 correction, calibrated to an exogenous 18 mM phosphate phantom**	PCr concentration > 1 mmol/L wet tissue, PME CoV > 70%, PDE CoV > 60% (CoV cutoff increased as sensitivity correction adds ~50% error)

9.2. Methods comparison

9.2.1. Acquisition: long vs. short protocol

9.2.1.1. Pipeline

Two protocols were compared as described in Chapter 4: a 16 × 16 × 8 matrix with 10 averages (28 min 10 s scan time), and a 12 × 12 × 8 matrix (interpolated to 16 × 16 × 8) with 6 averages (10 min scan time).

The spectra were then processed with the pipeline described in the previous section. Both datasets were analysed using the semi-constrained Voigt prior knowledge described in Chapter 5. Saturation-correction was performed with the $\boldsymbol{B}_1^+$ values at the centre of each voxel, determined from the field maps acquired in Chapter 7. Voxels were discarded if they had PCr amplitude greater than five (i.e. contaminated by skeletal muscle), or a Cramér-Rao lower bound (CRLB), i.e. a measure of the uncertainty in the fit (3), greater than 20% for any PME peak or greater than 10% for any PDE peak. Concentrations were then calculated relative to an endogenous γ-ATP reference, with the γ-ATP concentration taken as 2.65 mmol/L wet volume (1, 2) .

9.2.1.2. Quality

In the 28-min protocol, an average of 228 ± 49 voxels fell within the ROI, which had a coverage of 92 ± 34%, i.e. approximately the whole liver. 134 ± 21 voxels passed the pre-fit quality assurance test and 113 ± 17 had a good fit and γ-ATP SNR greater than 5. This left 19 ± 9 high quality voxels, which had good SNR, were well fitted, and were reliably localized to the liver. As the resolution of the 10-min protocol is interpolated online on the scanner by zero-padding of k-space up to 16 × 16 × 8, the number of voxels within the ROI was the same as for the long protocol. 133 ± 23 voxels passed the pre-fit quality assurance test and 118 ± 20 had a good fit and γ-ATP SNR greater than 5. There were 13 ± 9 high quality voxels.

The large cut at the final stage of the fitting was because of the stringent final QA criteria. Many of the high SNR voxels will come from closer to the coil – i.e. from the area of the liver close to skeletal muscle. The CRLB criteria on the PME and PDE peaks also exclude many voxels where the shim is poor due to breathing or tissue movement. This could potentially be improved prospectively through gating. However, the variable T_R or long scan times that this would introduce make retrospective QA a more attractive approach.

After the final QA, the mean γ-ATP linewidth was 29 ± 6 Hz for the 28-min protocol, which was not significantly different to the short protocol (30 ± 6 Hz, $P = 0.36$). The ratio of residual PCr signal to γ-ATP for the long protocol was not significantly different to the short protocol (0.36 ± 0.12 vs 0.41 ± 0.13, $P = 0.19$). The mean γ-ATP SNR (amplitude / noise SD) was the same for both protocols (23 ± 4 vs 23 ± 6, $P = 0.5$). These are indications that the automatic quality assurance protocol is working equally well in both cases. The difference should be expected to be in the number of "high quality" voxels remaining, and therefore the extent of coverage of the liver.

The nominal voxel size was 6.3 mL for the 28-min protocol, but acquisition weighting means that the 50% maximum PSF volume was 47.1 mL (9, 10). In comparison, the nominal voxel size for the 10-min protocol was 11.3 mL, and the 50% maximum PSF volume was 89.4 mL. The 10-min protocol is therefore expected to have more contaminated voxels, due to the larger voxel size. Indeed, the short protocol had fewer voxels after QA (13 ± 9 vs 19 ± 9) than the 28-min protocol. But despite having fewer voxels, the total liver coverage (accounting for voxel overlap) was not significantly different (23 ± 11% vs 20 ± 7%, $P = 0.24$).

Table 9.2. Acquisition methods errors comparison. Abbreviations: CoR, coefficient of repeatability; CLRB, Cramér-Rao lower bound; SD standard deviation.

	Concentration / mmol/L wet tissue	CoR / mmol/L wet tissue	Mean CRLB / mmol/L wet tissue	Mean intrasubject SD / mmol/L wet tissue	Intersubject SD / mmol/L wet tissue
12 × 12 × 8					
α-ATP	2.45 ± 0.12	0.3 ± 0.18	0.25 ± 0.07	0.2 ± 0.05	0.17
GPC	2.85 ± 1.16	1 ± 0.74	0.19 ± 0.04	0.6 ± 0.23	0.43
PEP / PtdC	1.87 ± 0.23	1 ± 0.62	0.39 ± 0.07	0.8 ± 0.66	0.49
16 × 16 × 8					
α-ATP	2.46 ± 0.33	0.3 ± 0.17	0.25 ± 0.06	0.3 ± 0.07	0.12
GPC	3.07 ± 0.95	1 ± 1.46	0.19 ± 0.03	0.5 ± 0.27	0.35
PEP / PtdC	1.18 ± 0.20	0.5 ± 0.29	0.34 ± 0.05	0.5 ± 0.17	0.18

9.2.1.3. Repeatability

The Bland-Altman plot comparing the long and short protocols is shown in Fig 8.1. None of the mean differences are significantly different from zero at $P = 0.05$ level.

The two protocol coefficients of repeatability (CoRs), Cramér-Rao lower bounds (CRLBs) and inter- and intra-subject SDs are given in Table 8.2 for α-ATP, GPC and PEP/PtdC. The errors for PEP/PtdC were significantly lower for the long protocol than for the short protocol ($P < 0.05$). These differences are also present for NAD$^+$ and UDPG.

The short protocol adds additional uncertainty to several of the peak parameters. As this uncertainty is not large for most peaks, it could be a reasonable trade-off for the reduction in scan time. However, PEP/PtdC and UDPG have not been investigated using ^{31}P-MRS in the diseased liver, and NAD$^+$ has shown potential as a marker for non-alcoholic fatty liver disease (4). Therefore the reduced error of the longer method is preferred. Additionally, the lack of significant time pressure for the remaining experiments performed here mean that there is no benefit in reducing the scan time.

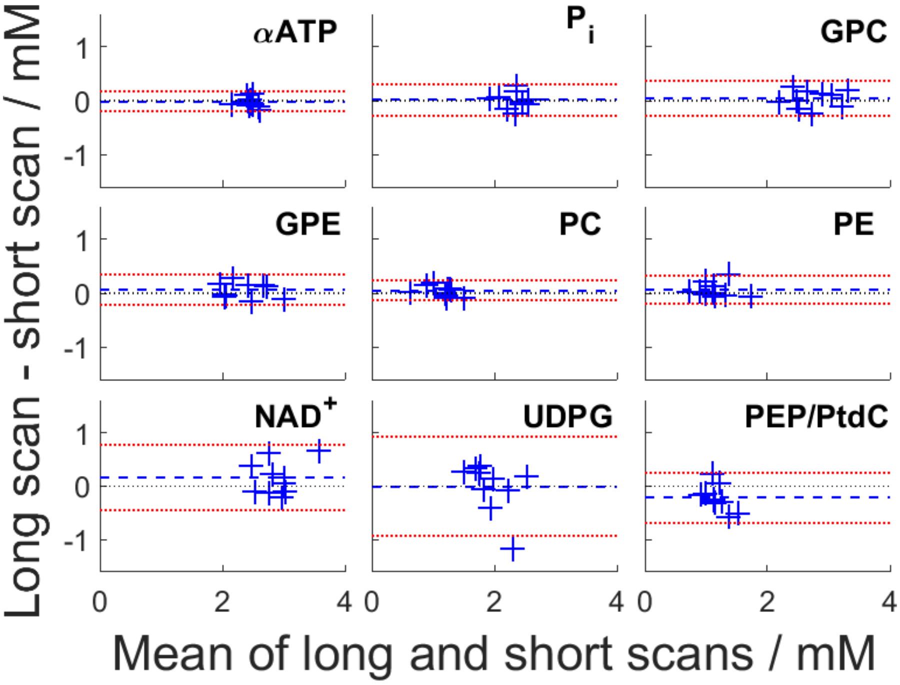

Fig 9.2. Bland-Altman plots of the concentrations of the long and short scans. Each blue cross marks a different subject. The blue dashed line is the mean difference and the red dashed line is 1.96 × standard deviation, i.e. the 95% confidence interval. y = 0 is marked by a black dashed line. In this case, "mM" is defined as mmol / L of wet tissue. The concentrations are determined using a 2.65 mM endogenous γ-ATP reference.

9.2.2. Analysis: constrained vs. semi-constrained

9.2.2.1. Pipeline

Two analysis methods were compared as described in Chapter 5: in the first, the linewidths of all the peaks were constrained to a single Voigt lineshape plus a metabolite specific Lorentzian component; in the second the linewidths of $\mathrm{NAD^+}$, UDPG and PtdC were allowed to vary independently. The first method will be referred to as 'Constrained', and the second method 'Semi-constrained'.

Linewidth constraining was tested using the 28-min protocol data. Saturation-correction was performed with the $\boldsymbol{B}_1^+$ values at the centre of each voxel, determined from the field maps acquired in Chapter 8. Voxels were discarded if they had PCr amplitude greater than five, or a CRLB greater than 20% for any PME peak or greater than 10% for any PDE peak. Concentrations were then calculated relative to an endogenous γ-ATP reference, with the γ-ATP concentration taken as 2.65 mmol/L wet volume.

9.2.2.2. Repeatability

For the constrained Voigt analysis, the mean γ-ATP Voigt linewidth was 24 ± 6 Hz, and the mean γ-ATP CRLB was 8.65 ± 2.19%. For the semi-constrained Voigt analysis, the approximate mean γ-ATP Voigt linewidth was 22 ± 6 Hz, and the mean γ-ATP CRLB was 8.81 ± 2.24%.

The CoR and CRLB are not significantly different between the two analysis methods for α-ATP and GPC (values given in Table 9.3, $P > 0.1$ for all comparisons). Although the CoR and SDs are not significantly different for PEP/PtdC, the CRLB is lower for the constrained fitting ($P < 0.0001$). This is a natural consequence of the additional prior knowledge, and only reduces the lower bound on the error, and not necessarily the error itself (as seen from the CoR and SD).

The Bland-Altman plot for the difference between the two methods is shown in Fig 9.3. There is a small, but statistically significant, negative bias in GPC ($P < 0.0001$) and GPE ($P = 0.005$), and a large, significant, positive bias in UDPG and PEP/PtdC ($P < 0.0001$). These biases are slightly lower than expected from the simulations run in Chapter 5.3.2, as the mean bias across all peaks was 6.4% in vivo compared to 16% in simulations. The true $\Delta LW_{intrinsic}$ values for PEP/PtdC, NAD^+, and UDPG are therefore likely to be less than the values given in Table 5.2. As there is no significant improvement in reproducibility using the constrained analysis over semi-constrained, and there is a significant increase in bias, the semi-constrained analysis was selected for the final protocol.

Table 9.3. Analysis methods errors comparison.

	CoR / mmol/L wet tissue	Mean CRLB / mmol/L wet tissue	Mean intrasubject SD / mmol/L wet tissue	Intersubject SD / mmol/L wet tissue
Constrained				
α-ATP	0.3 ± 0.18	0.23 ± 0.05	0.24 ± 0.08	0.10
GPC	1 ± 1.68	0.17 ± 0.03	0.5 ± 0.25	0.35
PEP/PtdC	0.5 ± 0.33	0.21 ± 0.04	0.6 ± 0.31	0.28
Semi-constrained				
α-ATP	0.3 ± 0.17	0.25 ± 0.06	0.26 ± 0.07	0.12
GPC	1 ± 1.46	0.19 ± 0.03	0.5 ± 0.27	0.35
PEP/PtdC	0.5 ± 0.29	0.34 ± 0.05	0.5 ± 0.17	0.18

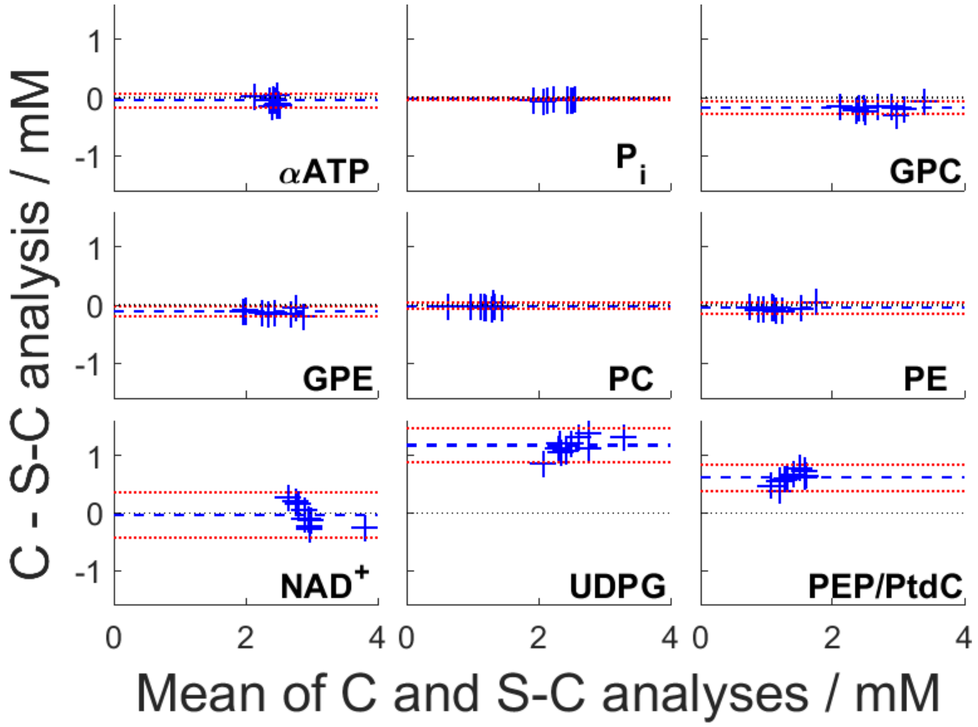

Fig 9.3. Bland-Altman plots of the concentrations of the constrained (C) and semi-constrained (S-C) analyses. Each blue cross marks a different subject. The blue dashed line is the mean difference and the red dashed line is 1.96 × standard deviation, i.e. the 95% confidence interval. y = 0 is marked by a black dashed line. In this case, "mM" is defined as mmol / L of wet tissue. The concentrations are determined using a 2.65 mM endogenous γ-ATP reference.

9.2.3. Normalization and calibration

9.2.3.1. Pipeline

Two absolute quantification methods were compared: in the first, concentrations were calculated using an endogenous γ-ATP reference, with the γ-ATP concentration taken as 2.65 mmol/L wet volume; in the second, sensitivity correction was performed using part of the uniform sensitivity Roemer combination formula (see Eq. [7.5]), and the results were calibrated to an 18 mM $KH_2PO_{4(aq)}$ phantom. In both cases saturation-correction was performed with the $\boldsymbol{B}_1^+$ values at the centre of each voxel, determined from the phantom field maps acquired as described in Chapter 8. The first method will be referred to as 'endogenous reference' quantification, and the second method 'exogenous reference' quantification.

The long protocol datasets were used for this comparison and the semi-constrained Voigt prior knowledge was used for analysis. For the endogenous reference method, voxels were discarded if they had PCr amplitude greater than five, or a CRLB greater than 20% for any PME peak or greater than 10% for any PDE peak. For the exogenous reference method, voxels were discarded if they had PCr concentration greater than 1 mmol/L wet tissue, or a CRLB greater than 70% for any PME peak or 60% for any PDE peak. Different cut-offs were required for the exogenous reference method, as it inherently includes higher error than the endogenous reference method. If the same cut-offs had been used, there would have been no "high quality" voxels for the exogenous reference method. The new cut-offs were selected to give the same average number of "high quality" voxels, thereby reducing selection bias between the two methods.

9.2.3.2. Concentrations

The mean γ-ATP concentration determined using the exogenous reference was 1.88 ± 0.25 mmol/L wet tissue for the first scan and 2.01 ± 0.32mmol/L wet tissue for the second scan. The concentrations for α-ATP, GPC and PEP/PtdC are given in Table 9.4. As the γ-ATP concentrations are determined by the exogenous reference method are lower than 2.65 mmol/L wet tissue (the endogenous reference value), and since the sensitivity scaling factors are comparable for all metabolites, it is not surprising that the other peak concentrations are also lower.

Table 9.4. Quantification methods concentration comparison.

	Scan 1 / mmol/L wet tissue	Scan 2 / mmol/L wet tissue
Exogenous reference		
γ-ATP	1.88 ± 0.25	2.01 ± 0.32
α-ATP	1.80 ± 0.25	1.94 ± 0.25
GPC	1.59 ± 0.36	1.69 ± 0.35
PEP/PtdC	0.73 ± 0.17	0.79 ± 0.20
Endogenous reference		
γ-ATP	2.65	2.65
α-ATP	2.47 ± 0.12	2.40 ± 0.16
GPC	2.69 ± 0.35	2.86 ± 0.59
PEP/PtdC	0.99 ± 0.18	1.16 ± 0.17

9.2.3.3. Repeatability

As the concentrations are significantly different between methods (which was not the case in any of the other comparisons), the repeatability and variability values are given in Table 9.5 with percentages of the determined concentration. The t-tests and F-tests were also performed with percentages rather than the absolute values. The intra- and intersubject SDs and the CRLBs were all significantly smaller for the endogenous reference method ($P < 0.05$). There was no significant differences between the GPC and PEP/PtdC CoR.

Table 9.5. Quantification methods error comparison.

	CoR / mmol/L wet tissue	Mean CRLB / mmol/L wet tissue	Mean intrasubject SD / mmol/L wet tissue	Intersubject SD / mmol/L wet tissue
Exogenous reference				
α-ATP	0.6 (34%) ± 0.4	0.8 (44%) ± 0.2	1.0 (55%) ± 0.3	0.25 (14%)
GPC	0.5 (107%) ± 0.4	0.7 (42%) ± 0.2	0.6 (35%) ± 0.1	0.36 (23%)
PEP/PtdC	0.3 (16%) ± 0.3	0.43 (65%) ± 0.08	0.5 (71%) ± 0.2	0.17 (23%)
Endogenous reference				
α-ATP	0.3 (12%) ± 0.17	0.25 (10%) ± 0.06	0.26 (10%) ± 0.07	0.12 (5.0%)
GPC	1 (120%) ± 1.5	0.19 (7.1%) ± 0.03	0.5 (20%) ± 0.27	0.35 (13%)
PEP/PtdC	0.5 (15%) ± 0.29	0.34 (38%) ± 0.05	0.5 (50%) ± 0.17	0.18 (18%)

The differences in error are expected, as the exogenous quantification method includes several additional steps, each of which introduces extra potential sources of error. The covariation of α- and γ-ATP can be seen when comparing the errors of α-ATP and the other peaks across the two methods. It can also be seen in the Bland-Altman plots for the two methods (see Fig 9.4 and Fig 9.5), where the relative 95% confidence intervals are smaller for ATP than other peaks when using γ-ATP as an endogenous reference, and larger for ATP than the other peaks when an exogenous reference is used. In other words, the endogenous reference is potentially obscuring information that is available from the metabolites, and might not be valid in pathology (5).

As this is the case, it is better to use the exogenous reference method to process the volunteer and patient data acquired in Chapter 4 despite the increase in variability.

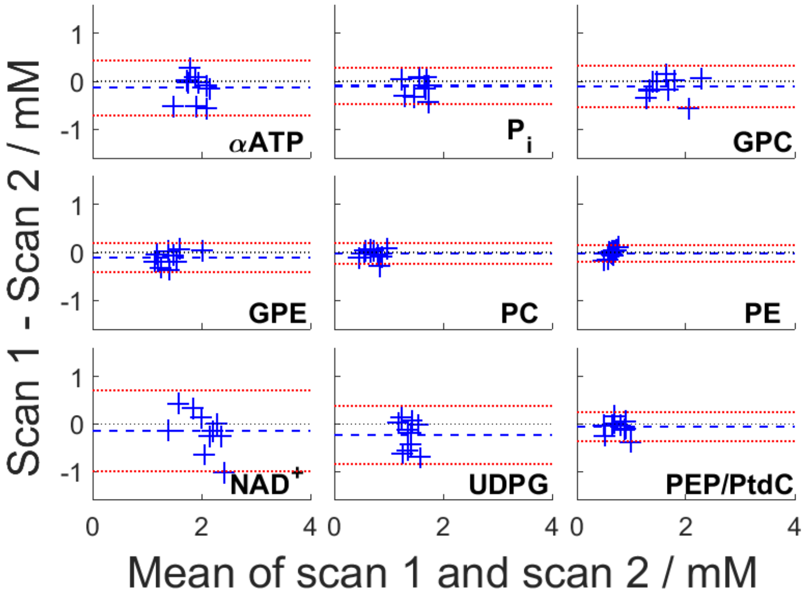

Fig 9.4. Bland-Altman plots of the concentrations of the two repeatability scans, quantified using an 18 mM $KH_2PO_{4(aq)}$ exogenous reference. Each blue cross marks a different subject. The blue dashed line is the mean difference and the red dashed line is 1.96 × standard deviation, i.e. the 95% confidence interval. y = 0 is marked by a black dashed line. In this case, “mM” is defined as mmol / L of wet tissue.

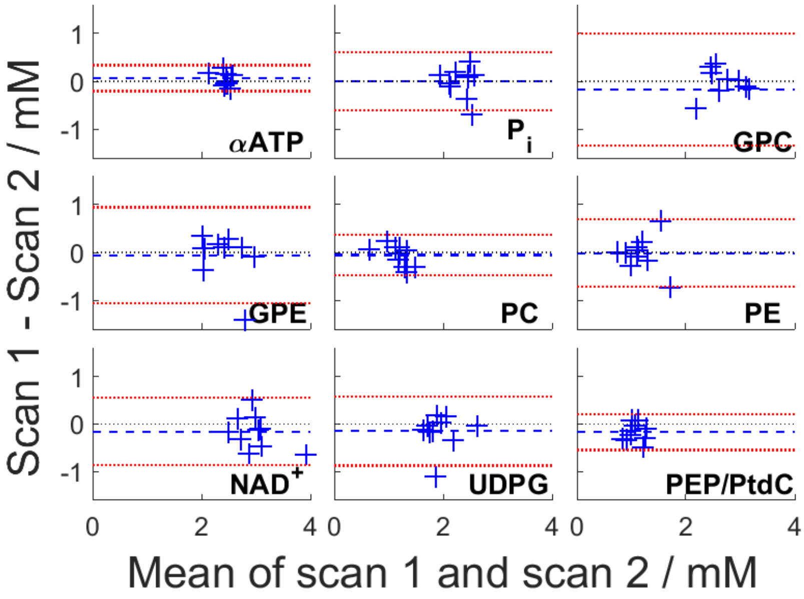

Fig 9.5. Bland-Altman plots of the concentrations of the two repeatability scans, quantified using a 2.65 mM γ-ATP endogenous reference. Each blue cross marks a different subject. The blue dashed line is the mean difference and the red dashed line is 1.96 × standard deviation, i.e. the 95% confidence interval. y = 0 is marked by a black dashed line. In this case, “mM” is defined as mmol / L of wet tissue.

9.3. Final hepatic ^{31}P-MRS 7T protocol and processing pipeline

9.3.1. Full protocol summary

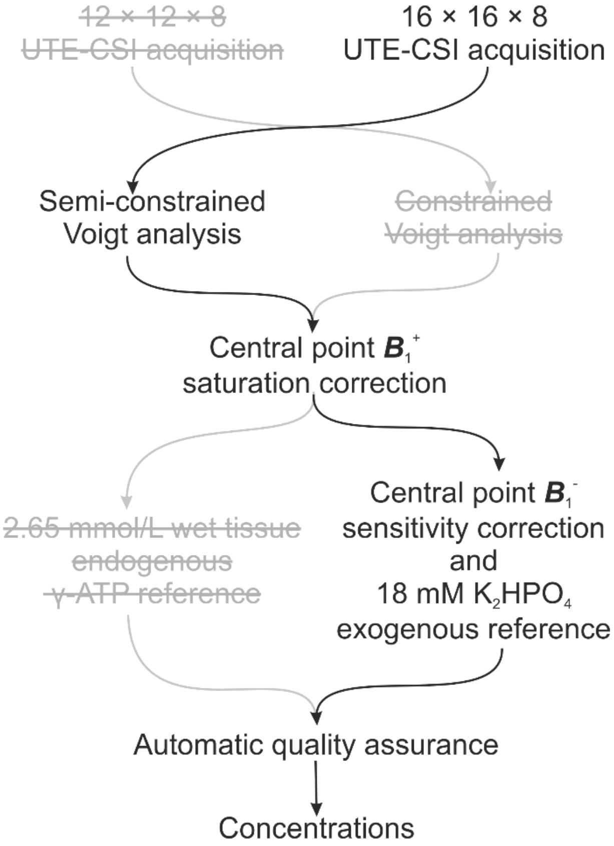

Fig 9.6. Flow chart of final protocol pipeline.

As the 16 channel receive array has no ^{1}H transmit/receive element, ^{1}H images were acquired separately from the main ^{31}P scan. Transverse, sagittal and coronal ^{1}H FLASH stacks of images for localization and dual-echo GRE field maps for $\boldsymbol{B}_0$ shimming were acquired using a 10 cm ^{1}H loop.

For ^{31}P, a 1s T_R, 10 average Hamming-weighted UTE-CSI sequence with a 2.4 ms shaped excitation pulse was used to acquire a 16 × 16 × 8 matrix of liver voxels over a 270 × 240 × 200 mm^3 FOV. A set of FLASH images and series of IR FIDs were acquired for five phenylphosphonic acid (PPA) fiducials. Data were acquired on a Siemens Magnetom 7 T scanner using a 16 channel ^{31}P array consisting of a single 28 × 27 cm^2 transmit loop and a 4 × 4 matrix of 8 × 5.5 cm^2 diameter flexible receive loops.

On the scanner, spectra from each receive element were combined online with WSVD combination to give a single uniform noise spectrum for each voxel.

The full grid of CSI spectra was then loaded into MATLAB using the OXSA toolbox (6). A ROI was manually drawn around the liver on a transverse ^{1}H localizer. Voxels were excluded if they were outside the ROI or if the mean of the absolute value of the first ten points of the FID was less than 2.0 (the noise level in each combined spectrum is scaled by WSVD to be $1/\sqrt{2}$ (7)). Each voxel was analysed using semi-constrained Voigt lineshape fitting with the AMARES algorithm as implemented in the OXSA toolbox (see Chapter 5). The prior knowledge is given in Table 5.3. After fitting, γ-ATP SNR was calculated as the maximum intensity signal over noise SD from the spectrum after it had been apodized to match the γ-ATP linewidth (8). Voxels with γ-ATP SNR less than five, or residual 2-norm greater than 80% of the original were excluded. Per-subject $\boldsymbol{B}_1^{\pm}$ maps were computed using field maps acquired from an 18 mM $KH_2PO_{4(aq)}$ phantom in a separate scan session and adjusted for coil loading and position using FIDs and FLASH images of the PPA fiducials attached to the coil housing. The $\boldsymbol{B}_1^{+}$ values were used to compute flip angles within each voxel, so that saturation correction factors could be calculated using previously measured T_1 values (see Chapter 6). Sensitivity correction was performed using the $\boldsymbol{B}_1^{-}$ maps and Eq. [8.6], calibrated to an 18 mM phosphate phantom (Method 2 from Chapter 8).

Voxels were discarded if they had PCr concentration greater than 1 mmol/L wet tissue (i.e. if they are contaminated by skeletal muscle), or if they had CRLB greater than 70% for any PME peak or greater than 60% for any PDE peak. These cut-offs were selected by using histograms to select the skeletal PCr concentrations below the normal distribution and PME or PDE CRLB more than two SD above the mean. This led to slightly relaxed cutoffs compared to the comparison to the endogenous γ-ATP reference. Fig 9.7(a) shows the decision tree for exclusion. Histograms of the data before and after exclusion were checked manually to ensure that no bias was introduced by using percentage CRLB as an exclusion criterion (9).

9.3.2. Automatic quality assurance

An average of 228 ± 49 voxels fell within the ROI, which had a coverage of 92 ± 34%, i.e. approximately the whole liver. 134 ± 21 voxels passed the pre-fit quality assurance test and 113 ± 17 had a good fit and γ-ATP SNR greater than 5. This left 39 ± 11 high quality voxels, which had good SNR, were well fitted, and were reliably localized to the liver.

Quality assurance in post-processing is important for CSI methods because the matrix of voxels acquired typically vary widely in SNR, $\boldsymbol{B}_0$ homogeneity and contamination. Automatic methods for the selection of high quality voxels reduce observer bias and the need for post-processing by experts. In addition, they reduce the time required for quality assurance, which is necessary for a protocol to be clinically viable. The trade-off is the possibility of including voxels that would be discarded by an expert. In this study, the performance of the quality assurance pipeline shown in Fig 9.7 was checked by manual inspection of 100 randomly selected voxels that had been assigned as high quality; all of these voxels had negligible skeletal muscle contamination (PCr), blood contamination (where the 2,3-DPG peaks would overlap with the PME peaks increasing the CoV) or other artefacts. In healthy volunteers, there was an average PCr/ATP ratio of 0.23 ± 0.06 in liver for the long protocol. As PCr/ATP in skeletal muscle is approximately four, this suggests that skeletal muscle contamination contributes at most 6% of the ATP signal in the “liver” spectra, which is below the noise level in this data.

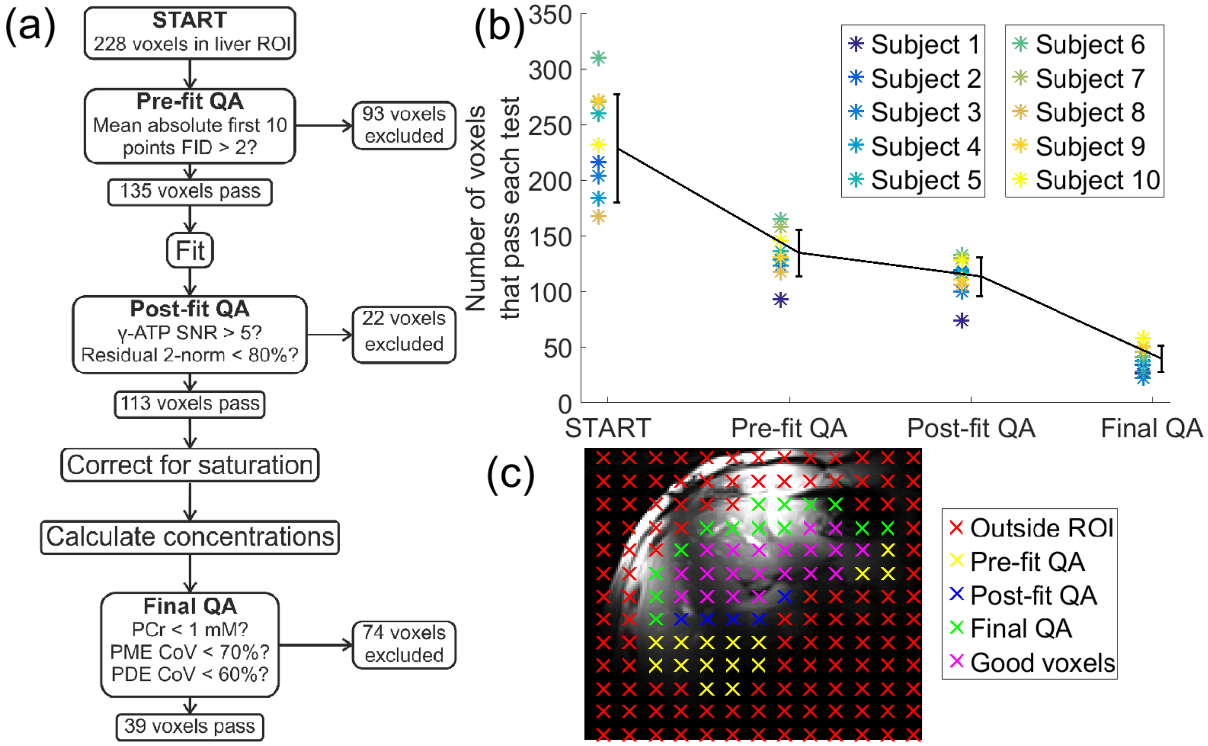

Fig 9.7. Liver CSI quality assurance. (a) shows the decision tree of quality assurance (QA) tests for excluding voxels in the analysis of the CSI grid of the liver. The mean number of voxels remaining at each step are given. (b) shows the number of voxels that pass each test. The black line shows the mean ± standard deviation of the values. The stars show individual values, with each colour representing a different subject. (c) shows the locations of a single slice of CSI voxels overlaid on a ^{1}H localizer. Each colour indicates a different exclusion parameter.

9.3.3. Data quality comparison to literature

9.3.3.1. Results summary

The nominal voxel size was 6.3 mL, but acquisition weighting means that the 50% maximum PSF volume was 47.1 mL (10, 11). The average liver volume was 1.69 ± 0.20 L, and accounting for voxel overlap the average volume within each liver that was analysed was 0.63 ± 0.13 L. The mean total liver coverage was therefore 38 ± 10%. The mean γ-ATP linewidth was 31 ± 8 Hz, and the average spectral γ-ATP SNR (amplitude / noise SD) was 20 ± 2. The average ratio of the residual PCr signal to ATP was 0.25 ± 0.07 in the liver.

9.3.3.2. Discussion

A single voxel from the CSI grid has a 50% PSF volume of 47.1 mL. Combining the high quality voxels gives an average volume of 0.63 ± 0.13 L. For fully localized 3D-ISIS, voxel sizes have ranged between 75 and 500 mL (12-15). 3D-CSI therefore allows finer spatial resolution across a larger proportion of the liver than previous 3D-ISIS studies, while retaining a feasible scan time. In this study, the finer spatial resolution is used to discard low quality regions and get a more accurate mean value for each subject, under the assumption that the tissue is homogenous in healthy liver and in diffuse liver disease. The resolution could also be used to investigate heterogeneity in the liver, which is especially useful in focal liver diseases (16). For example, although imaging techniques are adept at locating liver tumours, spectroscopy can provide additional information about tumour metabolism (see Section 3.1.3.3), which can further improve disease management (17).

The mean γ-ATP fitting CRLB in this study was 1.6% (although this increases to 44% after normalization and calibration). The literature CRLB for fitting γ-ATP in the liver at 7 T using a 10 cm loop coil are 10.3% for a 20 min 3D-CSI scan and 7.6% for a 3 min 42 s 3D-ISIS scan (12). Accounting for the differences in acquisition time by multiplying by the square root of time, this protocol gives an 82% improvement over the 10 cm loop 3D-CSI scan (12), and a 43.9% improvement over the 10cm loop 3D-ISIS scan (12). If the difference in volume is also accounted for, the improvements are 70% and 67% respectively. This can be partly attributed to the difference in post-processing. The linewidth-constrained fit in OXSA improves the CRLB by including a relationship between the linewidths into the fitting (18). This is particularly important in the PDE/PME region of the spectra, where there are multiple overlapping peaks. Rerunning the analysis using the same prior knowledge as Chmelik et al. (12) reduced the number of high quality voxels to 25 ± 10 (from 39 ± 11). However, the γ-ATP CRLB of the remaining voxels was 1.65%

i.e. an improvement of 65% over the 10 cm loop CSI scan, and 62% over the ISIS scan. The remaining difference is likely due to increased SNR due to the receive array.

Chmelik et al. scanned the subject in a lateral position, and using a double-tuned coil (12). In our protocol, the ^{1}H loop used for localization and shimming had to be replaced was replaced by the ^{31}P array, and so subjects were scanned while supine to ease this coil-swap and increase their comfort. Both swapping the coil and scanning supine might have led to the increased linewidths in this protocol. However, the mean γ-ATP linewidth was 34 ± 11 Hz for the Chmelik et al. CSI protocol (12), compared to 31 ± 8 Hz in this protocol. So even the potentially sub-optimal subject positioning did not lead to a lower quality of the shim, though this might be attributed to the shimming method (19).

9.3.4. Repeatability

The Bland-Altman plot for the repeatability scans was shown in Fig 9.4. The average difference between the two measurements was not significant ($P > 0.1$ for all peaks). It is possible that the small (insignificant) variation observed reflects natural variations in liver metabolite concentrations. Metabolite concentrations in the liver are known to change with nutritional state (20, 21) . And although the subjects were scanned after an overnight fast, which should increase the consistency of the results (22), no studies have been reported measuring the consistency of metabolite concentrations in the fasted liver over a long period.

The coefficients of repeatability (CoR), CRLB and inter- and intra-subject SD for all peaks are given in Table 9.6. The NAD$^+$ peak has the largest CoR (133%) and the next largest was P_i (95%).

The average voxel overlap factor of 2.5 was not accounted for when calculating the intra-subject mean and SD, which led to an artificial reduction in the intra-subject SDs. Therefore, any comparison between the SDs should take this into account.

9.4. Developing new absolute quantification protocols

As hardware improves and targets change, new absolute quantification protocols will inevitably need to be developed. In this section, I will suggest certain factors that should be considered, with additional attention being given to potential pitfalls.

The first step to developing a quantification protocol is to decide the target, such as an organ or metabolite of interest. Once a target has been selected, it is straightforward to decide on an acquisition method. The excitation bandwidth, flip angle, and T_R can be optimised for the chosen metabolites, and the localization method can be decided based on time and SNR constraints.

When choosing the analysis, normalization, and calibration methods, errors should take into account both bias and variance (or repeatability). If the aim of the protocol is to get the most accurate possible value for the “true” metabolite concentration, then bias should be reduced even at the cost of increased variance. However, if the aim of the protocol is to stage disease, the perhaps a larger bias is an acceptable cost for a larger change in concentrations between stages. Minimizing the RMSE is a simple way to balance the trade-off between of bias and variance.

Table 9.6. Long protocol errors in metabolite concentrations. Coefficients of repeatability (CoR) in normals are given ± 95% confidence intervals. The intra-subject SDs are reduced compared to fully independent measurements, as there is no correction for voxel overlap. These values are different from those in Table 9.5 due choosing the cut-offs based on histograms rather than matching the number of voxels to the endogenous reference method.

Metabolite	CoR / mmol/L wet tissue	Mean CRLB / mmol/L wet tissue	Mean intrasubject SD (CoV) / mmol/L wet tissue	Intersubject SD (CoV) / mmol/L wet tissue
α-ATP	0.60 (33.5%) ± 0.41	0.83 (44.0%) ± 0.16	0.99 (54.9%) ± 0.31	0.25 (13.7%)
γ-ATP	0.56 (29.9%) ± 0.50	0.86 (43.5%) ± 0.17	0.96 (51.2%) ± 0.33	0.25 (13.5%)
P_i	0.40 (95.0%) ± 0.28	0.66 (42.7%) ± 0.12	0.59 (39.1%) ± 0.18	0.20 (13.2%)
GPC	0.45 (30.2%) ± 0.40	0.66 (42.0%) ± 0.15	0.55 (34.7%) ± 0.14	0.36 (22.8%)
GPE	0.36 (22.9%) ± 0.23	0.57 (42.2%) ± 0.13	0.52 (38.4%) ± 0.15	0.31 (23.0%)
PC	0.21 (15.5%) ± 0.21	0.30 (43.4%) ± 0.07	0.22 (31.1%) ± 0.04	0.16 (23.5%)
PE	0.17 (24.0%) ± 0.11	0.28 (44.6%) ± 0.05	0.24 (37.1%) ± 0.06	0.12 (18.5%)
NAD^+	0.86 (132.5%) ± 0.71	1.09 (62.1%) ± 0.19	1.29 (66.0%) ± 0.38	0.28 (14.6%)
UDPG	0.73 (37.6%) ± 0.48	1.00 (97.6%) ± 0.16	0.97 (77.5%) ± 0.21	0.17 (13.6%)
PEP/PtdC	0.31 (25.0%) ± 0.27	0.43 (65.1%) ± 0.08	0.52 (71.4%) ± 0.24	0.17 (23.1%)

Complex permittivity must be considered when selecting an exogenous reference. And as it changes with frequency, the static conductivity (such as estimated using the Biot-Savart law) cannot be assumed to be a good approximation for the conductivity at the target frequency.

If the acquisition parameters and hardware are not identical between scans, the scanner- and vendor-specific processing should be accounted for. For example, the standard Siemens CSI ICE code applies a scaling factor to give approximately the same signal intensity no matter the resolution.

To apply previously acquired field maps, the transformation of the data between different coordinate systems must be carefully checked. Small differences in position can lead to large errors, especially when the $\boldsymbol{B}_1$ is very inhomogeneous. Coil loading must also be accounted for.

The PSF will affect the correction. In many cases, the effect may not be large enough to be worth including, but it should still be considered. Similarly, the effect of phases across the PSF, and in array combination, should be considered.

Some of these considerations may seem minor, reducing the final error by only a percent or two. However, this should be compared to the improvements that can be gained through an expensive piece of new equipment. The increase in field strength from 3 T to 7 T increases ^{31}P SNR by up to 2.7 times (23). This allows faster, better quantified scanning protocols to be developed and has the potential to bring ^{31}P-MRS into the clinical regime. A 2.7 × increase in SNR from 5 to 13 gives about a 15% improvement in analysis. Increasing SNR from 10 to 27 gives a 10% improvement. So if the error in the quantification protocol can be improved by a single percent, then the value provided is equivalent to 5 – 10% of the difference between a 3 T and 7 T MR scanner. So even relatively small improvements should not be neglected.

9.5. Summary

1. The 16 × 16 × 8 CSI matrix size gave less variable results than the 12 × 12 × 8 matrix size.

2. The semi-constrained Voigt linewidth analysis had a lower bias than the constrained Voigt linewidth analysis, with the same variability.

3. The 18 mM phosphate exogenous reference gave more variable data than the γ-ATP endogenous reference, but allows greater insight into liver metabolism.

4. Accounting for time, volume and differences in prior knowledge, there was a 65% improvement in γ-ATP CRLB compared to a literature 3D CSI scan acquired with a 10 cm loop and a 62% improvement compared to 3D ISIS.

5. The CoR for the final protocol ranged from 16% (for PC) to 132% (for NAD^+).

9.6. References

1. Hultman E, von Nilsson LH, Sahlin K. Adenine Nucleotide Content of Human Liver Normal Values and Fructose-Induced Depletion. Scand J Clin Lab Invest. 1975; 35(3):245-51.
2. Inai K, Noriki S, Kinoshita K, Nishijima A, Sakai T, Kimura H, Naiki H. Feasibility of liver weight estimation by postmortem computed tomography images: An autopsy study. Pathol Int. 2014; 64(7):315-24.
3. Cavassila S, Deval S, Huegen C, van Ormondt D, Graveron-Demilly D. Cramér-Rao bounds: an evaluation tool for quantitation. NMR Biomed. 2001; 14(4):278-83.
4. Sevastianova K, Hakkarainen A, Kotronen A, Cornér A, Arkkila P, Arola J, Westerbacka J, Bergholm R, Lundbom J, Lundbom N, Yki-Järvinen H. Nonalcoholic Fatty Liver Disease: Detection of Elevated Nicotinamide Adenine Dinucleotide Phosphate with in Vivo 3.0-T 31P MR Spectroscopy with Proton Decoupling. Radiology. 2010; 256(2):466-73.
5. Valkovic L, Chmelik M, Krssak M. In-vivo P-31-MRS of skeletal muscle and liver: A way for non-invasive assessment of their metabolism. Anal Biochem. 2017; 529:193-215.
6. Purvis LAB, Clarke WT, Biasiolli L, Valkovic L, Robson MD, Rodgers CT. OXSA: An open-source magnetic resonance spectroscopy analysis toolbox in MATLAB. Plos One. 2017; 12(9):e0185356.
7. Rodgers CT, Robson MD. Receive Array Magnetic Resonance Spectroscopy: Whitened Singular Value Decomposition (WSVD) Gives Optimal Bayesian Solution. Magn Reson Med. 2010; 63(4):881-91.

8. Ernst RR, Bodenhausen G, Wokaun A. Principles of nuclear magnetic resonance in one and two dimensions. Oxford: Clarendon Press; 1987. xxiv, 610 p p.

9. Kreis R. The Trouble With Quality Filtering Based on Relative Cramer-Rao Lower Bounds. Magn Reson Med. 2016; 75(1):15-8.

10. Pohmann R, von Kienlin M. Accurate phosphorus metabolite images of the human heart by 3D acquisition-weighted CSI. Magn Reson Med. 2001; 45(5):817-26.

11. Mareci TH, Brooker HR. Essential Considerations for Spectral Localization Using Indirect Gradient Encoding of Spatial Information. J Magn Reson. 1991; 92(2):229-46.

12. Chmelik M, Považan M, Krššák M, Gruber S, Tkačov M, Trattnig S, Bogner W. In vivo 31P magnetic resonance spectroscopy of the human liver at 7 T: an initial experience. NMR Biomed. 2014; 27(4):478-85.

13. Abrigo JM, Shen J, Wong VWS, Yeung DKW, Wong GLH, Chim AML, Chan AWH, Choi PCL, Chan FKL, Chan HLY, Chu WCW. Non-alcoholic fatty liver disease: Spectral patterns observed from an in vivo phosphorus magnetic resonance spectroscopy study. J Hepatol. 2014; 60(4):809-15.

14. Mann DV, Lam WW, Magnus Hjelm N, So NM, Yeung DK, Metreweli C, Lau WY. Biliary drainage for obstructive jaundice enhances hepatic energy status in humans: a 31-phosphorus magnetic resonance spectroscopy study. Gut. 2002; 50(1):118-22.

15. Laufs A, Livingstone R, Nowotny B, Nowotny P, Wickrath F, Giani G, Bunke J, Roden M, Hwang J-H. Quantitative liver 31P magnetic resonance spectroscopy at 3T on a clinical scanner. Magn Reson Med. 2014; 71(5):1670-5.

16. Qayyum A. MR Spectroscopy of the Liver: Principles and Clinical Applications. Radiographics. 2009; 29(6):1653-64.

17. ter Voert EG, Heijmen L, van Laarhoven HW, Heerschap A. In vivo magnetic resonance spectroscopy of liver tumors and metastases. World J Gastroenterol. 2011; 17(47):5133-49.

18. Purvis LAB, Clarke WT, Biasiolli L, Robson MD, Rodgers CT. Linewidth Constraints in Matlab AMARES using per-Metabolite T_2 and per-Voxel Delta B_0. In the Proceedings of the 22nd Annual Meeting of ISMRM, Milan, Italy, 2014. p. 2885.

19. DelaBarre L, Neubauer S, Robson MD, Vaughan JT, Rodgers CT. B_0 shimming further improves human cardiac ^{31}P-MRS at 7 tesla. In the Proceedings of the 23rd Annual Meeting of ISMRM, Toronto, Canada, 2015. p. 3152.

20. Brinkmann G, Melchert UH, Muhle C, Brossmann J, Link J, Reuter M, Heller M. Influence of different fasting periods on P-31-MR-spectroscopy of the liver in normals and patients with liver metastases. Eur Radiol. 1996; 6(1):62-5.

21. Fritsch M, Koliaki C, Livingstone R, Phielix E, Bierwagen A, Meisinger M, Jelenik T, Strassburger K, Zimmermann S, Brockmann K, Wolff C, Hwang J-H, Szendroedi J, Roden M. Time course of postprandial hepatic phosphorus metabolites in lean, obese, and type 2 diabetes patients. The American Journal of Clinical Nutrition. 2015; 102(5):1051-8.

22. Schilling A, Gewiese R, Stiller D, Römer T, Wolf KJ. Einfluß der Ernährungslage auf das 31P-MR-Spektrum der gesunden Leber. Fortschr Röntgenstr. 1990; 153(10):369-72.

23. Rodgers CT, Clarke WT, Snyder C, Vaughan JT, Neubauer S, Robson MD. Human cardiac 31P magnetic resonance spectroscopy at 7 Tesla. Magn Reson Med. 2014; 72(2):304-15.

10. Absolute quantification of ^{31}P metabolites in healthy and cirrhotic livers

In Chapters 4 to 9, an absolute quantification protocol for human hepatic ^{31}P-MRS at 7 T was developed, meeting the primary aim of this thesis. The secondary aim was to demonstrate that this protocol is feasible to use in clinical studies, and show its potential as a clinical tool. Therefore in this chapter, we compare the results of the quantification of concentrations in 10 normal volunteers to literature values, and to 11 patients with liver cirrhosis. A description of the subjects and data acquisition was given in Section 4.5.

10.1. Normal values

In addition to the absolute quantification protocol described in Chapter 8, metabolites were also quantified as a ratio to the total phosphorus (i.e. the sum of all metabolite peaks). Automatic quality assurance for the ratios used cut-offs matching those used for the endogenous reference (i.e. voxels excluded if PCr amplitude > 5 a.u., PME CoV > 20%, PDE CoV > 10%), rather than the ones used in the final protocol (i.e. voxels excluded if PCr > 1mmol/L wet tissue, PME CoV > 70%, PDE CoV > 60%), to give a similar mean number of voxels for both methods. The ratios of each metabolite to total phosphate are given in Table 10.1, where only the value from the first 28 min normal volunteer scan is given (i.e. not including the repeat 28 min scan). Metabolite concentrations computed for both sets of volunteer scans are given in Table 10.2. When comparing to literature values and to patients with cirrhosis, the values from the first scan of each subject were used. The total PDE concentration measured in healthy volunteers was 2.94 ± 0.65 mmol/L wet tissue, of which 1.59 ± 0.36 mmol/L wet tissue was from GPC and 1.35 ± 0.31 mmol/L wet tissue from GPE. The PtdC/PEP concentration was 1.38 ± 0.31 mmol/L wet tissue.

Part of this chapter has been published in Purvis LAB et al. Phosphodiester content measured in human liver by in vivo ^{31}P MR spectroscopy at 7 tesla. Magn Reson Med. 2017; 78(6):2095-105.

Table 10.1. Mean ± SD of ratios to total phosphate for 10 normal volunteers and 11 patients with cirrhotic livers from a 28 min 3D CSI acquisition. Total phosphate was calculated as the sum of all visible peaks. The normal liver ratios are from the first volunteer scan. Significant differences between healthy and cirrhotic ratios are marked with stars: * $P < 0.05$, ** $P < 0.01$.

Metabolite	Normal liver ratio to total phosphate / %	Cirrhotic liver ratio to total phosphate / %
α-ATP	14.1 ± 0.9	14.4 ± 0.8
γ-ATP	13.7 ± 0.5	13.6 ± 0.5
P_i	11.3 ± 1.0	10.0 ± 1.2**
GPC	11.7 ± 2.0	12.8 ± 2.8
GPE	7.6 ± 1.2	9.1 ± 2.2 *
PC	5.3 ± 0.8	4.7 ± 1.2
PE	3.8 ± 0.7	3.8 ± 0.6
NAD^+	12.2 ± 0.5	12.2 ± 1.7
UDPG	10.1 ± 1.0	10.0 ± 1.6
PtdC/PEP	6.8 ± 1.3	5.4 ± 1.6 *

10.1.1. Metabolite quantification

The easiest method for comparing quantification methods is the γ-ATP concentration, which is assumed to be constant in the healthy liver. However, published "absolute quantification" γ-ATP concentrations have varied widely (1.9 ± 0.4 to 3.8 ± 0.3 mmol/L wet tissue) (1-5). Our results fall at the bottom end of this range (1.88 ± 0.25 mmol/L wet tissue). In vitro, γ-ATP concentration has been determined as 2.65 mmol/L wet volume (6, 7) . However, this value could be lower than the in vivo concentration due to metabolite fluctuations during the cold storage process (8). On the other hand, it may be *higher* than the in vivo concentration, as some portion of ATP might be invisible to MR methods (see Section 3.2.1).

Table 10.2. Mean ± SD of concentrations for 10 normal volunteers and 11 patients with cirrhotic livers from a 28 min 3D CSI acquisition. The PDE concentration is the sum of the GPC and GPE concentrations, and the PME concentration is the sum of the PC and PE concentrations. Significant differences between healthy and cirrhotic concentrations are marked with stars: * $P < 0.05$, ** $P < 0.01$. The values from the first normal liver scans are plotted with the values from the cirrhotic liver in Fig 10.4.

Metabolite	Normal liver: scan 1 / mmol/L wet weight	Normal liver: scan 2 / mmol/L wet weight	Cirrhotic liver / mmol/L wet weight	Difference between normal (scan 1) and cirrhotic livers/ %	*P*-value
α-ATP	1.80 ± 0.25	1.94 ± 0.25	1.49 ± 0.37	-17.60	0.01 *
γ-ATP	1.88 ± 0.25	2.01 ± 0.32	1.52 ± 0.29	-19.25	0.003 **
P_i	1.50 ± 0.20	1.60 ± 0.20	1.14 ± 0.29	-24.00	0.002 **
GPC	1.59 ± 0.36	1.69 ± 0.35	1.59 ± 0.43	0.09	0.50
GPE	1.35 ± 0.31	1.47 ± 0.24	1.52 ± 0.38	12.56	0.14
PC	0.69 ± 0.16	0.71 ± 0.18	0.55 ± 0.17	-20.93	0.03 *
PE	0.65 ± 0.12	0.66 ± 0.05	0.67 ± 0.14	3.13	0.36
NAD^+	1.95 ± 0.28	2.09 ± 0.49	1.69 ± 0.35	-13.59	0.035 *
UDPG	1.25 ± 0.17	1.48 ± 0.23	1.09 ± 0.37	-12.69	0.11
PtdC/PEP	0.73 ± 0.17	0.79 ± 0.20	0.60 ± 0.19	-18.16	0.05 *
PDE	2.94 ± 0.65	3.16 ± 0.56	3.11 ± 0.75	5.83	0.29
PME	1.34 ± 0.26	1.37 ± 0.19	1.22 ± 0.24	-9.33	0.13

The variation between centres using exogenous references is greater than the variation within studies at a particular centre (9). It might be possible to resolve these differences in a large multi-centre study, but until then each centre must be self-referenced (i.e. compare to its own normal values). That way, relative differences can still be detected in the diseased state even when variation between centres is large enough to preclude comparison of absolute values.

Coil loading must also be accounted for. In this study we used the signal from a reference fiducial. Alternatively, one could use the ERETIC (electronic reference to access in vivo concentrations) method, which uses an electronic reference signal transmitted by a broadband antenna as the calibration reference (10). The broadband antenna is practically immune to changes in loading during transmission of the reference signal. Meanwhile reception of the reference signal is affected by coil loading in the same way as reception of the NMR signal from the body. The advantage of ERETIC is that the signal is already present within the main acquisition, can be precisely calibrated, switched on/off on demand, and placed spectrally away from any resonances of biological interest, whereas the fiducial method requires running a series of inversion-recovery FIDs.

Despite the feasibility of resolving individual PME and PDE peaks at 3 T and below using ^{1}H-decoupling, there has been only one study that has successfully quantified their concentrations separately (4). In other studies either PC/PE or GPC/GPE were not well resolved (2), or only concentration ratios were reported (11-13).

The study by Li et al. which achieved quantification of these metabolites used ^{1}H-decoupling, NOE-enhancement and phospholipid-saturation (4). Li et al. did not quantify UDPG concentration. The spectra were localized using fully-sampled 3D CSI with nominal voxel size of 27 or 64 mL, allowing the quantitation of only a single voxel per subject. They reported significantly larger concentrations for all peaks except NAD^+ ($P < 0.05$). However, if their results are scaled to give the same γ-ATP concentration as in this study, the PC concentration would be 0.56 ± 0.05 mmol/L wet tissue which is significantly smaller than our value (0.69 ± 0.16 mmol/L wet tissue, $P = 0.01$) but there are no other significant differences. This indicates that the difference between the two studies may arise solely from calibration errors.

At 7 T, ^{1}H-decoupling, NOE-enhancement and phospholipid saturation is not necessary to resolve the PDE region, and the added SNR allows better localization with three to ten times smaller voxels than used by Li et al. (4).

Although PC and PE are the dominant peaks in the PME region, it is likely that there are other metabolites in that region (14). It is therefore possible that using ^{1}H-decoupling would further enhance quantitation in that region, as well as increasing SNR. We were not able to attempt ^{1}H-decoupling because the coil used for this work was single-resonance. However, it should be noted that even if a suitable coil were available, decoupling may be undesirable at 7 T: ^{1}H-decoupling demands high power, which would likely exceed the legal SAR limits (15).

A simpler improvement to the protocol, if we had had access to a suitable dual-tuned coil, would have been NOE, which does not demand such high SAR. In the brain, this has been shown to increase SNR for ^{31}P-MRS, albeit with the potential of adding variability in metabolite quantitation (15).

By combining the PME and PDE peaks, we can compare our results with more studies. Fig 10.1 compares the results of this study with five previous studies, one using an endogenous reference (14), and four using an exogenous reference (1-4). Two studies ran at 3 T, one at 1.6 T and two at 1.5 T.

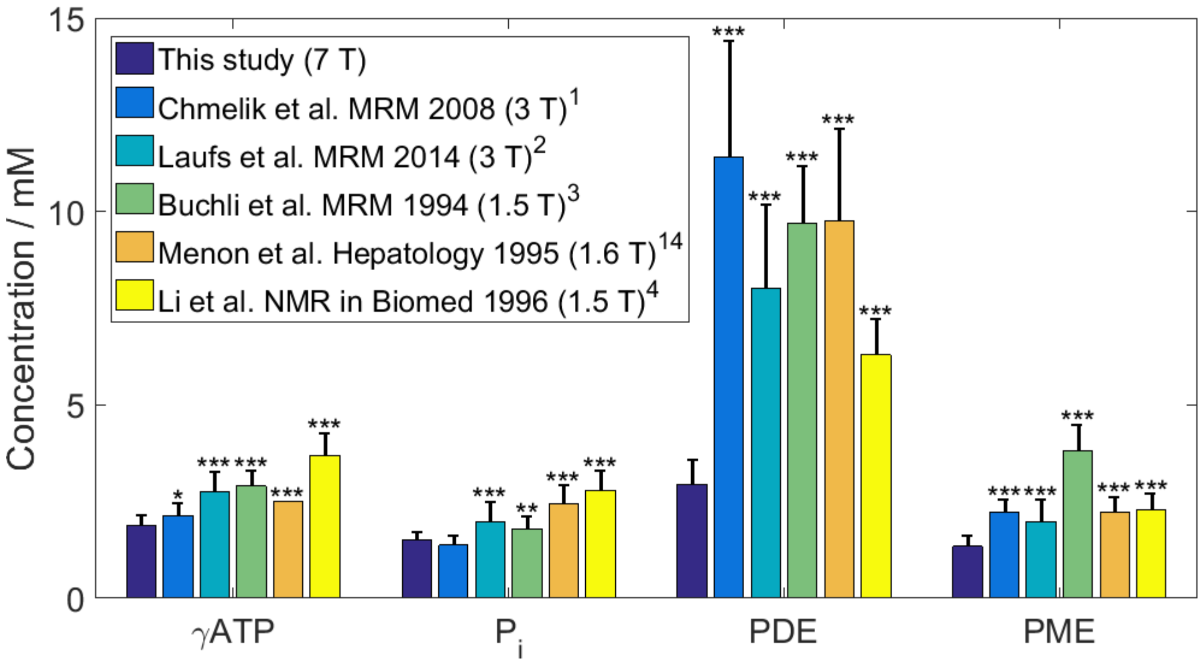

Fig 10.1. Comparison of healthy ^{31}P liver metabolite values against the literature. Normal liver ^{31}P metabolite concentrations from this study are compared against the refs. (1-4, 14). Standard deviations are shown by the error bars on each bar. Stars indicate level of significance of the difference from this study: * $P < 0.05$, ** $P < 0.01$, *** $P < 0.001$.

The concentration of P_i is significantly smaller here than in refs (2-4, 14) ($P < 0.01$). PME is significantly smaller than in each of the other studies ($P < 0.0001$, 0.6 – 2.5 mmol/L wet tissue difference), but the difference for PDE is larger in all cases ($P < 0.0001$, 3.4 – 8.4 mmol/L wet tissue difference). Part of this difference may therefore be explained by calibration differences, and as discussed above it is challenging to know the "correct" answer. In fact, if the literature values are scaled to match our γ-ATP concentration, only the PDE concentrations stand out from the literature values (see Fig 10.2).

At low field strength, it is difficult to distinguish the PEP/PtdC peak from the PDE peak because the peaks strongly overlap (16). But the differences are still significant in the studies where the peaks were quantified separately (2, 4).

One possible explanation for this difference is the underlying resonance from endoplasmic reticulum, which lies in the same spectral region as PDE. In a direct comparison between

1.5 T and 3 T, there was a small reduction in the underlying broad peak and a small positive difference between PME/PDE ratios (11). This effect is likely to have become more prominent at 7 T, because the endoplasmic reticulum peak will have broadened even further, and may be below the signal-to-noise threshold for detection.

In vitro concentrations for GPE (2.59 ± 0.39 mmol/L wet tissue) and GPC (2.48 ± 0.48 mmol/L wet tissue) (17), converted from the published mmol/kg wet weight values using 1.054 kg/L specific gravity (7), match this study more closely than any study except perhaps Li et al. (4). On the other hand, the PC and PE concentrations measured in the in vitro study were even lower (0.17 ± 0.03 and 0.17 ± 0.04 mmol/L wet tissue) than the ones reported here. This is possibly due to metabolite fluctuations in cold storage which do not affect the PDE peaks (8), but it is also likely that signal from smaller peaks in the region is included in our analysis (17).

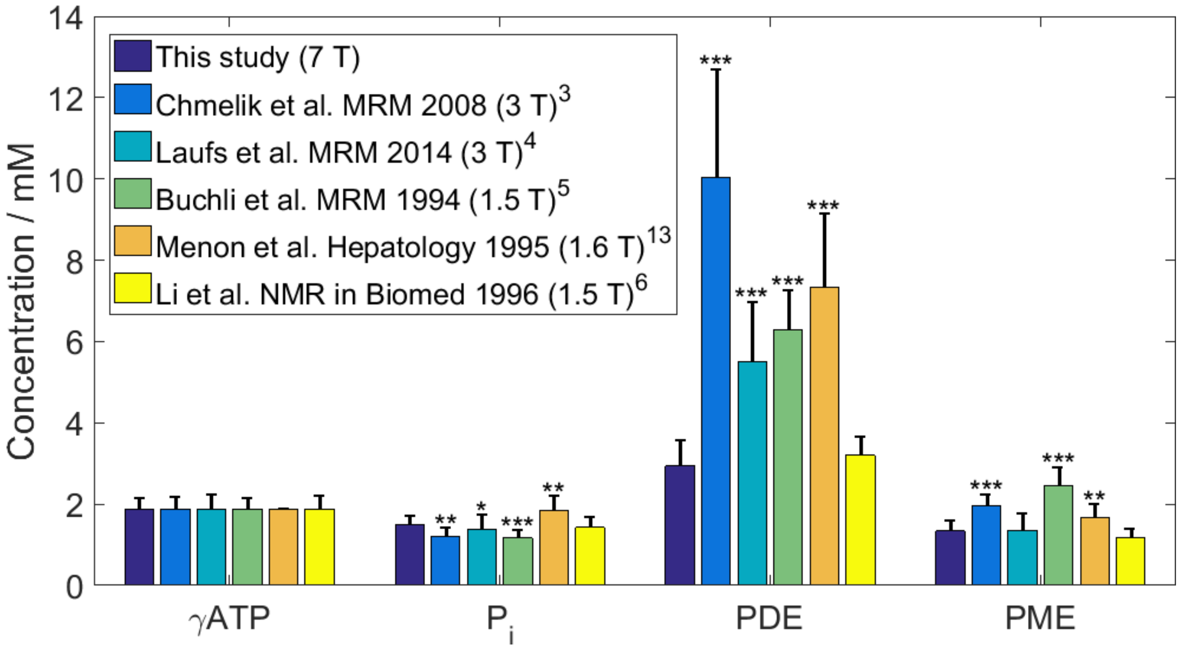

Fig 10.2. Comparison of healthy ^{31}P liver metabolite values against the literature, with all studies scaled to our γ-ATP concentration of 1.88 mmol/L wet tissue. Normal liver ^{31}P metabolite concentrations from this study are compared against the refs. (1-4, 14). Standard deviations are shown by the error bars on each bar. Stars indicate level of significance of the difference from this study: * $P < 0.05$, ** $P < 0.01$, *** $P < 0.001$.

10.2. Application in patients with liver cirrhosis

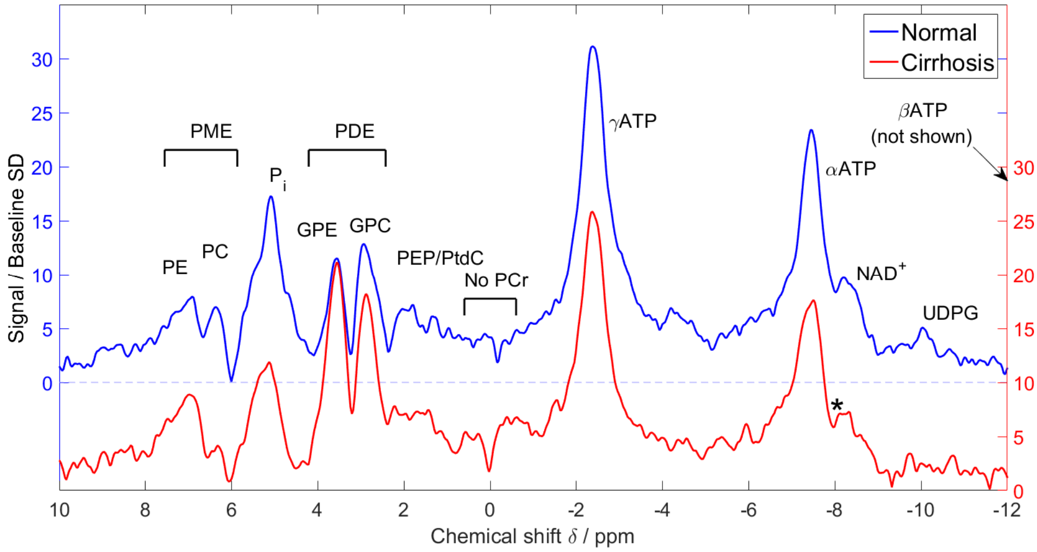

Fig 10.3. Representative spectra from a healthy volunteer (in blue) and a patient with liver cirrhosis (in red). The spectra were selected such that saturation- and sensitivity-corrections were approximately equal.

10.2.1. Results

Representative spectra from a healthy volunteer and patient with liver cirrhosis are shown in Fig 10.3. Average metabolite concentrations for cirrhotic liver are also given in Table 10.2, and the concentrations for individual patients are given in Table 10.3 with their diagnoses. The mean total liver volume for cirrhotic liver was 1.76 ± 0.22 L, and the mean volume analysed in cirrhotic liver was 0.63 ± 0.27 L from 40 ± 20 voxels. The coverage was 37 ± 17%, which was not significantly different than in healthy volunteers (38 ± 10%). The average γ-ATP linewidth was 30 ± 10 Hz for patients indicates that the shim was also not significantly different from in healthy volunteers (31 ± 8 Hz, $P = 0.4$). On the other hand, the SNR was significantly lower (20 ± 2 vs 17 ± 3, $P = 0.007$). This 15% reduction in SNR mimics the 20% reduction in γ-ATP concentration.

Table 10.3. Metabolite concentrations of 11 patients with liver cirrhosis. Concentrations are given as mean ± inter-voxel SD. Five have been diagnosed with Hepatitis C (HCV), three with non-alcoholic fatty liver disease (NAFLD), two with alcoholic steatohepatitis (ASH), and one with auto-immune hepatitis (AIH). The inter-voxel SDs are reduced compared to fully independent measurements, because these data have not been corrected for voxel overlap. Inter-subject means are given in Table 10.1. These concentrations are plotted with concentrations from the first normal volunteer scan in Fig 10.4.

Subject	**1**	**2**	**3**	**4**	**5**	**6**	**7**	**8**	**9**	**10**	**11**
Diagnosis	**HCV**	**HCV**	**HCV**	**HCV**	**HCV**	**NAFLD**	**NAFLD**	**NAFLD**	**ASH**	**ASH**	**AIH**
α-ATP / mmol/L wet tissue	2.45 ± 1.32	1.09 ± 0.35	1.39 ± 0.57	1.34 ± 0.30	1.12 ± 0.28	1.44 ± 0.38	1.45 ± 0.62	1.70 ± 0.66	1.32 ± 0.44	1.58 ± 0.40	1.47 ± 0.50
γ-ATP / mmol/L wet tissue	2.17 ± 1.09	1.12 ± 0.39	1.49 ± 0.51	1.45 ± 0.26	1.16 ± 0.20	1.50 ± 0.38	1.66 ± 0.61	1.73 ± 0.61	1.34 ± 0.41	1.66 ± 0.41	1.45 ± 0.43
P_i / mmol/L wet tissue	1.92 ± 0.77	0.95 ± 0.30	1.05 ± 0.31	1.03 ± 0.17	0.84 ± 0.17	1.04 ± 0.28	1.25 ± 0.28	1.22 ± 0.32	0.95 ± 0.27	1.07 ± 0.21	1.26 ± 0.37
GPC / mmol/L wet tissue	1.59 ± 0.70	0.74 ± 0.26	1.51 ± 0.36	1.52 ± 0.26	1.51 ± 0.23	1.47 ± 0.39	1.60 ± 0.44	1.97 ± 0.46	1.71 ± 0.52	2.53 ± 0.59	1.30 ± 0.38
GPE / mmol/L wet tissue	1.90 ± 0.72	0.64 ± 0.23	1.80 ± 0.42	1.15 ± 0.21	1.46 ± 0.25	1.43 ± 0.40	1.45 ± 0.46	1.84 ± 0.47	1.47 ± 0.47	1.90 ± 0.48	1.73 ± 0.53
PC / mmol/L wet tissue	0.93 ± 0.33	0.74 ± 0.22	0.50 ± 0.16	0.71 ± 0.15	0.34 ± 0.10	0.46 ± 0.19	0.48 ± 0.13	0.41 ± 0.13	0.47 ± 0.17	0.45 ± 0.12	0.55 ± 0.20
PE / mmol/L wet tissue	0.84 ± 0.44	0.64 ± 0.19	0.62 ± 0.19	0.45 ± 0.14	0.54 ± 0.08	0.94 ± 0.24	0.79 ± 0.20	0.63 ± 0.18	0.55 ± 0.15	0.64 ± 0.17	0.68 ± 0.33
NAD$^+$ / mmol/L wet tissue	1.80 ± 1.10	1.26 ± 0.66	1.55 ± 0.69	1.77 ± 0.57	1.23 ± 0.36	2.28 ± 0.68	1.66 ± 0.67	2.15 ± 1.11	1.37 ± 0.63	1.96 ± 0.82	1.53 ± 0.46
UDPG / mmol/L wet tissue	1.43 ± 1.06	0.55 ± 0.30	1.03 ± 0.74	1.07 ± 0.67	0.91 ± 0.47	1.51 ± 0.69	1.35 ± 0.98	1.38 ± 0.93	0.82 ± 0.59	1.50 ± 0.74	0.48 ± 0.21
PtdC/PEP / mmol/L wet tissue	0.83 ± 0.38	0.60 ± 0.50	0.54 ± 0.26	0.70 ± 0.37	0.33 ± 0.18	0.32 ± 0.17	0.82 ± 0.46	0.79 ± 0.50	0.62 ± 0.42	0.67 ± 0.26	0.34 ± 0.10
PDE / mmol/L wet tissue	3.48 ± 1.32	1.38 ± 0.48	3.31 ± 0.76	2.67 ± 0.46	2.97 ± 0.46	2.91 ± 0.78	3.05 ± 0.82	3.81 ± 0.91	3.18 ± 0.97	4.43 ± 1.04	3.03 ± 0.90
PME / mmol/L wet tissue	1.77 ± 0.68	1.38 ± 0.39	1.12 ± 0.30	1.16 ± 0.24	0.88 ± 0.16	1.40 ± 0.40	1.28 ± 0.27	1.04 ± 0.26	1.02 ± 0.29	1.09 ± 0.24	1.23 ± 0.46

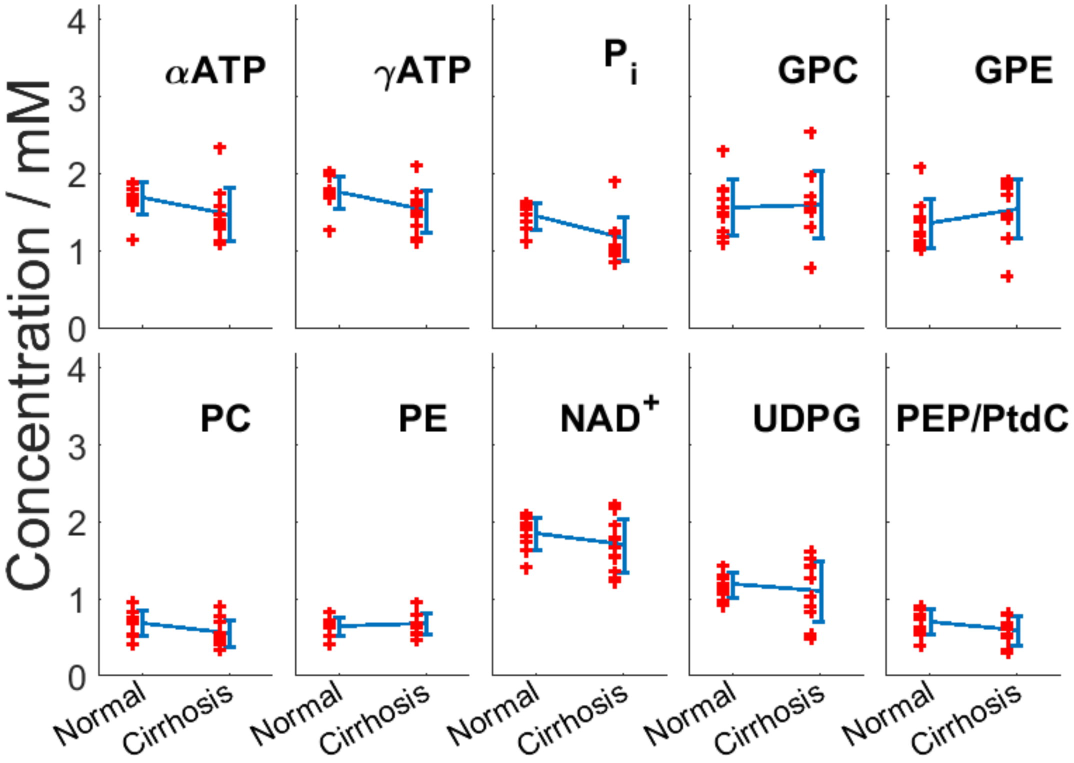

Fig 10.4. **Concentrations in normal volunteers and patients.** Each red '+' marks a subject. The blue line shows the mean ± SD of each group. ATP, P_i, PC, NAD^+ and PtdC/PEP are significantly lower in cirrhosis than in normal volunteers ($P < 0.05$). In this case, "mM" is defined as mmol / L of wet tissue. The mean ± SD of each group are given in Table 10.2, and the individual concentrations of the patient group are given in Table 10.3.

As would be expected, patients with very high BMI allow much lower coverage than the others because the liver is further away from the RF coil. The lowest coverages were 18% for a patient with BMI of 43.9 $kg.m^{-2}$, and 11.5% for a patient with BMI of 35.6 $kg.m^{-2}$. Only NAD^+ has a significantly larger variance than in healthy volunteers (0.35 vs 0.28, F-test, $P = 0.01$). Our protocol can therefore be considered effective in patients with cirrhosis.

Fig 10.4 shows the concentrations for each volunteer and patient. There is significant reduction in α-ATP, γ-ATP, P_i, PC, NAD^+ and PEP/PtdC concentrations ($P < 0.05$). GPE concentrations increased by 13%, but the change was not significant ($P = 0.14$). The reduction in P_i and PEP/PtdC, and an increase in GPE were significant when comparing the metabolite ratios to total phosphorus (see Table 10.1).

The PCr/ATP ratio is significantly higher in cirrhosis (0.49 ± 0.11 vs 0.42 ± 0.07, $P = 0.05$). Although this could be caused by increased muscle contamination, this change has been seen in other studies (18). The automatic removal of spectra that are contaminated by PCr in our study limits this comparison. However, the mean analysed volume was the same for healthy volunteers and patients, and no additional voxels were discarded. This indicates that the change is real and is not due to increased contamination.

10.2.2. Comparison to literature

Two studies have investigated the differences between healthy and cirrhotic livers using ^{31}P-MRS. Both studies were performed at 1.5 T, but while Noren et al. used DRESS localization, Dezortova et al. used 2D CSI localization (19, 20). Dezortova et al. reported a lower P_i concentration than Noren et al. ($P = 0.002$). However, both studies show the same trends in PME, PDE, P_i and ATP, between healthy volunteers and patients with liver cirrhosis. As Dezortova et al. scanned a larger number of patients (80 vs 16), and found larger changes (20), we will compare our values to theirs, rather than Noren et al.

Dezortova et al. reported 21% decrease in ATP in cirrhosis, which matches the finding of a 19% decrease in this study (20). A possible reason for this change in ATP might be the presence of fatty infiltrations, which affects the assumption of homogenous metabolite distribution across the voxels. This could potentially be addressed in future studies by a lipid partial volume correction.

There was a significant 24% reduction in P_i ($P = 0.002$), which agrees with the 18% change reported by Dezortova et al. in patients with cirrhosis. A reduction in P_i has been previously correlated with an increase in hepatic inflammation (21-23).

On the other hand, Dezortova et al. found a significant 34% reduction in PDE, whereas we saw a 13% increase in GPE (P = 0.14). This difference is partially accounted for by the 18% reduction in PEP/PtdC (P = 0.05). Dezortova et al. reported a 14% increase in PME. In this study, while the PE concentration increased by 3%, the overall PME concentration decreased by 9%. This was driven by the 21% reduction in PC (P = 0.03). The difference between the normal concentrations of PDE and PME between the two studies was proposed in Section 9.1.1 to be due, in part, to changes in the underlying phospholipid signal. In that case, the changes seen by Dezortova et al. could be due to changes in the phospholipid signal, rather than changes in the PME and PDE concentrations themselves. An increase in PDE and decrease in PME might be surprising, as the opposite change has been seen in cirrhosis not only at lower field strengths in vivo, but also in vitro (24). However, the same study showed no correlation between in vitro data and in vivo data (24). This suggests there may be a systematic difference in what is actually being measured at lower field strengths and at 7 T, and in vitro and in vivo. Another possibility is that the T_1 values significantly change between the healthy volunteers and patients. However, a 90% decrease in GPE was seen in vitro, compared to the 13% increase we found (24). For T_1 to be the sole cause of this difference, it would have to increase from 4.4 s to 117 s (for a voxel acquired with our protocol and a 31° flip angle).

10.2.3. Hepatic ^{31}P-MRS as a clinical tool

Using either a cut-off of 1.73 mmol/L wet tissue for γ-ATP or 1.26 mmol/L wet tissue for P_i allows the separation of normal and cirrhotic livers with 91% sensitivity (i.e. 10 out of 11 patients with cirrhosis positively identified) and 90% specificity (i.e. 1 out of 10 healthy volunteers falsely identified). All the patients have mild liver cirrhosis (Child-Pugh score 5 or 6), so the next step would be to test the ability of this protocol to distinguish between different Child-Pugh stages. It is expected that the changes would be more significant with more severe cirrhosis.

10.3. Summary

1. The γ-ATP concentration determined using this 7 T liver protocol (1.88 ± 0.25 mmol/L wet tissue) was at the lower end of literature values (1.9 – 3.8 mmol/L wet tissue).

2. PME and PDE concentrations were even lower relative to reported literature values (0.6 – 8.4 mmol/L wet tissue difference, $P < 0.001$).

3. The data from patients with cirrhosis was of similar quality to the data from healthy volunteers (37 ± 17% vs 38 ± 10% coverage; 30 ± 10 Hz vs 31 ± 8 Hz γ-ATP linewidth).

4. ATP, P_i, PC, NAD^+ and PtdC/PEP were significantly lower in cirrhosis than in healthy volunteers (14 – 25% reduction, $P < 0.05$).

5. Using either a cut-off of 1.73 mmol/L wet tissue for γ-ATP or 1.26 mmol/L wet tissue for P_i allows the separation of normal and cirrhotic livers with 91% sensitivity and 90% specificity in this pilot cohort.

10.4. References

1. Chmelik M, Schmid AI, Gruber S, Szendroedi J, Krssak M, Trattnig S, Moser E, Roden M. Three-dimensional high-resolution magnetic resonance spectroscopic imaging for absolute quantification of P-31 metabolites in human liver. Magn Reson Med. 2008; 60(4):796-802.
2. Laufs A, Livingstone R, Nowotny B, Nowotny P, Wickrath F, Giani G, Bunke J, Roden M, Hwang J-H. Quantitative liver 31P magnetic resonance spectroscopy at 3T on a clinical scanner. Magn Reson Med. 2014; 71(5):1670-5.
3. Buchli R, Meier D, Martin E, Boesiger P. Assessment of absolute metabolite concentrations in human tissue by 31P MRS in vivo. Part II: Muscle, liver, kidney. Magn Reson Med. 1994; 32(4):453-8.
4. Li CW, Negendank WG, Murphy-Boesch J, Padavic-Shaller K, Brown TR. Molar Quantitation of Hepatic Metabolites In Vivo in Proton-decoupled, Nuclear Overhauser Effect Enhanced 31P NMR Spectra Localized by Three-dimensional Chemical Shift Imaging. NMR Biomed. 1996; 9(4):141-55.
5. Rajanayagam V, Lee RR, Ackerman Z, Bradley WG, Ross BD. Quantitative P-31 MR spectroscopy of the liver in alcoholic cirrhosis. J Magn Reson Imaging. 1992; 2(2):183-90.
6. Hultman E, von Nilsson LH, Sahlin K. Adenine Nucleotide Content of Human Liver Normal Values and Fructose-Induced Depletion. Scand J Clin Lab Invest. 1975; 35(3):245-51.
7. Inai K, Noriki S, Kinoshita K, Nishijima A, Sakai T, Kimura H, Naiki H. Feasibility of liver weight estimation by postmortem computed tomography images: An autopsy study. Pathol Int. 2014; 64(7):315-24.

8. Changani KK, Fuller BJ, Bell JD, Taylor-Robinson SD, Moore DP, Davidson BR. Improved preservation solutions for organ storage - A dynamic study of hepatic metabolism. Transplantation. 1999; 68(3):345-55.
9. Sijens PE, Dagnelie PC, Halfwerk S, van Dijk P, Wicklow K, Oudkerk M. Understanding the Discrepancies Between 31P MR Spectroscopy Assessed Liver Metabolite Concentrations from Different Institutions. Magn Reson Imaging. 1998; 16(2):205-11.
10. Barantin L, LePape A, Akoka S. A new method for absolute quantitation of MRS metabolites. Magn Reson Med. 1997; 38(2):179-82.
11. Wylezinska M, Cobbold JFL, Fitzpatrick J, McPhail MJW, Crossey MME, Thomas HC, Hajnal JV, Vennart W, Cox IJ, Taylor-Robinson SD. A comparison of single-voxel clinical in vivo hepatic 31P MR spectra acquired at 1.5 and 3.0 Tesla in health and diseased states. NMR Biomed. 2011; 24(3):231-7.
12. Sevastianova K, Hakkarainen A, Kotronen A, Cornér A, Arkkila P, Arola J, Westerbacka J, Bergholm R, Lundbom J, Lundbom N, Yki-Järvinen H. Nonalcoholic Fatty Liver Disease: Detection of Elevated Nicotinamide Adenine Dinucleotide Phosphate with in Vivo 3.0-T 31P MR Spectroscopy with Proton Decoupling. Radiology. 2010; 256(2):466-73.
13. Abrigo JM, Shen J, Wong VWS, Yeung DKW, Wong GLH, Chim AML, Chan AWH, Choi PCL, Chan FKL, Chan HLY, Chu WCW. Non-alcoholic fatty liver disease: Spectral patterns observed from an in vivo phosphorus magnetic resonance spectroscopy study. J Hepatol. 2014; 60(4):809-15.
14. Menon DK, Sargentoni J, Taylor-Robinson SD, Bell JD, Cox IJ, Bryant DJ, Coutts GA, Rolles K, Burroughs AK, Morgan MY. Effect of functional grade and etiology on in vivo hepatic phosphorus-31 magnetic resonance spectroscopy in cirrhosis: biochemical basis of spectral appearances. Hepatology. 1995; 21(2):417-27.
15. Lagemaat MW, van de Bank BL, Sati P, Li SZ, Maas MC, Scheenen TWJ. Repeatability of P-31 MRSI in the human brain at 7T with and without the nuclear Overhauser effect. NMR Biomed. 2016; 29(3):256-63.
16. Chmelík M, Valkovič L, Wolf P, Bogner W, Gajdošík M, Halilbasic E, Gruber S, Trauner M, Krebs M, Trattnig S, Krššák M. Phosphatidylcholine contributes to in vivo 31P MRS signal from the human liver. Eur Radiol. 2015:1-8.
17. Bell JD, Cox IJ, Sargentoni J, Peden CJ, Menon DK, Foster CS, Watanapa P, Iles RA, Urenjak J. A P-31 and H-1-Nmr Investigation in-Vitro of Normal and Abnormal Human Liver. Biochim Biophys Acta. 1993; 1225(1):71-7.
18. Traussnigg S, Kienbacher C, Gajdošík M, Valkovič L, Halilbasic E, Stift J, Rechling C, Hofer H, Steindl-Munda P, Ferenci P, Wrba F, Trattnig S, Krššák M, Trauner M. Ultra-high-field magnetic resonance spectroscopy in non-alcoholic fatty liver disease: Novel mechanistic and diagnostic insights of energy metabolism in non-alcoholic steatohepatitis and advanced fibrosis. Liver Int. 2017; 37(10):1544-53.
19. Noren B, Dahlqvist O, Lundberg P, Almer S, Kechagias S, Ekstedt M, Franzén L, Wirell S, Smedby Ö. Separation of advanced from mild fibrosis in diffuse liver disease using 31P magnetic resonance spectroscopy. Eur J Radiol. 2008; 66(2):313-20.
20. Dezortova M, Taimr P, Skoch A, Spicak J, Hajek M. Etiology and functional status of liver cirrhosis by 31P MR spectroscopy. World J Gastroenterol. 2005; 11(44):6926-31.
21. Jalan R, Sargentoni J, Coutts GA, Bell JD, Rolles K, Burroughs AK, Taylor Robinson SD. Hepatic phosphorus-31 magnetic resonance spectroscopy in primary biliary cirrhosis and its relation to prognostic models. Gut. 1996; 39(1):141-6.
22. Taylor-Robinson SD, Sargentoni J, Bell JD, Thomas EL, Marcus CD, Changani KK, Saeed N, Hodgson HJF, Davidson BR, Burroughs AK, Rolles K, Foster CS, Cox IJ. In vivo and in vitro hepatic phosphorus-31 magnetic resonance spectroscopy and electron microscopy in chronic ductopenic rejection of human liver allografts. Gut. 1998; 42(5):735-43.
23. van Wassenaer-van Hall HN, van der Grond J, van Hattum J, Kooijman C, Hoogenraad TU, Mali WP. 31P magnetic resonance spectroscopy of the liver: correlation with standardized serum, clinical, and histological changes in diffuse liver disease. Hepatology. 1995; 21(2):443-9.
24. Taylor-Robinson SD, Sargentoni J, Bell JD, Saeed N, Changani KK, Davidson BR, Rolles K, Burroughs AK, Hodgson HJF, Foster CS, Cox IJ. In vivo and in vitro hepatic P-31 magnetic resonance spectroscopy and electron microscopy of the cirrhotic liver. Liver. 1997; 17(4):198-209.

11. Conclusions

The aim of this work was to develop an absolute quantification protocol for human hepatic ^{31}P-MRS at 7 T and to demonstrate its feasibility for use in clinical studies.

11.1. Specific achievements

I developed an acquisition protocol that gives high SNR ^{31}P spectra from the human liver in vivo, while also providing good spatial localization and spectral resolution (described in Chapter 4). I updated the group's internal MATLAB cardiac ^{31}P analysis tools, adapting them for the liver, adding a Gaussian component to the fitting which allowed Voigt lineshapes to be used, and writing documentation and tests so that this tool could be released open-source at https://github.com/OXSAtoolbox/OXSA/ (1) (as described in Chapter 5). I determined T_1 relaxation times at 7 T for all metabolites that were visible with the chosen protocol, i.e. except β-ATP (as described in Chapter 6).

I have also thoroughly explored the problem of "absolute" quantification of metabolite concentrations in mmol/L wet tissue. In Chapter 7 I made a series of electromagnetic modelling simulations to determine design criteria for calibration phantoms at 7 T, compared to 1.5 T and 3 T. I then compared three candidate approaches for absolute quantification using data acquired with a simple 10 cm loop coil. Finally, in Chapter 8, I extended these approaches to a clinically-realistic system using a 16-element receive array coil.

The full protocol was applied to 10 healthy volunteers and 11 patients with liver cirrhosis to determine reproducibility (in Chapter 9) and the difference between healthy and diseased liver (in Chapter 10). This protocol allows the distinction between healthy and cirrhotic livers with 90% specificity and sensitivity in this pilot cohort, using cut-offs in either γ-ATP or P_i concentrations.

In conclusion, the intended absolute quantification protocol has indeed been developed, and each of the steps within its creation has moved ^{31}P-MRS towards clinical utility.

11.2. Applications

The first and most obvious application for this protocol is to increase the number of participants in the cirrhosis study. This would allow a greater focus on individual aetiologies and a comparison to other diagnostic methods. It would also allow greater scope for investigation of using multiple markers for disease differentiation, rather than just single peaks. For example, with enough subjects machine learning methods could be used to find the best combination of predictors for cirrhosis (2, 3). This may be possible with as few as 20 subjects per class (4), but, of course, more data is better (5).

Our current tests have 90% specificity and sensitivity in this pilot cohort, which is better than serum tests, conventional ultrasound, or transient elastography but worse than enhanced ultrasound or magnetic resonance elastography (which has up to 100% sensitivity and 96% specificity) (6). However, both ultrasound and elastography rely on changes in liver stiffness, which mean that they are less sensitive to the early stages of liver disease (7). As changes in metabolism have been proposed as the cause of steatosis, ^{31}P-MRS, which measures metabolism directly, has the potential to be a better marker for the early detection liver disease (8).

The resolution of the individual PME and PDE peaks also allows the examination of differences between “healthy” volunteers. Further investigation of the fed and fasted liver may give insight into the optimal state for scans targeting a particular metabolite. Although the scans in this work were performed after an overnight fast, it could be that the change in the GPE peak (for example) is more apparent in the fed state. Another factor that could require further investigation is the effect of age. In a 3 T study, age was not found to significantly change liver metabolism (9). However, the PME and PDE peaks were not fully resolved in that study.

The link between cirrhosis and cancer has been proposed to be due to senescent cells (10). Phospholipid concentration changes depending on the average number of cells in each different phase of the cell growth cycle (11), so ^{31}P-MRS may be able to detect the number of senescent cells. Our protocol is potentially more sensitive to these changes, as the PME and PDE peaks are quantified individually. If it is proven that ^{31}P-MRS is able to detect senescent cells, the link between senescent cells and cancer can be investigated in vivo, potentially revealing an early marker for liver cancer.

Recruitment is ongoing for a study with Prof. Leanne Hodson from OCDEM investigating the effect of a two week isocaloric high-sugar diet on de novo lipogenesis (DNL) and a subset of those subjects will be scanned using the 7T ^{31}P-MRS protocol developed in this thesis. High-sugar diets have been proposed as a cause of the metabolic syndrome (12), potentially through DNL (13). Both DNL and sugar metabolism are closely linked to phosphorus energetics within the liver (14), and so ^{31}P-MRS would allow investigation of the changes in liver metabolism that are expected to be caused by the high-sugar diet.

11.3. Extensions and potential improvements

One target for improving the overall protocol is the automatic quality assurance. Although our method has been manually checked to ensure high accuracy and precision, it is expected that some high quality liver voxels are excluded and that some lower quality voxels are still included. This is an ideal problem for machine learning techniques, as thousands of voxels are acquired in each scan, and there are many different parameters to determine “quality” (15, 16). However, the limiting factor is the creation of a training dataset. This requires laborious manual labelling of many voxels, ideally by many experienced analysts.

The analysis of the spectra could potentially be improved by fitting multiple peaks to the P_i region. Although only a single peak is visible, it does not look like it has a Voigt lineshape. One possible reason for multiple peaks would be if both mitochondrial and cytosolic P_i were visible, from within the cell, with extra-cellular P_i also contributing to the overall signal.

To extend this protocol to other organs, additional CST simulations should be run to determine optimal conductivities for use in an ideal reference phantom. Simply applying the 18 mM field maps acquired for liver to other organs might give unacceptable errors.

The CST simulations were run for the 10 cm loop. Ideally, additional simulations should be run for individual coils. For more complex coils, such as the flexible 16 channel array, such simulations are challenging to set up correctly, requiring manual optimisation of meshing, tuning, and matching, and would be extremely time consuming. However, they would give a more accurate understanding of the effect of materials on each coil, and would allow more thorough investigation of the array combination methods described in Chapter 8.

This work can be used to guide the development of clinical applications at other field strengths. Both ATP and P_i, our proposed markers for cirrhosis, can be well resolved at 3 T, though there is potentially some contamination of the P_i peak by the underlying resonance from the endoplasmic reticulum. With the reduced field strength, the errors introduced by phantom composition will be smaller than at 7 T. This would also reduce the errors from the array combination. And with proper ^{1}H-decoupling and NOE enhancement, the difference between 3 T and 7 T can be minimized. Combined with the reduced scanner cost, 3 T systems are the clinically attractive choice. However, as development continues on 7 T systems, it may be found that the extra cost is worthwhile for specific applications.

To further improve the clinical relevance of the protocol at 7 T, it would be helpful to either make it shorter, improve the repeatability, or focus on a single parameter such that the difference between healthy and diseased livers is more prominent.

As the largest change is seen in γ-ATP and P_i, the 12 × 12 × 8 matrix could be used without a loss in diagnostic ability, as the increased errors were largely confined to PEP/PtdC, NAD^+, and UDPG. It may even be possible to target solely γ-ATP using an imaging method to obtain the highest possible resolution without diminishing SNR, or increasing scan time.

If the field map quality were improved, the errors in correction could be reduced. However, with the current phantom, it would be difficult to improve the field maps without increasing the acquisition time to an unreasonable length. It might be possible to add some other phosphorus containing compound to the phosphate solution to increase the phosphorus concentration without changing the conductivity or permittivity.

Improved hardware may also reduce errors. My colleagues in Oxford have recently published proof-of-concept with a new whole-body ^{31}P transmit coil, with a 35 kW ^{31}P RF amplifier and a 30-element receive array (17). Theory predicts that this will be able to achieve adiabatic excitation across the whole liver, with excellent receive SNR too. This would eliminate $\boldsymbol{B}_1^+$ from the $\boldsymbol{B}_1^-$ determination and saturation correction steps (because the flip angle of adiabatic pulses does not depend significantly on $\boldsymbol{B}_1^+$ above the adiabatic onset).

The other source of error in saturation correction is the T_1 relaxation time. In this work, the change in T_1 between healthy subjects and in cirrhotic livers was assumed to add negligible error to the final result. However, ^{31}P T_1 has been shown to change in liver disease, so this may not be entirely true (18). With a much shorter protocol, T_1 can be investigated across a larger range of healthy volunteers and patients.

One promising strategy to increase the difference between healthy and cirrhotic livers is to change from a static protocol to a dynamic protocol. For example, fructose could be infused (or ingested) to cause a change in metabolite concentrations (19, 20), or magnetization transfer methods could be used to probe kinetics as well as time-averaged metabolite concentrations (21, 22).

Whether at 7 T or at lower field strengths, the clinical relevance of ^{31}P-MRS will be improved by combining it with other modalities. For example, magnetic resonance elastography, or ^{1}H spectroscopy, imaging, and relaxation time mapping. Each of these provides additional information to enhance the diagnosis and staging of liver disease. For an effective clinical scan, the hardware would have to be combined to allow the acquisition of all relevant data in a single scan session.

The ^{31}P-MRS absolute quantification protocol that I have developed is an important first step in fully utilising the increased SNR afforded by the 7 T scanner. It offers valuable insight into liver metabolism, particularly in applications related to the cell growth cycle, and paves the way for other novel ^{31}P-MRS methods to be developed in the liver at 7 T or at lower field strengths.

11.4. References

1. Purvis LAB, Clarke WT, Biasiolli L, Valkovic L, Robson MD, Rodgers CT. OXSA: An open-source magnetic resonance spectroscopy analysis toolbox in MATLAB. Plos One. 2017; 12(9):e0185356.
2. Hastie T, Tibshirani R, Friedman J. The elements of statistical learning: Springer; 2001.
3. James G, Witten D, Hastie T, Tibshirani R. An introduction to statistical learning: Springer.
4. Beleites C, Neugebauer U, Bocklitz T, Krafft C, Popp J. Sample size planning for classification models. Anal Chim Acta. 2013; 760:25-33.
5. Halevy A, Norvig P, Pereira F. The Unreasonable Effectiveness of Data2009. 8-12 p.
6. Sharma S, Khalili K, Nguyen GC. Non-invasive diagnosis of advanced fibrosis and cirrhosis. World J Gastroenterol. 2014; 20(45):16820-30.
7. Tsochatzis EA, Gurusamy KS, Ntaoula S, Cholongitas E, Davidson BR, Burroughs AK. Elastography for the diagnosis of severity of fibrosis in chronic liver disease: A meta-analysis of diagnostic accuracy. J Hepatol. 2011; 54(4):650-9.
8. Hotamisligil GS. Endoplasmic Reticulum Stress and the Inflammatory Basis of Metabolic Disease. Cell. 2010; 140(6):900-17.
9. Szendroedi J, Chmelik M, Schmid AI, Nowotny P, Brehm A, Krssak M, Moser E, Roden M. Abnormal hepatic energy homeostasis in type 2 diabetes. Hepatology. 2009; 50(4):1079-86.
10. Ramakrishna G, Rastogi A, Trehanpati N, Sen B, Khosla R, Sarin SK. From Cirrhosis to Hepatocellular Carcinoma: New Molecular Insights on Inflammation and Cellular Senescence. Liver Cancer. 2013; 2(3-4):367-83.
11. Sanchez-Alvarez M, Zhang Q, Finger F, Wakelam MJO, Bakal C. Cell cycle progression is an essential regulatory component of phospholipid metabolism and membrane homeostasis. Open Biology. 2015; 5(9):150093.
12. Høstmark AT. The Oslo Health Study: Soft drink intake is associated with the metabolic syndrome. Applied Physiology, Nutrition, and Metabolism. 2010; 35(5):635-42.
13. Hellerstein MK. De novo lipogenesis in humans: metabolic and regulatory aspects. Eur J Clin Nutr. 1999; 53:s53.
14. Berg JM, Tymoczko JL, Stryer L. Biochemistry. Fifth Edition ed: W.H. Freeman; 2002.
15. Pedrosa de Barros N, McKinley R, Knecht U, Wiest R, Slotboom J. Automatic quality control in clinical 1H MRSI of brain cancer. NMR Biomed. 2016; 29(5):563-75.
16. Menze BH, Kelm BM, Weber MA, Bachert P, Hamprecht FA. Mimicking the human expert: Pattern recognition for an automated assessment of data quality in MR spectroscopic images. Magn Reson Med. 2008; 59(6):1457-66.
17. Valkovič L, Dragonu I, Almujayyaz S, Batzakis A, Young LAJ, Purvis LAB, Clarke WT, Wichmann T, Lanz T, Neubauer S, Robson MD, Klomp DWJ, Rodgers CT. Using a whole-body 31P birdcage transmit coil and 16-element receive array for human cardiac metabolic imaging at 7T. Plos One. 2017; 12(10):e0187153.
18. Cox IJ, Coutts GA, Gadian DG, Ghosh P, Sargentoni J, Young IR. Saturation effects in phosphorus-31 magnetic resonance spectra of the human liver. Magn Reson Med. 1991; 17(1):53-61.
19. Bawden SJ, Stephenson MC, Ciampi E, Hunter K, Marciani L, Macdonald IA, Aithal GP, Morris PG, Gowland PA. Investigating the effects of an oral fructose challenge on hepatic ATP reserves in healthy volunteers: A P-31 MRS study. Clin Nutr. 2016; 35(3):645-9.
20. Oberhaensli RD, Taylor DJ, Collins JE, Schwarz H, Rajagopalan B, Radda GK, Leonard JV, Herschkowitz N. Study of Hereditary Fructose Intolerance by Use of P-31 Magnetic-Resonance Spectroscopy. Lancet. 1987; 2(8565):931-4.
21. Schmid AI, Szendroedi J, Chmelik M, Krššák M, Moser E, Roden M. Liver ATP Synthesis Is Lower and Relates to Insulin Sensitivity in Patients With Type 2 Diabetes. Diabetes Care. 2011; 34(2):448-53.
22. Valkovič L, Bogner W, Gajdošík M, Považan M, Kukurová IJ, Krššák M, Gruber S, Frollo I, Trattnig S, Chmelík M. One-dimensional image-selected in vivo spectroscopy localized phosphorus saturation transfer at 7T. Magn Reson Med. 2014; 72(6):1509-15.